



**US Army Corps  
of Engineers**  
Waterways Experiment  
Station

# **Nonlinear, Incremental Structural Analysis for the Lower Miter Gate Monolith at Olmsted Locks and Dam**

by *Barry D. Fehl, Sharon Garner, WES*  
*Randy J. James, Robert S. Dunham, L. Zhang,*  
*ANATECH Research Corporation*



*"Original contains color plates: All DTIC reproductions will be in black and white"*



Approved For Public Release; Distribution Is Unlimited

19951011 017

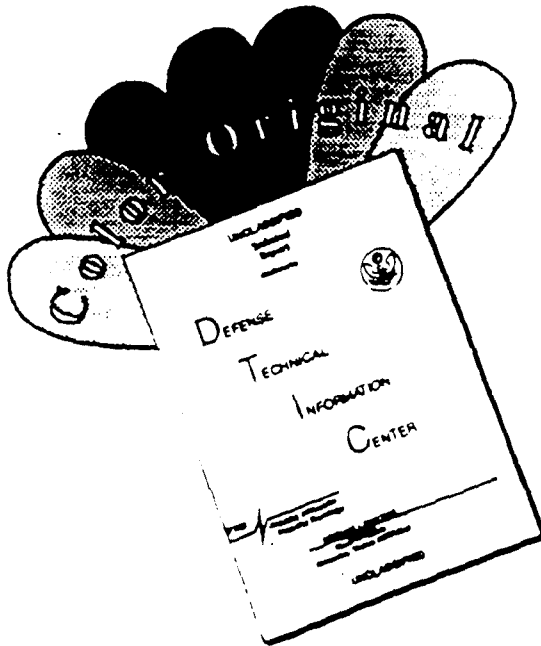
DTIC QUALITY INSPECTED 5

The contents of this report are not to be used for advertising, publication, or promotional purposes. Citation of trade names does not constitute an official endorsement or approval of the use of such commercial products.



PRINTED ON RECYCLED PAPER

# DISCLAIMER NOTICE



THIS DOCUMENT IS BEST  
QUALITY AVAILABLE. THE COPY  
FURNISHED TO DTIC CONTAINED  
A SIGNIFICANT NUMBER OF  
COLOR PAGES WHICH DO NOT  
REPRODUCE LEGIBLY ON BLACK  
AND WHITE MICROFICHE.

CEWES-ID-E

**MEMORANDUM FOR RECORD**

**SUBJECT: Blank Pages Not Numbered in Technical Report ITL-95-6**

1. Due to the fact that it is cost efficient to make one-sided copies of colored pages, please note that the following pages are not numbered and remain blank in Technical Report ITL-95-6, "Nonlinear, Incremental Structural Analysis for the Lower Miter Gate Monolith at Olmsted Locks and Dam"; 20, 22, 24, 26, 30, 38, 40, 46, 48, 54, 58, 62, 64, 68, 70, 72, 78, 80, 82, 84, 88, 90, 106, 108, 110, 112, 114, 116, 118, 120, 122, 124, 130, 132, 158, 160, 164, 166, 168, 170, 182, 184, 186, 188, 190, 192, 194, 196, 198, 204, 206, 208, 210, 212, 218, 220, 222, 224, 228, 230, 234, 236, 240, 242, 244, 248.
2. It should be further noted that pages 245-246 are out of place in this technical report. These two pages appear after page 247 instead of before it.



**BARRY D. FEHL**  
Civil Engineer

# Nonlinear, Incremental Structural Analysis for the Lower Miter Gate Monolith at Olmsted Locks and Dam

by Barry D. Fehl, Sharon Garner

U.S. Army Corps of Engineers  
Waterways Experiment Station  
3909 Halls Ferry Road  
Vicksburg, MS 39180-6199

Randy J. James, Robert S. Dunham, L. Zhang  
ANATECH Research Corporation  
5435 Oberlin Drive  
San Diego, CA 92121

Accession For	
NTIS	CRA&I
DTIC	TAB
Unannounced	
Justification _____	
By _____	
Distribution / _____	
Availability Codes	
Dist	Avail and / or Special
A-1	

Final report

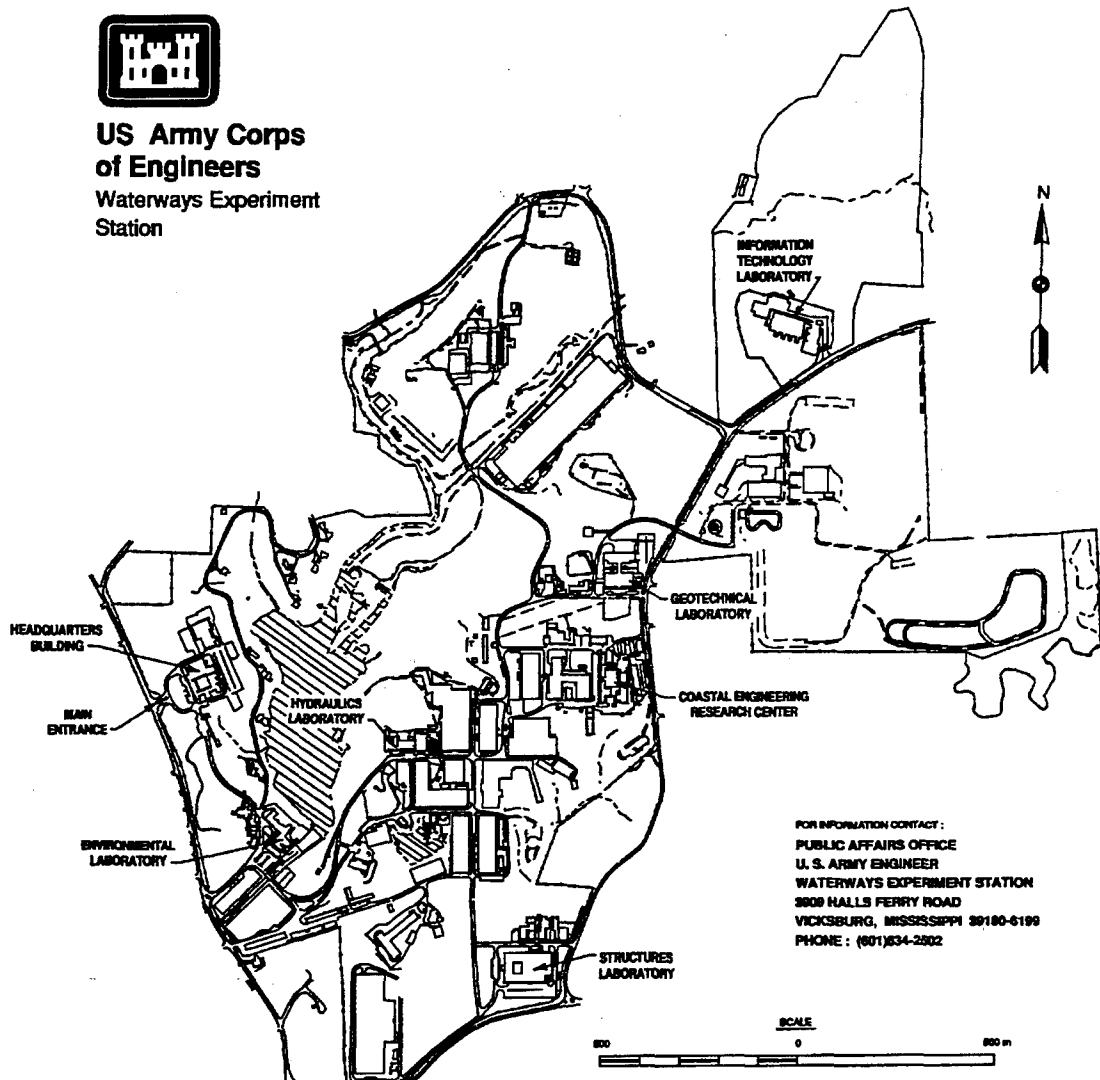
Approved for public release; distribution is unlimited

"Original contains color  
plates: All DTIC reproductions  
will be in black and  
white"



**US Army Corps  
of Engineers**

Waterways Experiment  
Station



**Waterways Experiment Station Cataloging-in-Publication Data**

Nonlinear, incremental structural analysis for the lower miter gate monolith at Olmsted Locks and Dam / by Barry D. Fehl ... [et al.] ; prepared for U.S. Army Engineer District, Louisville. 272 p. : ill. ; 28 cm. — (Technical report ; ITL-95-6)

Includes bibliographic references.

1. Locks (Hydraulic engineering) — Ohio River. 2. Structural analysis (Engineering) 3. Thermal stresses — Computer programs. 4. Hydraulic gates. I. Fehl, Barry D., 1957- II. United States. Army. Corps of Engineers. Louisville District. III. U.S. Army Engineer Waterways Experiment Station. IV. Information Technology Laboratory (U.S. Army Engineer Waterways Experiment Station) V. Series: Technical report (U.S. Army Engineer Waterways Experiment Station) ; ITL-95-6.

TA7 W34 no.ITL-95-6

# Contents

---

Preface . . . . .	v
Conversion Factors, Non-SI to SI Units of Measurement . . . . .	vii
1—Introduction . . . . .	1
Background and Objectives . . . . .	1
Scope and Approach . . . . .	3
2—Staged Construction Analysis . . . . .	5
Construction Parameters . . . . .	6
Coupled Thermal-Stress Procedure . . . . .	8
Material Properties . . . . .	8
Concrete Material Model . . . . .	10
3—Preliminary Calculations . . . . .	16
Baseline Mesh . . . . .	16
Reduced Mesh . . . . .	18
Conclusions . . . . .	28
4—Two-Dimensional Transverse Slice . . . . .	34
Model Description . . . . .	34
Baseline Analysis . . . . .	36
Placement Increment Study . . . . .	51
Floor Insulation Study . . . . .	59
Conclusions . . . . .	73
5—Two-Dimensional Longitudinal Slice . . . . .	75
Model Description . . . . .	75
Riverside Chamber Analysis . . . . .	76
Landside Chamber Analysis . . . . .	76
Conclusions . . . . .	87

6—Three-Dimensional Analysis . . . . .	92
Model Description . . . . .	92
Service Loads . . . . .	97
Analysis Results . . . . .	104
Conclusions . . . . .	135
7—Slab Redesign Analysis . . . . .	140
Design and Model Description . . . . .	140
Unit Cell Evaluation . . . . .	141
Analysis Results . . . . .	151
Conclusions . . . . .	175
8—Three-Dimensional Parametric Heat Transfer Study . . . . .	178
General . . . . .	178
Parameters of the Study . . . . .	178
Results of Analyses . . . . .	179
Conclusions . . . . .	199
9—Analysis of Heavily Insulated Floor . . . . .	201
Analysis Parameters . . . . .	201
Analysis Results . . . . .	203
Conclusions . . . . .	233
Heat Transfer Analysis with $R = 10$ . . . . .	245
10—Summary, Conclusions, and Recommendations . . . . .	250
Summary and Conclusions . . . . .	250
Recommendations . . . . .	251
References . . . . .	253
Appendix A: Subroutine HETVAL . . . . .	A1
Appendix B: Lift Placement Sequence . . . . .	B1
SF 298	

## Preface

---

The work described in this report was conducted for the U.S. Army Engineer District, Louisville, by the Computer-Aided Engineering Division (CAED), Information Technology Laboratory (ITL), and the Structural Mechanics Division (SMD), Structures Laboratory (SL), U.S. Army Engineer Waterways Experiment Station (WES), and the ANATECH Research Corp. The investigation was authorized by DD form 448, MIPR No. RMB-92-800, dated 3 Jun 1992.

The investigation was accomplished under the general supervision of Dr. N. Radhakrishnan, Director, ITL; Mr. Bryant Mather, Director, SL; and Mr. James T. Ballard, Assistant Director, SL, and under the direct supervision of Dr. Reed L. Mosher, SMD (formerly of CAED), Mr. H. Wayne Jones, CAED, and Dr. Robert L. Hall, SMD. This report was prepared by Mr. Barry D. Fehl of CAED, Ms. Sharon Garner, SMD, and Mr. Randy J. James, Dr. Robert S. Dunham, and Ms. L. Zhang of ANATECH Research Corp. The authors would like to acknowledge Mr. Byron McClellan and Mr. Jeff Bayers, CEORL-ED-DS, for their support and encouragement during the performance of the work described herein.

The work contained in this report is a portion of the Phase III, Nonlinear, Incremental Structural Analysis (NISA) Study of the Olmsted Locks. Analyses of a typical chamber monolith and a culvert valve monolith were also performed as part of the Phase III Study. The Phase III Study was a combined effort of Ms. Sharon Garner, SL, Messrs. Chris Merrill and Barry Fehl, ITL, and, working under contract to WES, Mr. Randy James and Dr. Robert Dunham, ANATECH. The entire Phase III NISA Study was a closely coordinated effort which included review meetings attended by representatives from Headquarters, the Ohio River Division, and the Louisville District. The Phase III NISA Study was a part of a larger WES effort on the Olmsted Project with Mr. Glenn Pickering of the WES Hydraulics Laboratory acting as the point of contact.

Review and direction of the work was provided by an Olmsted review team consisting of Messrs. McClellan and Bayers, Louisville District, Mr. Fehl, WES, Messrs. Don Dressler, Joe Hartman, and Tony Liu, Headquarters, U.S. Army Corps of Engineers, and Ms. Anjana Chudgar and Mr. Tom Hugerberg, Ohio River Division.

At the time of publication of this report, Director of WES was Dr. Robert W. Whalin. Commander was COL Bruce K. Howard, EN.

*The contents of this report are not to be used for advertising, publication, or promotional purposes. Citation of trade names does not constitute an official endorsement or approval of the use of such commercial products.*

# Conversion Factors, Non-SI to SI Units of Measurement

---

Non-SI units of measurement used in this report can be converted to SI units as follows:

Multiply	By	To Obtain
Btu/day/in./°F	498.4516	watts per meter kelvin <sup>1</sup>
Btu/day-in. <sup>2</sup> -°F	19,619.712	watts per day per meter per kelvin <sup>1</sup>
Btu/lb/°F	4,186.8	joules per kilogram per kelvin <sup>1</sup>
Fahrenheit degrees	5/9	degrees Celsius or kelvins <sup>1</sup>
feet	0.3048	meters
in./in./°F	9/5	meters per meters per degree Celsius
in. <sup>2</sup> -day-°F/Btu	0.00005097	meters squared per day per kelvin <sup>1</sup> per watt
kips/inch	1.213659	kilonewtons per meter
pounds per cubic foot	16.01846	kilograms per cubic meter
pounds per cubic inch	27,679.899	kilograms per cubic meter
pounds (force) per square inch	0.006894757	megapascals
square feet	0.09290304	square meter

<sup>1</sup> To obtain Celsius (C) temperature readings from Fahrenheit (F) readings, use the following formula:  $C = (5/9)(F - 32)$ . To obtain kelvin (K) readings, use:  $K = (5/9)(F - 32) + 273.15$ .

# 1 Introduction

---

## Background and Objectives

In September 1992, ANATECH Research Corp. began assisting the U.S. Army Engineer Waterways Experiment Station (WES) in the nonlinear incremental structural analysis (NISA) of Monolith 19 for the Olmsted Lock System to be constructed on the Ohio River at mile 964.4 below Paducah, KY. This lock is designed as a series of independent monoliths, each founded on piles and consisting of a thick slab section supporting three walls to form a W-frame cross section containing two parallel lock chambers. The monoliths are approximately 350 ft wide<sup>1</sup>, and in total they form a lock 1,200 ft long. Monolith 19, shown in Figure 1, houses the lower miter gates and also the crossovers of the four internal drains. These drains are 14-ft by 18-ft culverts embedded within the 28-ft-thick slab section that must sweep 90 deg to divert the longitudinal flow of water out the side of the monolith. This monolith is 134.5 ft long and, because of its length, it requires multiple concrete placements (lifts) along its length, thus creating vertical lift joints within the structure.

The objective of the analysis reported herein is to determine constructability of the structure by providing a basis for selecting the construction parameters to mitigate cracking during the construction process. The construction parameters of interest are the placing temperature of the concrete, the placement increments between lifts, the lift heights and geometry, and insulation requirements. In addition, the stresses across vertical lift joints are required for joint construction detailing, and reinforcing bar integrity must be evaluated if cracking does occur. Engineer Technical Letter (ETL) 1110-2-324, dated 30 March 1990, entitled "Special Design Procedures for Massive Concrete Structures," was provided to ANATECH by WES for guidance in this analysis effort. A WES March 1992 report entitled "Nonlinear, Incremental Structural Analysis for Olmsted Locks and Dam" (Garner et al. 1992) detailing previous work in this area was

---

<sup>1</sup> A table of factors for converting non-SI units of measurement to SI units is presented on page vi.

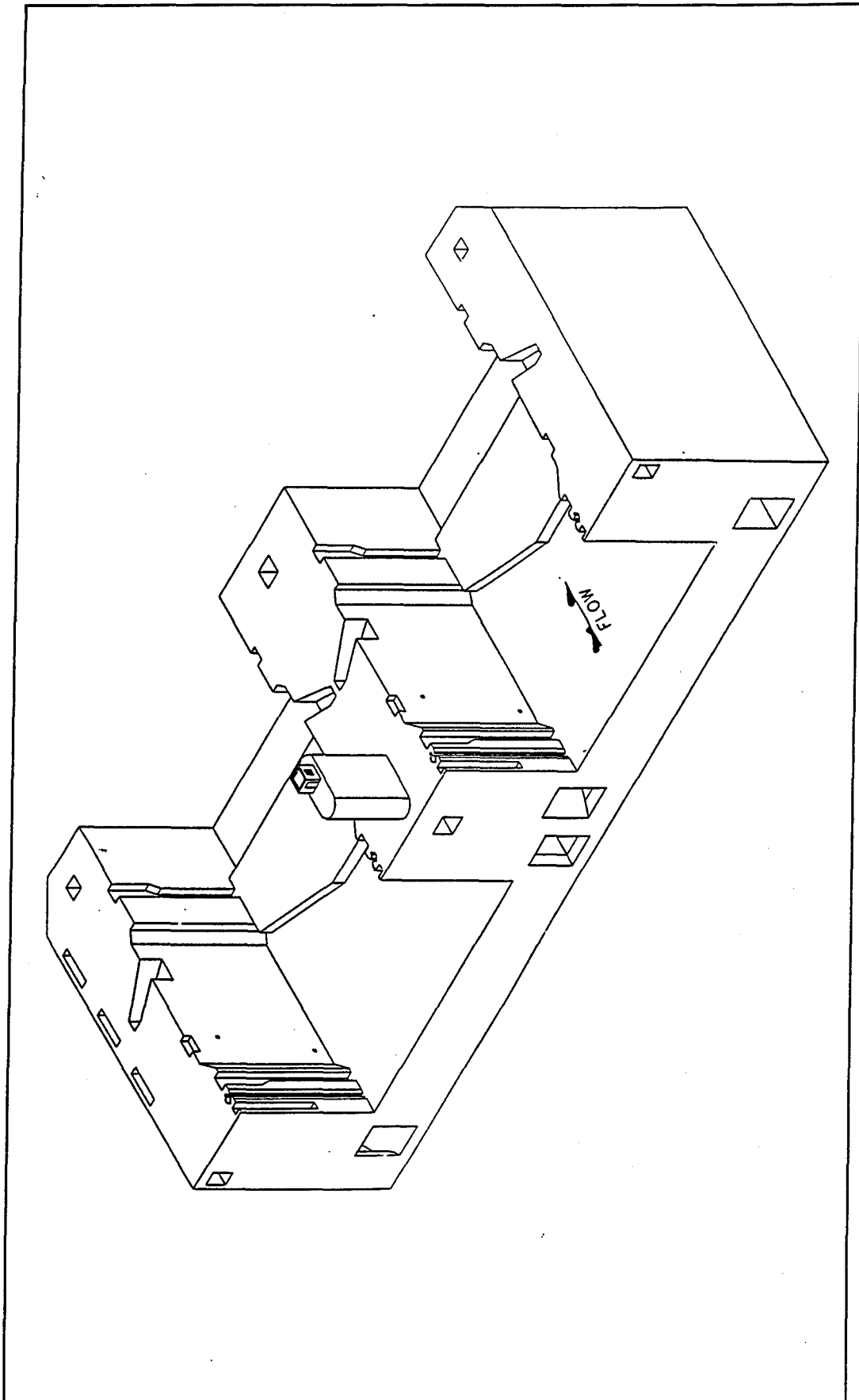


Figure 1. Lower miter gate monolith (M19) of Olmsted Locks

also provided by WES. This report is used extensively for establishing material properties and other modeling parameters, such as pile stiffness, for the current effort.

Review and direction of this work was provided by an Olmsted NISA review team consisting of personnel from Headquarters, U.S. Army Corps of Engineers; U.S. Army Engineer Division, Ohio River; U.S. Army Engineer District, Louisville; and WES.

## Scope and Approach

When a new concrete lift is placed during the construction process, the chemical reaction leading to hardening of the concrete produces heat within the material while the remaining exposed surfaces of the lift connect heat to and from the ambient environment. Because of the large number of lifts required (approximately 50), construction of the monolith will require a minimum of 250 days to complete, assuming 5 days between lifts, so that the structure will be subjected to both minimum and maximum ambient temperatures ranging from the low 20's to the mid 80's °F. Thus, for such massive structures, the thermal gradients and the constraint against thermal expansion can be substantial, leading to thermal-induced tensile stresses and potential cracking. To properly model this incremental construction process, the elements modeling each new lift must be added to those of the previous lifts, and the thermal response must be calculated and coupled to the stress solution. Mechanically, the material cannot carry load until it has aged sufficiently. Thus, the early time effects of creep, shrinkage, and aging must be adequately calculated for each lift in the time-and-temperature-history-dependent stress analysis. This dictates that a large number of load increments are required to properly model the history of each lift. The culvert geometry and lift sequence require a three-dimensional (3D) analysis; however, the size of the grid and the number of increments preclude 3D analyses for the needed parameter studies within the constraints of time and budget for the Olmsted project.

To meet the above-mentioned objectives in a timely and cost-effective manner, the following strategy was devised. Two-dimensional (2D) slice analyses will be used to evaluate the effects of required parameters on M19. These 2D parameter studies will establish the best estimates for the construction parameter optimizations. A final 3D analysis will then be used to establish 3D effects. Since few such 3D analyses have been performed and since they are more difficult to model and evaluate, ANATECH recommended that all initial design decisions be based on the 2D analyses. Guidance in ETL 1110-2-324 (based on previous 2D analyses) for element sizes in lifts may be restrictive in creating a 3D grid that can be solved in a timely manner. Thus, the first task of this effort was to qualify a mesh of less refinement than that established in ETL 1110-2-324 for both the 2D parametric studies and the 3D analysis. This will be done by comparisons of results for 2D analysis between a mesh density as

established in ETL 1110-2-324 and one more appropriate for 3D analysis under current computing resources.

Chapter 3 of this report describes these preliminary calculations to establish the mesh density to be used in subsequent calculations. Chapters 4 and 5 then describe the results of the 2D studies for transverse and longitudinal slices, respectively. Chapter 6 presents the results of the 3D analysis using the parameters selected from the 2D calculations. Chapter 7 provides results of a 3D analysis for a new and innovative composite slab design concept for massive concrete structures that evolved during the course of this project. Chapter 8 describes a parametric study of several proposed solutions for reducing the thermal gradient at the surface of the slab. Chapter 9 presents the results of a full heat transfer and stress analysis of the solution selected from the parametric study in Chapter 8. First, Chapter 2 follows describing general analysis procedures and material properties common to all the analyses.

## 2 Staged Construction Analysis

---

One of the more important design features of the miter gate monolith is the thickness of the slab. At 26 to 28 ft, it is the thickest of all the Olmsted monolith slabs. Although the slab thickness was not a parameter that was varied in these analyses, it has an important effect on the stresses induced in the slab by shrinkage and the temperature drop that corresponds to the coldest winter day. In general, the thicker the slab, the greater the induced thermal stresses. This occurs because the increased thickness increases the flexural stiffness of the slab, which in turn increases the restraint on the deformations. If the slab is free to expand or contract, there would be almost no thermally induced stresses. Therefore, the greater the restraint on the thermally induced deformations, the greater the corresponding stresses.

This chapter is devoted to a description of some of the features of the models and analyses that are common to all the subsequent chapters. This includes sections which describe the design parameters studied, the analysis procedure used to conduct the coupled thermal and mechanical analyses, the mechanical and thermal properties, and the concrete material model and its associated model fitting.

In evaluating the results of these analyses, it is important to remember that these are complex and sophisticated models and analytical algorithms. The analyses are nonlinear and the effects of parameter changes do not follow the usual principle of superposition. The state of the art being utilized here is well beyond the boundaries of linear elastic analysis. The reader is cautioned not to base conclusions or decisions on extrapolations from linear elastic analysis experience. Analytical evaluation is recommended because in these nonlinear analyses there can be unexpected synergisms.

## Construction Parameters

There are many important design parameters that affect the thermally induced stresses and associated cracking. These include:

- a. The size of the monolith, the lift placement sequence, and the number and height of lifts.
- b. The time between lift placement.
- c. The ambient temperature environment.
- d. The date construction begins.
- e. The temperature at which the concrete is placed.
- f. The time that the concrete sets.
- g. The reinforcement in the concrete.
- h. The effectiveness of insulation.
- i. The thermal and mechanical properties of the concrete.

Obviously, not all these parameters were varied in the analyses. The size of the monolith, the construction start date, and the concrete set time were not varied. The effects of changing the number of lifts or the placement temperature or the lift placement sequence were not studied. However, the lift placement sequence was changed by the Louisville District Office, and the placement temperature was set after the preliminary calculations were completed and reviewed. The 2D transverse and longitudinal slice and 3D models reported herein used the updated lift placement sequence and a maximum placement temperature of 60 °F.

The time between lift placements was studied in the analyses. Placement intervals of 5 and 10 days were studied. It is likely that there is a close relationship between the effects of the time between lift placements, the ambient temperature environment, and the date construction begins, particularly for a structure this large. Since there are 50 lifts, if there are 5 days between lifts, then the time to completion of construction is over 8 months. If there are 10 days between lifts, then construction will require more than 1 year and 4 months. Obviously, when construction is extended this long, the start date is significant because the critical stresses for cracking generally occur at the coldest winter day. For long construction sequences, it is possible that the most extreme conditions will not occur until the second year. Thus, is it possible to abate the extreme ambient conditions until the structure is in operation and partially submerged so that extreme low temperatures in the slab are avoided.

All of ANATECH's analyses of Monolith 19 were based on a June 20 start date. This was not varied. Two ambient temperature conditions were used in the analyses. An "average" ambient temperature was used in some of the preliminary analyses. The average ambient temperature varied from a high of 77 °F on day 25 (July 15) to a low of 32 °F on day 205 (December 22). The "extreme" ambient temperature was used for all subsequent 2D and 3D analyses. In making design decisions related to the ambient temperature, the reader is cautioned to take into account that the extreme ambient condition is ~10 °F colder on the coldest winter day. This is important because a drop of 10 °F can induce up to 40 microns of strain, and this is 40 percent of the cracking criterion. The decision to use the extreme ambient conditions was based on the recommendation of the Olmsted NISA review team.

Another parameter strongly related to the ambient temperature is the maximum placement temperature. This is controlled in order to reduce the temperature drop from the time of placement to the coldest winter day. Again, this was varied in the preliminary analyses which used average ambient temperature placement, 70 °F maximum placement temperature, and 60 °F maximum placement temperature. In order to control shrinkage and thermal stresses, a maximum placement temperature of 60 °F was used for the parameter studies.

The time following placement in which the concrete sets (that is, becomes sufficiently stiff that it begins to carry stress) is a parameter that has a noticeable effect on the analysis results at early time, but it appears to have a small effect at long times (>30 days). Still, the Olmsted NISA team was concerned about this parameter. Some of the preliminary analyses used a 6-hr set time. Following a careful study by the team, it was decided that under typical ambient conditions set occurred at 12 hr. This value was used in all subsequent analyses, and the effect of this change was not studied further. The set time also is important to the coupling between the thermal and mechanical solutions because, during the set time, the new elements in the lift are active and generating heat, while these same elements are not yet active in the mechanical solution.

Reinforcement of the concrete with steel reinforcing bars is standard Corps practice for this type of structure. Reinforcement is used to provide conventional slab flexural resistance and to reinforce galleries and culverts. Reinforcement also resists crack formation. However, reinforcement is not as efficient in resisting thermal cracking in mass concrete structures as it is in providing conventional flexural resistance. This is because the reinforcing bars provide only about 10 percent of the combined concrete/reinforcing bar stiffness. Some of the preliminary analysis models did not include reinforcement. The subsequent transverse slice and 3D analyses included reinforcement in the models.

Since the critical stresses are thermally induced, the thermal boundary conditions are important parameters, particularly when they can be effectively used to reduce heat loss in the coldest winter period. Obviously,

there are important interactions here between the start date, the lift placement schedule, and the thermal boundary conditions. The thermal boundary conditions that vary are the time interval that the slab and wall insulation is maintained and its "R" level and the covering of the gallery/culvert openings. Systematic parameter studies of these effects were not conducted. In general, the thermal boundary conditions used in the analyses followed the recommendations of the Olmsted NISA review team.

Obviously, the thermal and mechanical properties of the concrete are important parameters. However, these have not been varied; rather, the best estimates of these properties have been used in the analyses reported herein. These properties are described in the next sections. The same properties have been used in all analyses.

## Coupled Thermal-Stress Procedure

In order to predict the stresses induced by temperature, aging, shrinkage, and creep in the monolith, it is necessary to carry out a coupled analysis of the thermal and mechanical responses. Since the thermal response is independent of the mechanical response, but the mechanical response is dependent on the thermal response, the thermal analysis is conducted for the entire construction under the relevant ambient temperature history first. Once the thermal analysis is complete, the mechanical analysis is run using the temperature history computed and saved from the thermal analysis. This is a complex procedure that requires creating two separate ABAQUS input files for the thermal and mechanical analyses (with Diffusion and Continuum elements, respectively), but with exactly the same grid of nodes and elements for the concrete. A totally different set of boundary conditions must be applied to the thermal and mechanical solutions. A similar set of model changes to the active grid is made in order to support the 50 lifts, and the solution time steps are likewise similar. However, the two solution strategies and time steps are not identical. Note that in the mechanical solution it is not necessary to use exactly the same time steps used in the thermal solution. Usually the steps are the same, but if they are different, then the mechanical solution will interpolate the thermal solution at the necessary times. As discussed earlier, the thermal model for the new lifts is activated at the start of lift construction, and the mechanical model is activated after the new lift has set, 6 or 12 hr later.

## Material Properties

All of the thermal and mechanical properties used in the analyses were based on data described in WES Technical Report SL-91-9. Two different final mixes were studied; these were identified as Mixture 6 and Mixture 11

in the report. The material properties used in the analyses were chosen based on the recommendations of the Olmsted NISA review team.

### Thermal properties

Generally, the thermal properties of the two Olmsted mixes were similar. The means of the measured values for the linear coefficient of thermal expansion (this is more appropriately a mechanical property) of the two mixes were  $3.85$  and  $3.81 \times 10^{-6}$  in./in./°F. The value used in all the analyses was  $4 \times 10^{-6}$  in./in./°F.

The mean values of the measured thermal diffusivity of the two mixes were  $0.0335$  and  $0.0349$  ft<sup>2</sup>/hr. The mean values of the measured specific heat of the two mixes were the same,  $0.219$  Btu/lb/°F. The values of the thermal conductivity, which were calculated in accordance with CRD-C 44-63 (1990), were  $1.08$  and  $1.12$  Btu/hr/ft<sup>2</sup>/°F. The unit weights measured for the two mixes were  $143$  lb/ft<sup>3</sup> and  $153$  lb/ft<sup>3</sup>. Table 1 summarizes the thermal properties used in the analyses. The table also includes the thermal properties used for the soil.

**Table 1**  
**Thermal Properties**

Property	Units	Concrete	Soil Layers	
			Bottom	Top
Unit weight	lb/in. <sup>3</sup>	0.0845	0.0683	0.06366
Specific heat	Btu/lb/°F	0.22	0.395	0.263
Conductivity	Btu/day/in./°F	2.24	1.525	1.663

The adiabatic temperature rise data for Mixture 11 were used to develop an internal heat generation model for ABAQUS using user subroutine HETVAL. A listing of this subroutine, coded for 5-day placement increments, is provided in Appendix A. These data gave a temperature rise of  $12$  °F in 1 day and reached a maximum rise of  $45$  °F in 27 days.

A heat transfer boundary condition was used to model the heat conduction to and from the imposed ambient temperature history. Table 2 provides the film coefficients, by time of year, used in the analyses.

### Mechanical properties

The mechanical properties of the concrete and reinforcement used in the analyses likewise were taken from the WES Report SL-91-9 and were

**Table 2**  
**Film Coefficients for Heat Transfer Analysis**

Time Period	Film Coefficient (Btu/day-in. <sup>2</sup> -°F)			
	Wind Only	Wind and Forms	1-ft Sand Insulation	R = 2, Vertical Insulation
Jun - Sep	0.4727	0.1295	0.1591	—
Oct	0.5552	0.1350	0.1675	—
Nov - Apr	0.6998	0.1421	0.1786	0.0745
May	0.5387	0.1340	0.1659	—

approved by the Olmsted NISA review team. Some of the data from the report was used to fit the concrete material models described in the next section. These include the concrete modulus (aging), shrinkage, and creep models.

The unit weight of the concrete used to define the gravity loads was 0.0845 lb/in.<sup>3</sup> (146 lb/ft<sup>3</sup>). The linear coefficient of thermal expansion of the concrete was  $4 \times 10^{-6}/^{\circ}\text{F}$ , and the Poisson's ratio was 0.15. In general the mechanical properties were taken from the Mixture 11 data except for the shrinkage, which was based on Mixture 6 data because of the unusual characteristics of the Mixture 11 shrinkage. The compressive strength of the concrete is not an important parameter in the analyses because the compressive stresses are well below yield (that is, the strength). The compressive strengths of the two mixes were nearly the same. They varied from 675 psi at 3 days to about 5,000 psi at 180 days.

## Concrete Material Model

Modeling the constitutive (stress-strain) behavior of young concrete, that is, concrete younger than 30 days, is an extremely difficult task. As specified in the ETL 1110-2-324, the Olmsted concrete material behavior was modeled with the ANATECH ANACAP-U constitutive model (see ANATECH Reports ANA-92-0129, User's Manual, March 1992, and ANA-92-0130, Theory Manual, May 1992). In fact, the ANATECH ANACAP-U young concrete model was specifically developed under an earlier WES contract in order to more accurately model the aging, shrinkage, and creep behavior of these concretes (see WES Reports SL-91-7 and REMR-CS-15 (1988), and ANATECH Report ANA-85-0027). During the course of this Olmsted analysis, it was necessary to make some modifications to the ANACAP-U concrete constitutive model (ANACON) in addition to incorporating the Olmsted model fits into ANACON. The modifications that were required were:

- a. Converting the aging effects on the creep compliance back to the original 1987 formula.
- b. Eliminating the effects of temperature on the aging magnitude and the magnitude of the creep compliance.
- c. Correcting the time-temperature shift function, and limiting the effect of temperature to the shifting of the time increment to an equivalent increment at ambient temperature.
- d. Modifying the cracking interaction curve to properly account for the effects of aging.

The effects of the first three modifications are considered to be minor, other than matching the original intent of the creep compliance model fitting. While temperature undoubtedly has an effect on the magnitude of aging and creep, this has not been quantified and cannot be adequately treated during model fitting. Eliminating these temperature effects and adding the temperature shifting of the time increment appear to have substantially improved the performance of the model as well as reducing the complexity of the model fitting.

The modification of the cracking interaction curve to properly account for the effects of aging is described below.

### Shrinkage, creep, and aging

The development of the shrinkage, creep, and aging models was based on the data and model fitting described in Technical Report SL-91-9. The aging model is based on the Mixture 11 modulus data which were fit to the following decaying exponential series.

$$E(t) = E_o + \sum E_i \left( 1 - e^{-\sum r_i (t-1)} \right)$$

where

i	$E_i$ (psi)	$r_i$ (1/days)
0	$0.570 \times 10^6$	
1	$2.860 \times 10^6$	0.0595
2	$2.632 \times 10^6$	0.883
3	$-0.978 \times 10^6$	2.65

Thus, the modulus increases from  $0.57 \times 10^6$  psi at 1 day to  $2.1 \times 10^6$  at 3 days to  $5 \times 10^6$  at about 120 days. The aging function is defined to be the ratio of the modulus at any age to the modulus at 3 days, which is taken as the reference age for material property specification.

The shrinkage model likewise is defined using a series of decaying exponentials.

$$S(t) = \sum S_i (1 - e^{-r_i t})$$

where for Mixture 6

I	$S_i$ (in./in.)	$r_i$ (1/day)
1	$58.69 \times 10^{-6}$	0.0226
2	$9.46 \times 10^{-6}$	0.15

As discussed earlier, the Mixture 6 shrinkage data were used because of the unusual nature of the Mixture 11 shrinkage. To account for data scatter and in order to promote conservatism in the stress predictions, the Olmsted NISA team recommended following ETL 1110-2-324 guidelines for shrinkage factoring. Thus, the shrinkage equation described above was multiplied by 1.1 in all analyses.

Fitting the creep compliance coefficients to match the measured Mixture 11 creep data is difficult because the effects of aging and shrinkage cannot be separated in the testing. Also, in the ANATECH ANACON concrete model, the aging factor has an effect on the creep compliance so that the compliance coefficients that are input to the model do not correspond one-to-one to the predicted creep response. Thus, the model fitting typically is an iterative process. The specific creep compliance also is fit to a decaying exponential series.

$$J(t) = \sum A_i (1 - e^{-r_i t})$$

where for Mixture 11

I	$A_i$ (in./in.)	$r_i$ (1/day)
1	$0.39486 \times 10^{-6}$	0.05298
2	$0.22632 \times 10^{-6}$	0.6623
3	$0.12595 \times 10^{-6}$	2.649

## Cracking criteria

The cracking criteria used in the ANACON concrete constitutive model are critically important to the analyses of the Olmsted monoliths, and they were the subject of intense scrutiny by the Olmsted NISA team. As discussed earlier, a modification to the criteria was made in order to correct an error in the cracking behavior for young concrete. This correction was reviewed and accepted by the team.

For mature concrete, ANATECH's cracking criteria have always been in the form of an interaction curve between the stress and strain normal to a potential crack plane. This interaction curve for a typical 3,000-psi concrete is illustrated in Figure 2 for a typical 3,000-psi concrete. The interaction curve is anchored to the uniaxial tensile failure point, which the Corps of Engineers has always accepted to occur at a strain of 100 m and a stress of  $E (3 \times 10^6 \text{ psi})$  in Figure 2 times 100 m, or 300 psi. The interaction curve is based on numerous observations that cracking at biaxial or triaxial tensile states occurs at higher stresses and lower strains than uniaxial, and that cracking on planes with high transverse compression occurs at lower stresses and higher strains than uniaxial. Figure 2 illustrates typical triaxial tensile cracking and split cracking, that is, cracking at very low stress but high transverse compression.

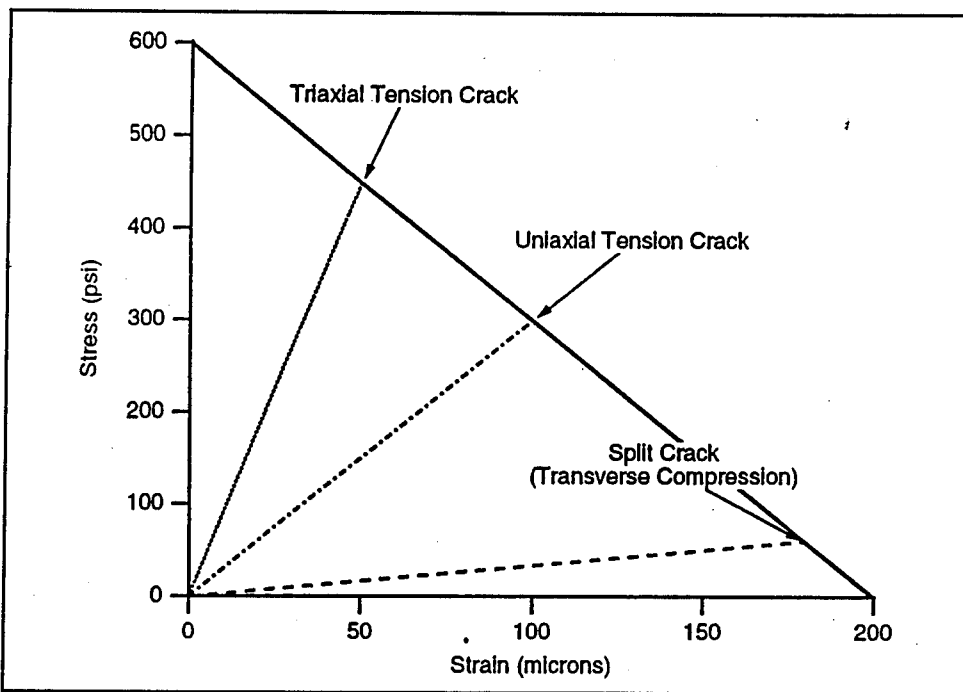


Figure 2. Mature concrete cracking interaction curve

Figure 3 shows the cracking criteria recommended by ANATECH and accepted by the Olmsted NISA team for the young Olmsted concrete. The 1-day, 3-day, and 30-day cracking and uniaxial stress-strain tension response are shown in Figure 3. These criteria are based on the assumption

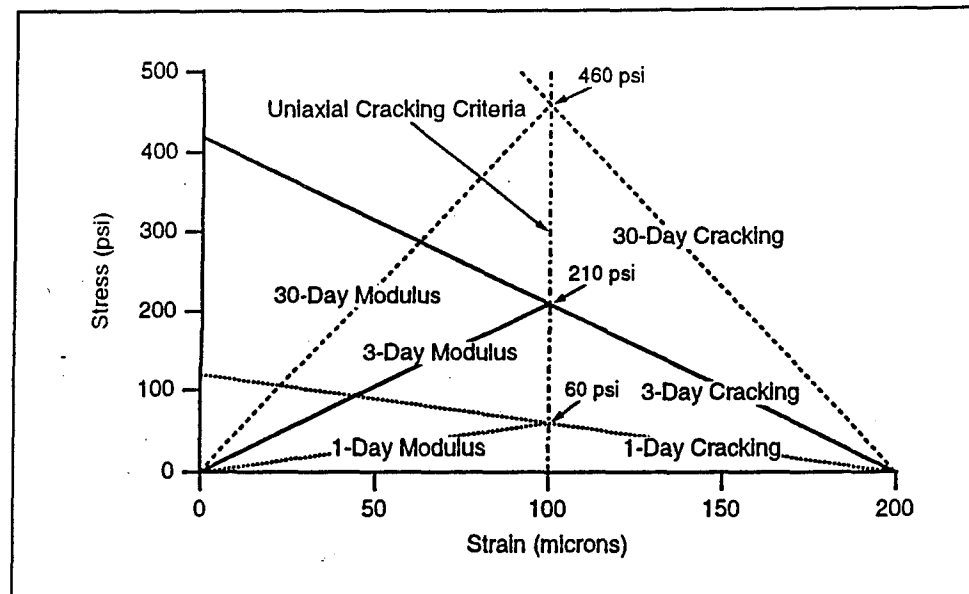


Figure 3. Olmsted cracking interaction criteria

that all uniaxial cracking occurs at 100 m. While there needs to be additional data taken to validate this assumption, it is consistent with the criteria used for mature concrete and with all available Corps of Engineers data. Also, as shown in Figure 4, the Olmsted criteria are in excellent agreement with the ETL 1110-2-324 recommendation on concrete tensile strength.

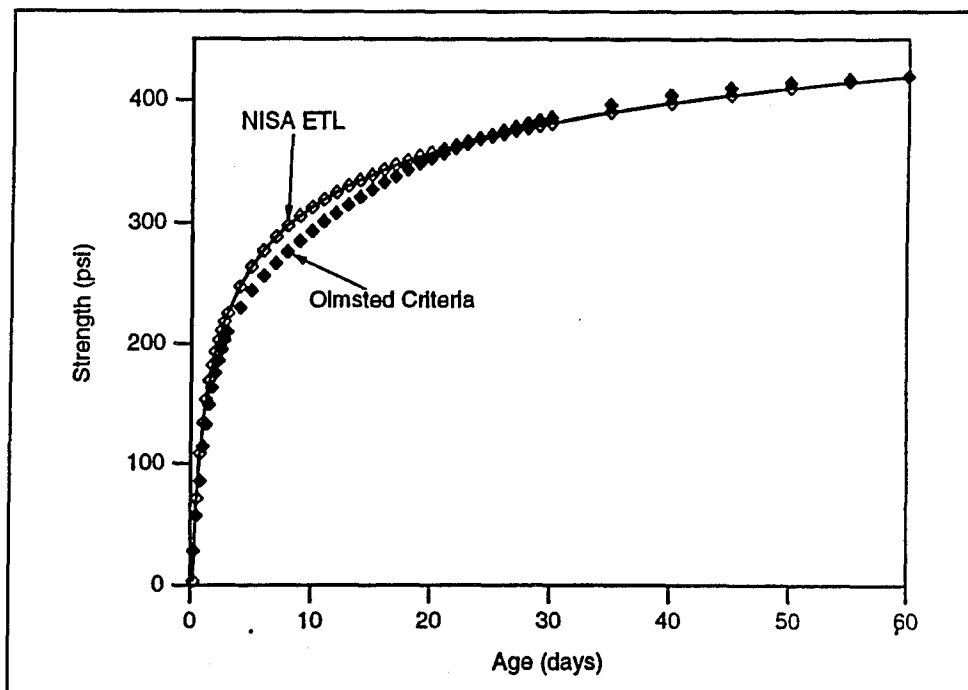


Figure 4. Comparison of cracking strengths with age

## Cracking potential

One of the most important objectives of these analyses is to assess the cracking potential of the monolith. As shown in Figures 3 and 4, this is a difficult task because the strength of the concrete is changing very rapidly up to an age of 30 days. To this end, ANATECH enhanced the ANACAP-U package such that contour plots of the cracking potential could be obtained. The cracking potential is defined to be the fraction of the cracking criteria obtained by the various stress and strain states. The cracking potential interaction curves for Olmsted 3-day concrete are shown in Figure 5, and note that the 3-day cracking criteria shown in Figure 5 are the same as Figure 3. Thus, the cracking potential is a function of the stress and strain across a potential crack and the age of the concrete.

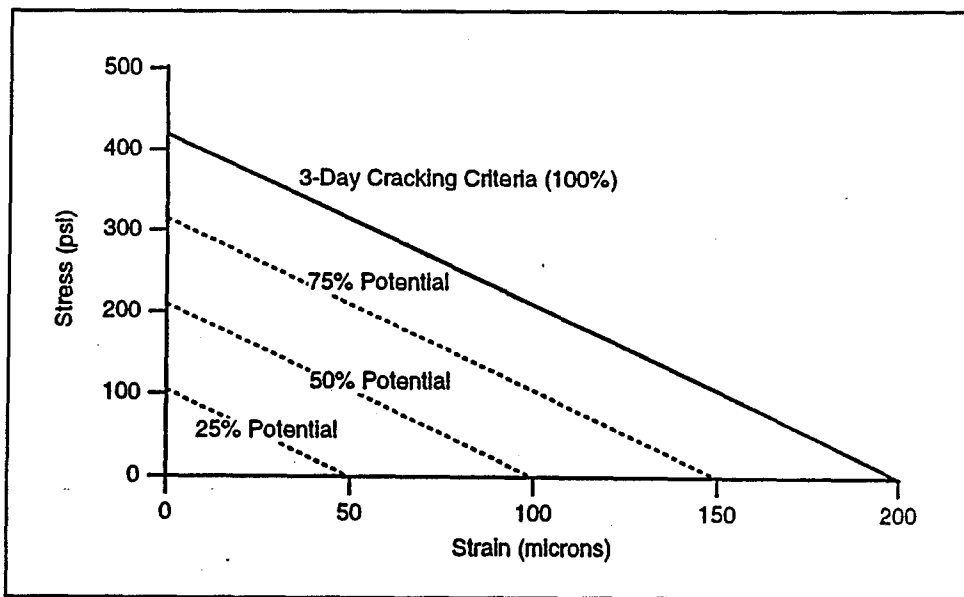


Figure 5. Olmsted 3-day cracking potential

# 3 Preliminary Calculations

---

The primary objective of this effort was to establish construction parameters through NISA procedures that mitigate cracking potential in Monolith 19 of the Olmsted Lock System. In light of the current unknowns in extrapolating 3D results from 2D analyses, the size, geometry, and placement sequences for this structure dictate that a 3D analysis is required to capture all potential cracking effects. However, it was obvious that 3D analyses based on the guidelines of ETL 1110-2-324 for NISA procedures could not be accomplished under the current constraints of budgets and schedules, especially considering the combinations of construction parameters that were to be investigated. Therefore, the first task was to define modeling techniques, as extensions to the guidelines in ETL 1110-2-324, that will substantially reduce the computational effort needed, while maintaining acceptable levels of accuracy in the cracking potential predictions. This chapter describes this task of establishing and qualifying a reduced density mesh to be used in subsequent calculations. The two areas of investigation for mesh reduction are: (a) elimination of modeling the complete walls, and (b) relaxation of the guideline requiring two layers of elements through the thickness of each lift. The first eliminates elements in regions of low cracking potential, and the second will substantially reduce the remaining mesh if one element can be used through the thickness of each lift. The evaluation for acceptable levels of accuracy will be made by comparison of results from a mesh fully compliant with ETL 1110-2-324 with that from a reduced mesh.

## Baseline Mesh

The baseline construction parameters and material properties described in Chapter 2 were used as the basis for these mesh qualification studies. The mesh shown in Figure 6 was developed in strict adherence to ETL 1110-2-324 guidelines recommending two elements through the thickness of each lift. This mesh models all lifts forming the complete wall heights. The transient thermal solution was calculated using 0.25-day time steps during lift placement, as recommended in ETL 1110-2-324 based on the element size of approximately 2 ft through the vertical dimension as the critical direction of heat flow. This recommendation is based on studies

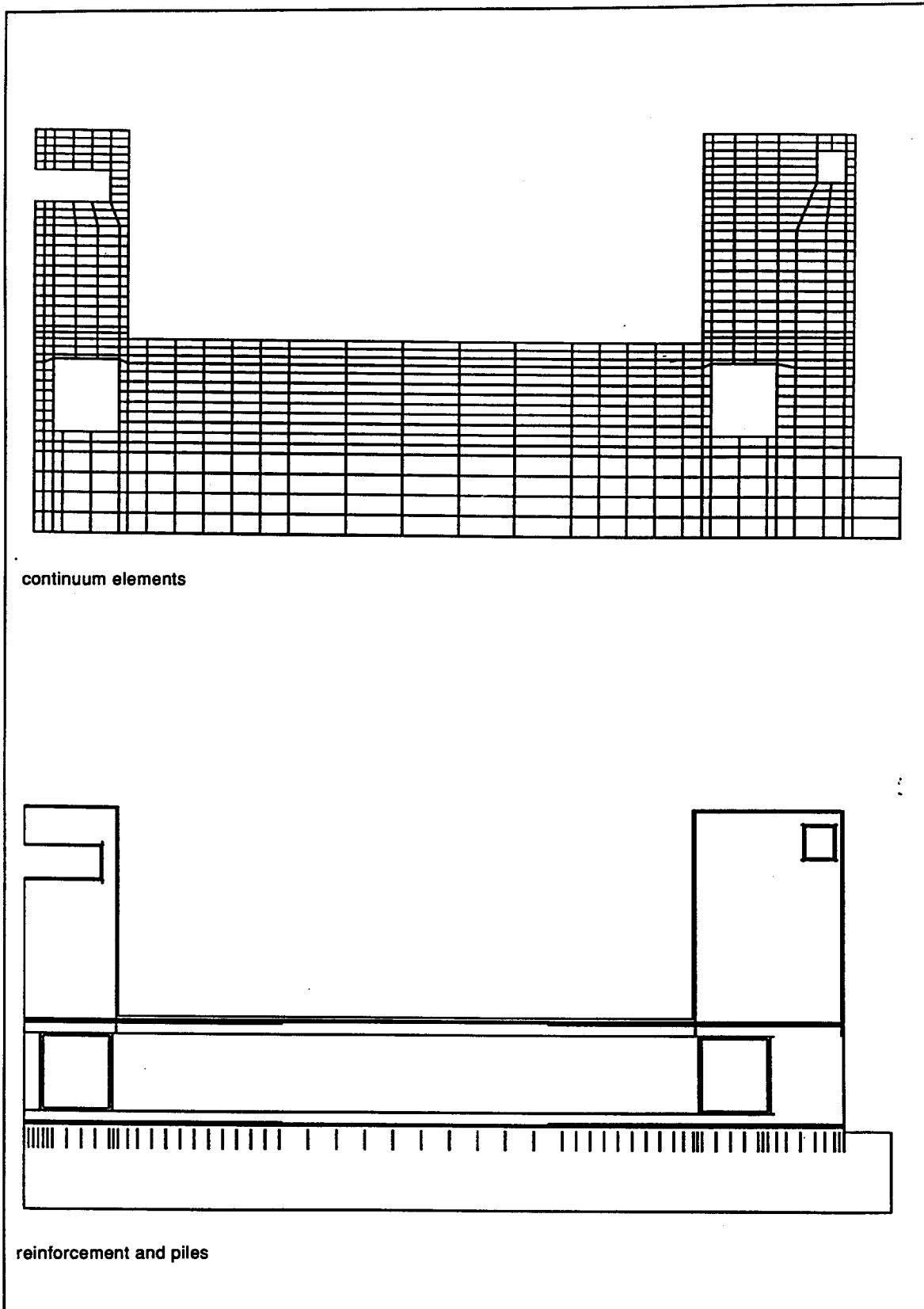


Figure 6. Finite element model for baseline mesh analysis

using 0.25-day increments for evaluating the early time concrete creep response. For transient heat transfer calculations, the element size is related to the time step size for stable integration as defined in the ABAQUS manuals. Figure 7 shows thermal contours for the indicated snapshots in time. These plots clearly show the thermal gradients that develop as the interior of the slab generates heat due to the heat of hydration and the heat flows toward free surfaces to be convected to cooler ambient temperatures. These plots show that the ambient temperature, and thus the concrete surface temperature, drops faster than the heat is conducted away from the interior so that larger thermal gradients can exist across the slab even late in time when the interior has cooled significantly. The stress analysis was then conducted using the established procedures coupled to these nodal temperature histories. Figure 8 shows maximum principal stress contours for the indicated points in time. These plots clearly show that the potential for cracking in the walls is very low compared with that in the base slab and in the junctions of the slab and the walls. These results are used to justify eliminating the majority of the walls from the stress analysis, provided a comparable temperature distribution can be maintained in the remaining stub walls in the thermal solution.

## Reduced Mesh

The reduced mesh or coarse grid shown in Figure 9 was developed for comparison of results with the baseline mesh described above. This grid employs stub walls in which only three lifts of the walls are modeled for the stress solution. To address the requirement of preserving the temperature distribution in the areas of these stub walls, an extra lift on each wall is included in the thermal solution to capture the heat generated on top of the stub wall. In addition, as the next lift is placed above, the surface of the thermal stub wall is held in an adiabatic condition so that no heat is lost across this boundary. This reduced mesh also uses only one quadratic displacement element through the thickness of each lift. The exception is seen to be the lift that forms the roof of the culverts. However, this was chosen only for ease of modeling the 1-ft offset between the lift height and the culvert height and not for any perceived need for capturing thermal or stress gradients in this lift. Since the element size in the critical heat flow direction has doubled, the thermal time step is doubled for consistency with ETL 1110-2-324 guidelines, and the thermal solution is calculated with 0.5-day time increments during lift placements.

The resulting thermal contours at selected points in time corresponding to the baseline mesh are shown in Figure 10. The thermal contour shapes and minimum and maximum temperatures are seen to be very consistent between this analysis and the previous baseline analysis. The temperature distributions in the stub wall areas are in excellent agreement. Complete temperature history comparisons of selected points midway in the first and last layer of lifts are shown in Figure 11. These figures demonstrate

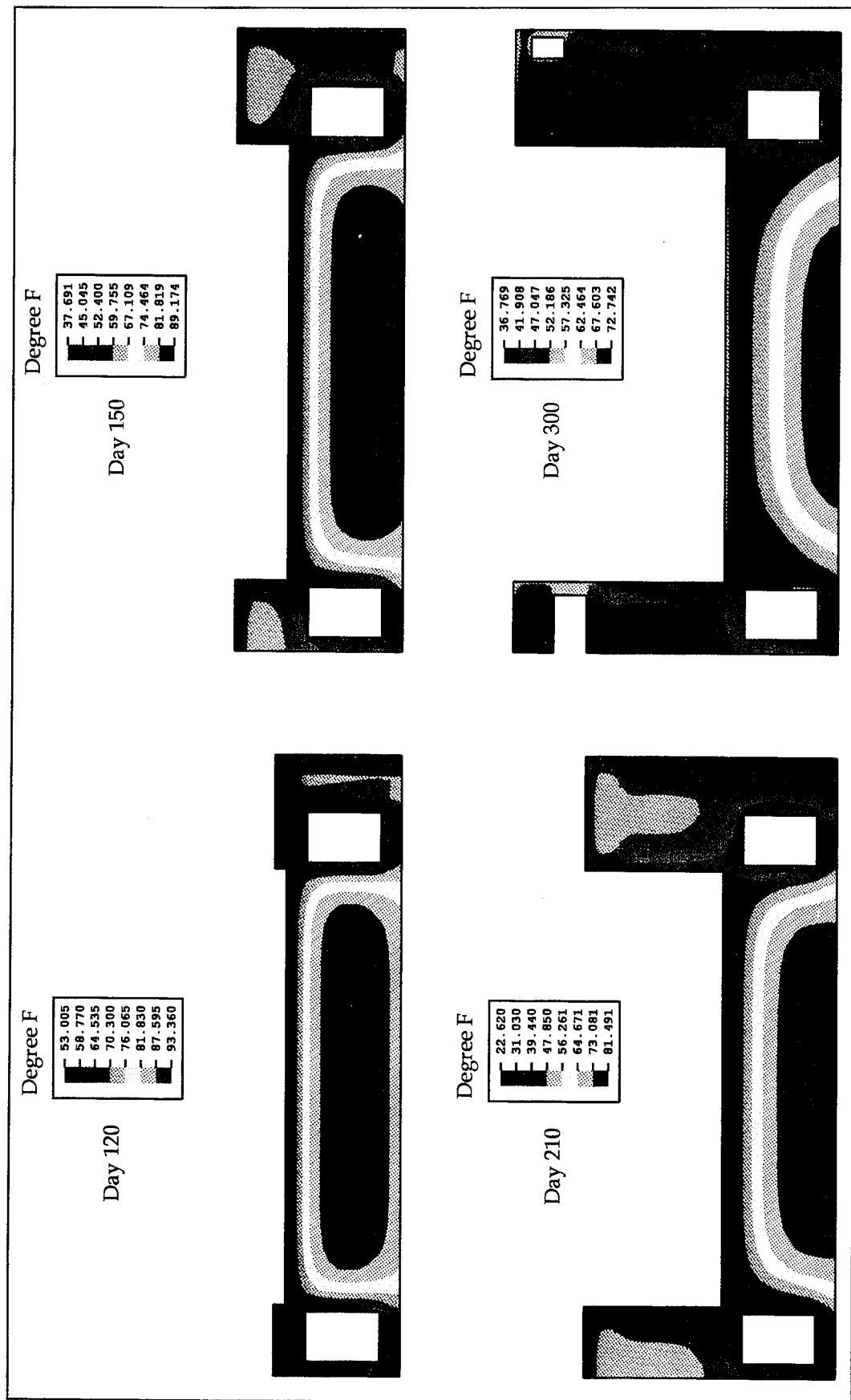
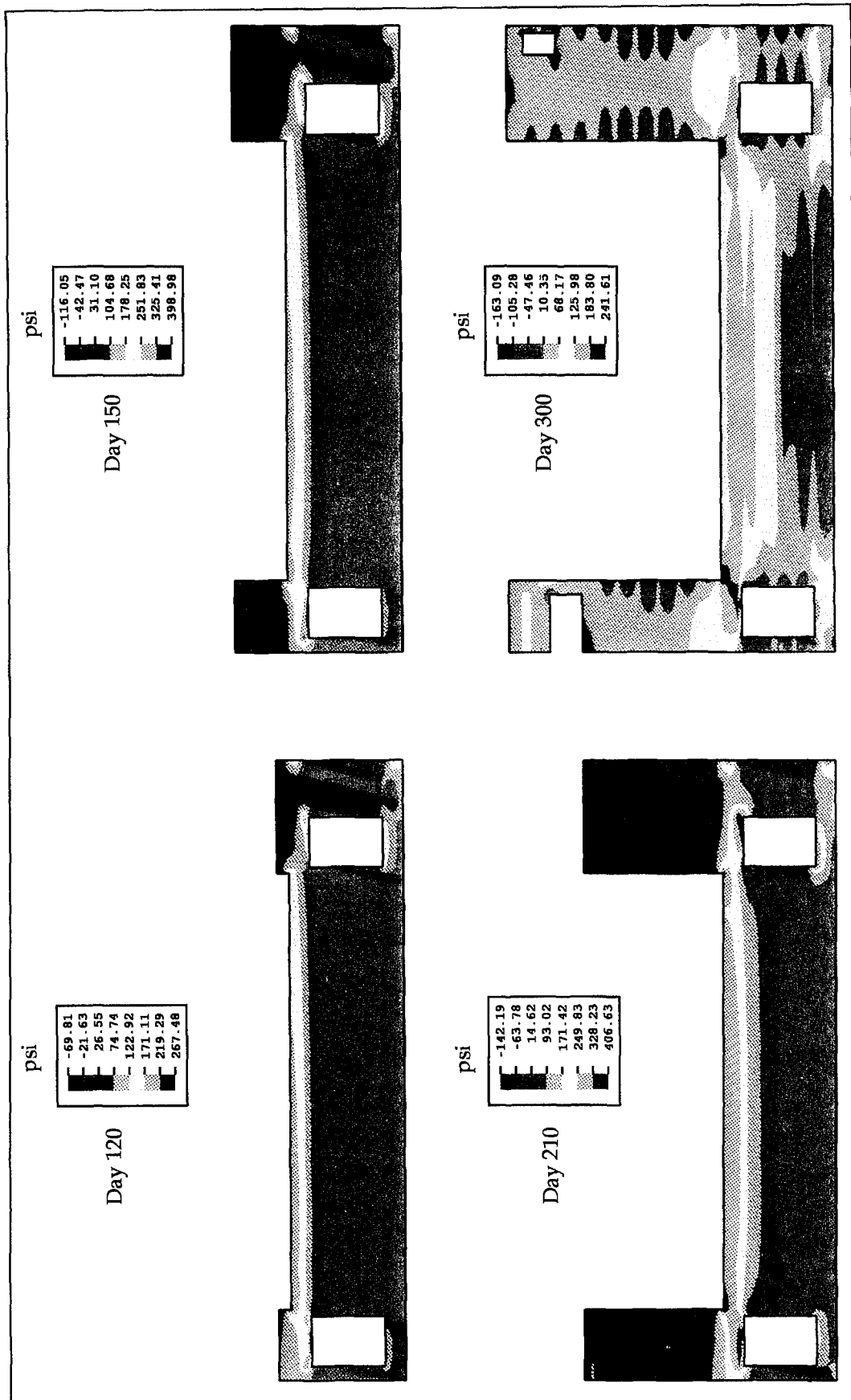
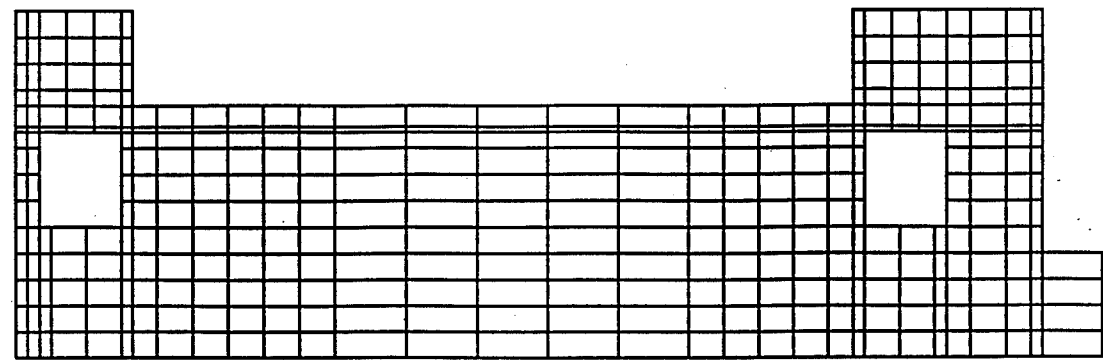
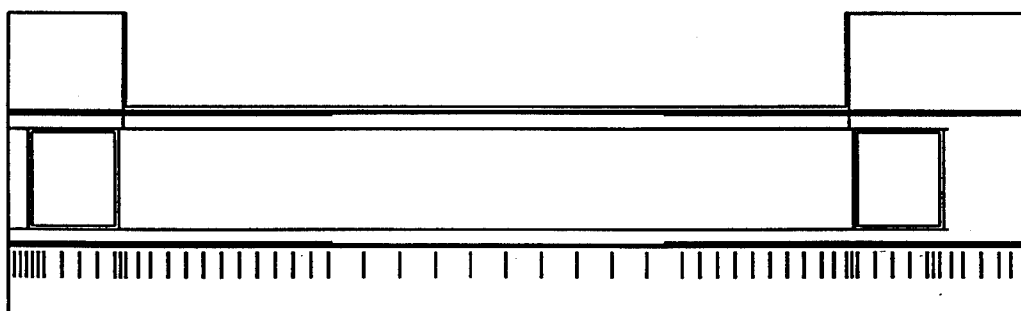


Figure 7. Baseline mesh thermal contours





continuum elements



reinforcement and piles

Figure 9. Finite element model for reduced mesh analysis

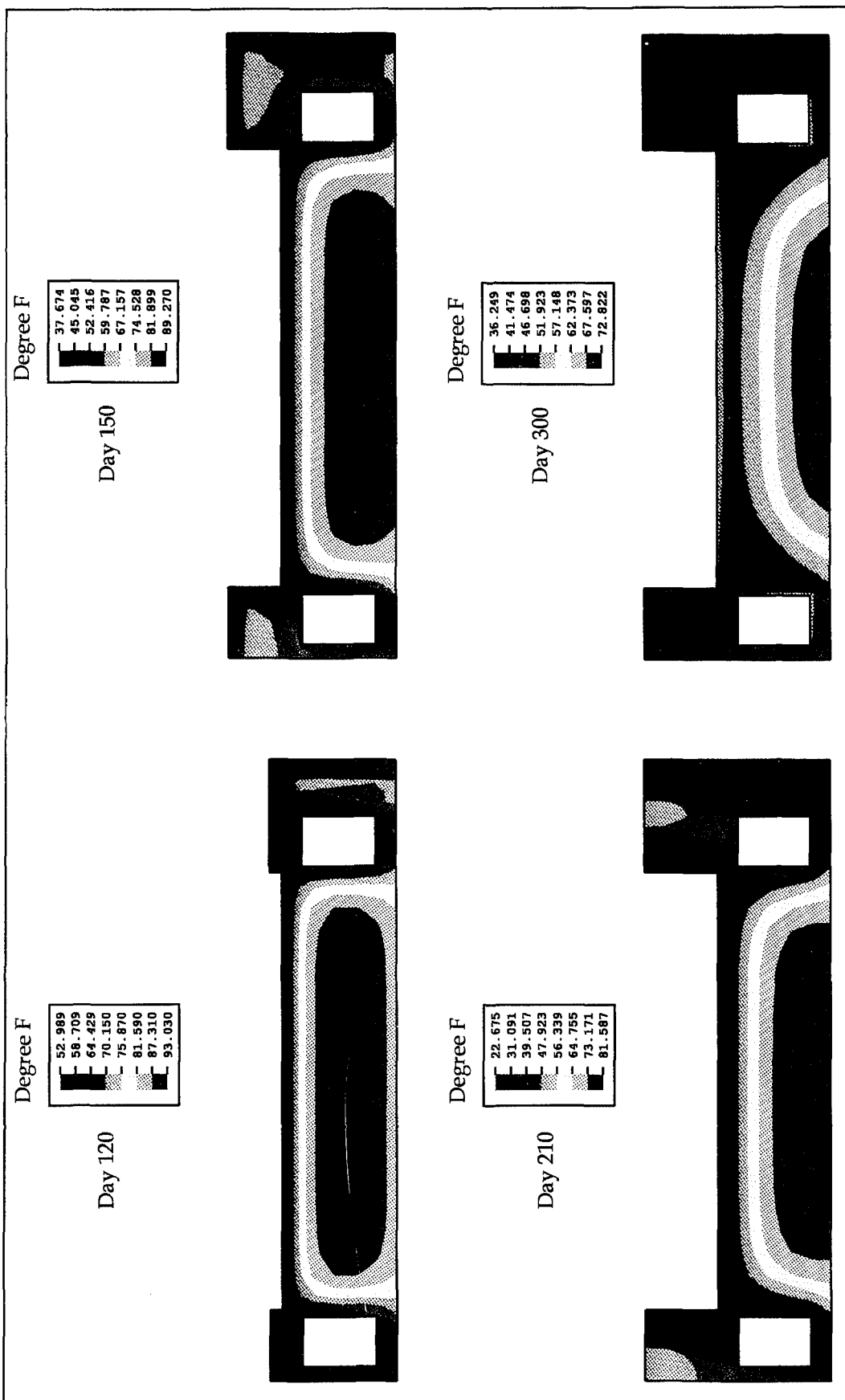


Figure 10. Reduced mesh thermal contours

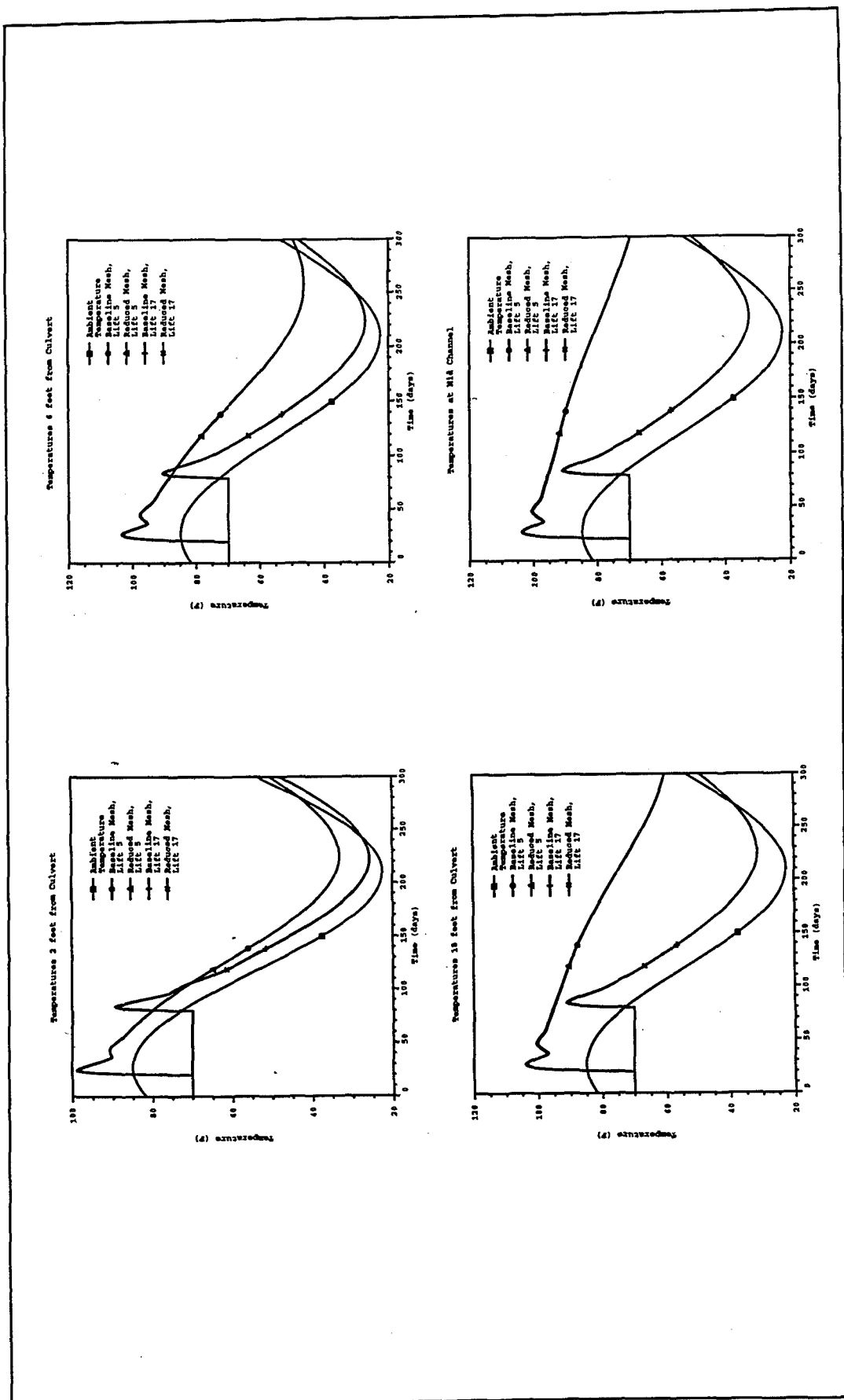


Figure 11. Baseline versus reduced mesh temperature history comparison

that the reduced mesh produced no degradation in accuracy for temperatures compared with the accepted baseline calculation.

Now it remains to evaluate the stress solution from the reduced mesh to determine if accuracy is degraded due to a need to capture stress gradients from thermal-induced bending or surface effects through the depth of each lift. The stress analysis was conducted using 0.25-day increments during each lift placement with interpolation of the temperature distributions from the temperature histories calculated at 0.5-day increments. This feature of ABAQUS was tested and found to work very well. Maximum principal stress contours at times corresponding to those for the standard mesh are shown in Figure 12. These plots indicate a good correlation in magnitudes and distribution for tensile principal stress with the solution obtained from the standard mesh. A critical area with high cracking potential is in the top lift of the slab near the re-entrant corners formed by the walls. The complete stress histories of selected points in these regions are compared for the two analyses in Figure 13. These comparisons are in good agreement; the higher stress seen in the standard mesh run is attributed to the integration point being nearer the surface than in the reduced mesh which has a larger element size. Further confirmation of the ability of the reduced mesh to capture the correct stress distribution is seen in Figure 14 which compares the stress profiles through the slab thickness at selected points in time between the two analyses.

## Conclusions

It is concluded that the reduced mesh, which will reduce the 2D problem size by a factor of 4 and the corresponding 3D computational size by at least a factor of 40, produces no significant degradation in thermal or stress accuracy. Since little potential for cracking is anticipated high in the walls of this monolith, these lifts need not be modeled. The technique developed for simulation of the temperature distribution in the remaining stub walls and the use of larger thermal time steps provides excellent agreement with the thermal solution obtained from the standard mesh. The stress solution using the reduced mesh also maintains a good degree of accuracy compared with the standard mesh. This is expected since the stresses are thermally driven in this application, and the constraints due to gravity and piles prevent large bending gradients across the slab. Thus, the mesh density defined by the reduced mesh study is deemed acceptable for use in the 3D analysis. Subsequent 2D parameter studies will employ the stub wall modeling technique while retaining the standard mesh density. This is appropriate since the mesh size is not critical in these 2D analyses, and the increased density of material points provides better resolution of cracking potentials for the parametric studies for selecting construction parameters to be used in the 3D analysis. These preliminary calculations also served as scoping studies to provide initial data for establishing baseline parameters for the next phase of 2D parameter studies.

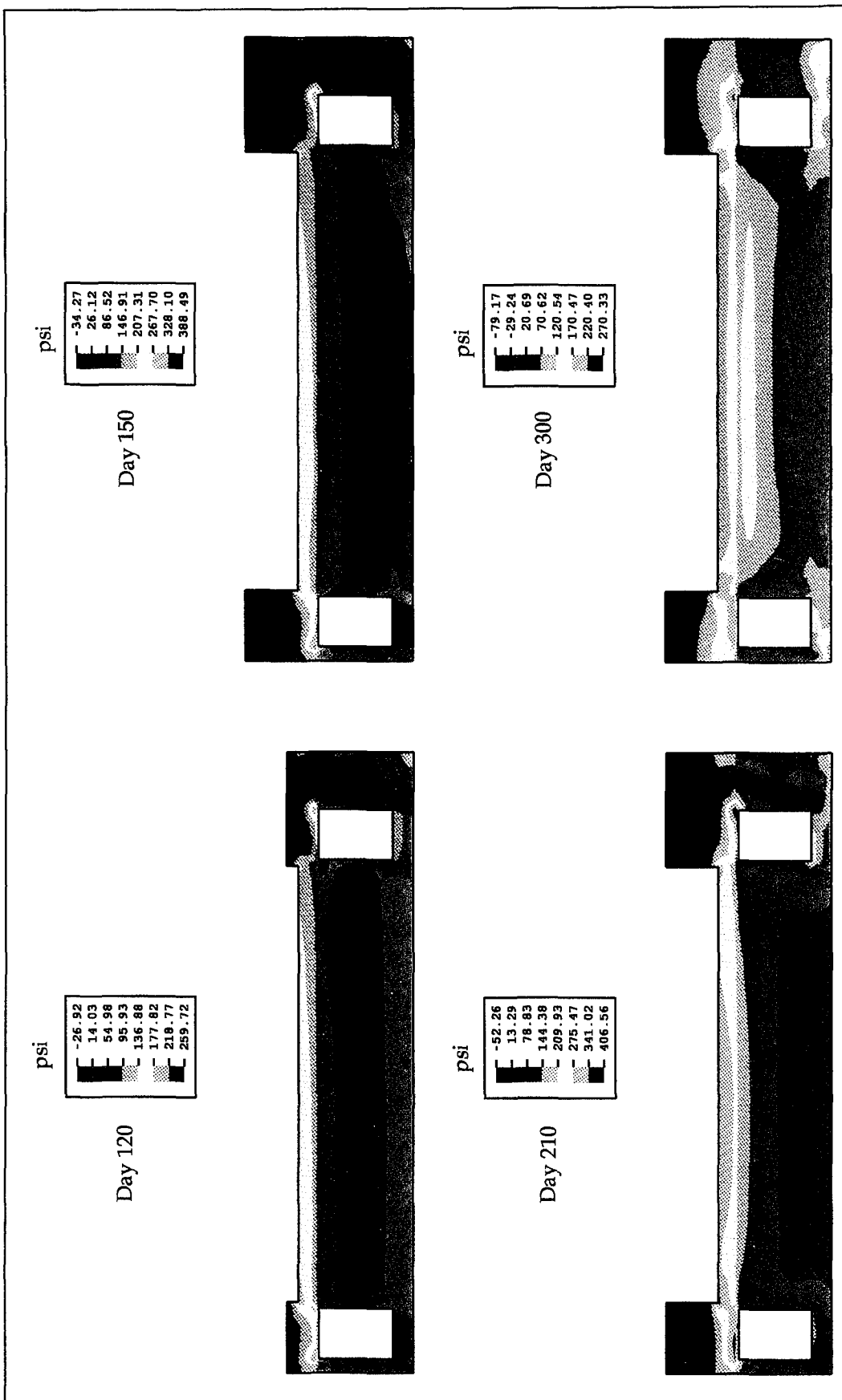


Figure 12. Reduced mesh maximum principal stress contours

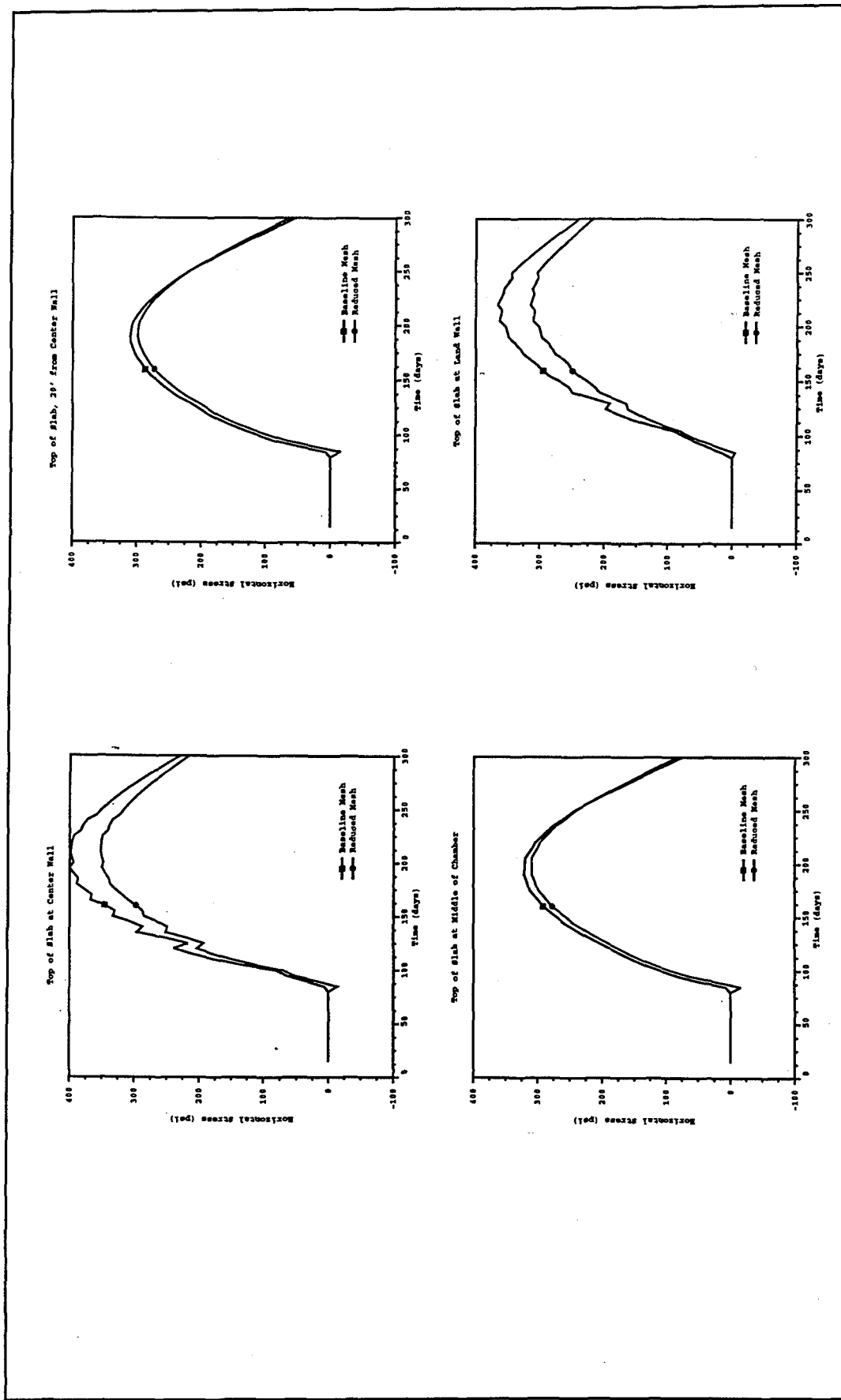


Figure 13. Baseline versus reduced mesh stress history comparison

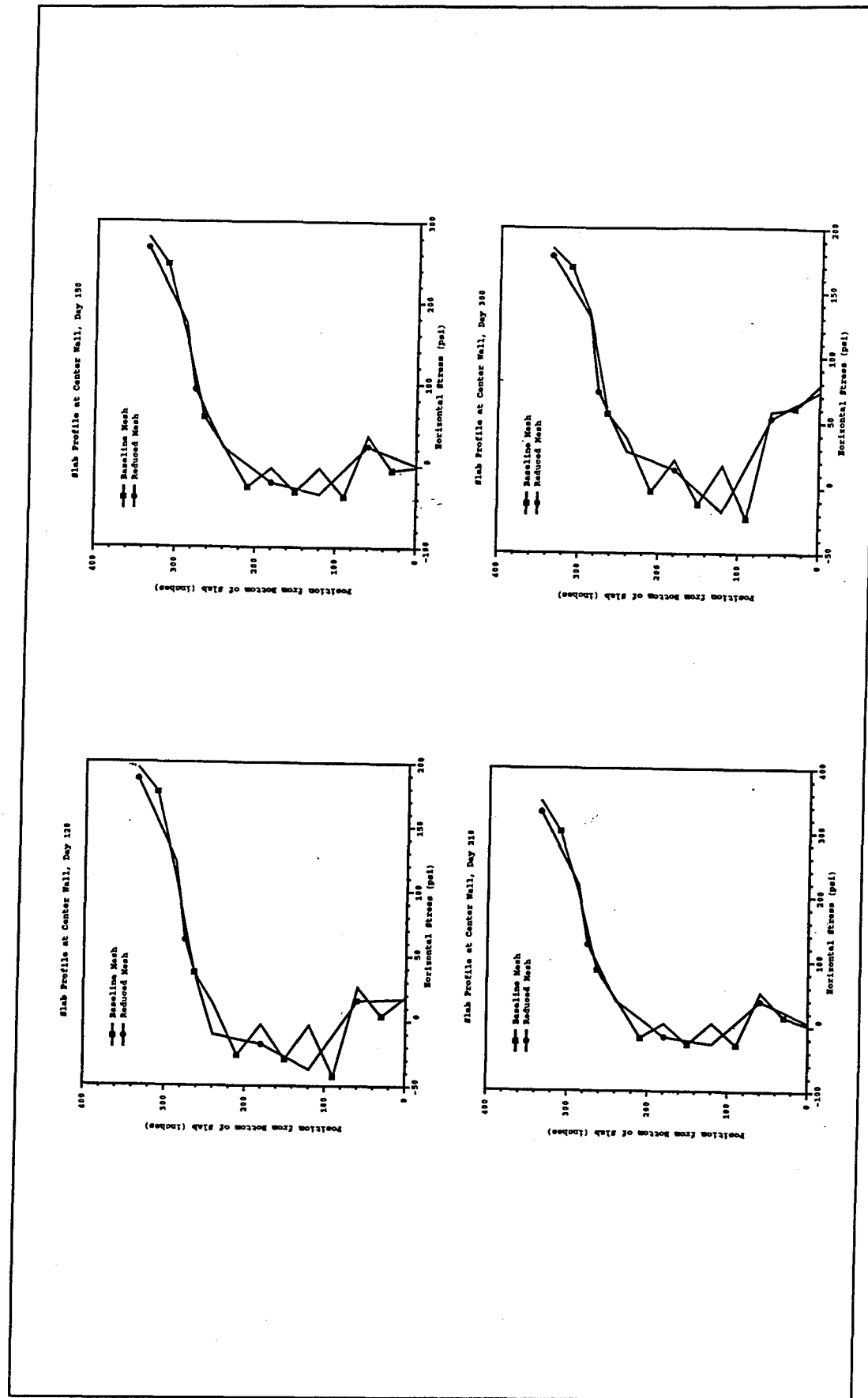


Figure 14. Baseline versus reduced mesh stress profile comparison

Some of these optimizations based on this scoping information are discussed in Chapter 4 for the baseline configuration.

## 4 Two-Dimensional Transverse Slice

---

### Model Description

Based on previous experience at ANATECH with thermal-induced cracking in thick-sectioned concrete structures such as spent-fuel-storage pools at nuclear reactors, a cross section containing significant mass adjacent to re-entrant corners or thinned sections is assumed to be the most susceptible to cracking. This is because the larger mass generates more heat and typically provides more restraint against free expansion or contraction, and the thinned sections or corners provide weakened areas and stress concentrations. Accordingly, a transverse section for the landside chamber of the monolith near the upstream edge was chosen as a representative section for conducting parameter studies. This section contains a large expanse of the full thickness of the slab with the two culvert openings under the center and end walls. The finite element mesh for this transverse slice model is shown in Figure 15. This section includes Lift 3 (5 ft) that forms the bottom of the slab, then Lifts 4, 5, and 6 (each 5 ft) that form the section between the culvert and the landside edge, the middle section between culverts, and the end section at the symmetry line, respectively. Lifts 7, 8, and 9 are the next 5-ft lifts on top of Lifts 4, 5, and 6, respectively. Lifts 10, 11, and 12 are each 5 ft on top of Lifts 4, 5, and 6, respectively. Lift 14 spans the entire section and is 4 ft thick, and it completes the culvert geometry. Lift 17, also 4 ft thick, spans the entire section, forms the top of the slab, and also contains the additional 1-ft section for the roof of the culverts. The center wall is then formed with Lift 20 (3 ft), and Lifts 22, 25, 28, and 31 (thermal model only) with each lift 5 ft. The outer or landside wall is formed from Lifts 21, 26, 29, and 32 (thermal model only) with each lift 5 ft except Lift 21 being 3 ft.

Based on the results of the preliminary calculations, two modifications to the proposed geometry and lift schedule were incorporated into this model to mitigate cracking potential. The preliminary calculations showed a high potential for cracking in the roof of the culverts and also between the corners of the culvert and the top of the slab. The original lift schedule called for the 1-ft culvert roof section to be placed with

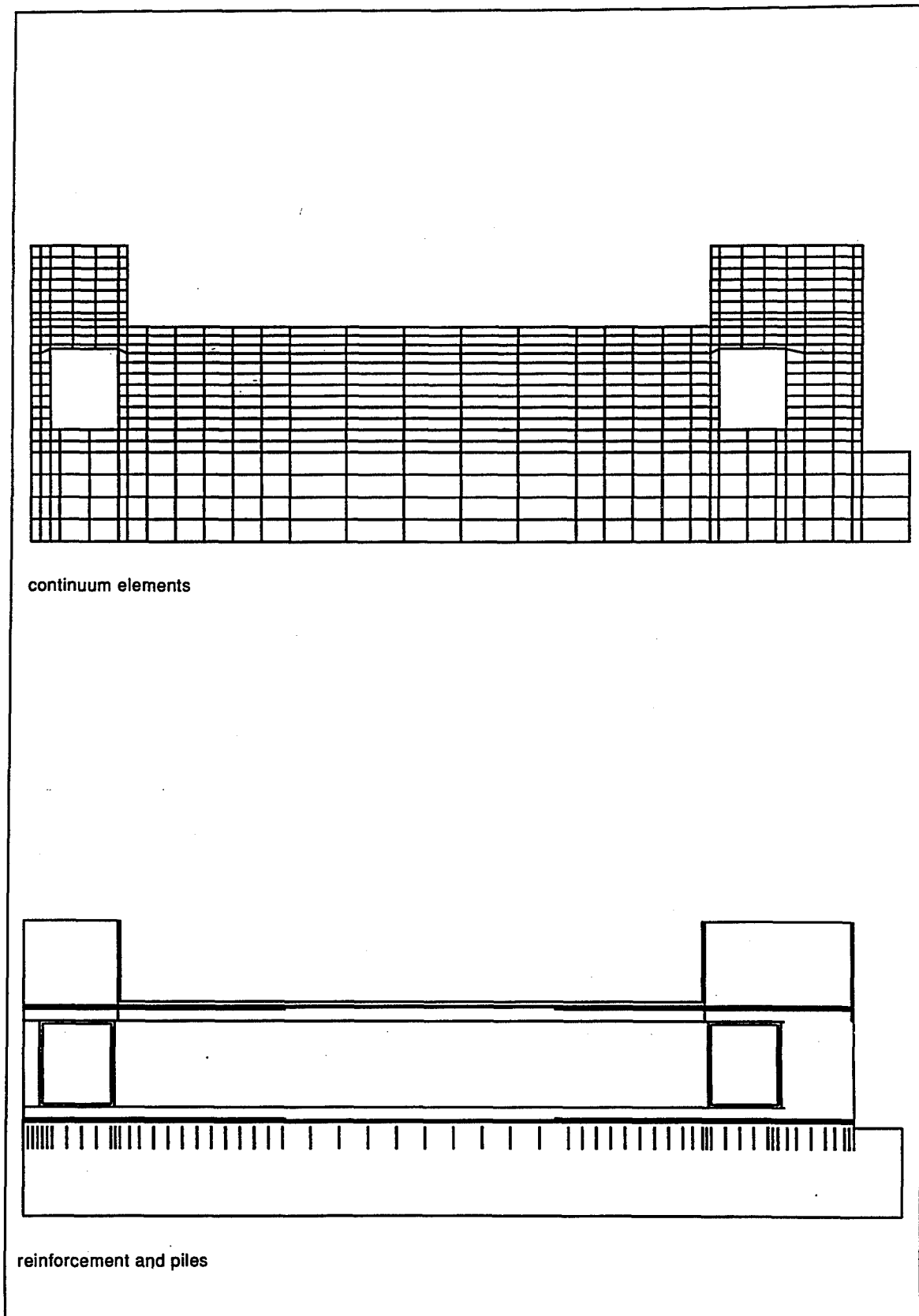


Figure 15. Finite element model for transverse slice parameter study

Lift 14 forming the top edges of the culverts. This 1-ft section spanning the 4-ft-wide culvert then carried the weight from the next lift above at only 10 days of age, thus creating significant bending. The lift geometry was then changed to include this 1-ft roof section with Lift 17 so that the complete 5 ft of concrete spanning the culverts and forming the roof section is supported on formwork and is made in an integral placement. The other modification incorporated from the preliminary calculations was to add 2 ft of concrete across the top of the floor sections. The original geometry of a 26-ft-thick slab allowed only 2 ft above the culverts and created a very thin section between the corners of the culverts and the top of the slab. This is due to the positioning of the culverts under the walls with only a 1-ft offset from the edge of the chamber walls to the edge of the culverts. Based on the potential to crack through between the top of the slab and the corner of the culverts, an additional 2 ft of concrete was added to the slab thickness. Note that this change was already incorporated into the standard and reduced mesh models described in the previous section.

## Baseline Analysis

The preliminary calculations used a maximum placement temperature of 70 °F for the concrete. Since these calculations indicated a high potential for cracking, a 60 °F maximum placing temperature was set for the baseline analysis. To summarize, the baseline analysis used the following construction parameters:

- 60 °F maximum and 40 °F minimum placement temperatures
- 5-day lift increments
- Minimum creep (0.9 factor) and maximum shrinkage (1.1 factor)
- No insulation after form removal
- Open culverts with full air circulation
- Extreme ambient temperature definitions
- 600-day analysis without service loads
- Reinforcing bar included

Figure 16 shows thermal contours for the baseline thermal analysis at selected points in time, and Figure 17 shows complete temperature histories of selected points compared with the ambient temperature. These figures show the temperatures in Lift 3 near the culverts peak near 95 °F and the temperatures in Lift 17 closely following the ambient cycle. The temperature gradient across the slab is shown to be increasing until day 205

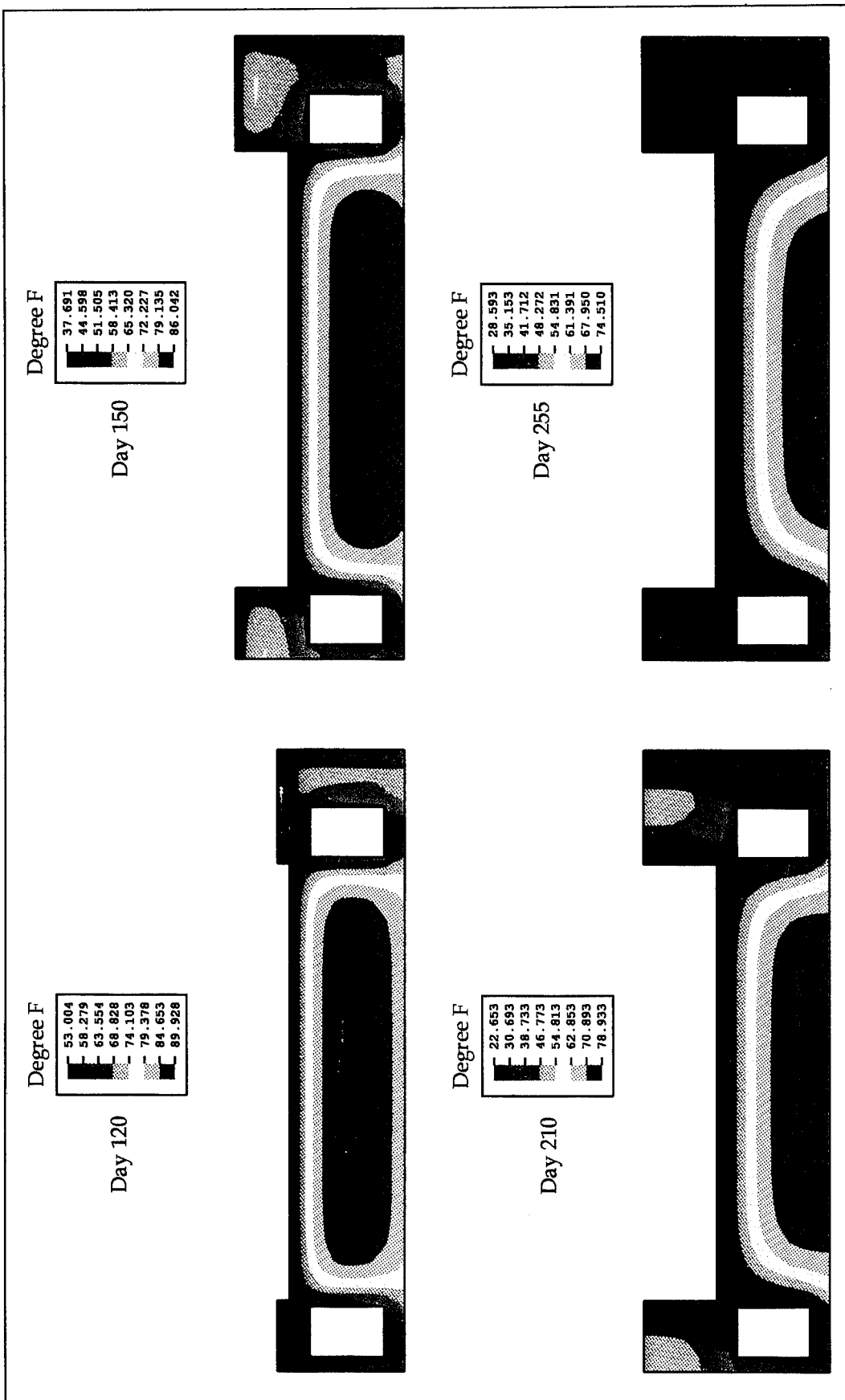


Figure 16. Transverse slice baseline analysis thermal contours (Continued)

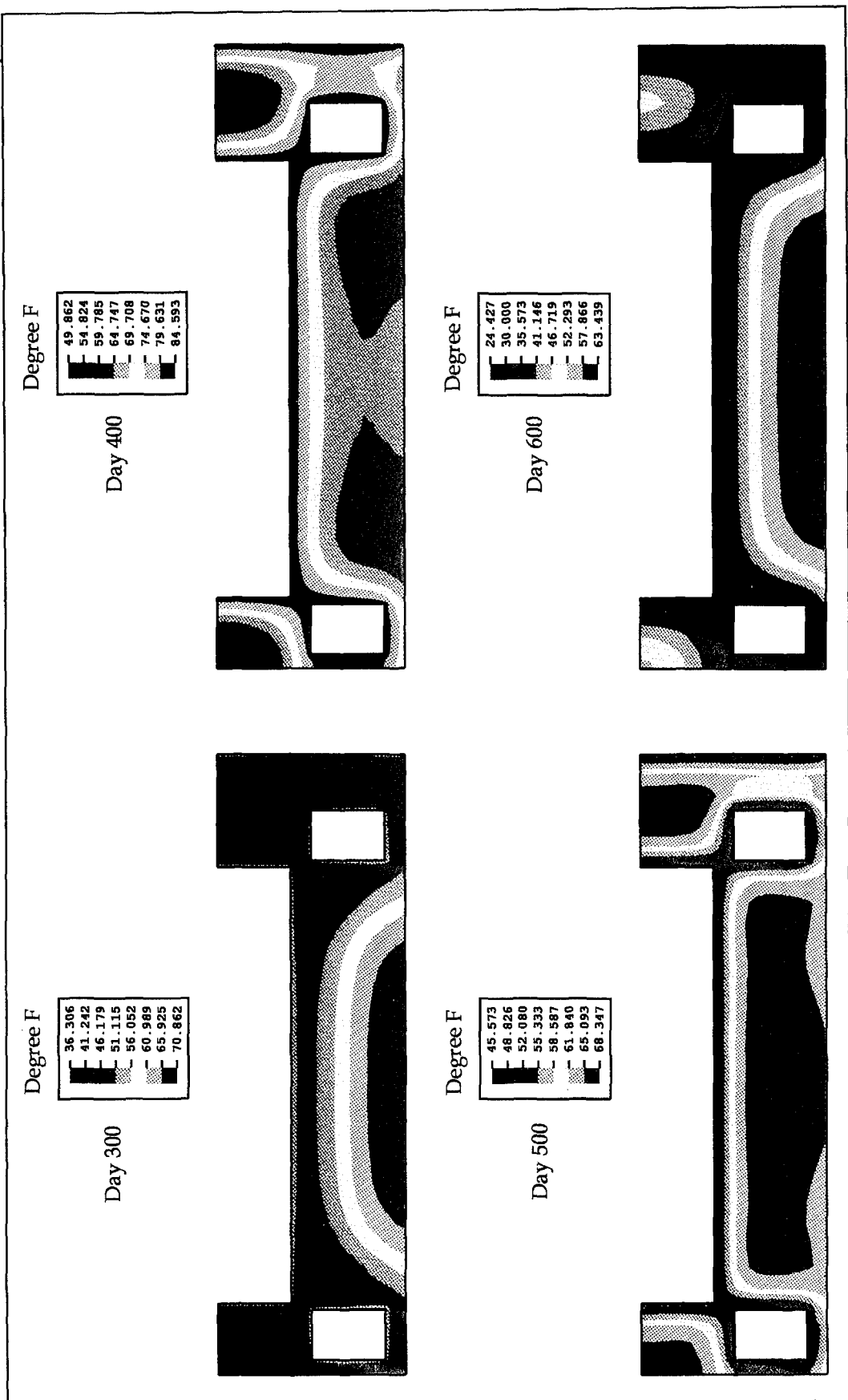


Figure 16. (Concluded)

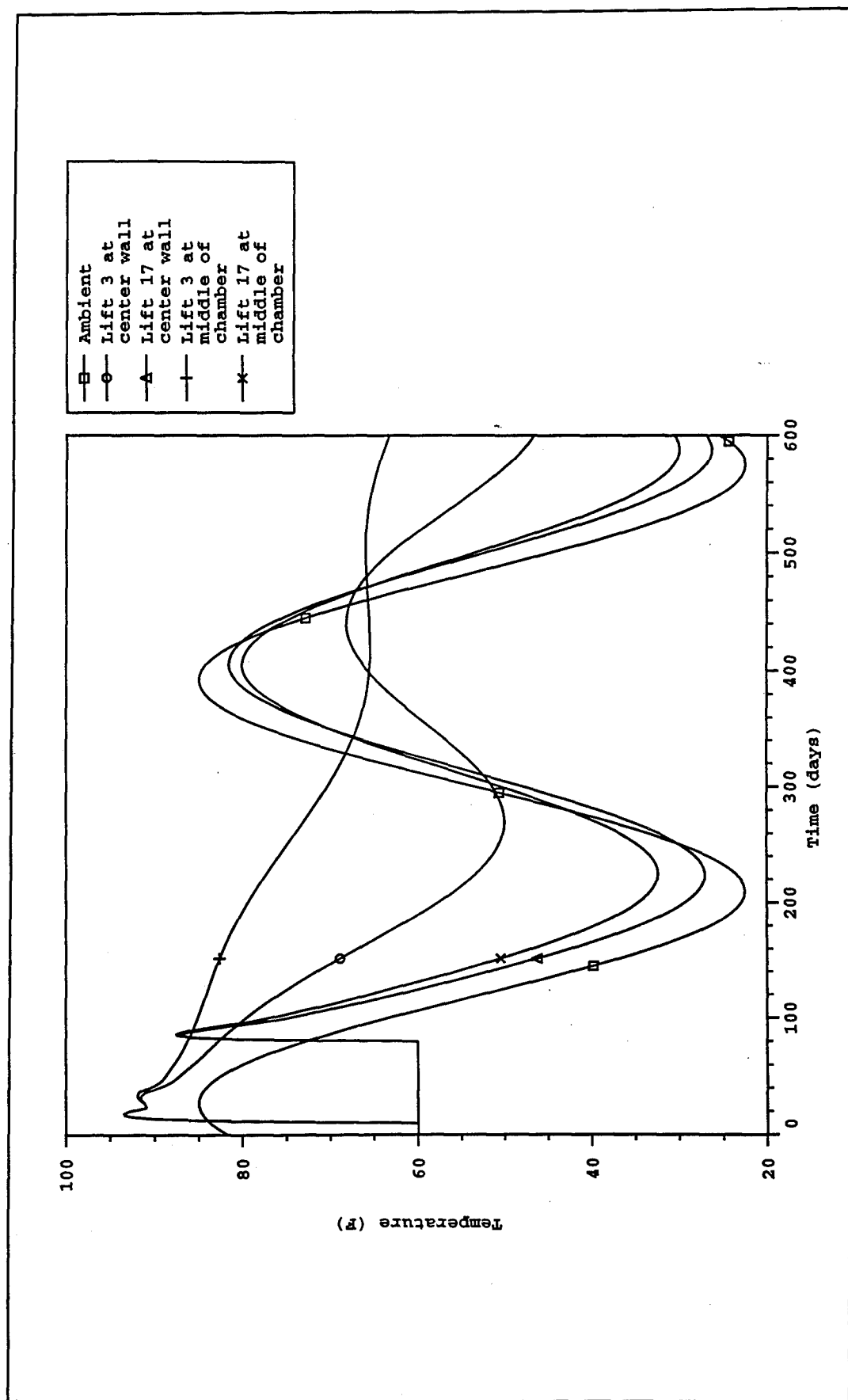


Figure 17. Transverse slice baseline analysis temperature history

as the ambient temperature drops more rapidly than the interior temperature. By the second winter, however, the gradient is approximately 15 °F less than during the first winter. Also note the reverse in thermal gradient across the slab during summer which peaks around day 400. The contours show the thermal gradients in the slab and the cooling zone around the free surfaces and the culverts. Figure 18 shows the cracking development predicted by this analysis, and Figure 19 shows cracking potential contours at selected days. Cracking initiates in the corners of the culvert beginning at day 135 and spreads through day 165. By day 165 cracking also appears in the top of the slab near the middle wall. By day 195, cracking has developed in the top of the slab near the landside wall and continues to spread into the slab near the middle wall. The crack potential contours also indicate a high potential for cracking (greater than 90 percent) over a wide area in the top of the slab. In the concrete material model, the cracks can close and re-open under cyclic loading. Once a crack forms, its direction is fixed. In these cracking pattern plots, only the open cracks are shown for clarity. The cracks emanating from the culverts close during the summer cycle, as seen on day 380, indicating that these cracks are due to seasonal changes and are more of a maintenance concern for long-term degradation than an immediate threat to structural integrity. The cracks in the top of the slab do not close under seasonal loading and require further investigation.

Figures 20 and 21 show the reinforcing bar stresses in each of the three #18 reinforcing bars near the top of the slab at the cracking location near the outer wall and near the middle wall, respectively. The reinforcing bars under the crack near the outer wall, Figure 20, clearly show when the crack initiates and that load is taken by the reinforcing bar. The load is seen to be distributed to each reinforcing bar based on the nearness of the reinforcing bar to the crack. The sawtooth pattern in these curves is due to increments in load being applied as lifts are added to form the walls. However, the reinforcing bar at the crack location near the middle wall, Figure 21, does not show this behavior and only exhibits some perturbations in stress as the crack grows through all three reinforcing bars. This reinforcing bar behavior indicates that the cracking is caused by two different structural response mechanisms at the two crack locations in the top of the slab. The cracking near the outer wall is caused by thermal-induced bending, so that when the crack develops, the continuing bending stress must be transferred to the reinforcing bar. The reinforcing bars take the load and the crack is arrested. The cracking near the middle wall, however, is dominated by tensile stress due to constraint against thermal contraction. The top of the slab is cooling below its placement temperature and wants to shrink toward the centerline. Near the middle wall, the constraint against shrinkage causes enough tensile stress to initiate cracking. Consider a block of concrete with a reinforcing bar down the middle and constrained at each end. If the block is cooled enough, a crack will occur in the middle, but the reinforcing bar will continue to see a thermal stress of  $E_s \alpha \Delta T$ , since the concrete cracking causes no change in the strain to the reinforcing bar. In fact, some thermal-induced stress is relieved as the concrete cracks. Thus the reinforcing bar at the crack near the middle

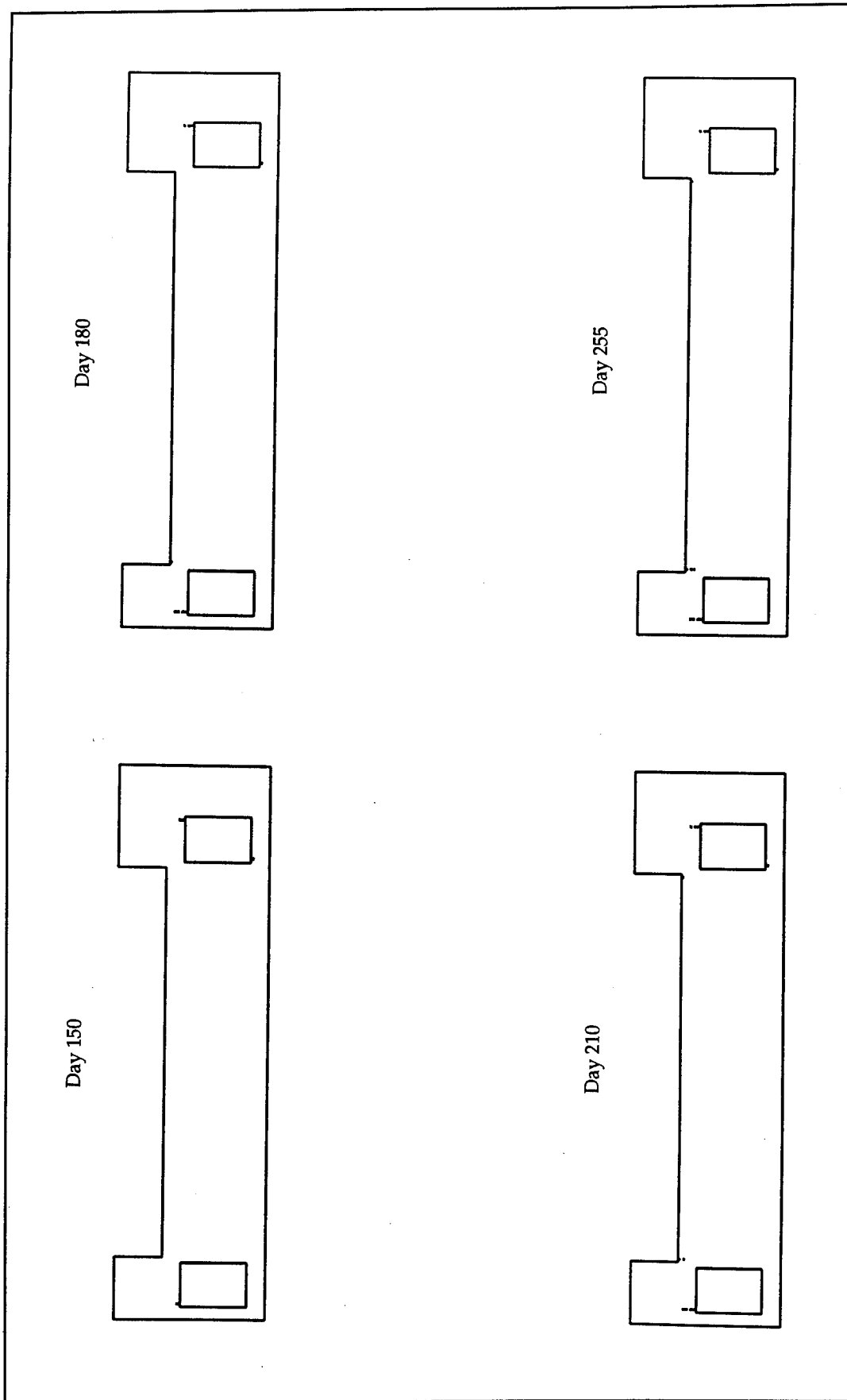


Figure 18. Transverse slice baseline analysis cracking development (Continued)

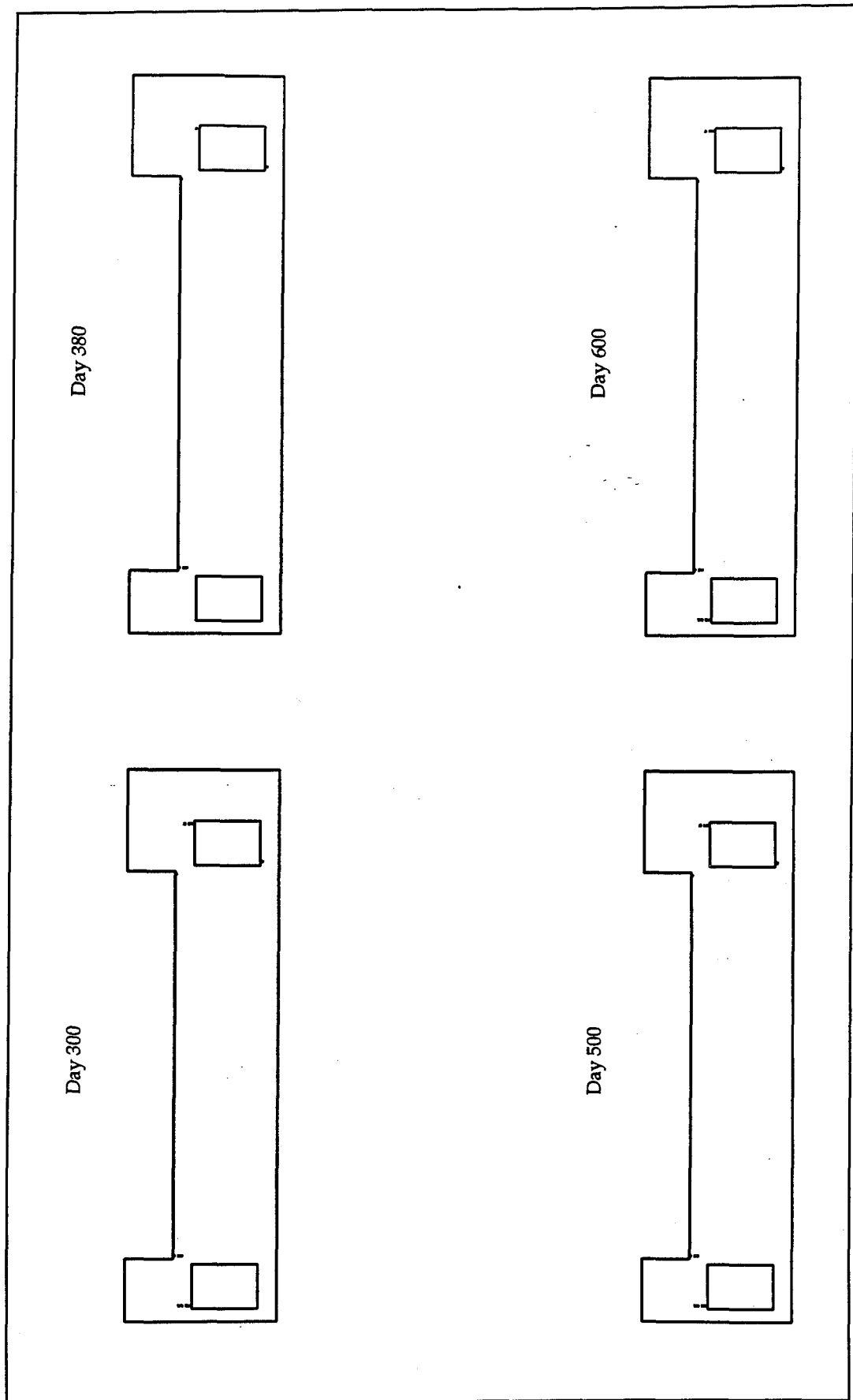


Figure 18. (Concluded)

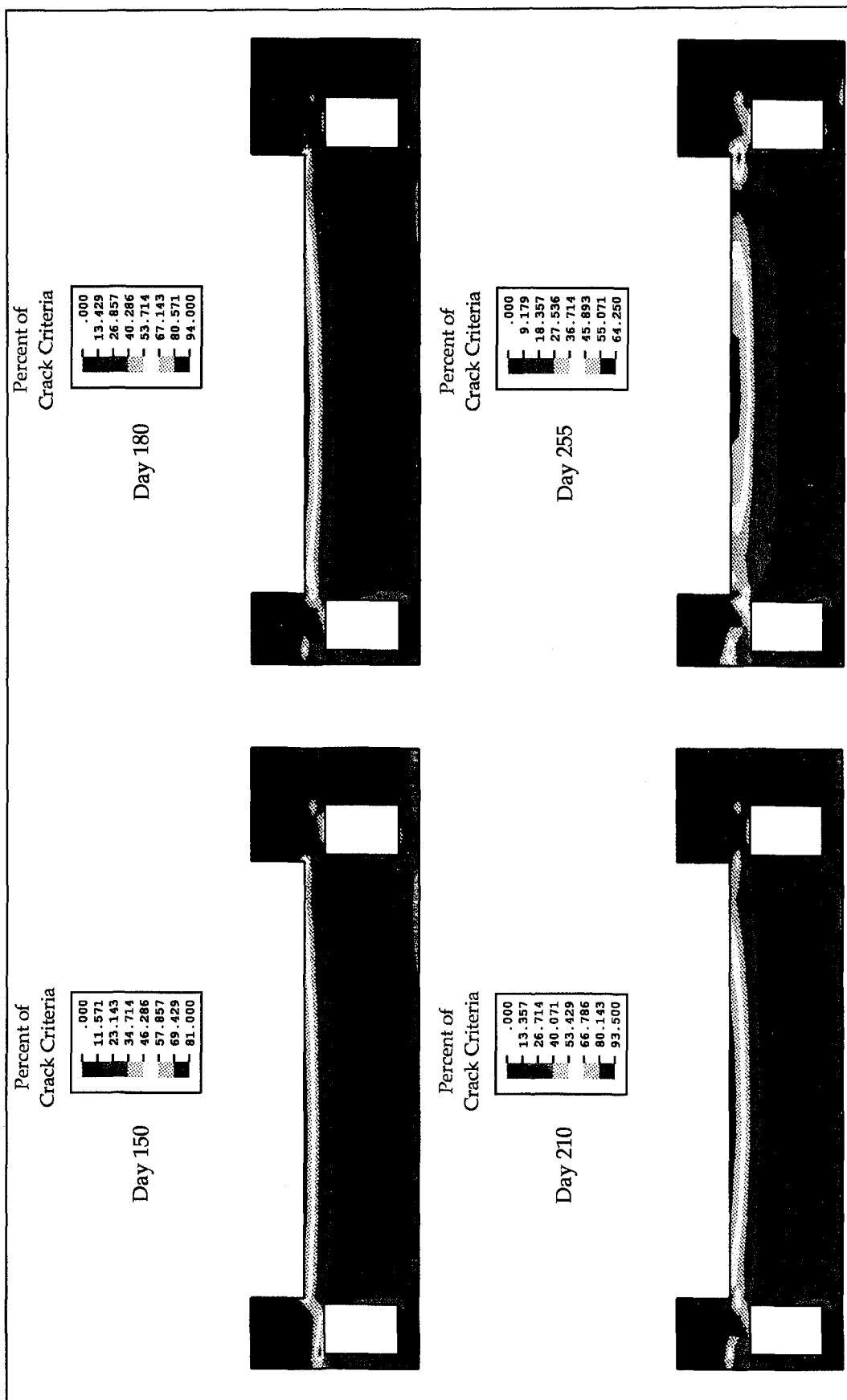


Figure 19. Transverse slice baseline analysis crack potentials (Continued)

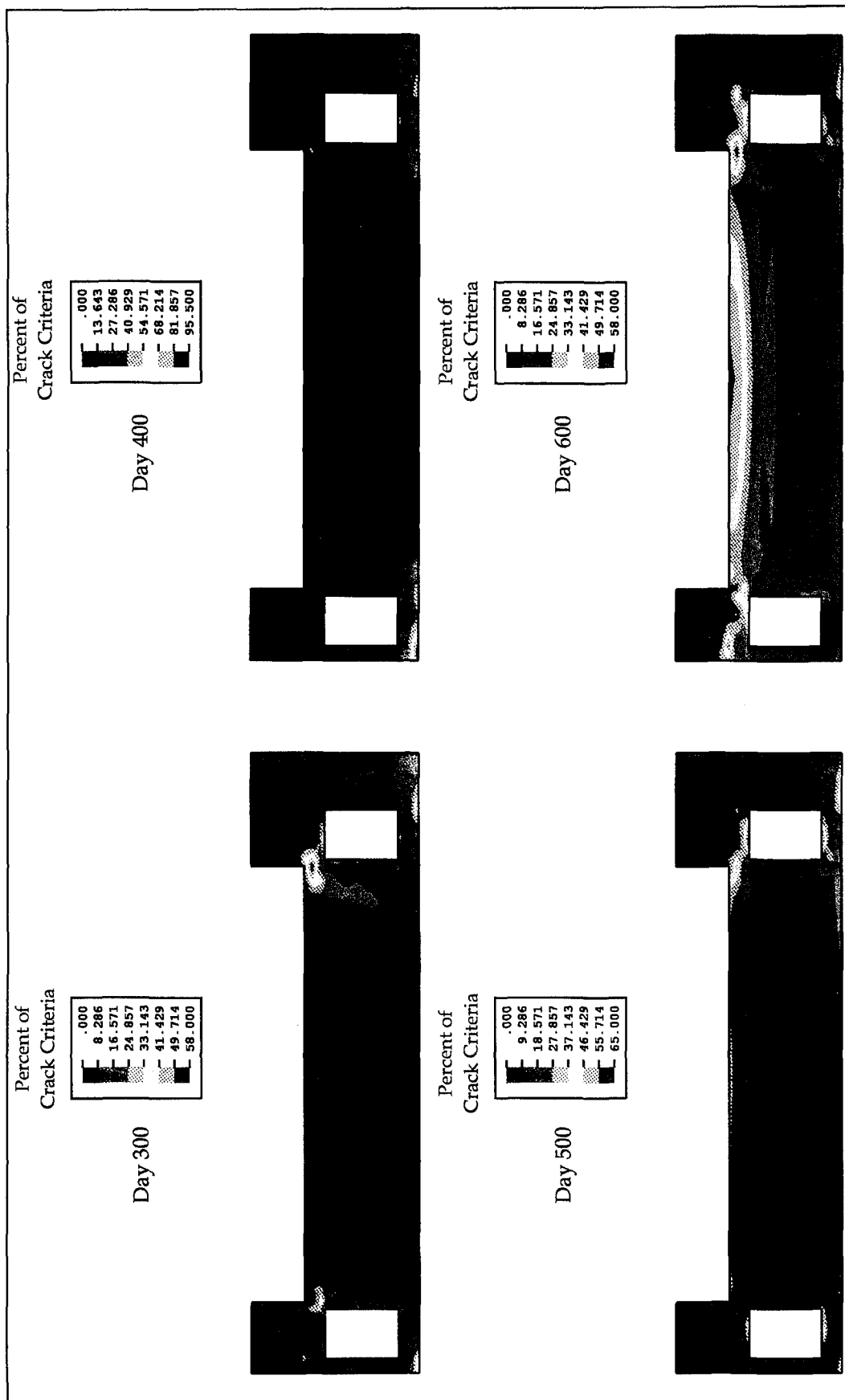


Figure 19. (Concluded)

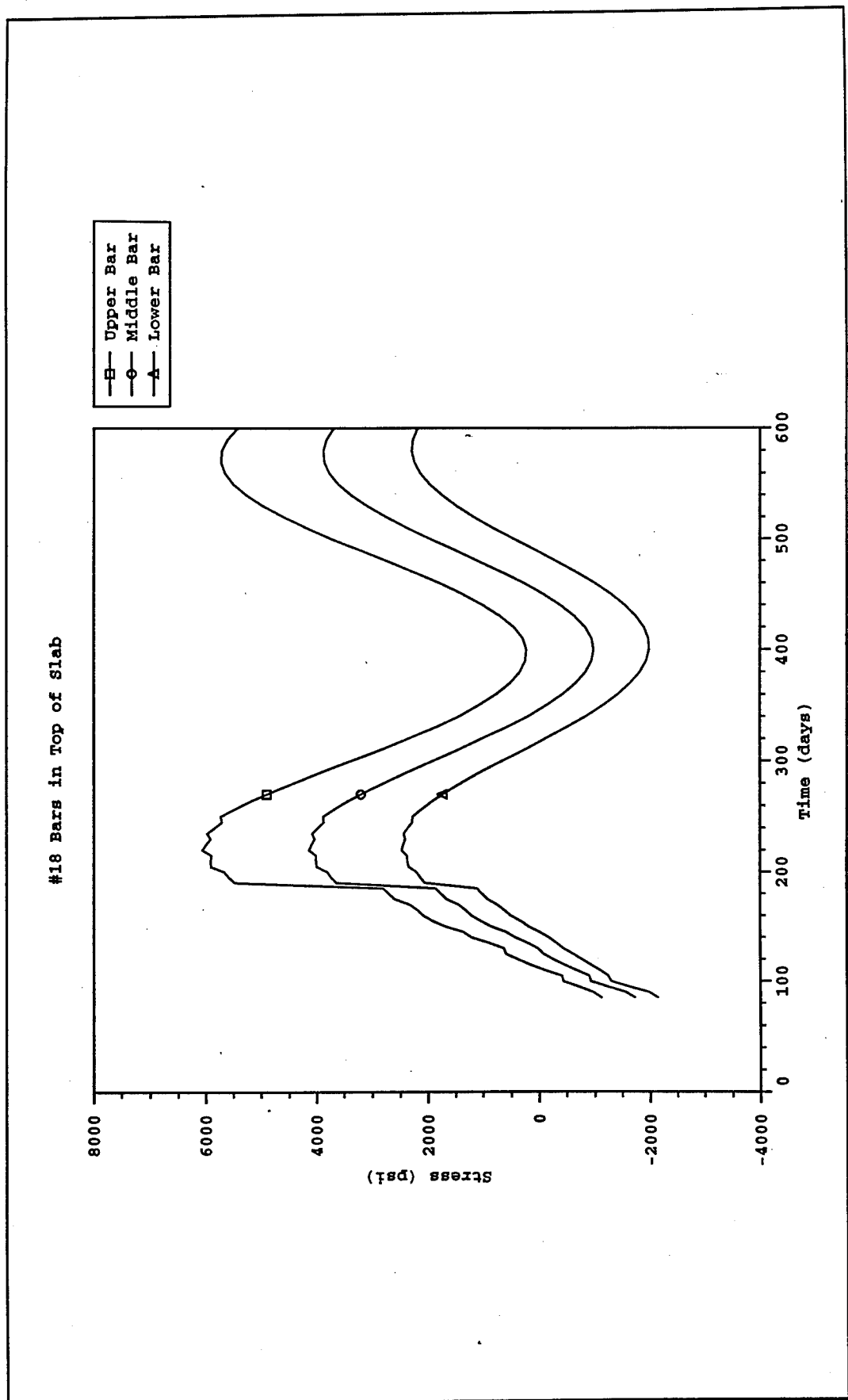


Figure 20. Reinforcement stresses at crack near land wall

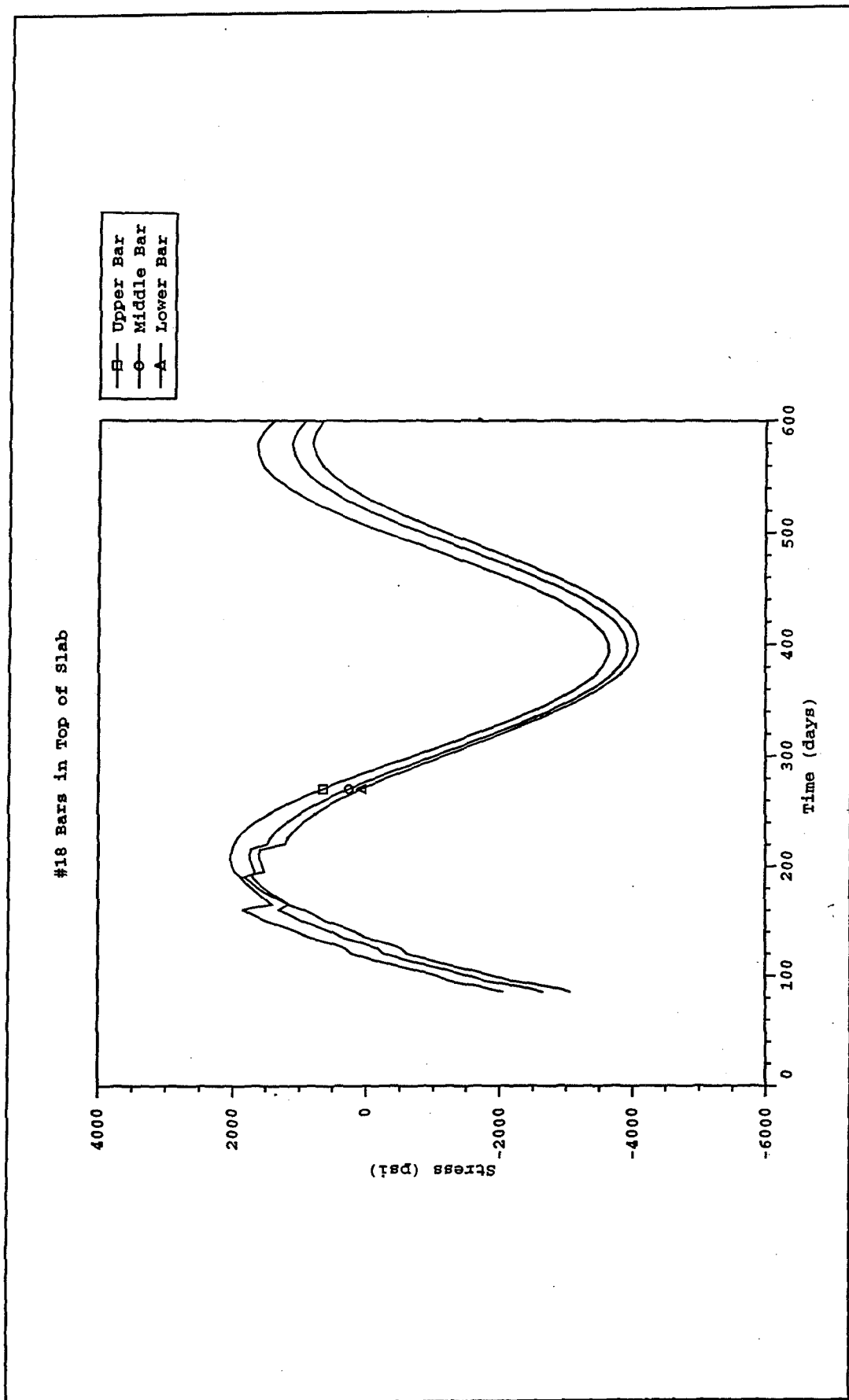


Figure 21. Reinforcement stresses at crack near center wall

wall is not effective in arresting this constraint-induced crack, and the crack continues to grow beyond the depth of the #18 reinforcing bars. To further evaluate the severity of these cracks, the relative displacement of nodes across the crack locations are plotted in Figure 22. The thermal shrinkage can be seen prior to cracking in this plot as the negative relative displacement. These plots can be used to evaluate crack opening and show that the cracks have a peak opening width of less than 0.01 in. and that they do tend to close after opening. This plot also further confirms the differences in cracking mechanisms in the two areas of the slab. By examining the slope of the curves after crack formation, one can see that the crack near the outer wall continues to have a driving force that opens the crack and is a global mechanism developing over a long period of time. In contrast, the driving force immediately decreases at the crack near the middle wall even as it propagates downward through subsequent

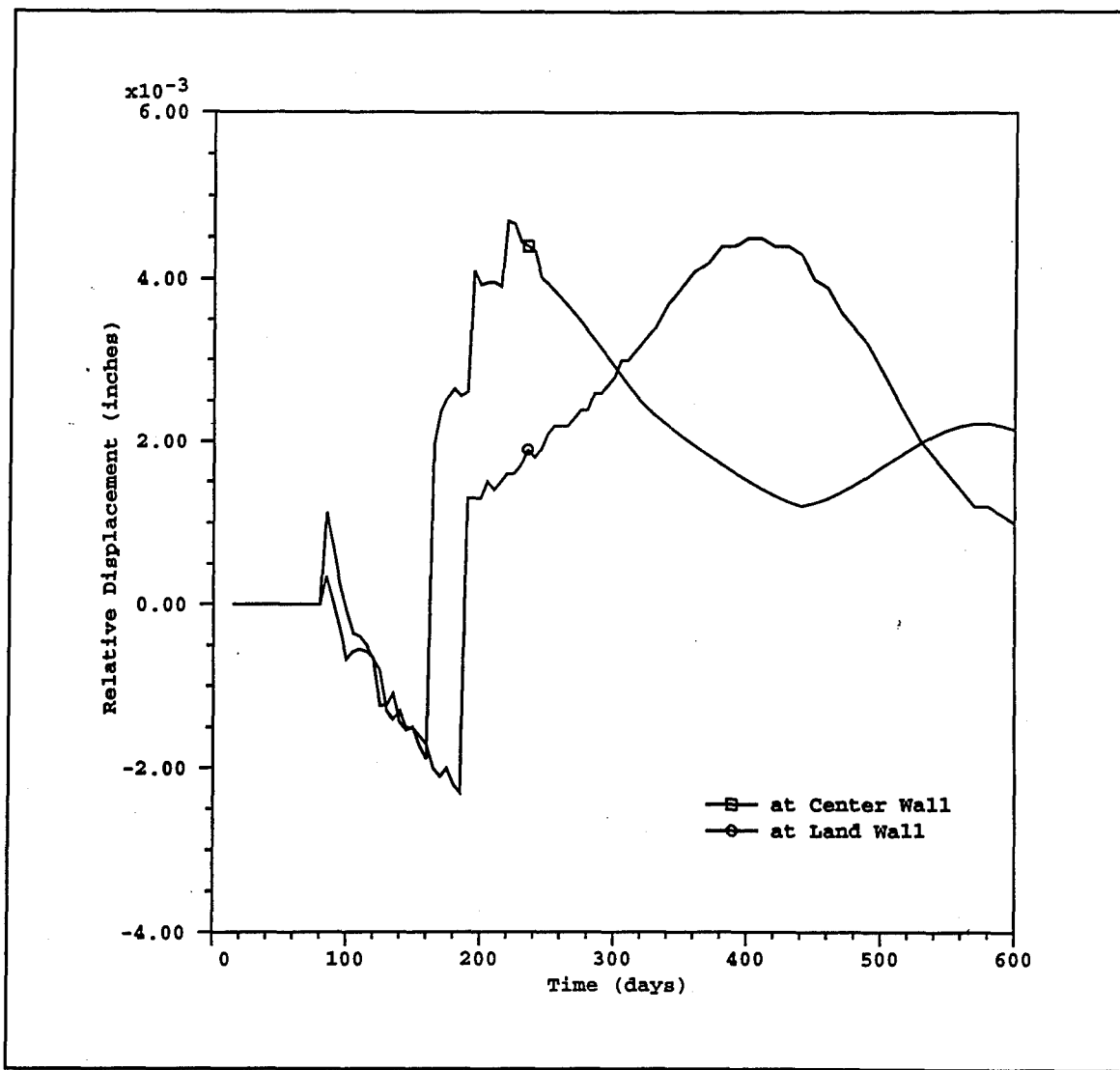


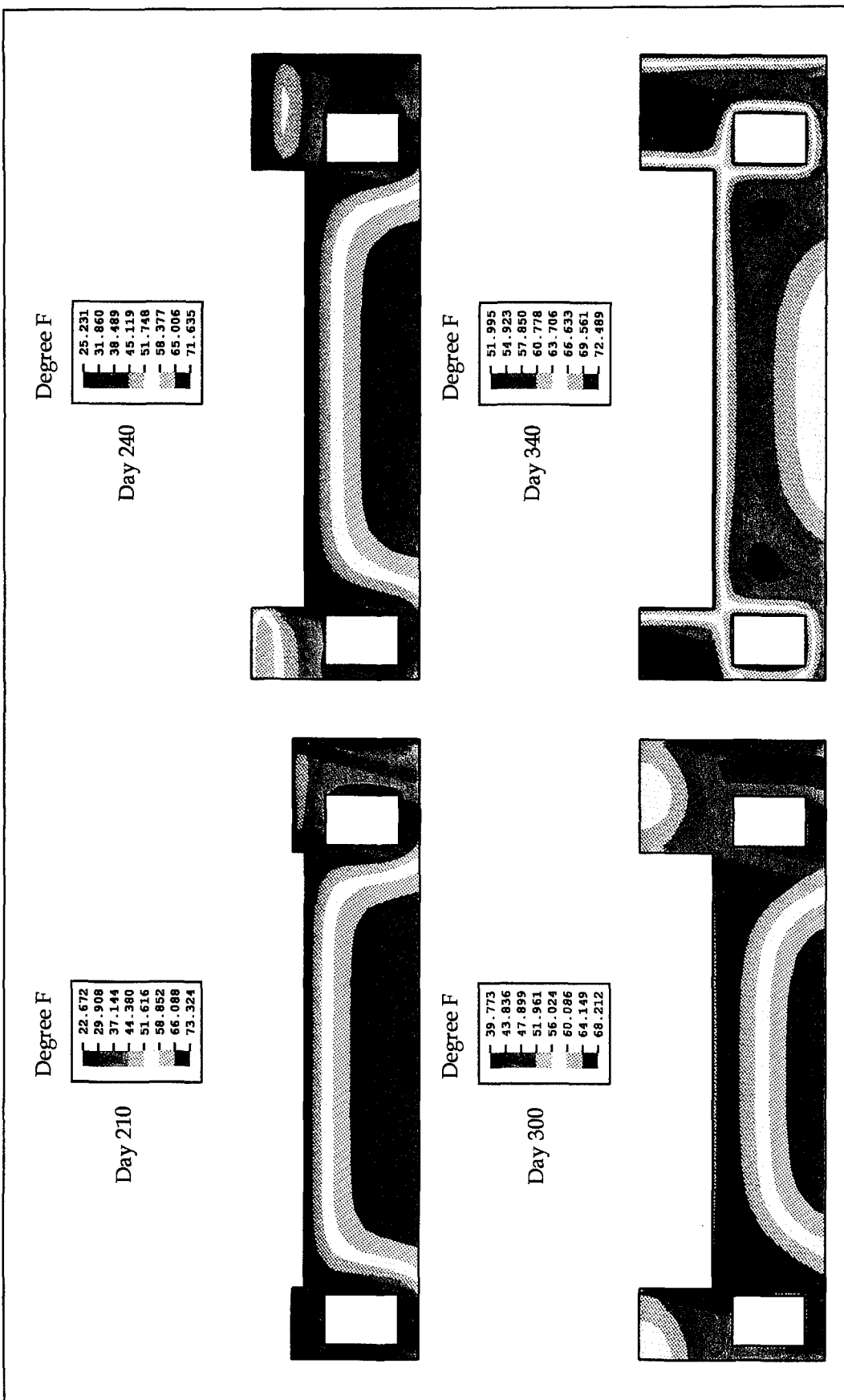
Figure 22. Relative displacements of nodes across cracks

material points into the slab (three points crack at this location). This indicates that the driving stress is relieved as the crack forms.

## Placement Increment Study

Since the cracking predicted in the baseline analysis is driven by the thermal gradients set up by the heat of hydration and the colder ambient temperature during fall and winter, an analysis considering longer placement times between lifts is of interest. This should allow for additional cooling of each lift, directly from convection from the free surface, before additional lifts are placed on top which traps the internal heat generation. Additionally, the top of the slab will be placed later in cooler months which should reduce the stress during the coldest winter months. The unknown factor is the additional aging that also occurs in a lift before a new lift is added above. This can cause significant differences in stiffness and thus abrupt changes in stress across the lift interfaces. This analysis uses 10-day placement increments for the lifts forming the slab and 5-day placement increments for the walls. All other construction parameters are identical to the baseline analysis.

Figure 23 shows the thermal contours for this analysis at times that correspond to the same stages of construction as the baseline analysis. Figure 24 compares the 10-day placement temperature histories with those of the baseline analysis. These show that the peak temperatures in Lift 3 are very similar to the baseline run but that more cooling takes place before the next spike occurs when a new lift is added. The temperature history of Lift 17 is significantly different since it is now placed at day 160, well into the colder months, causing a minimum placement temperature of 40 °F to be enforced. Figure 25 shows the cracking development predicted by this analysis, and Figure 26 provides some crack potential contours. These plots indicate that a completely different cracking mechanism develops in the structure for 10-day placement increments. Cracking begins before day 140 in the thin section below the culverts. This is due to a global structural response that is set up because of the interaction between the lift sequencing and the ambient temperature history. The thermal gradient across the slab, hotter on the bottom and colder on the top, induces a bending mechanism in the slab since the bottom of the slab must expand relative to the top. This gradient occurs in the span between the culverts and becomes larger as the ambient temperature drops into winter faster than the heat is removed from the bottom of the slab. For the 5-day placement increment scenario, the top lift is placed much earlier so that the full slab cross section provides stiffness restraint against this bending mechanism. However, the 10-day lift sequence has created a “notched beam” geometry that is susceptible to this bending around the weak section under the yet to be completed culverts and cracking develops. These cracks are driven by bending and propagate through the base of the slab. In the summer cycle, additional cracks occur on the base of the slab and stresses in the #18 bars reach 15 ksi, as seen in



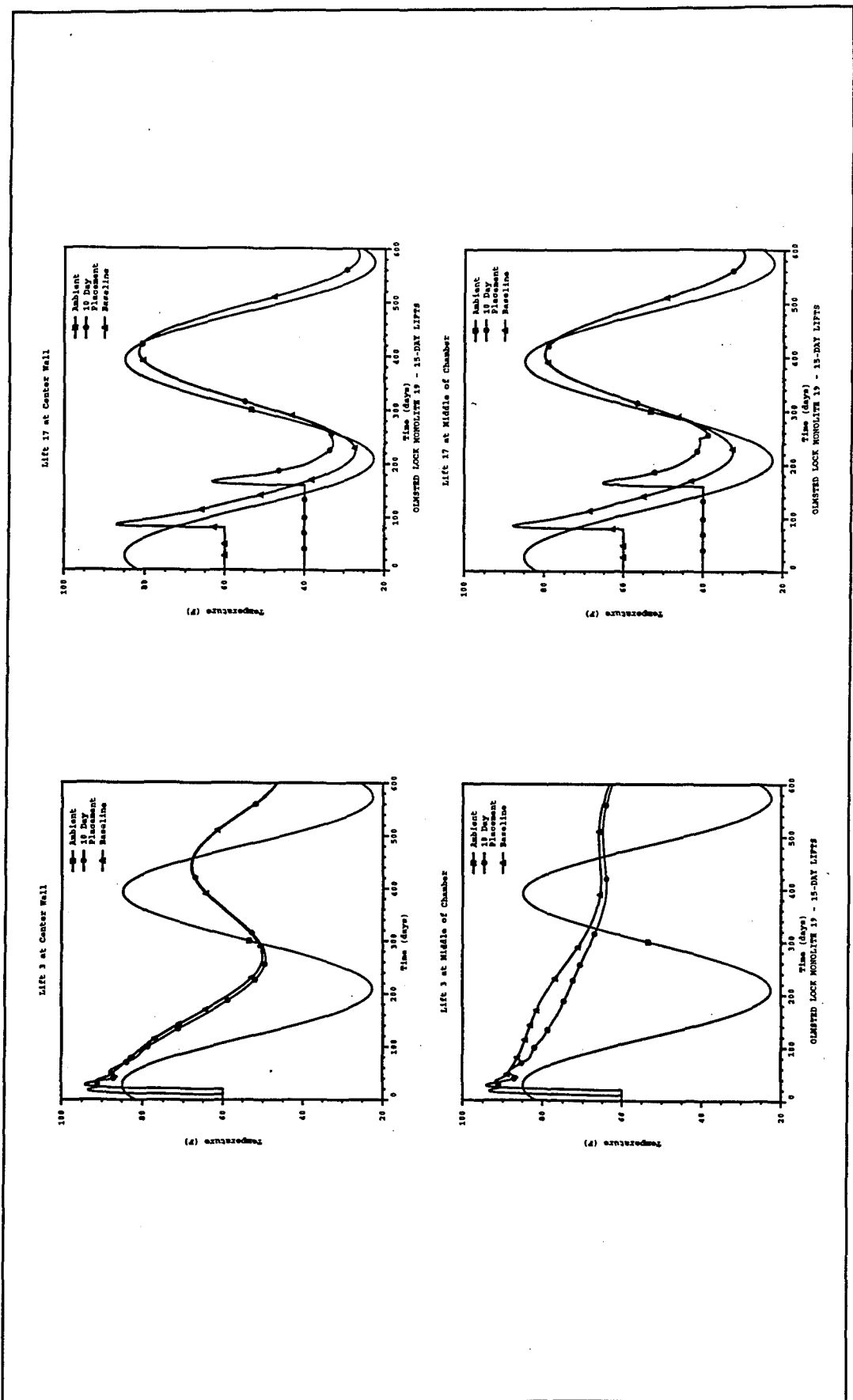


Figure 24. Ten-day placement versus baseline temperature histories

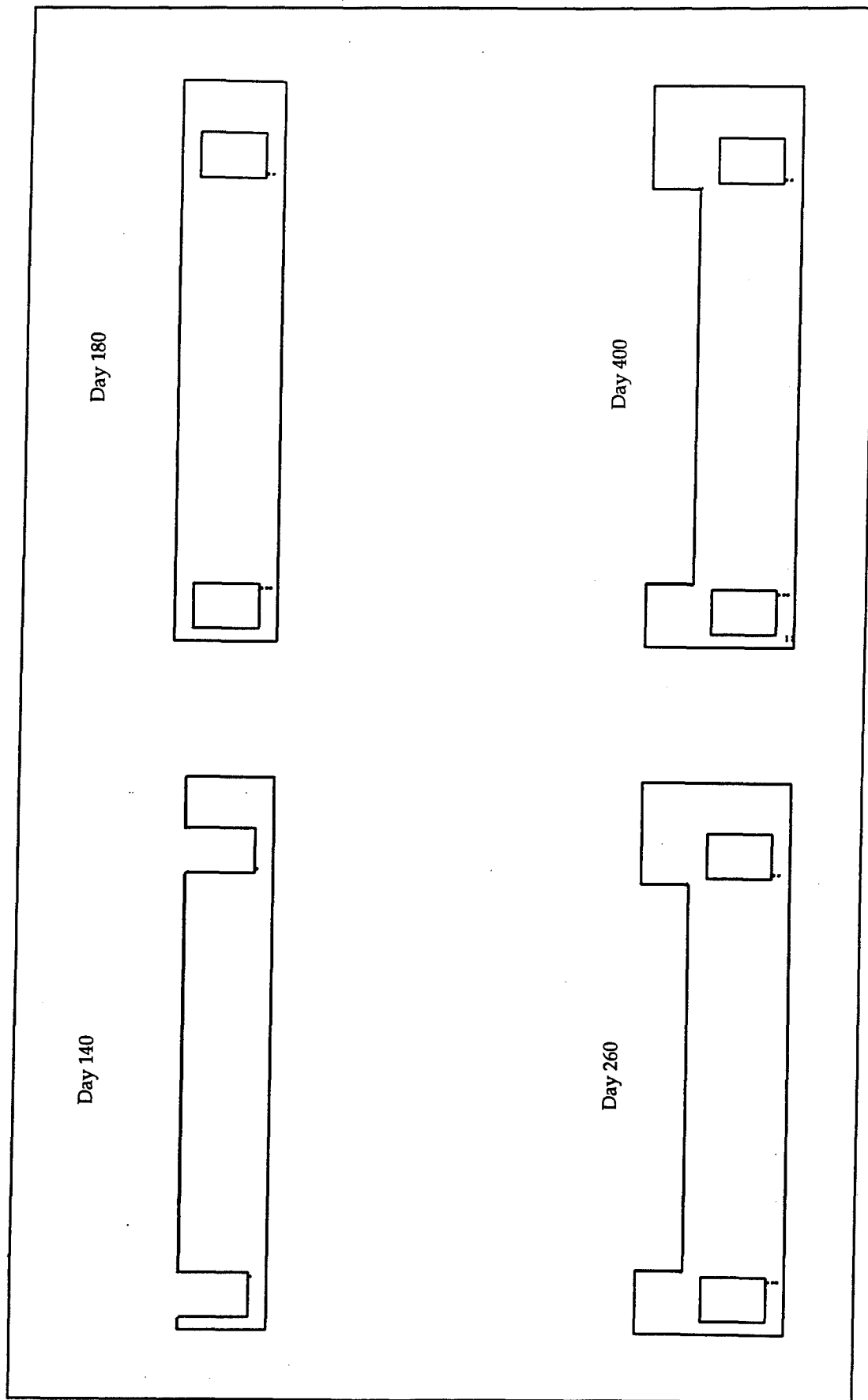


Figure 25. Ten-day placement analysis cracking development

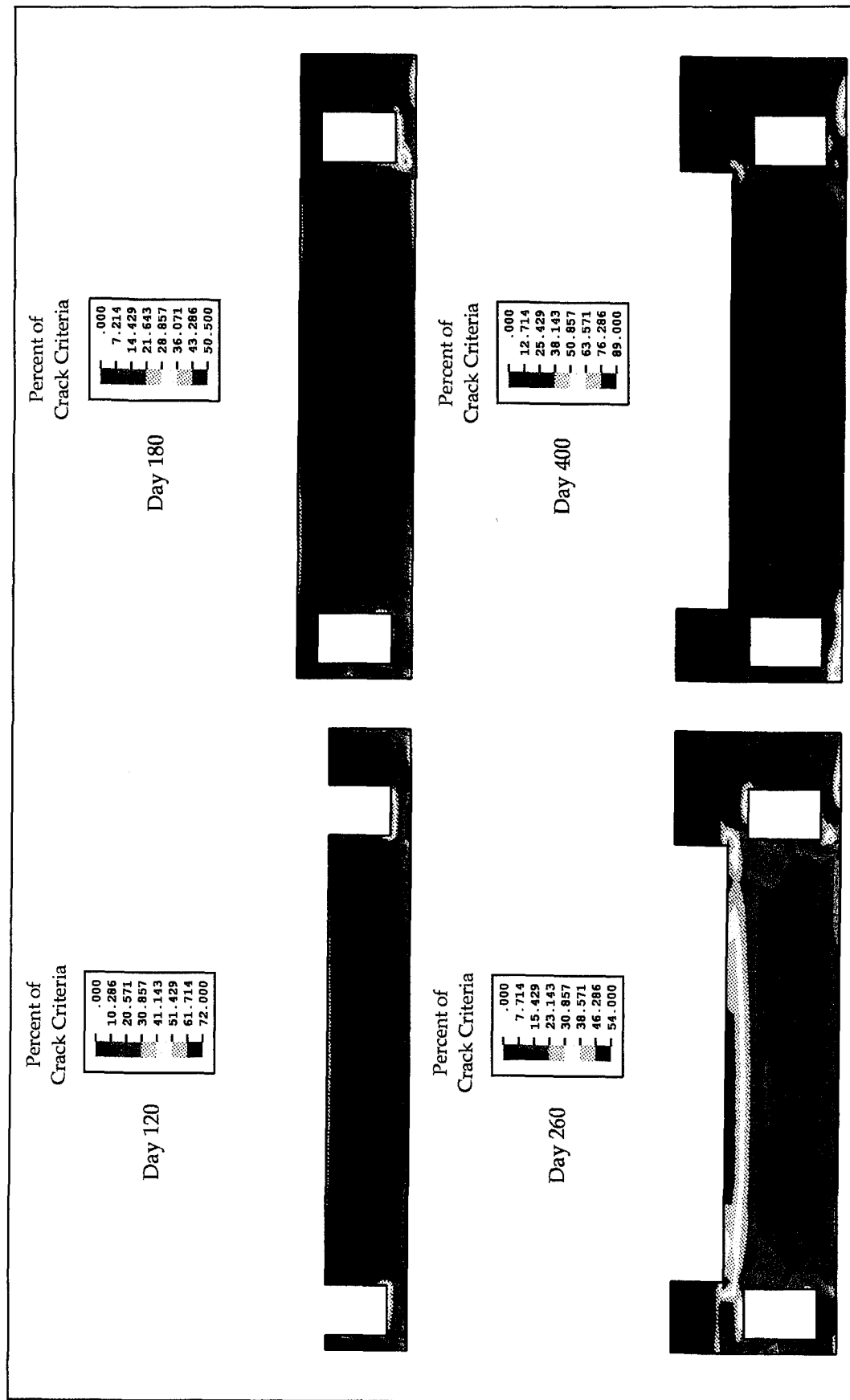


Figure 26. Ten-day placement analysis crack potentials

Figure 27. These results indicate a more severe cracking problem of a structural nature and serve as a warning that global structural response can cause problems not intuitive when considering only material behavior under changing construction parameters. However, notice that these parameters have indeed mitigated cracking potential along the top of the slab.

## Floor Insulation Study

The next construction parameter to investigate for mitigation of cracking potential predicted in the baseline analysis was insulating the floor of the chamber during the winter months. The intent here was to reduce the thermal gradient across the slab by insulating the surface against the cold ambient temperature. This study used 5-day placement increments and applied 1 ft of moist sand over the floor of the chamber 10 days after the slab was placed. The sand had an R-value of  $4.17 \text{ days-in}^2 \text{-}^{\circ}\text{F/Btu}$ , a unit weight of  $133.8 \text{ lb/ft}^3$ , and it was left on for the duration of the analysis. All other parameters were identical to the baseline analysis. Figure 28 provides the thermal contours for this analysis (compare with Figure 16 for the baseline analysis), and Figure 29 shows the temperature histories compared with the baseline analysis. Only a slight change in the temperature in the middle of Lift 17 is detected due to the floor insulation, and this indicates that this parameter may be more of a surface effect. Figure 30 shows the cracking development for this analysis, and Figure 31 shows crack potential contours for selected points in time. The behavior is very similar to the baseline analysis, as expected. The cracking around the culverts is the same, and the cracking in the top of the slab near the middle wall has been mitigated by the floor insulation. Relative to the baseline analysis, the cracking potential across the top of the slab has been reduced by approximately 5 percent. However, in absolute terms, it still shows a high potential for cracking at 90 percent, and this occurs over a fairly wide area. Thus, although very beneficial for surface effects, the applied floor insulation does not provide a significant factor for the mitigation of the cracking potential in the top of the slab. This is because the thermal gradient across the slab, which drives the cracking potential, is not significantly affected. Alternatively, the floor insulation must be significantly more effective, i.e., more adiabatic, to be of significance in mitigating cracking in the top of the slab.

## Conclusions

The following conclusions are summarized based on the 2D transverse slice parametric studies presented in this chapter. Recall that cycling through two winters was done in the absence of service loads in order to investigate the thermal-induced response without service loads.

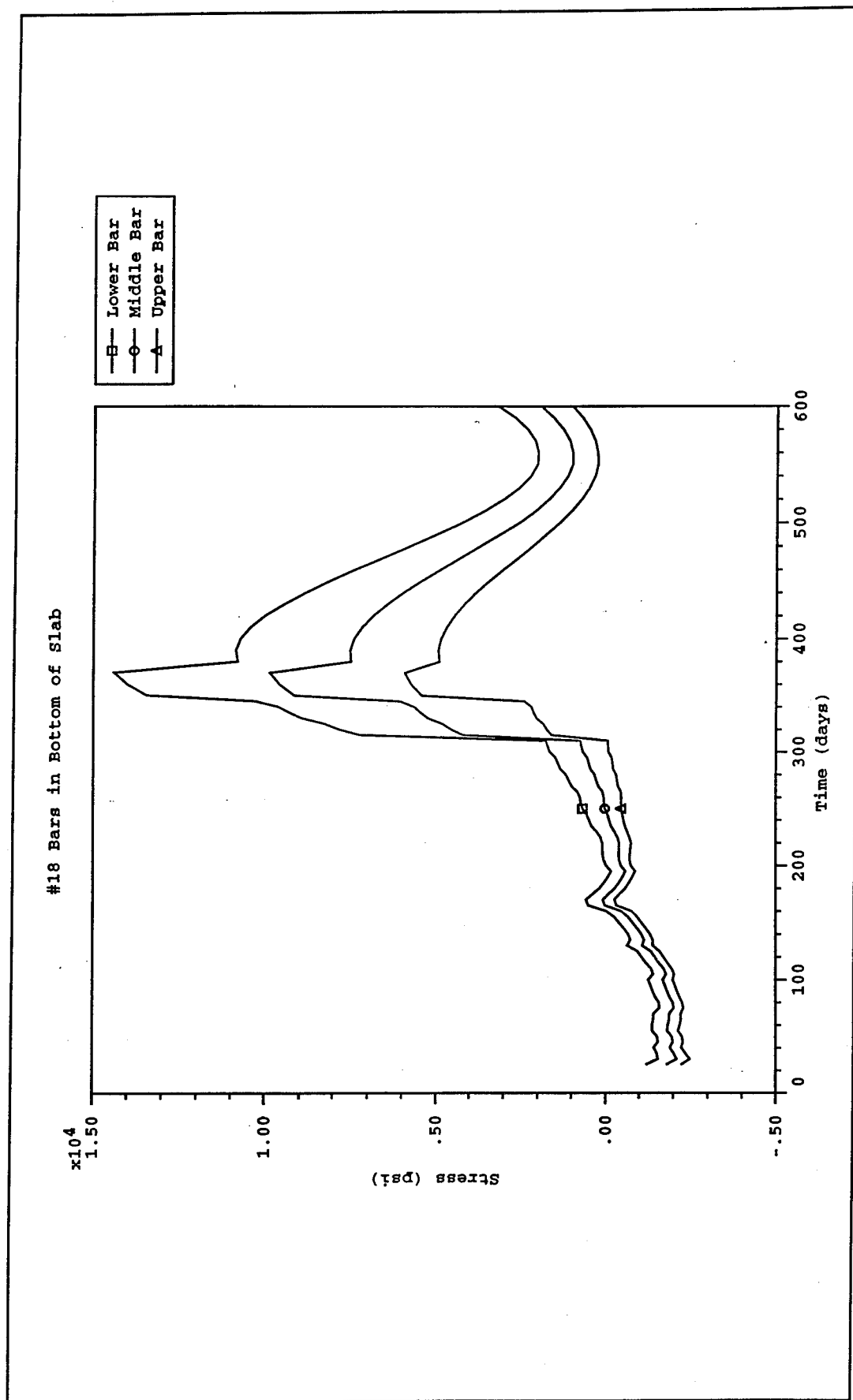


Figure 27. Reinforcement stresses under center wall culvert

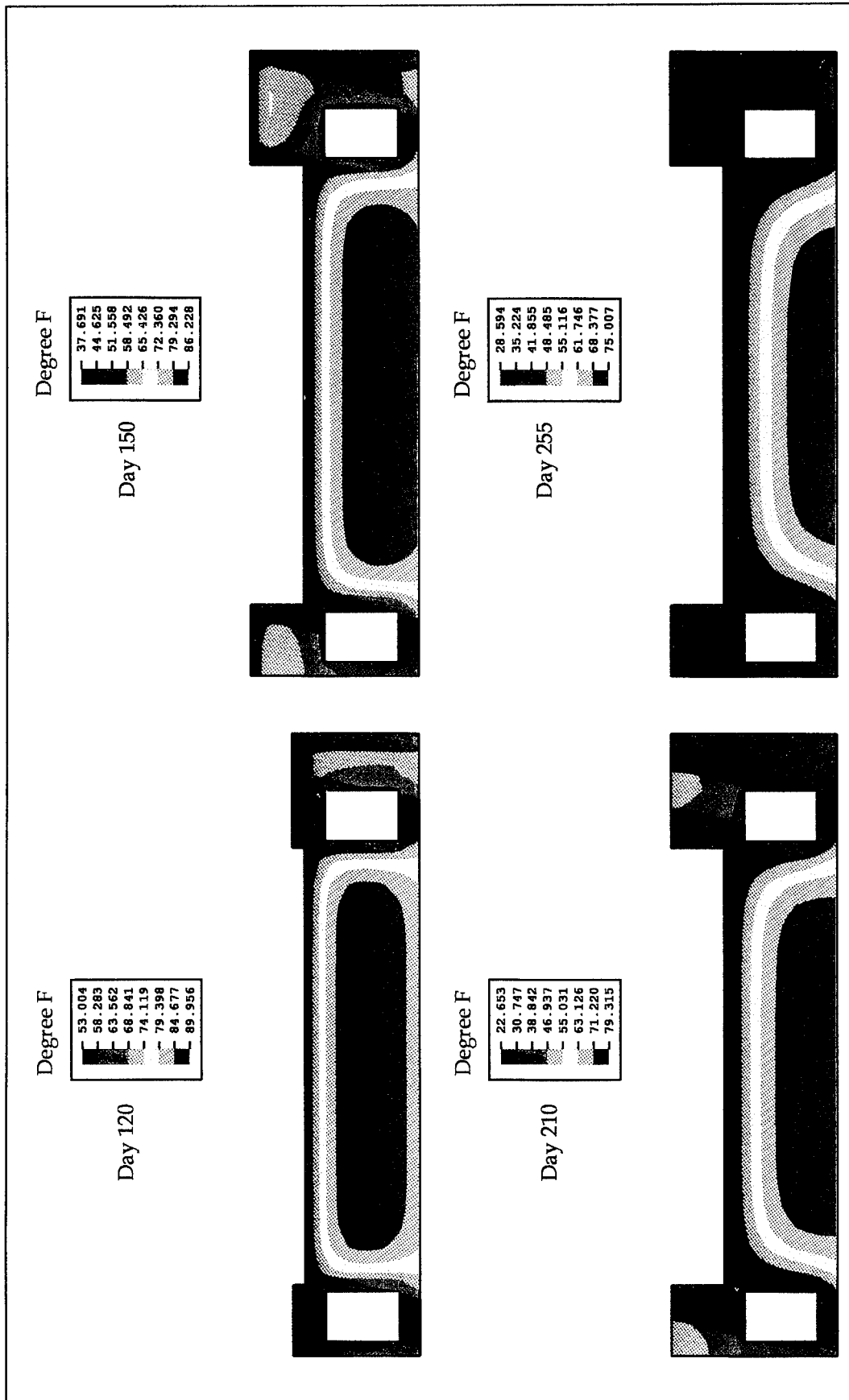
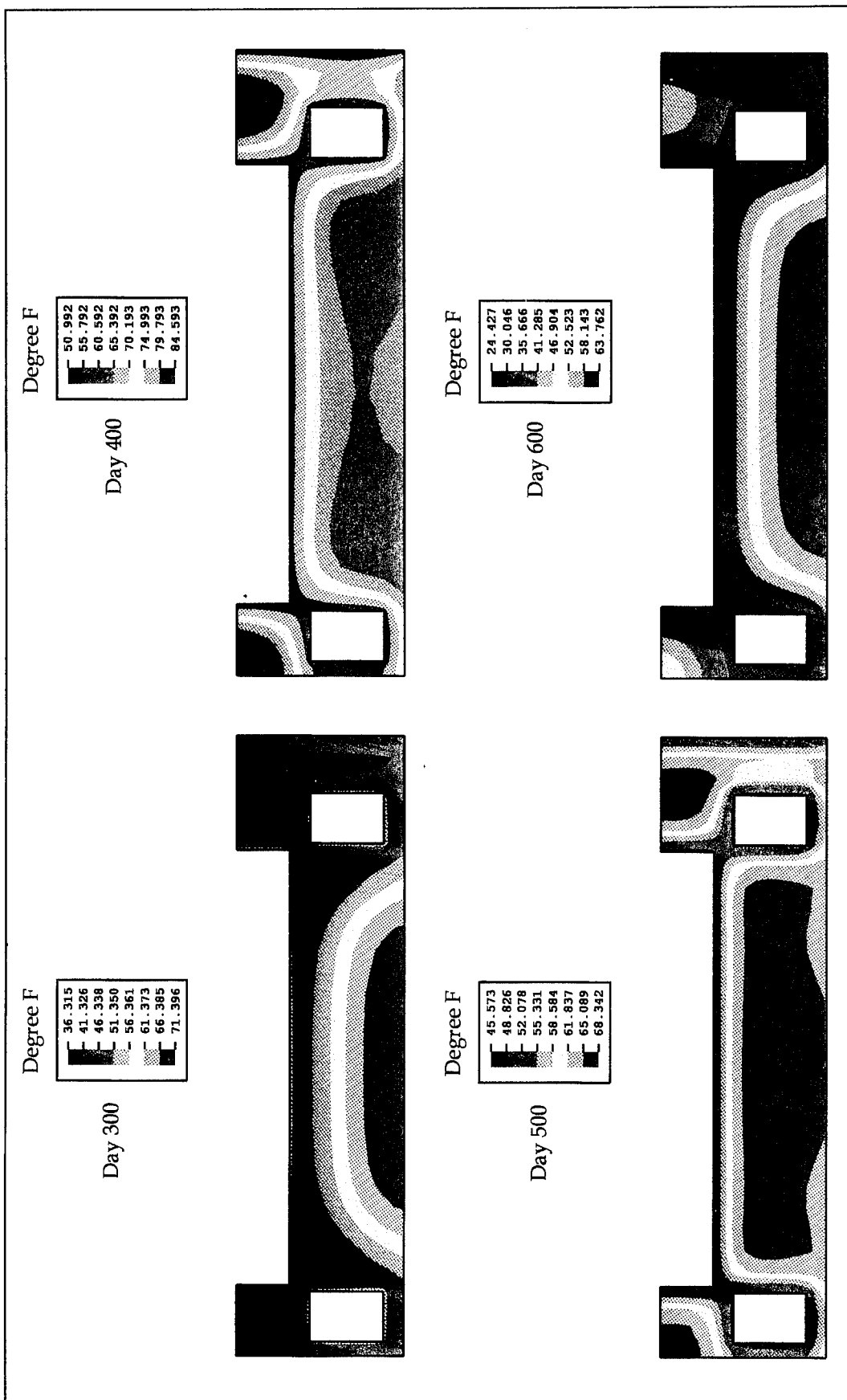


Figure 28. Floor insulation analysis thermal contours (Continued)



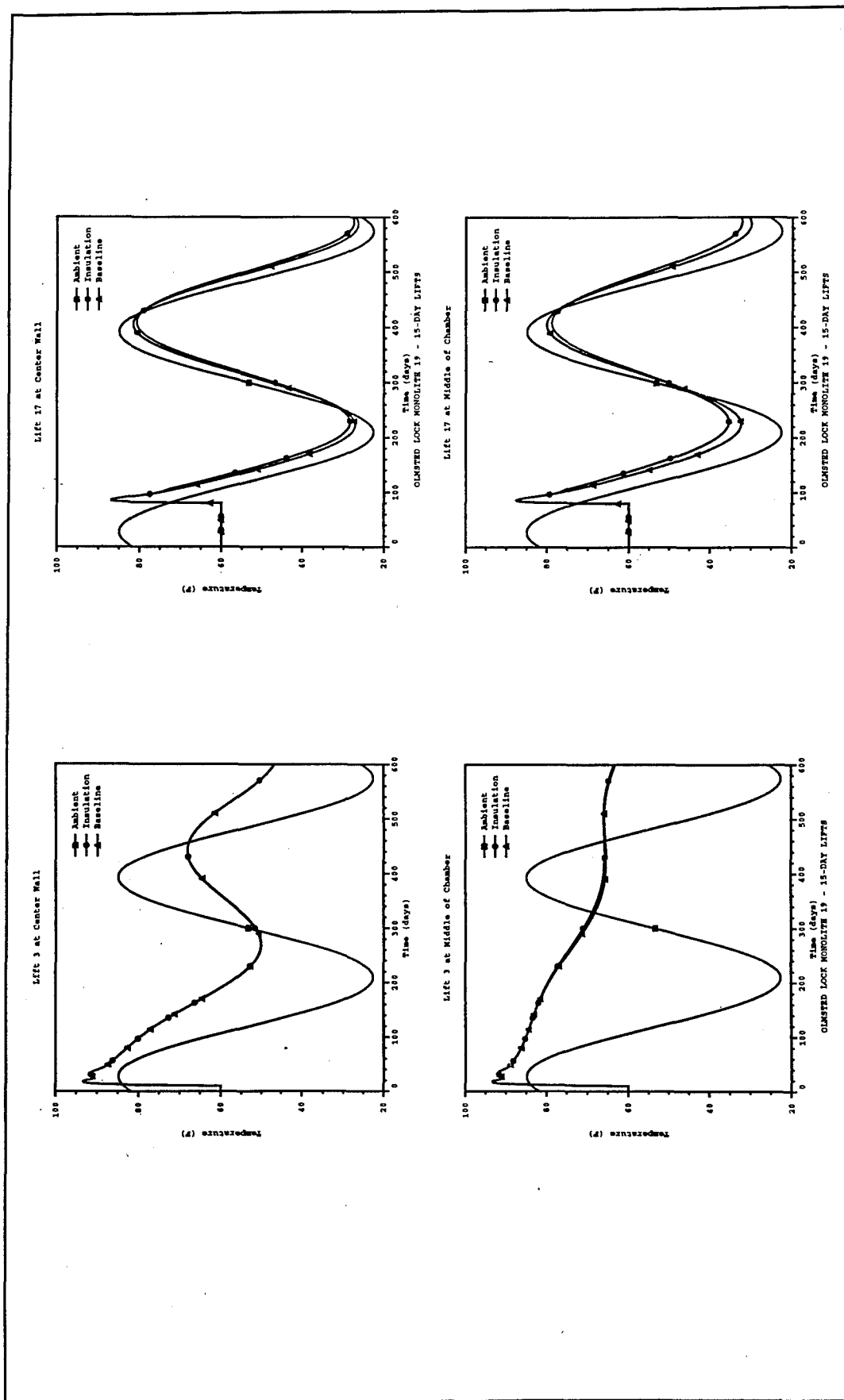


Figure 29. Floor insulation versus baseline temperature histories

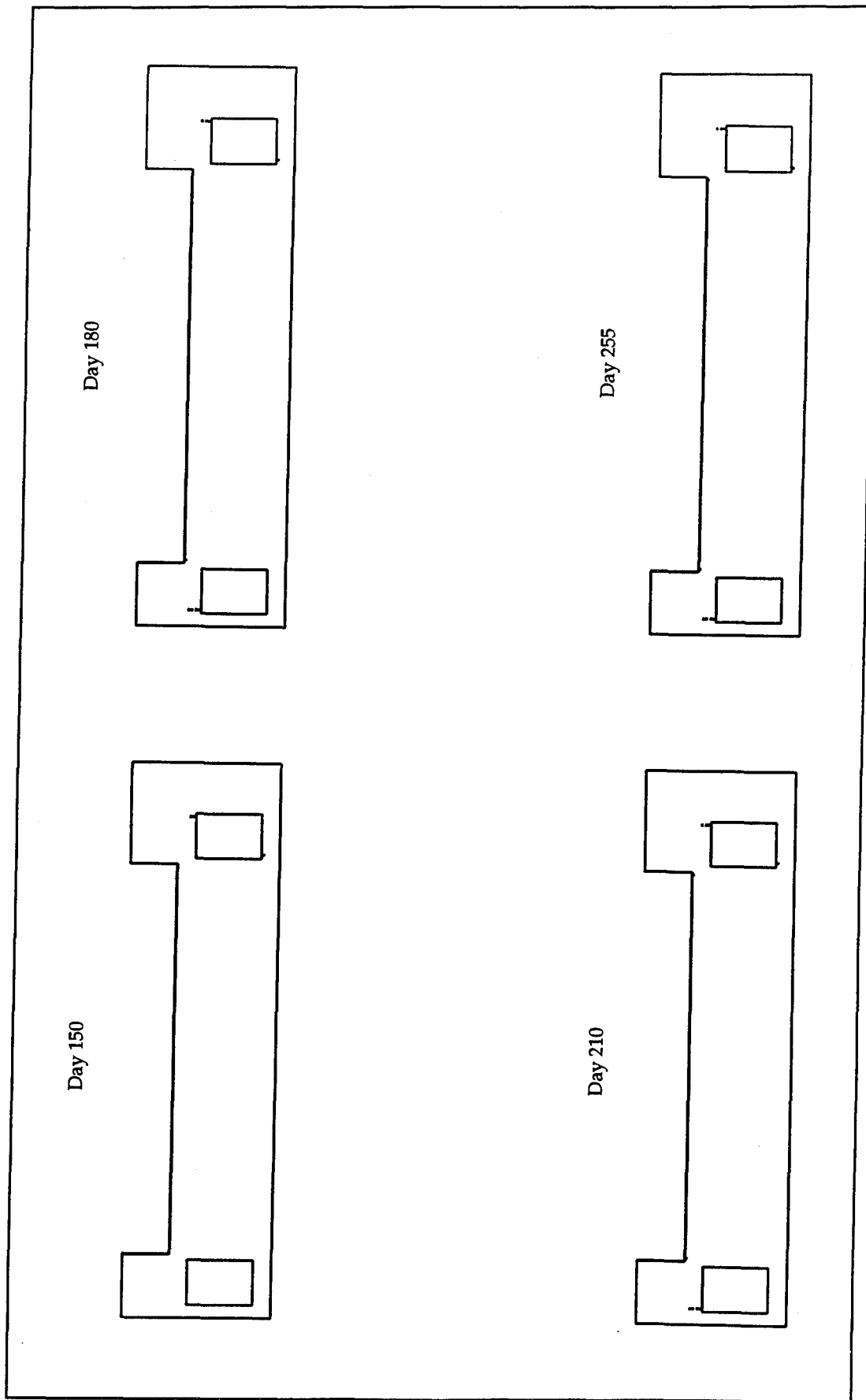
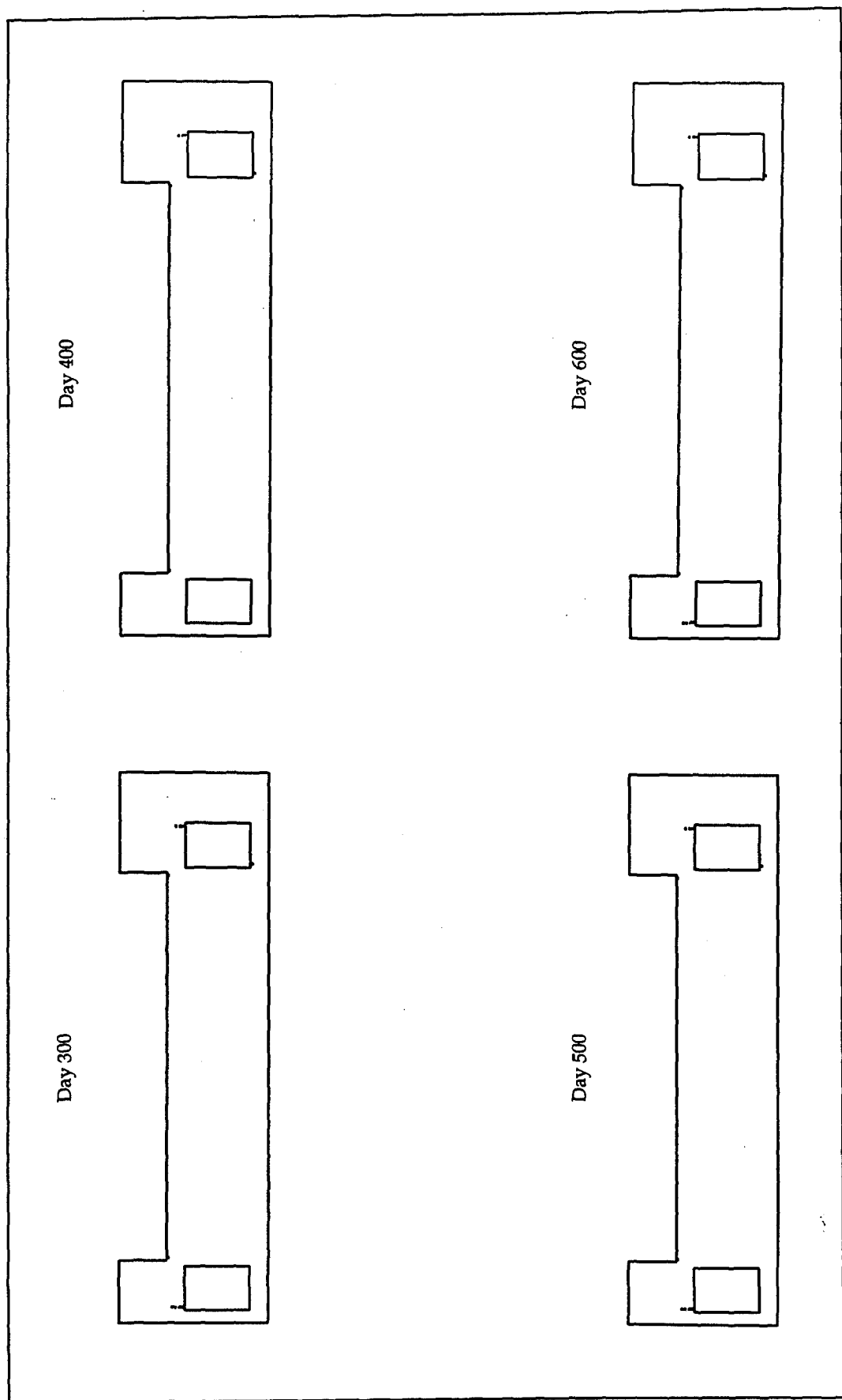


Figure 30. Floor insulation analysis cracking development (Continued)



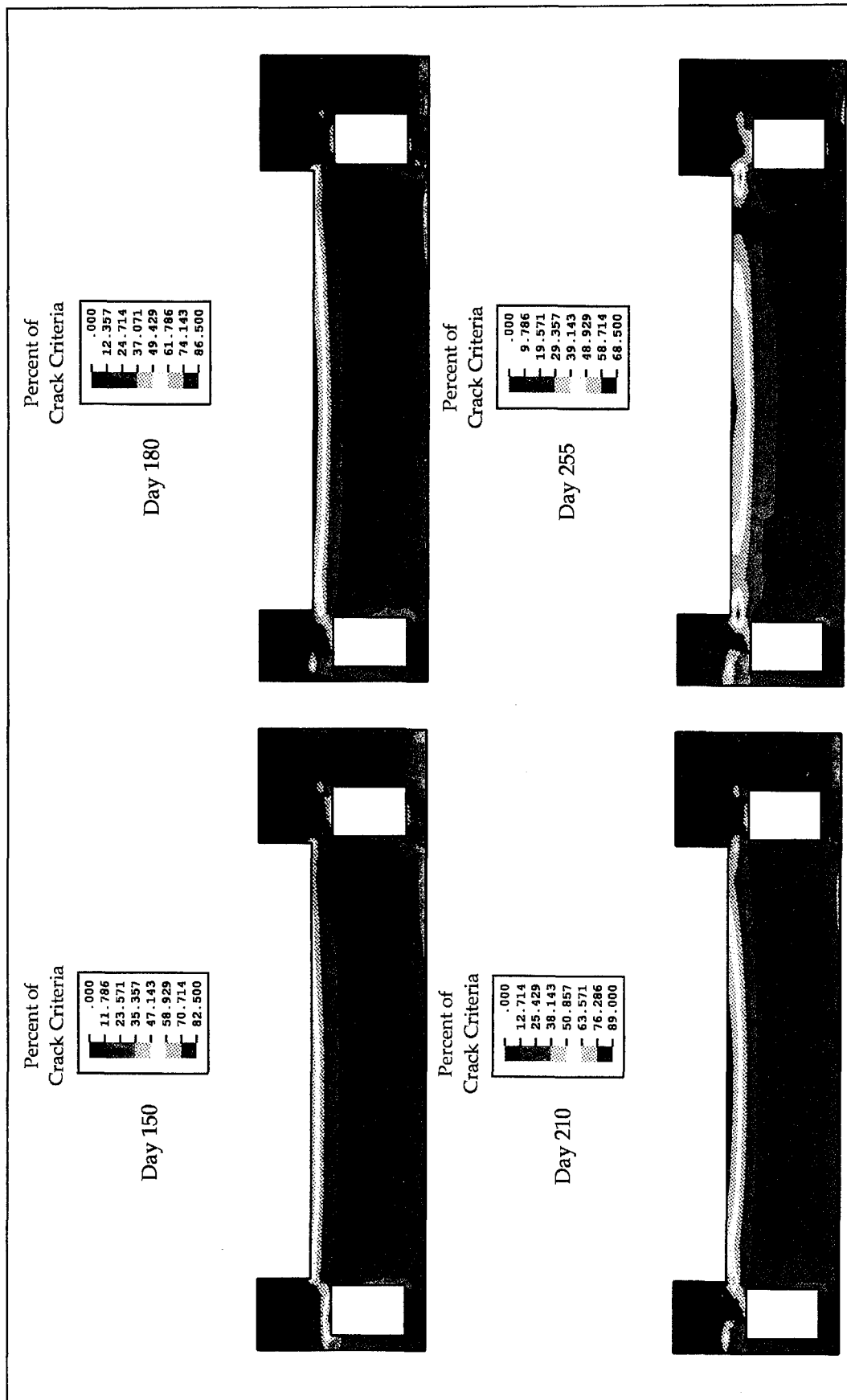


Figure 31. Floor insulation analysis crack potentials (Continued)

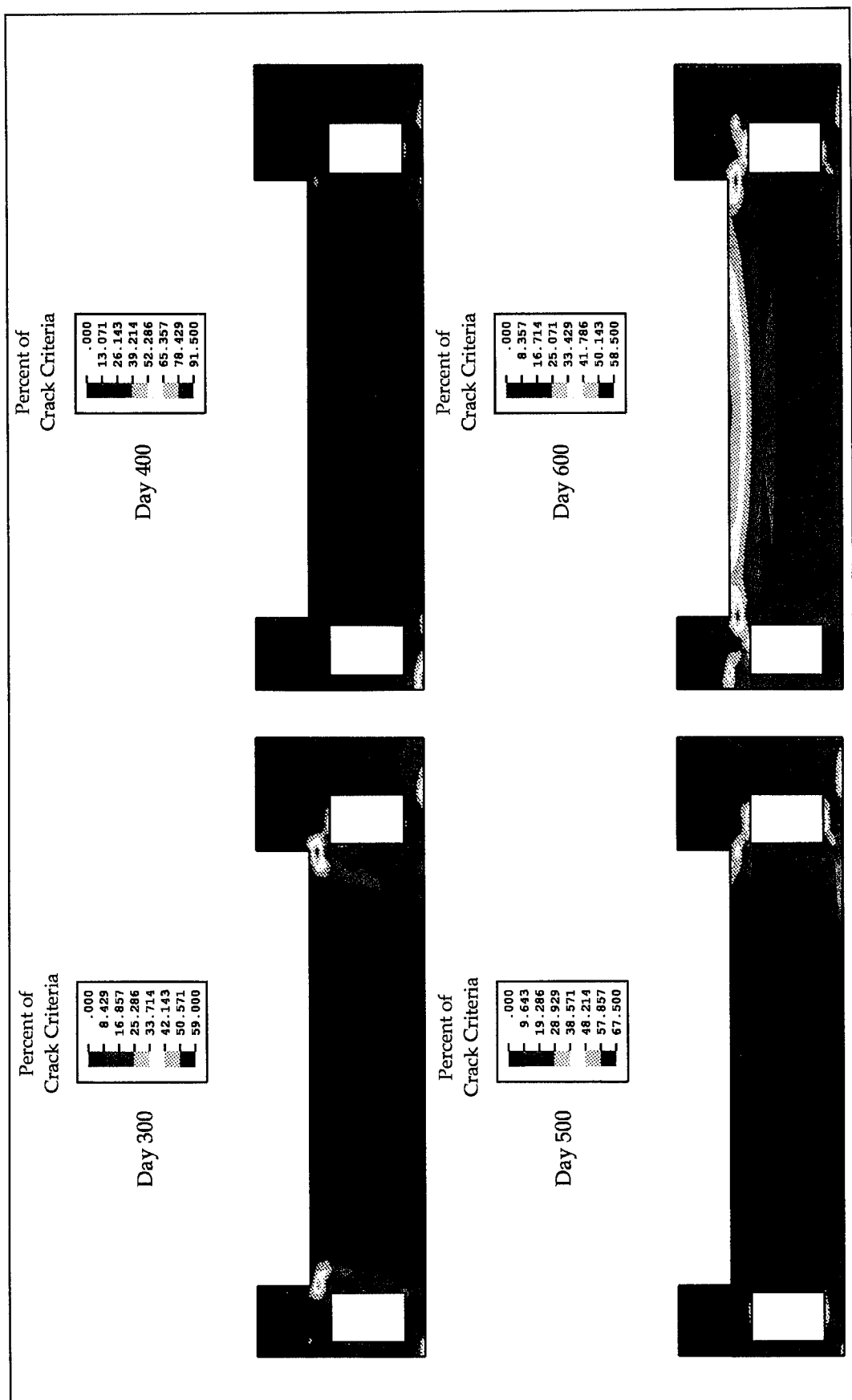


Figure 31. (Concluded)

- a. Cracking is indicated to occur around the culverts. The cracking around the top corners tends to open in winter and close in summer, and it is not considered a structural concern directly. However, maintenance to prevent degradation of the reinforcing bar and surface spalling may need to be addressed. Insulation effects from closing culvert openings should help mitigate these cracks. However, extrapolating from the floor insulation study, high insulating R-values may be required to provide significant relief from cracking.
- b. Cracking is also likely in the bottom corners of the culverts and on the bottom of the slab in summer due to thermal-induced bending. The reinforcing bar should be effective in carrying the load and arresting these cracks, and structural integrity should not be compromised.
- c. Cracking is indicated along the top of the slab. Cracks open in the top of the slab at the wall junctions, and the crack potentials exceed 90 percent over a large region of the span between the walls. Insulating the floor with sand provides some mitigation (~ 5 percent) for this cracking potential. However, an insulating technique providing much higher R-values appears to be required for crack prevention. An analysis using an easily applied adiabatic condition to this surface as a bounding case would be useful in quantifying the gain from pursuing alternative floor insulation.
- d. The cracking in the top of the slab near the outer wall is dominated by thermally induced bending and is arrested by the reinforcing bar. The cracking near the center wall is dominated by constraint against thermal shrinkage, and the reinforcing bar here, designed for slab bending, is not effective in arresting the crack. The cracks in both areas open to less than 0.01 in. and tend to close later in time. The maximum reinforcing bar stresses only reach 6 ksi. Thus, these cracks are not a structural concern under thermal loads. However, the presence of these cracks and the high potential for other cracks create a need to evaluate service loads in the structure under these construction parameters.
- e. The 10-day placement increment study indicated a more severe problem with cracking through the lift forming the base of the slab. This is due to a thermal-induced structural response acting on the notched beam geometry of the section before the culverts are completed. Reinforcing bar stresses on the bottom of the slab near the centerline reach 15 ksi, and cracking through the base into the culverts is predicted. Using a 10-day placement increment in the slab did provide a reduced cracking potential in the top of the slab, as intended, although this conclusion must be moderated somewhat since cracking does occur underneath the culverts. However, if the notched beam effect can be overcome, this construction parameter may warrant additional consideration. One method may be to enforce 5-day placement increments for lifts on the bottom and switch

to 10-day increments, say, half way up the slab. Other considerations may involve a shift in start dates or culvert construction detailing (such as reinforcing bar extending across the culverts during lift placements with later removal) or pile re-evaluation. Additional analyses for any mitigation measures are recommended since this global structural response under these construction conditions is not intuitive.

## 5 Two-Dimensional Longitudinal Slice

---

### Model Description

As a check to verify that the construction parameters used in the transverse slice studies did not pose any major problems in the longitudinal direction, two longitudinal slices were chosen for evaluation. These slices are down the center lines of each lock chamber. The model for the riverside chamber slice is shown in Figure 32, and the model for the landside chamber slice is shown in Figure 33. These models are shown with the upstream face to the left and show the sill on top of the chamber and the culverts and gallery intersecting the section. The riverside slice contains three culvert intersections, and the landside slice contains only the one culvert that starts under the landside wall and turns to exit the farthest downstream in the monolith. To speed model development and because it adds conservatism, the reinforcing bar in these sections was not modeled. All other construction parameters are identical to those used in the transverse slice baseline analysis. The lift sequencing changes to model the appropriate cross section of the structure.

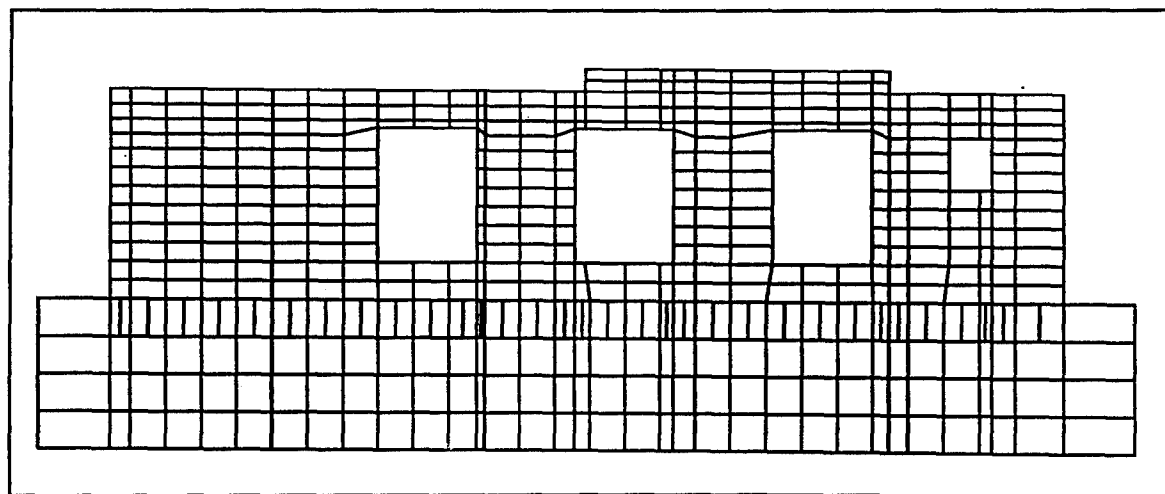


Figure 32. Riverside chamber longitudinal slice model

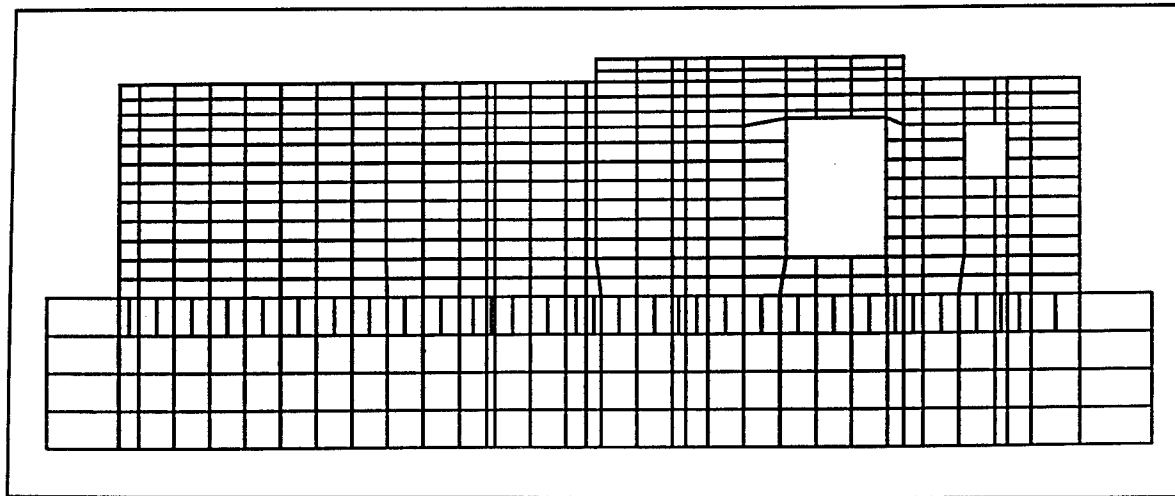


Figure 33. Landside chamber longitudinal slice model

## Riverside Chamber Analysis

Figure 34 shows the temperature distributions at selected times and Figure 35 shows temperature histories at selected points from the thermal analysis of the riverside chamber slice. Compared to the transverse slice baseline analysis, these temperature gradients are significantly lower. This is due to the reduced thermal mass of this section and the cooling surface provided by the culverts. No cracking is predicted in the stress analysis for this model. Figure 36 shows crack potential contours at selected times and indicates that acceptable levels of cracking potential (about 50 percent maximum) are predicted for this longitudinal slice. This peak potential occurs around day 170 and is located on top of the slab slightly upstream from the front edge of the sill due to a thermal-induced bending shape. Another potential hot spot is on the surface of the sill at midspan and along the bottom of the culverts.

## Landside Chamber Analysis

Figure 37 shows the temperature contours for the landside chamber slice at selected times. The gradients in this analysis are only slightly lower than the transverse baseline analysis since this cross-section has a similar amount of concrete mass. The temperatures are lower since the heat can flow to the upstream free surface as well as up to the floor free surface. Comparison of these contours with the riverside chamber analysis illustrates the benefit of reducing heat-generating thermal mass and providing more surface area for heat convection. Figure 38 provides temperature histories at selected points. The crack patterns shown in Figure 39 indicate that cracking will occur in the top of the slab at the upstream edge of the sill for these construction conditions and that the

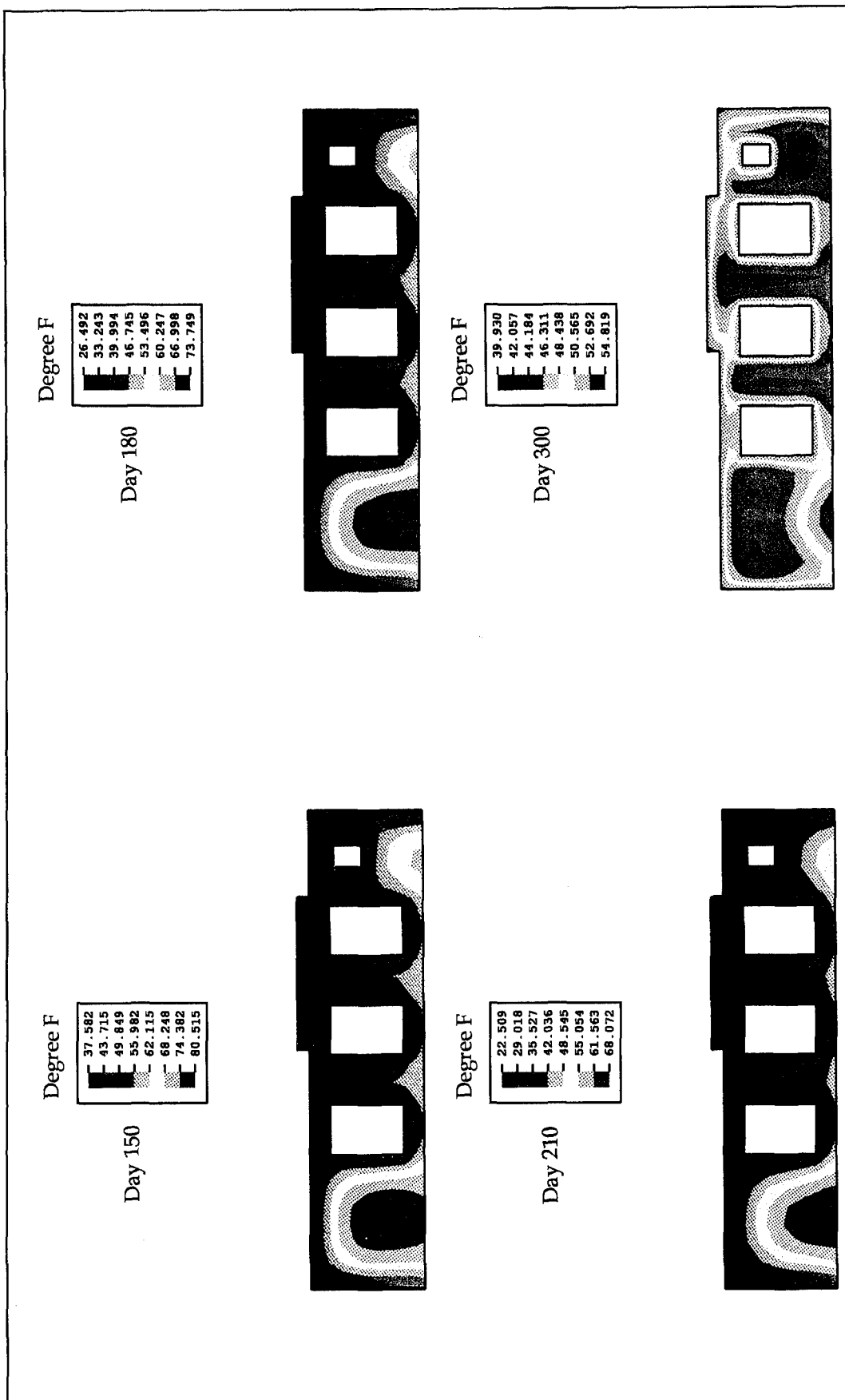


Figure 34. Riversid longitudinal slice thermal contours

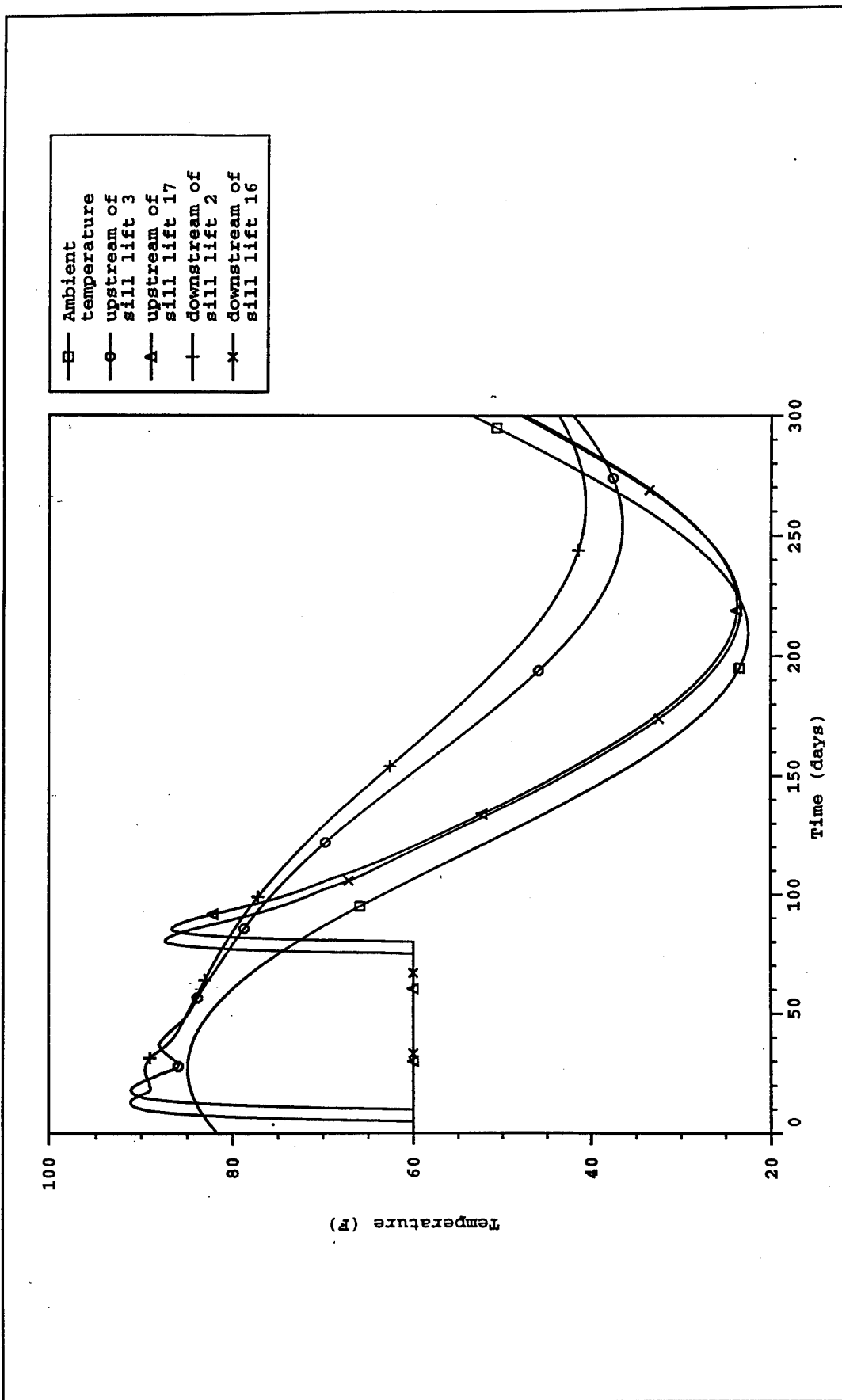


Figure 35. Temperature histories for riverside chamber slice

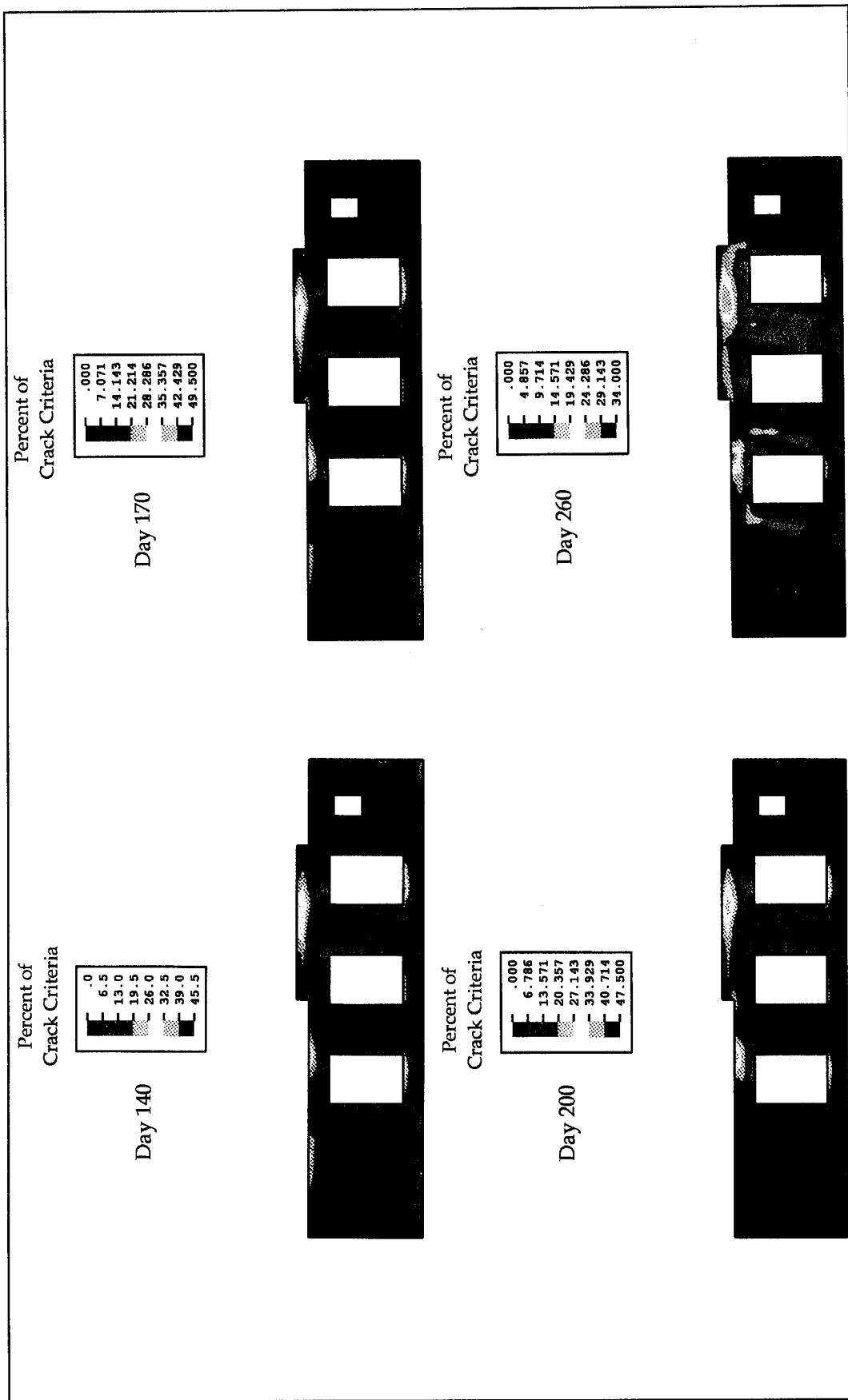


Figure 36. Riverside longitudinal slice crack potentials

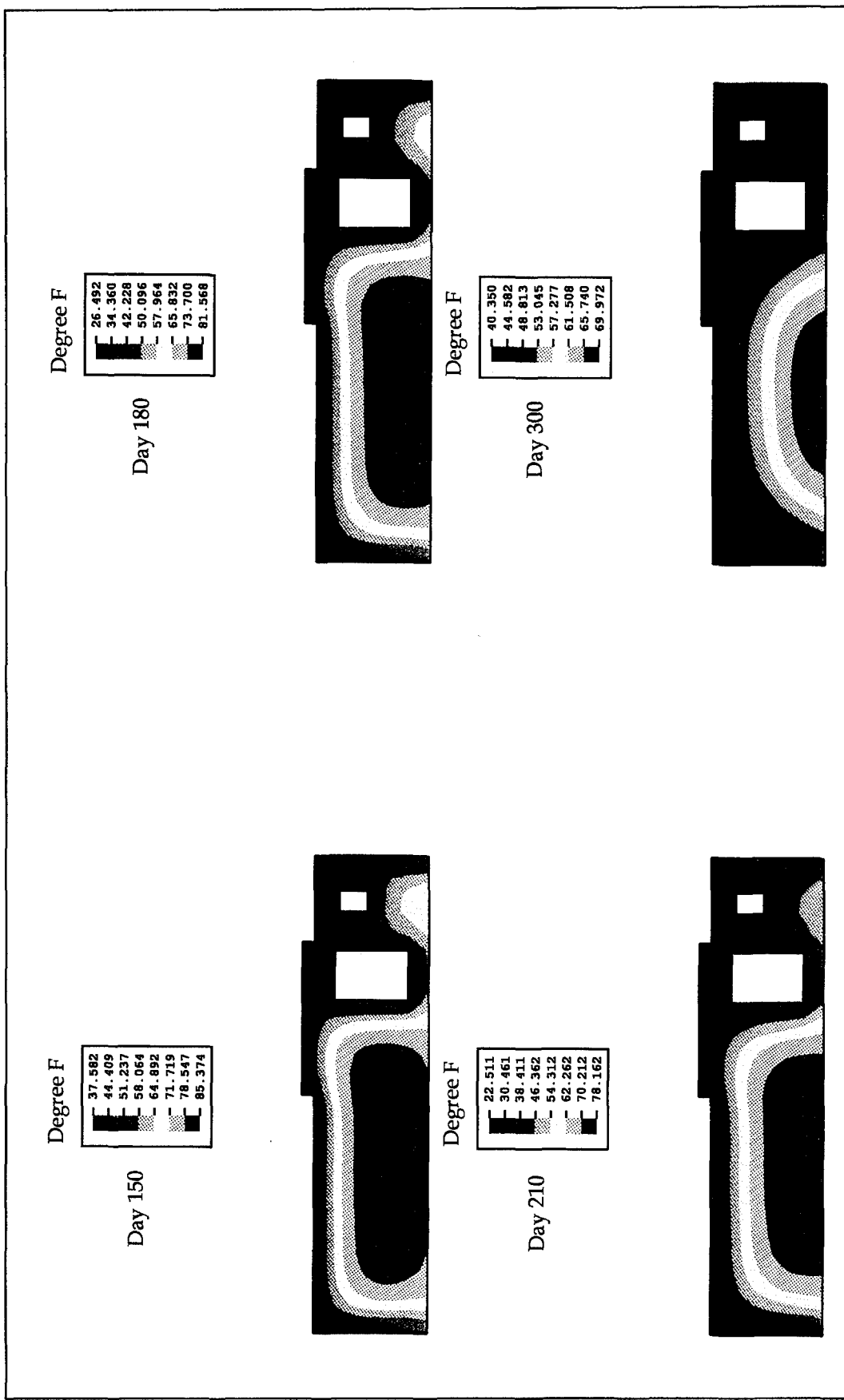


Figure 37. Landside longitudinal slice thermal contours

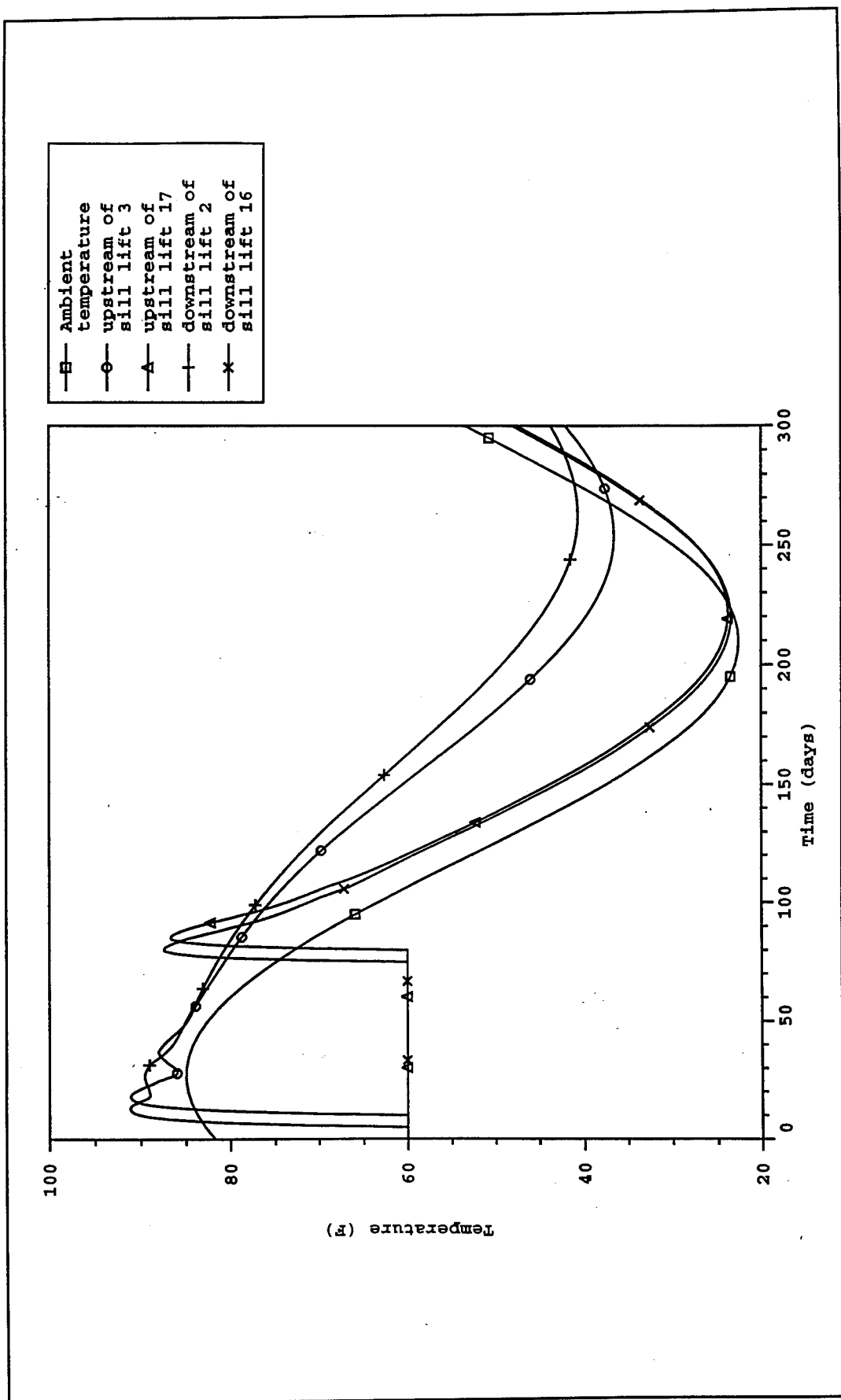


Figure 38. Temperature histories for landside chamber slice

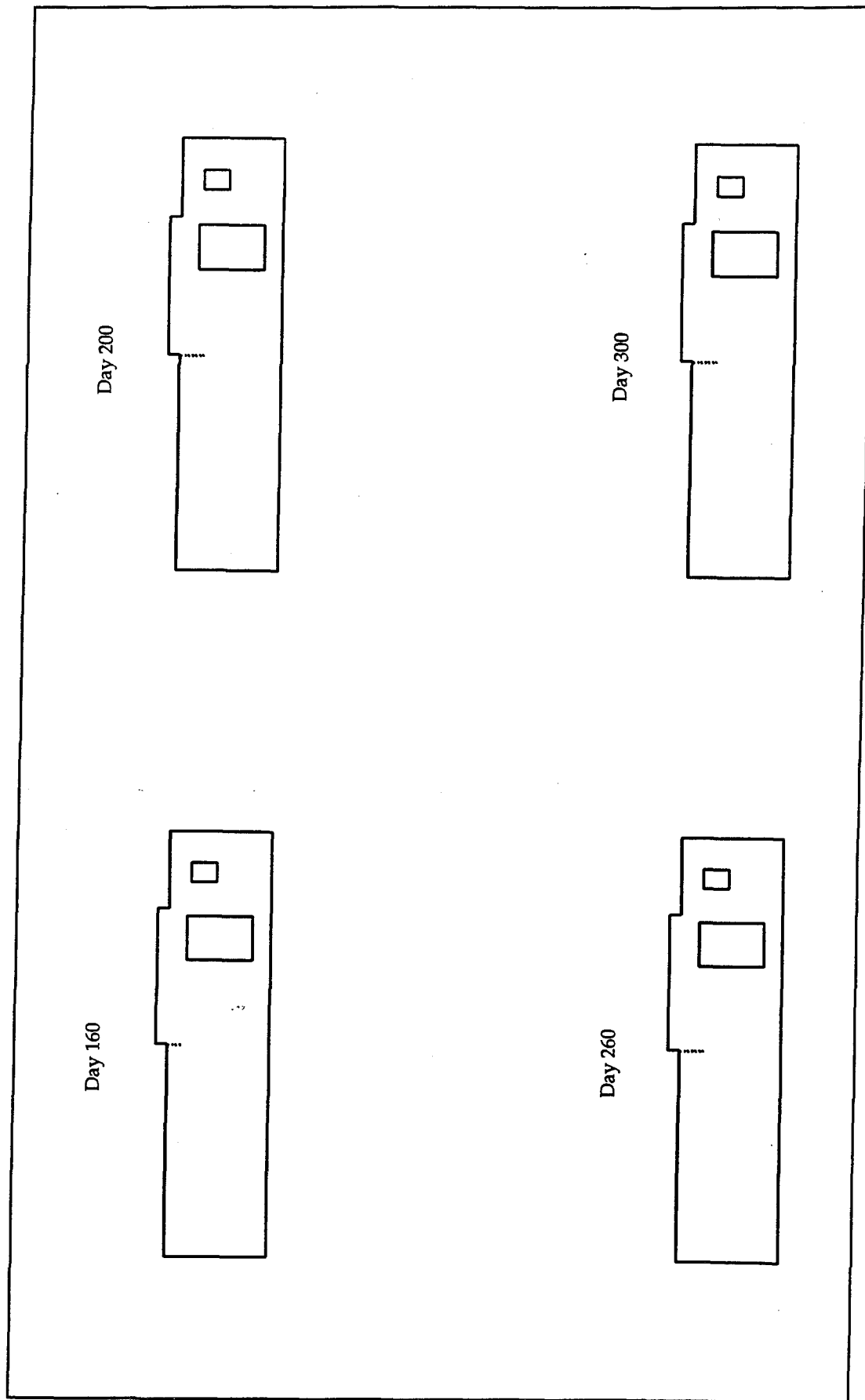


Figure 39. Landside longitudinal slice cracking development

tendency is to grow through the top lift of the slab. Figure 40 shows crack potential contours and indicates that other potential cracking areas are the corners of the culvert, the top of the sill, and the top of the slab upstream of the sill. However, these crack potentials are under 60 percent, and the top of the slab at the sill edge appears to be a locally concentrated area of cracking. Since this longitudinal slice model does not include reinforcing bar or floor insulation, it is anticipated that these factors, especially the presence of the reinforcing bar, will prevent the crack from growing to the depth indicated in this analysis.

Also of interest from these longitudinal analyses is the examination of the stresses across the vertical lift joints. This information will aid in evaluating the potential for growth of these built-in weak zones and for subsequent detailing for joint construction. Figure 41 shows representative stress histories across various joint locations. These are taken from the more critical landside chamber slice and are computed in the model by assuming the joint is fully bonded. The joints in the bottom of the slab typically show small early tension of 50 to 80 psi and later compression of 100 to 150 psi. The vertical joints nearer the top of the slab show peak tension during the winter from 100 to 200 psi. As expected, the most critical joint (200-psi tension) is shown to be between lifts 18 and 17 on the top of the slab upstream from the sill.

## Conclusions

The longitudinal slice analyses bear out the assumptions that the transverse slice is the more critical section and should be used in parameter studies for construction optimization. The landside chamber containing more mass in the cross section is the more critical of the longitudinal sections and indicates that cracking will occur in the top of the slab at the sill upstream edge, under the assumed construction parameters. Vertical joints on the top of the slab can experience up to 200-psi tension in winter without service loads and should be positioned as far from the sill edges as possible.

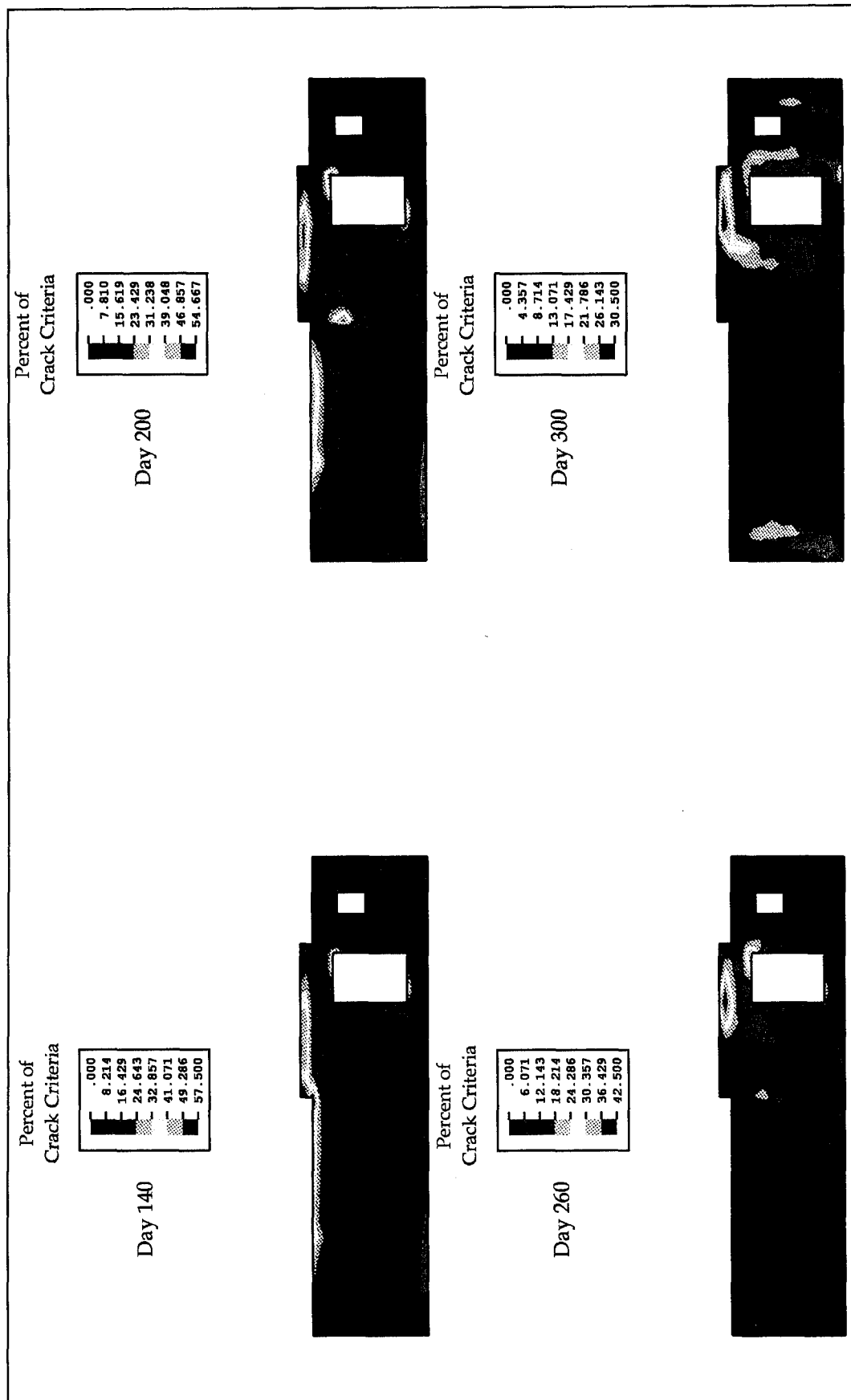


Figure 40. Landside longitudinal slice crack potentials

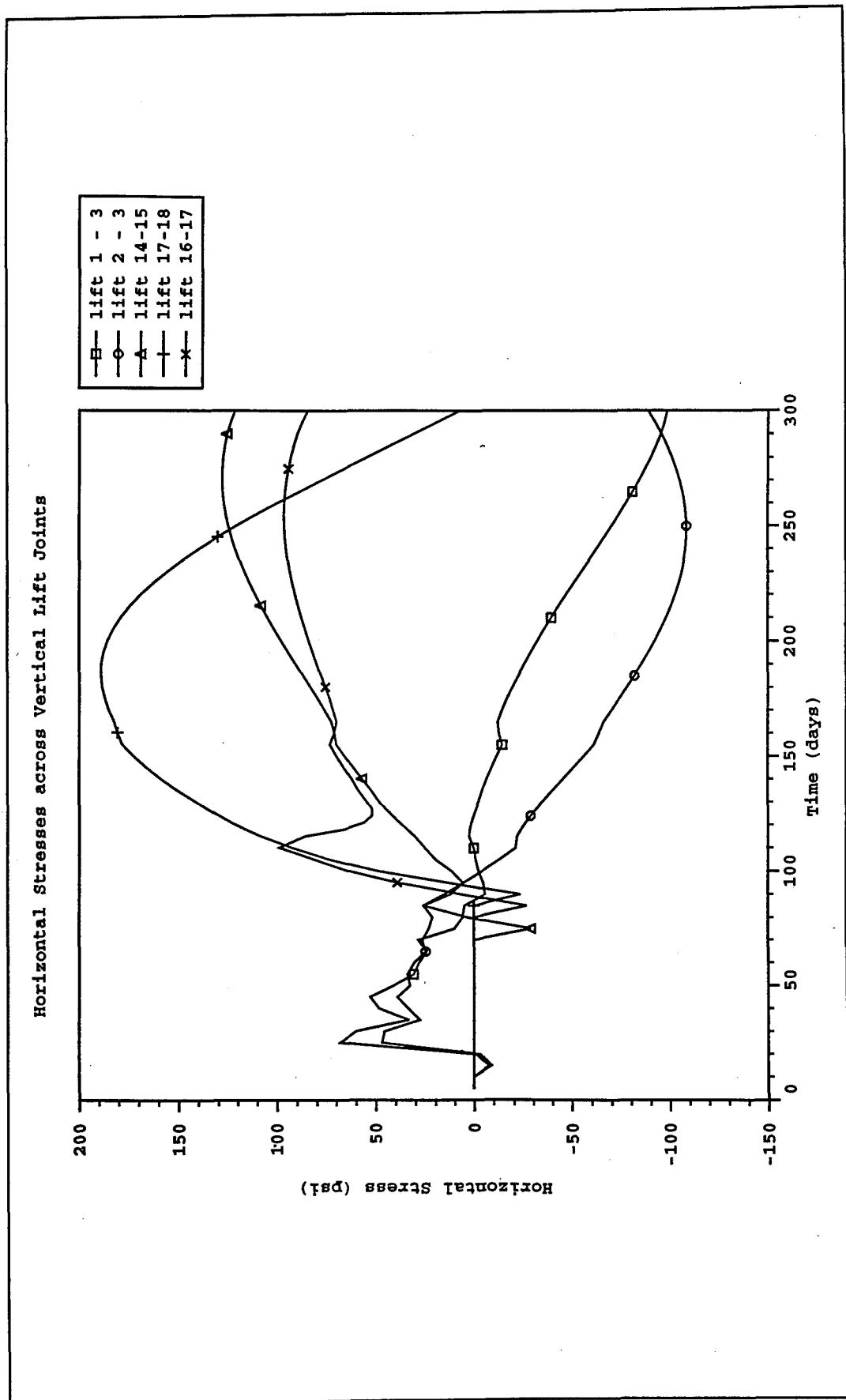


Figure 41. Lift joint stresses from landside chamber model

# 6 Three-Dimensional Analysis

---

The main goal of the 2D studies was to define the construction parameters to be used in a 3D analysis. However, the 2D analyses also provided valuable insight into the behavior of the monolith for understanding the important modeling considerations for building the 3D model. Although the 2D analyses did not reach the ultimate goal of finding optimal parameters that completely mitigated cracking predictions, encouraging results were obtained that predicted minimal cracking and showed that the cracking was not a serious threat to structural performance, at least in the absence of service loads. Based on early 2D results, changes in lift geometries were incorporated that mitigated cracking potentials around the culverts, and the important question of maximum placement temperature was established at 60 °F. The 2D results also established that the commonly accepted theory, which assumes longer placement intervals will lead to lower stresses because of lower temperature gradients, is structure dependent, and if considered for the current geometry and start date, then other cracking modes must be evaluated. For the 3D analysis, the combination of 60 °F maximum placement temperature, 5-day placement increments, the use of floor insulation, and the closing of culvert openings was set as the construction parameters for evaluation. Even though cracking is expected for these conditions, these parameters are felt to be advantageous for construction purposes since they follow common practice and should allow for reasonable construction costs. However, since cracking is expected and a high cracking potential is indicated for a large part of the top of the slab, it was also decided to include the service loads on the 3D model at the end of construction to further evaluate the consequences of these thermal-induced cracks.

## Model Description

The 3D analysis modeled the landside half of the monolith enforcing symmetry conditions along the center line of the structure. This was considered the more critical section because of the large expanse of the full

slab thickness between culverts. This assumption is confirmed by the results of the longitudinal slice analysis which show that the landside chamber slice is more susceptible to cracking. The use of stub walls and one quadratic displacement element through the thickness of each lift, as qualified in Chapter 3, is employed in the model. The design of the mesh in the plan view section is controlled by the pile locations, the culverts, galleries, walls, the sill, and the geometry of each lift placement. Twenty-node brick elements were used for the vast majority of the model, but 15-node prism elements were used for geometric shapes which cannot be modeled by brick elements without introducing distorted elements. Figure 42 shows the model in various stages of construction simulation. Figure 43 provides the IJK-node numbering system for the model and defines points and sections used in presenting results.

To reduce the modeling effort, some assumptions were introduced into the finite element model. For example, the downstream corner of the land wall was modeled with a right angle instead of the 45° chamfer design. The elevation of the gallery bottom surface was assumed to be at an elevation of 245 ft instead of 244 ft, as specified in the drawing, to correspond to existing nodal point lines. Similarly, the elevation of the gallery roof was modeled at 254 ft instead of 252 ft. This was necessary because of the reduced number of elements used in the vertical direction. The piles were placed at 5-ft spacing in the longitudinal direction and 6-ft spacing in the transverse direction. The soil foundation under the monolith was modeled for the thermal elements, but the soil-pile system was replaced in the stress analysis by spring elements. The pile spring models had stiffness in the axial, transverse, and longitudinal directions. The values of these spring constants are provided in Chapter 2. Note that on the symmetry line of the model, one-half the value of the spring constant must be used. For nodes on the bottom of the monolith not connected to piles, a vertical compression-only spring was used to model the support of the soil. Strictly speaking, the stiffness of the soil spring should be computed according to test data and the tributary area of that spring; thus the stiffness of the soil springs will typically be different for each node due to the nonuniform spacing of the mesh. However, to simplify the modeling, an approximate approach was used to compute an average stiffness for a soil spring. In this approach, a typical patch of mesh on the base of the monolith was considered and an average value calculated from the total area divided by the number of nodes. This average stiffness of 500 kips/in. was used for all nodes with soil springs.

Figure 44 shows a schematic of the reinforcement to be included in the model. This reinforcement includes two #18 bars at 12-in. spacing in the transverse direction spanning the slab on the top and bottom. A third #18 bar is included on the top and bottom under the walls, as shown. A 1-ft spacing between these bars is assumed with a 6-in. cover depth. In the longitudinal direction on the top and bottom of the slab, #9 bars at 12-in. spacing are used. In the transverse direction on the upstream and downstream faces, #9 bars at 12-in. spacing are also used. Tying the faces of each wall into the slab, #9 bars at 6-in. spacing are used vertically, and #9

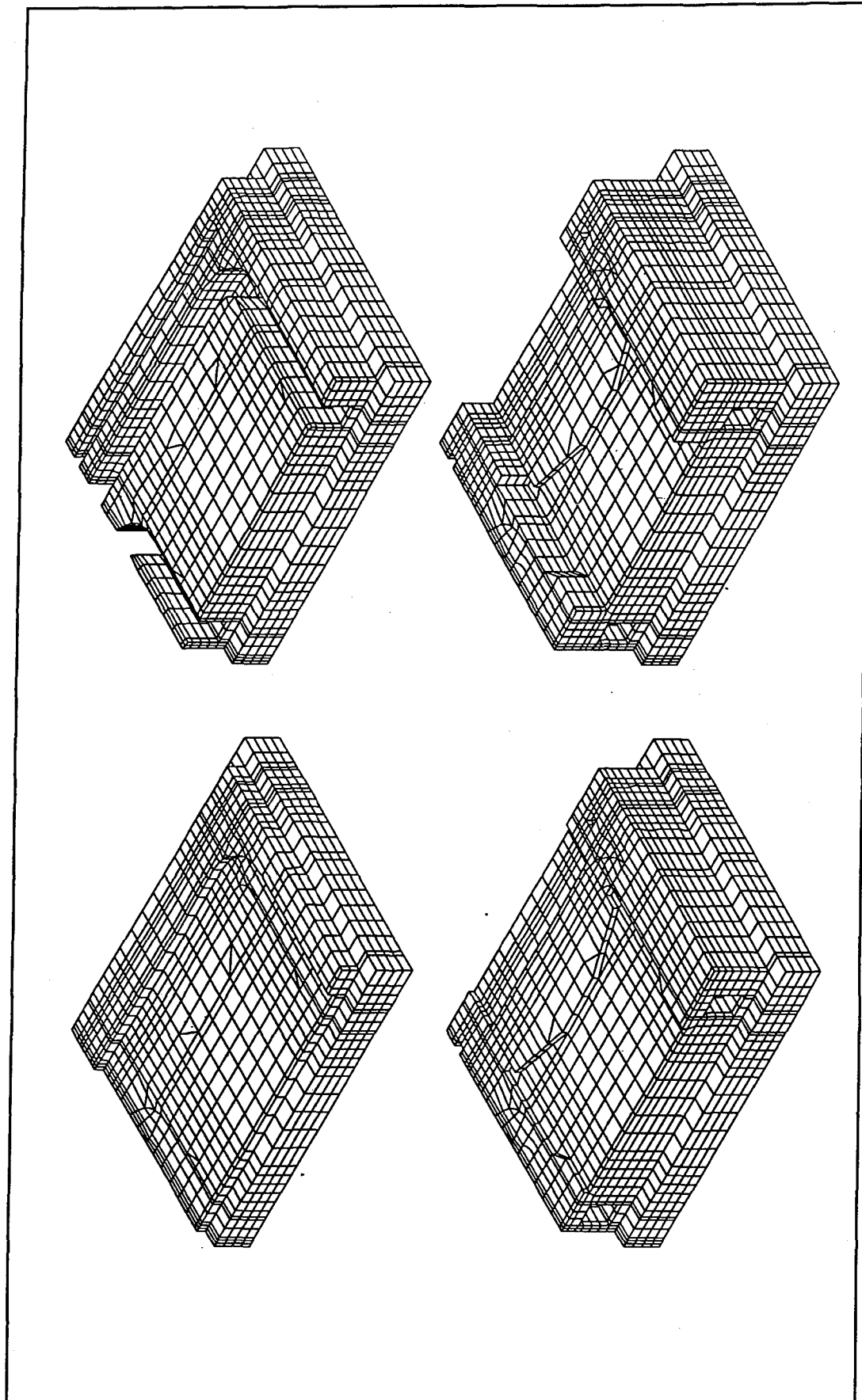


Figure 42. Three-dimensional finite element model showing four stages of construction

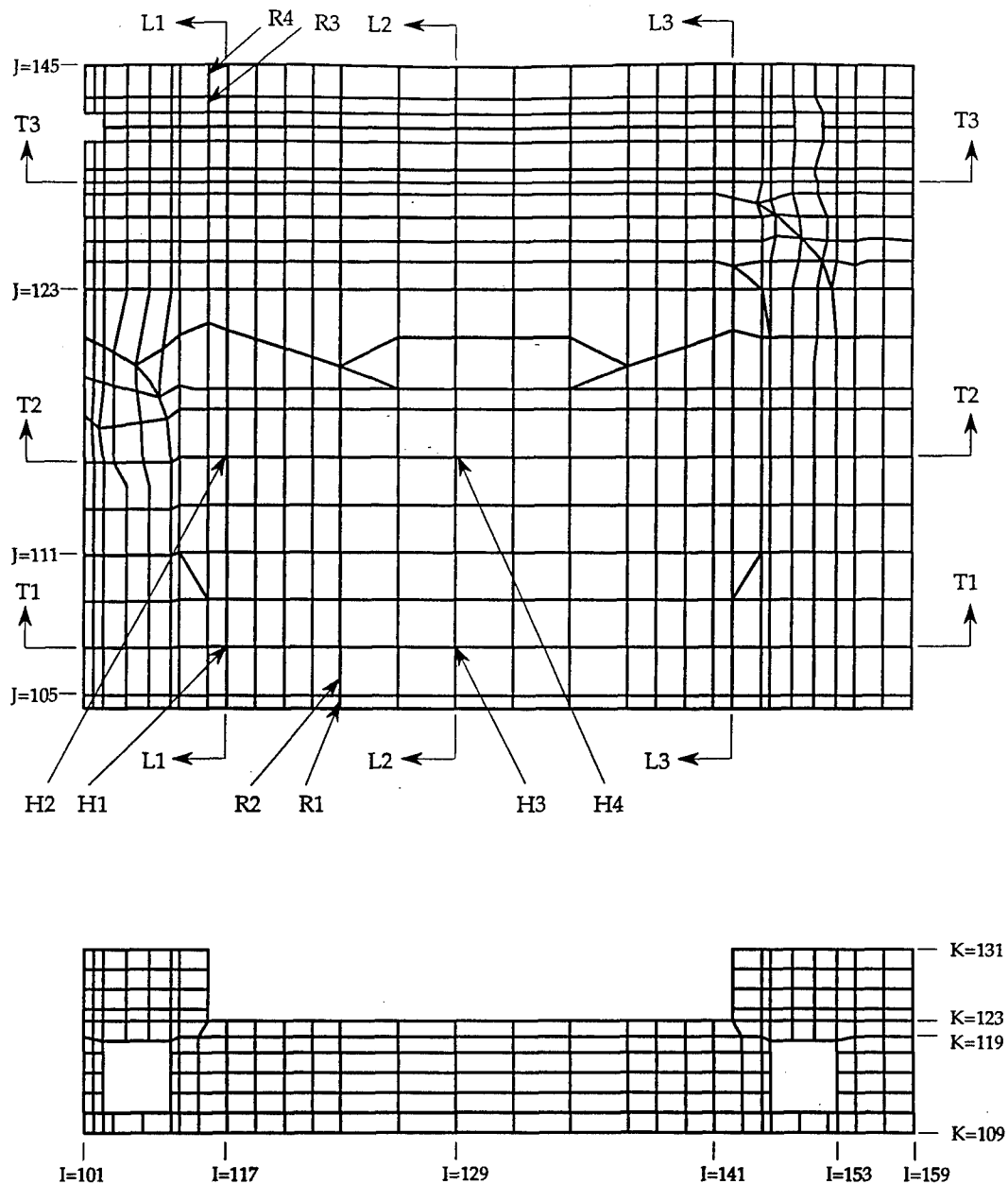


Figure 43. IJK-node numbering system for conventional slab model

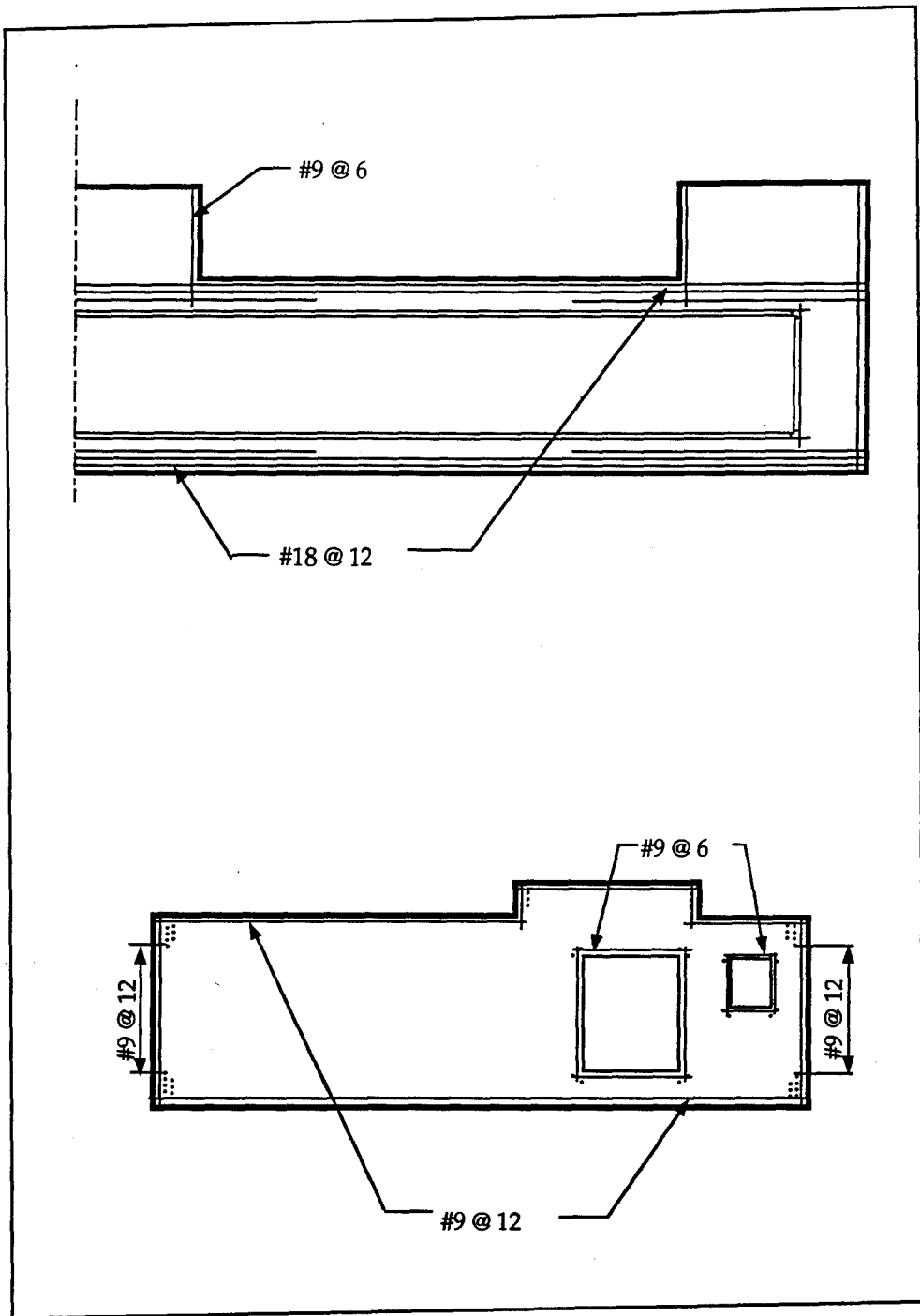


Figure 44. Schematic of reinforcement for conventional slab design

bars at 6-in. spacing are also used to form a cage around the culverts and galleries. In ABAQUS, these reinforcing bars are included in a continuum element by smearing the stiffness over a plane within the element. However, it was determined that ABAQUS could not properly model the reinforcing bar in prism elements. To overcome this difficulty, a group of dummy brick elements were generated to serve as reinforcing bar place holders. Each dummy brick element overlaid two prism elements, or one

prism element if it was adjacent to a free surface. Reinforcing bar was then generated in the dummy brick elements. These elements were given a small stiffness, and since they superimposed over the geometry of the prism elements, the stiffness of the reinforcing bar was properly included in the model. For those dummy elements carrying reinforcing bar on one side and extending into air on the other side, the nodes not connected to the model had to be constrained since they were associated with very little stiffness.

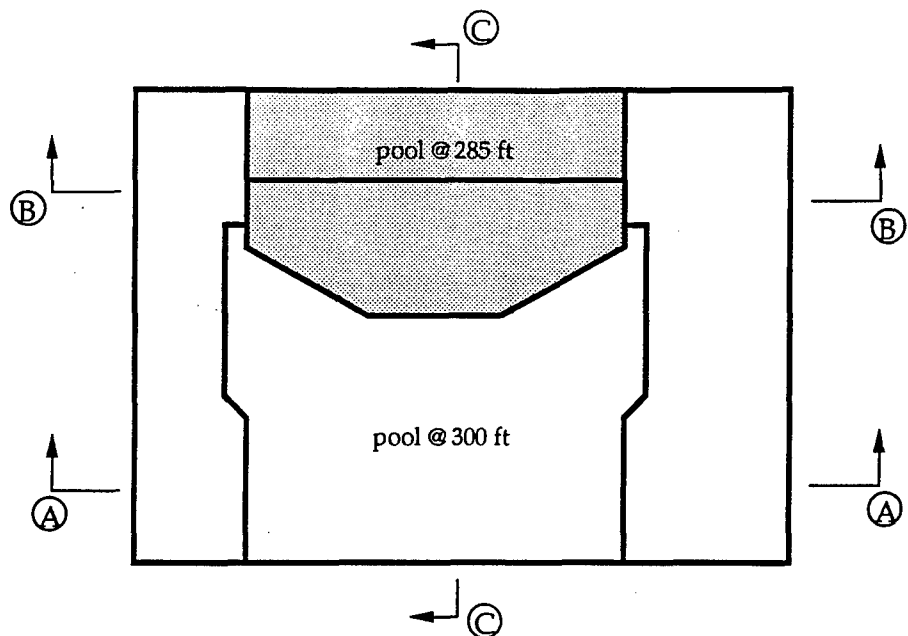
The thermal model, including soil but no pile springs or reinforcing bar, consisted of approximately 7,271 elements and 34,021 nodes with 25,269 degrees of freedom. The stress model, without soil elements but including spring and reinforcing bar modeling, used 4,163 elements and 20,661 nodes with 61,411 degrees of freedom.

## Service Loads

The service loads, shown schematically in Figure 45, were provided by the Louisville District Office and were applied to the model at the end of construction. Thermally, the service load consists of flooding the lock and culverts with water. Based on average water temperature data developed in Phase II of the Olmsted Locks and Dam NISA study (Garner et al. 1992), the water temperature on day 250 would be 40 °F. It was assumed that all surfaces exposed to water or saturated soil backfill would reach equilibrium with the water temperature fairly quickly. This condition was simulated in the analysis by ramping the film coefficients over 5 days from the normal air values to a value of 5.0 Btu/day-in.<sup>2</sup>-°F using the reference temperature of 40 °F. Because the inside surfaces of the galleries were associated in the model with the culvert surfaces, the galleries also received this boundary condition in the analysis.

Because of the mesh discretization and the use of stub walls in the 3D model, the application of the service loads in the stress analysis required considerable care and effort. For modeling purposes, the division of the two pools of water within the chamber were aligned with element boundaries. Thus, the sill and the area downstream of the sill front edge contained water to el 285 ft and the upstream portion of the chamber contained water to el 300 ft. All loads at and below el 271 ft (the top of the stub wall model) were applied directly from the service load specifications. Linearly distributed water and soil pressures were applied to the inside and outside surfaces of the walls, respectively. The culverts were pressurized at 6.5 psi on the top surface and 14.3 psi on the bottom surface, with linearly varying pressure on the vertical surfaces. The gate loads along the stub walls were applied as concentrated forces along the vertical line representing the gate contact block.

Loads acting on the monolith walls above the stub modeling must be converted into statically equivalent loads to be applied along the top of



(a) Top plan view

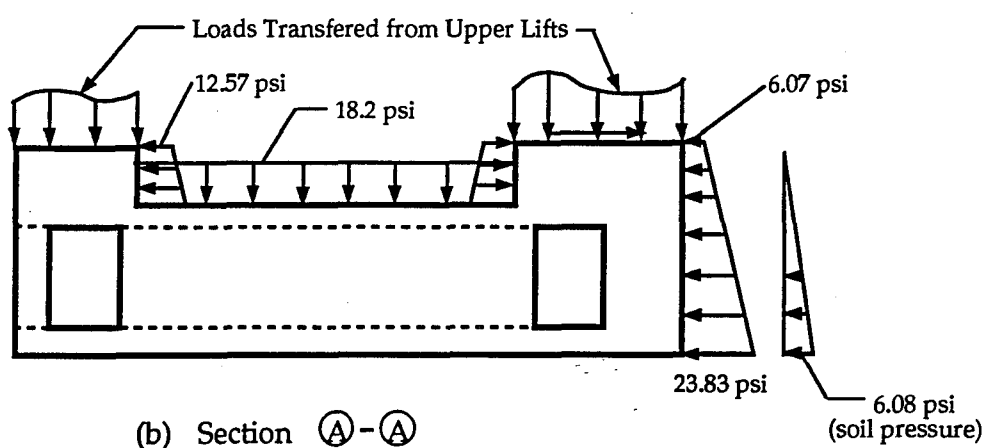


Figure 45. Service loads under normal operating conditions (Sheet 1 of 3)

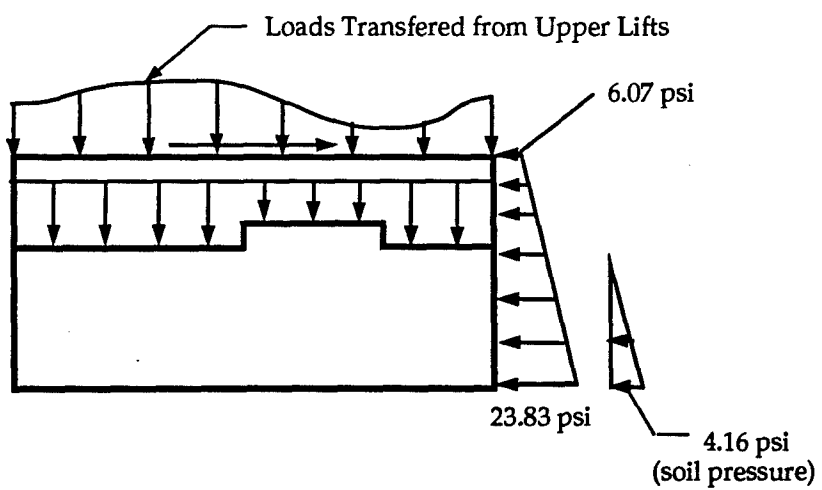
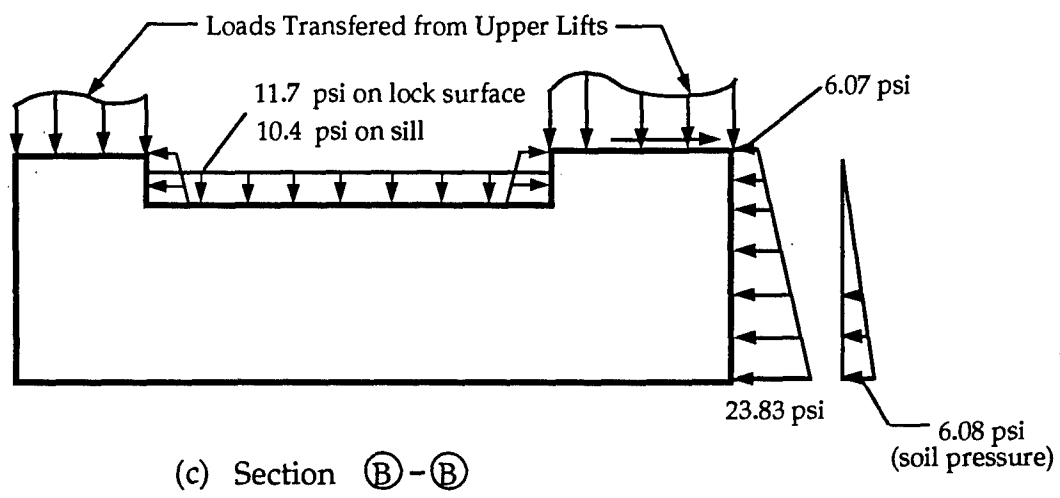
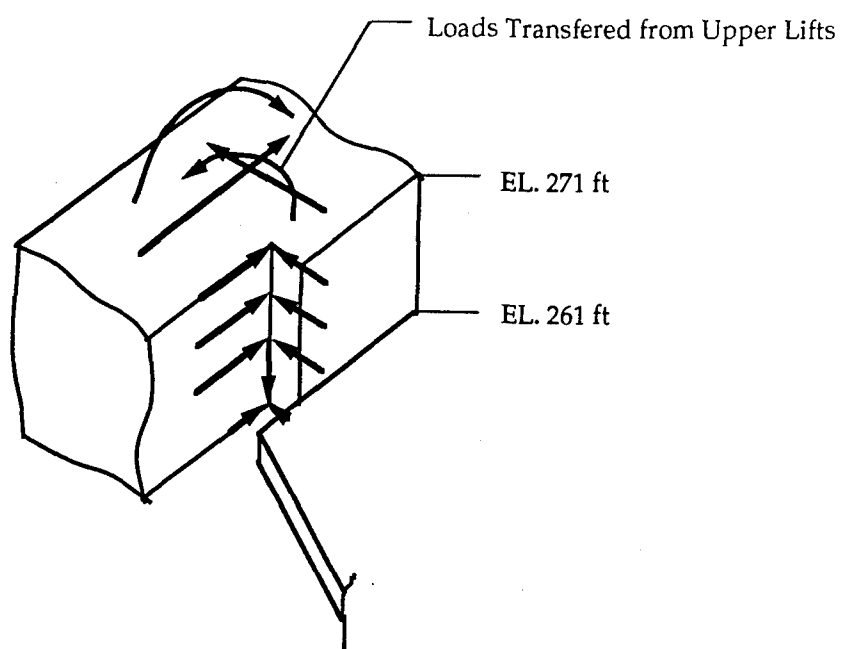
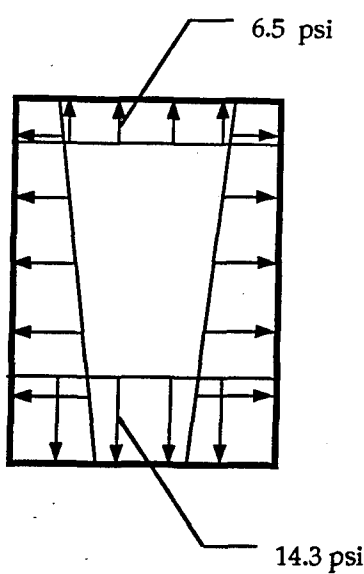


Figure 45. (Sheet 2 of 3)



(e) Mitergate Loads



(f) Culvert Hydrostatic Pressure

Figure 45. (Sheet 3 of 3)

the stub walls. These loads include the weight of the upper walls (already included in the construction phase), the miter gate weight, the miter gate normal operating loads, the difference in water pressure between the inside and outside surfaces, and the water pressure on the downstream edge of the monolith. Under normal operating conditions, the inside water elevation at the upstream part of the monolith is 15 ft higher than outside the land wall. This results in a total transverse force of 1,766 kips and a 19,750 kip-ft moment transferred to the stub wall. These forces are assumed to act over the entire thickness and along the affected length of the wall. The transferred moment is applied as a linearly distributed normal pressure, tension on the inside, compression on the outside across the face of the stub wall. The transverse force is applied through horizontal nodal forces with a parabolic distribution consistent with shear distribution across the wall. These equivalent forces are illustrated in Figure 46.

The equivalent force distribution on the stub walls from the gate loads is more complicated because of the geometry of the wall and the concentrated nature of the loads. Here it is not known what area of the wall is effective in carrying these loads. Since the transferred moment consists of applying tensile stress on the elements near the loads, the choice of contributed area directly impacts the amount of tension and, thus, the potential for cracking in these elements. This choice cannot be an arbitrary one. To establish the correct distribution of stress in the wall from these loads, a 3D test model of the complete wall was constructed, as shown in Figure 47. The base was fixed and the actual gate loads and downstream pressure loads were applied in a linear analysis. One analysis applies all transverse loads only and a second run applies only longitudinal loads. For each case, the stress distribution at el 271 ft (the plane of the top of the stub walls) was evaluated to determine the area effective in carrying the respective load. The stress distributions in the test model under transverse loading show that the force and moment are mainly transferred over the surrounding area of the applied loads, and the bending stresses do not exceed 10 psi. The stress distributions in the test model for longitudinal loads indicate that the wall stresses are dominated by the gate loads. These loads are transferred in two pocket areas near the location of the gate load, one in tension and the other in compression. These stress distributions serve as templates for distributing these loads to the stub walls. Figure 48 shows the applied stress distributions, again with transverse forces applied as nodal forces and with moments applied as linearly distributed pressure loads. The total forces and moments transferred to the stub walls due to gate loads and water pressure on the downstream side of the monolith are 1,236 kips and 10,662 kip-ft in the transverse direction and 695 kips and 6,934 kip-ft in the longitudinal direction.

For the middle wall, only the longitudinal components of the transferred loads need to be considered since the model is symmetric to the plane intersecting the middle wall. The transverse components of the loads on the inside of the wall are balanced by those on the other side of the wall. Similar to the calculation for the land wall, a 3D model was generated to simulate the stress distribution on the middle stub wall under all

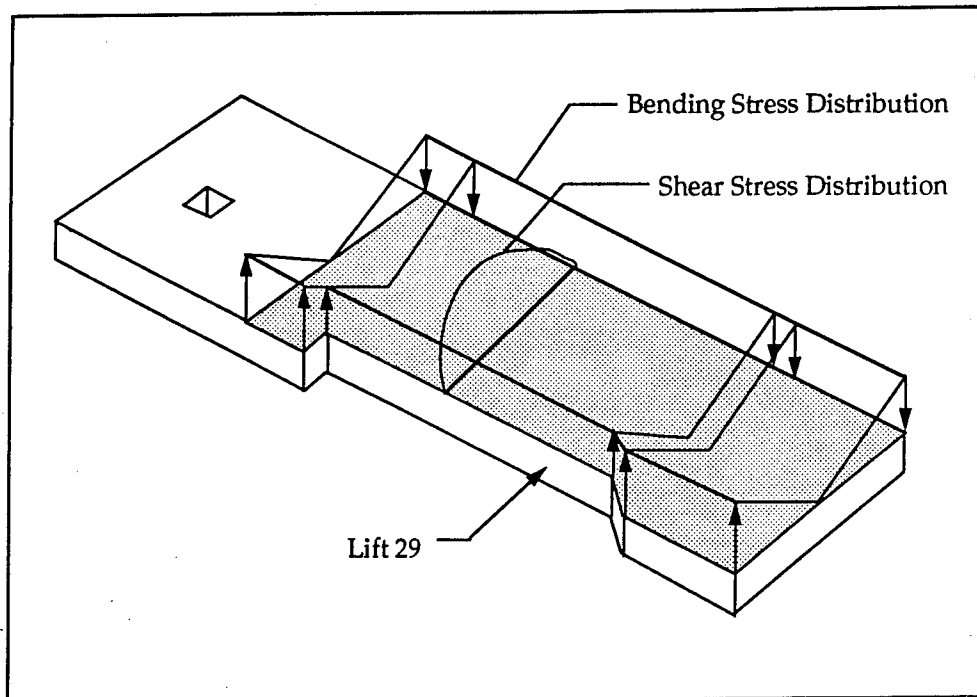


Figure 46. Stress distribution on stub wall due to unbalanced water pressure

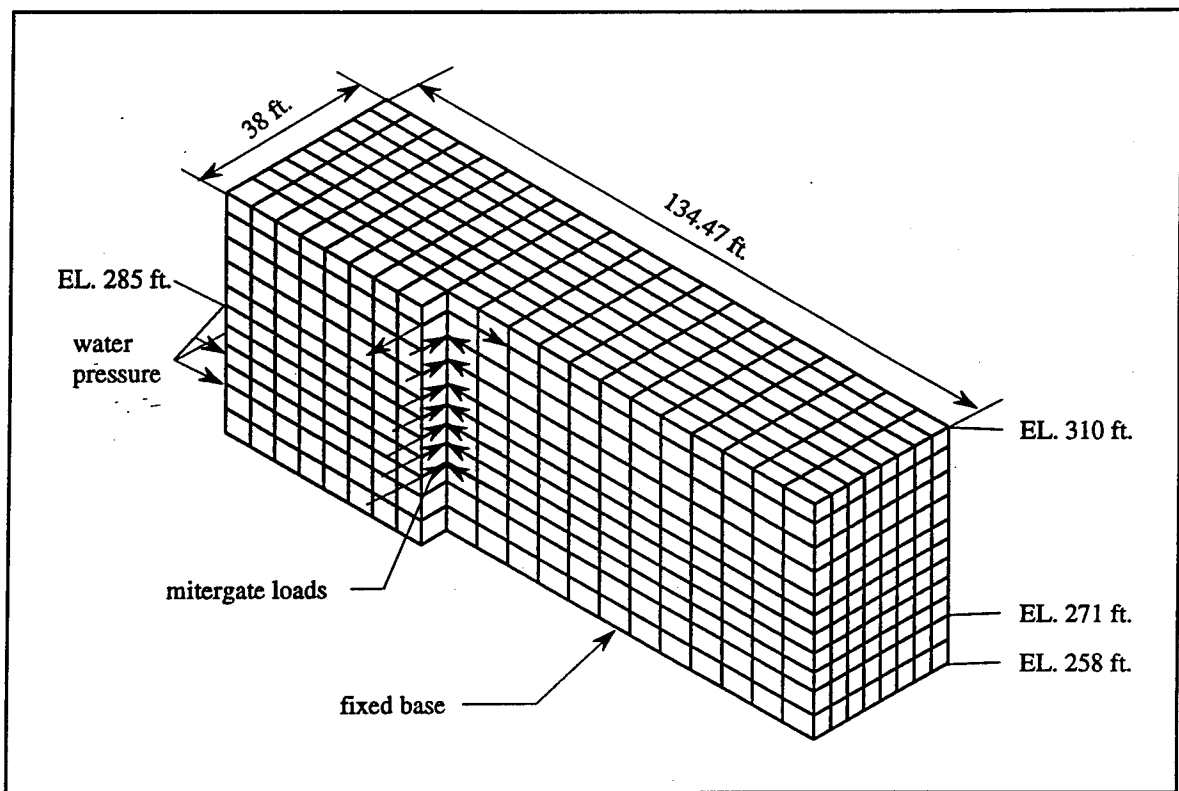
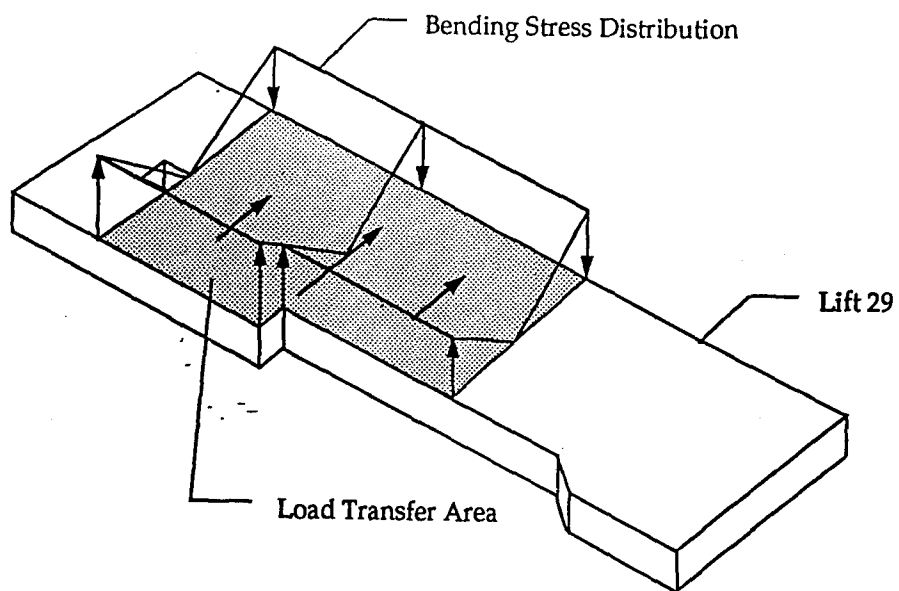
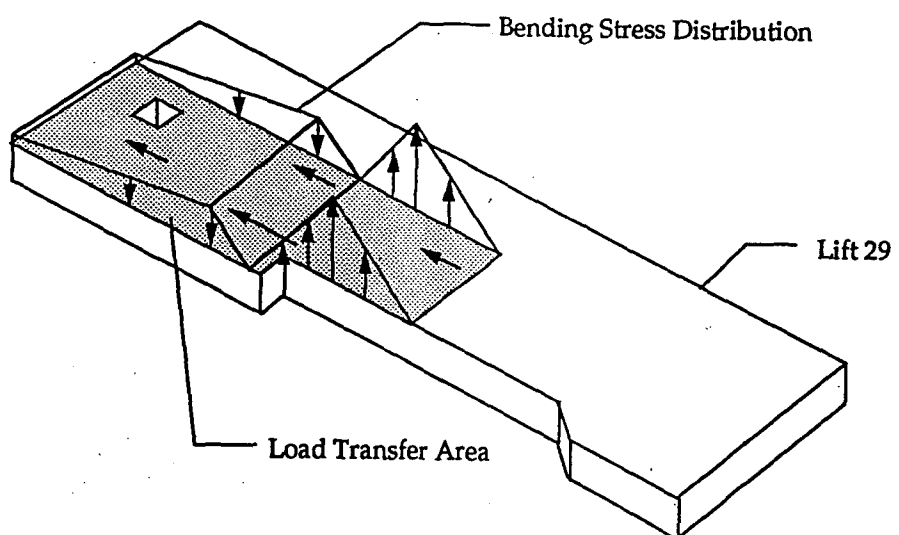


Figure 47. Three-dimensional land wall test model



(a) Stress Distribution due to Transverse Loads



(b) Stress Distribution due to Longitudinal Loads

Figure 48. Stress distributions on landside stub wall

longitudinal loads above el 271 ft. In this model, the base is fixed at el 258 ft and the nodes along the center line of the wall are constrained with rollers. The calculated stress distributions for this test show a pattern similar to that for the landside stub wall. Thus, a similar force distribution is used to simulate these loads.

## Analysis Results

### Thermal response

As in the 2D analyses, the thermal response is established by a series of thermal contours taken at discrete snapshots in time and with temperature histories of a few selected points. For 3D analyses, the contours also expand into slices at discrete sections of the model. Figure 49 shows thermal contours for plan view slices along the top of the first layer of lifts, and Figure 50 shows thermal contours along the top of the slab for increments in time. Figures 51, 52, and 53 show thermal contours for transverse slice sections T1 (near the upstream edge), T2 (a middle section), and T3 (near the downstream edge), respectively. Figures 54, 55, and 56 show thermal contours for longitudinal sections L1 (near the center culvert), L2 (near midchannel), and L3 (near the land wall culvert), respectively. Figure 57 shows temperature histories of points in the middle of the first lifts and in the middle of the top lifts at the locations defined in Figure 43 compared with ambient. These results show good general agreement with the 2D results for temperature distributions and temperature magnitudes. The plan view contours in Figure 49 show three small cold spots that appear to be localized perturbations in the model. These appear to be associated with prism elements and would seem to be connected with heat generation, since boundary condition errors would more likely cause adiabatic conditions and local hot spots. However, these areas do not appear to cause problems in the stress analyses since there is no cracking concentrated in these areas. Figure 58 shows crack potential contours for the plan view on the top of the bottom lifts at day 100 with cracking imminent. This figure identifies that the critical area for cracking is along the upstream edge of the monolith and particularly near the culverts. Note that this figure has no particular cracking bias around the cold spots shown in the thermal contour, although some cracking concentration around prism elements in general seems evident.

### Cracking development

If one considers the cracking patterns predicted by this analysis, it is evident that a substantial amount of cracking has occurred and that much of this cracking is not related to that predicted by the 2D analyses. A careful, step-by-step consideration of the progression and cause of the cracking is in order to establish that those mechanisms determined by the 2D

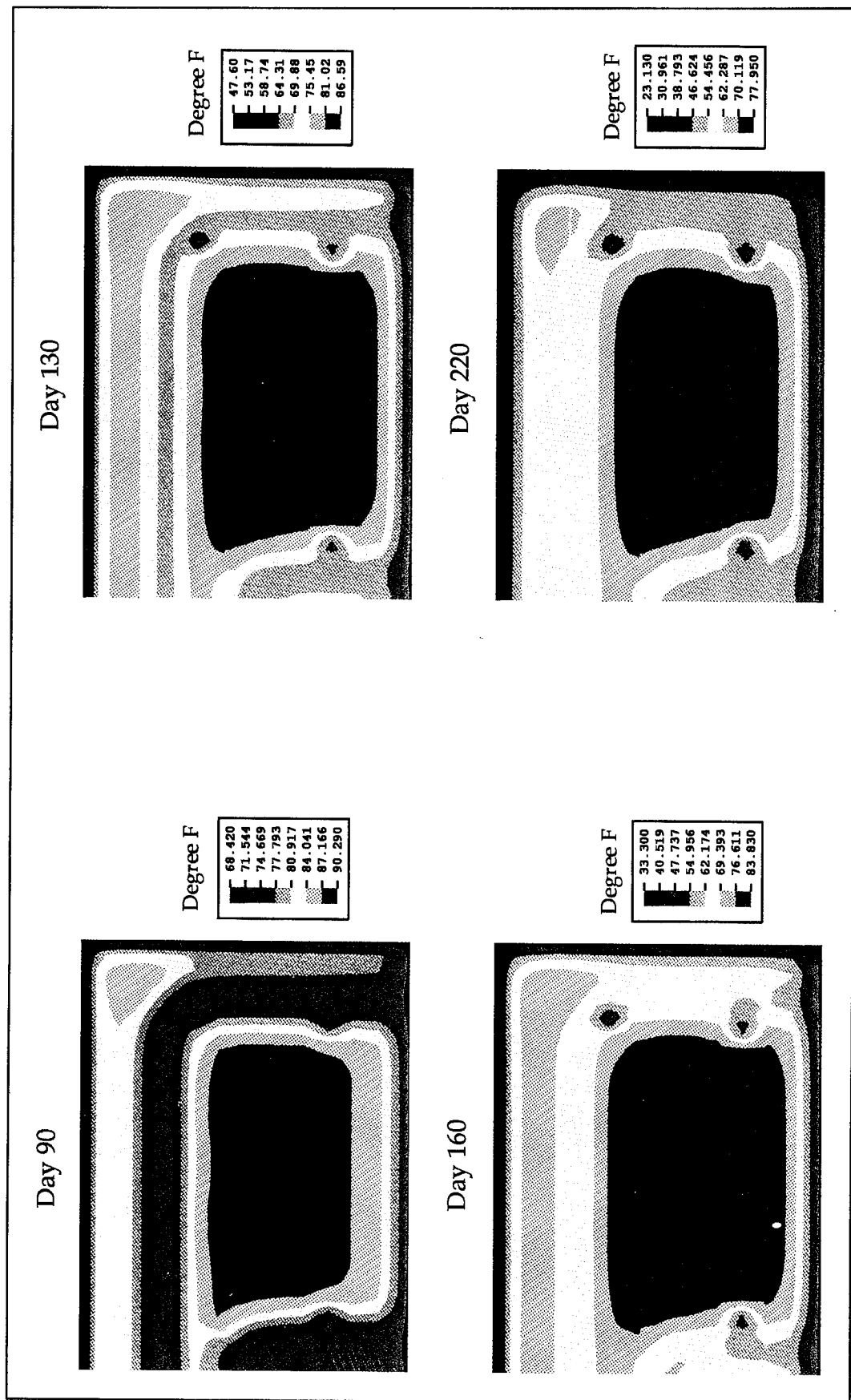


Figure 49. Three-dimensional thermal contours on top of bottom lifts

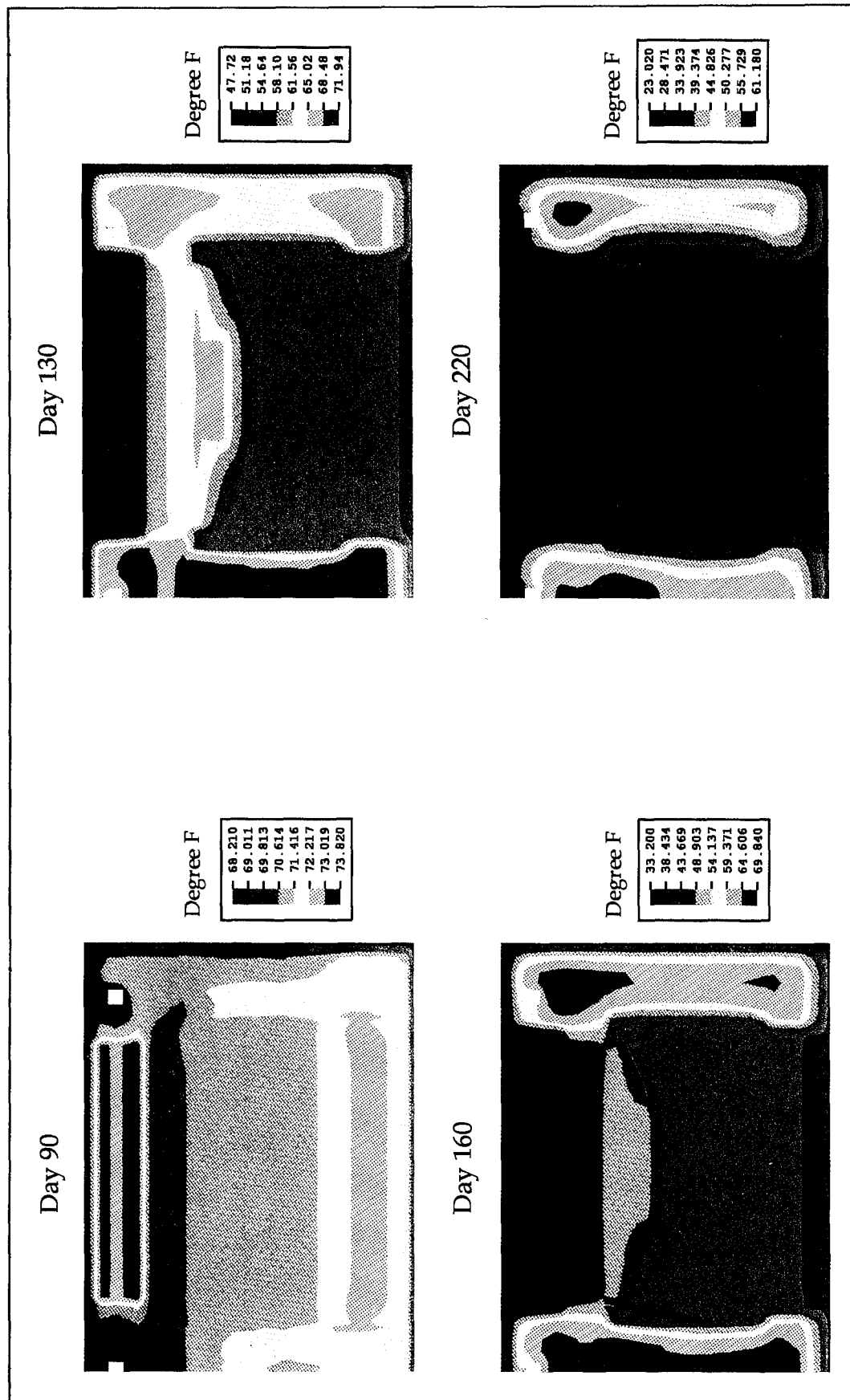


Figure 50. Three-dimensional thermal contours on top of slab

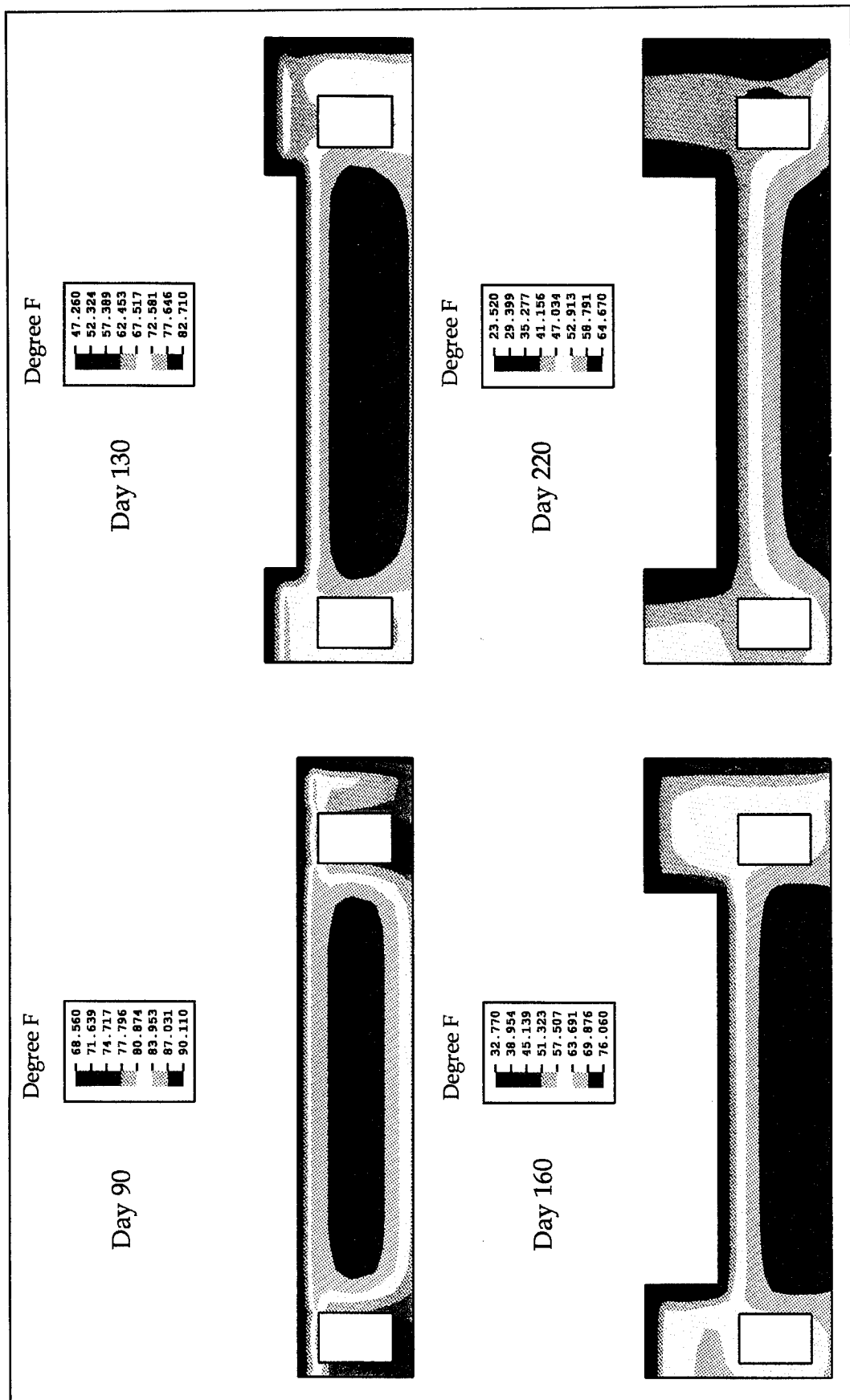


Figure 51. Three-dimensional thermal contours on transverse slice T1

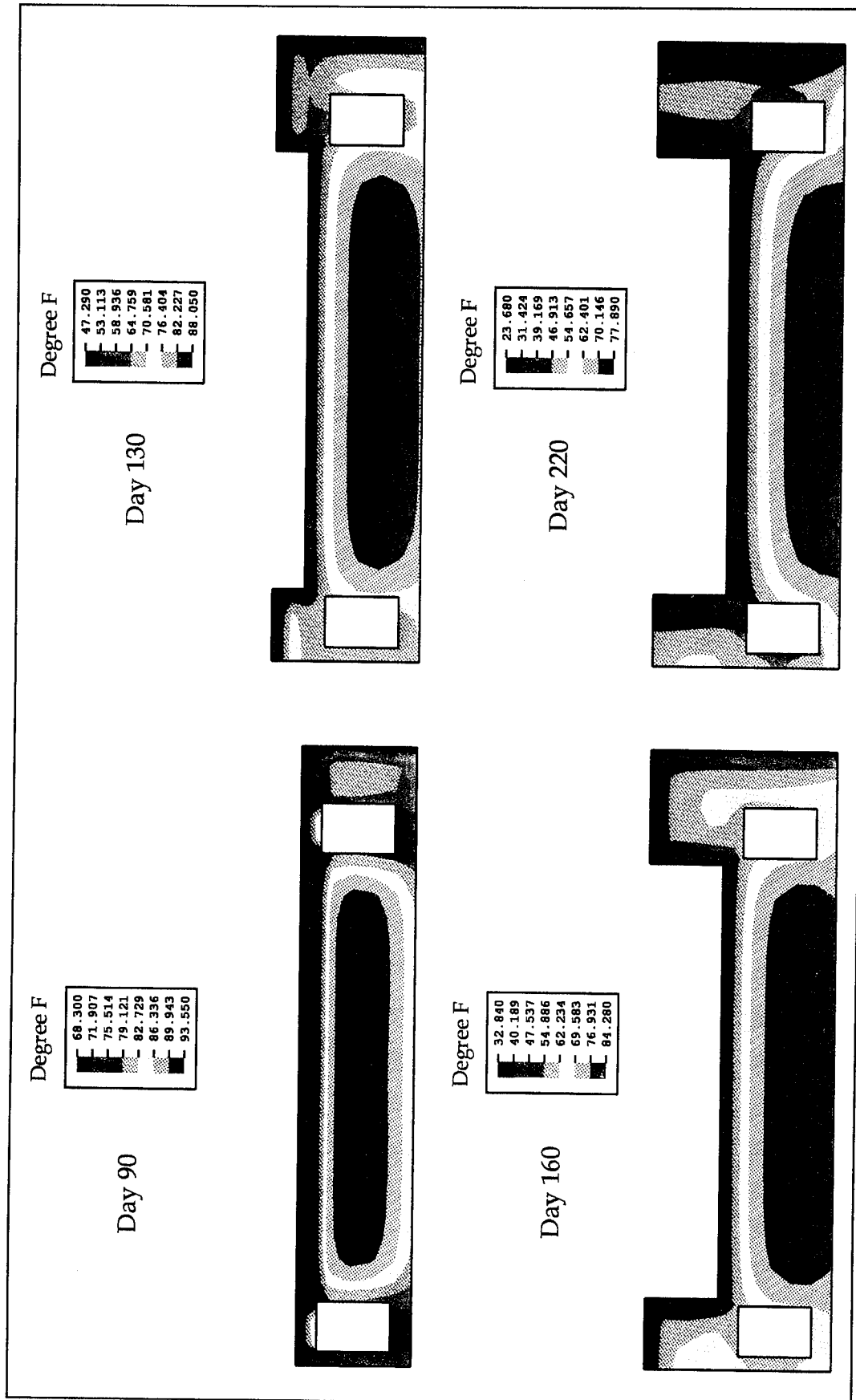


Figure 52. Three-dimensional thermal contours on transverse slice T2

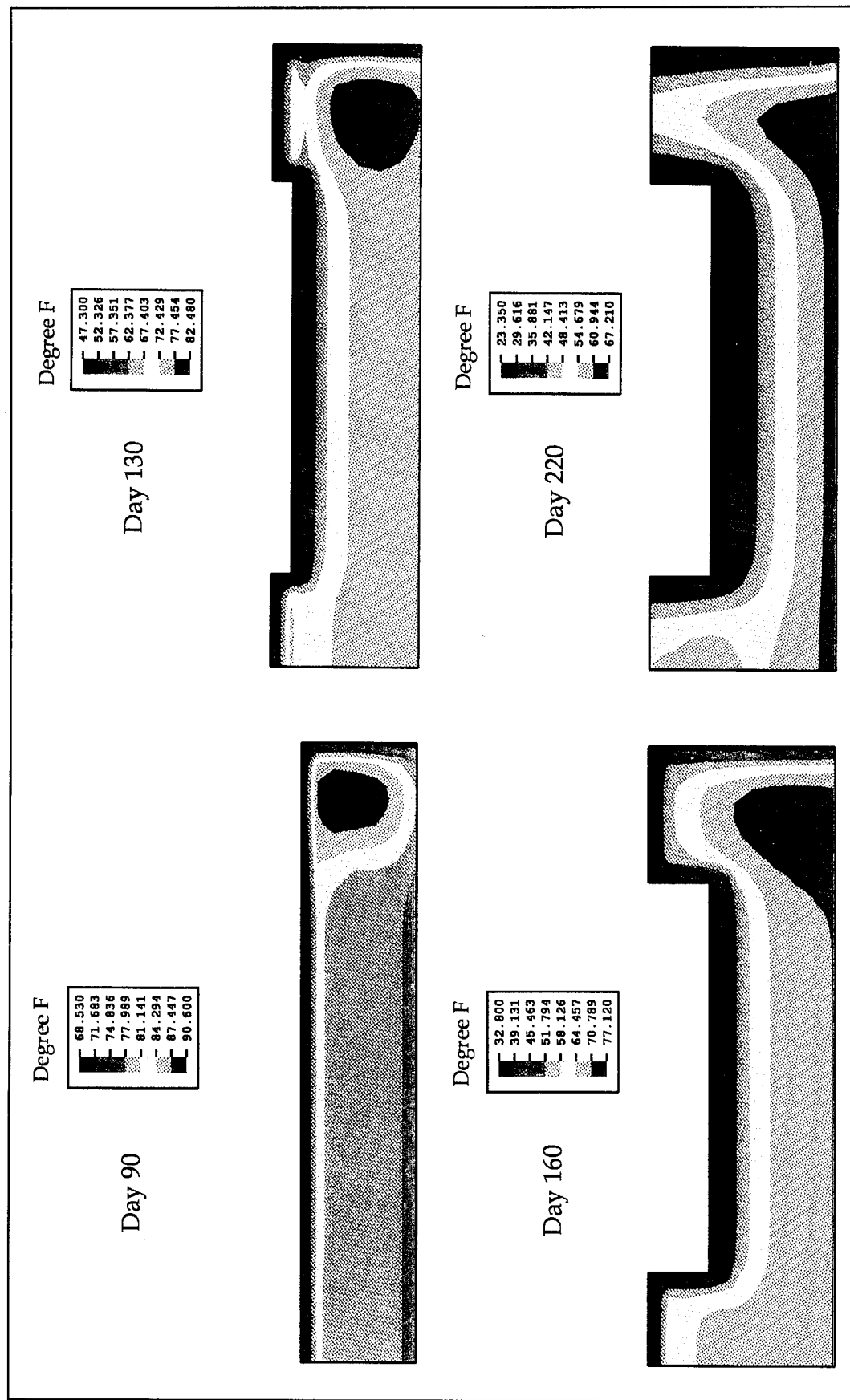


Figure 53. Three-dimensional thermal contours on transverse slice T3

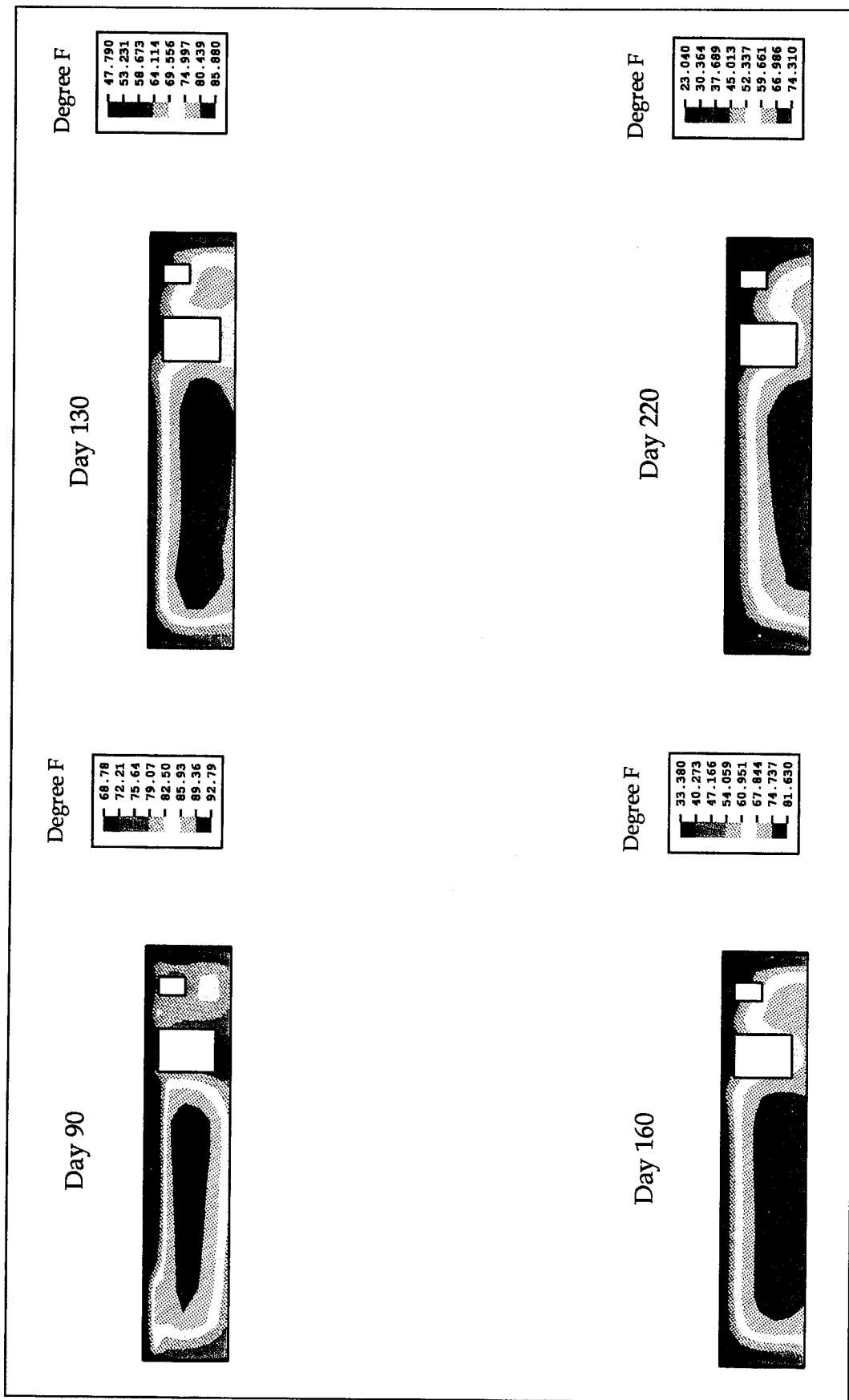


Figure 54. Three-dimensional thermal contours on longitudinal slice L1

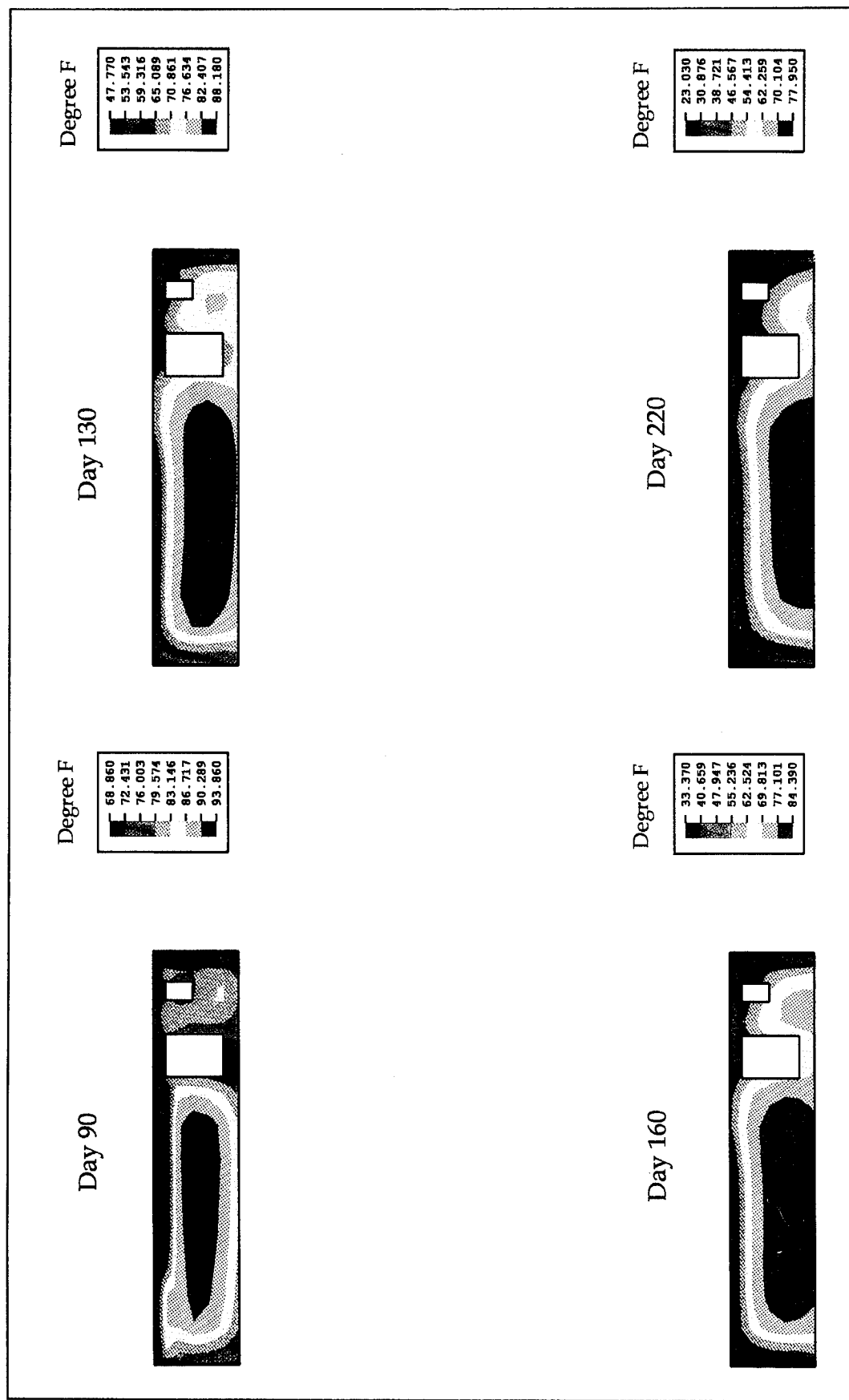


Figure 55. Three-dimensional thermal contours on longitudinal slice L2

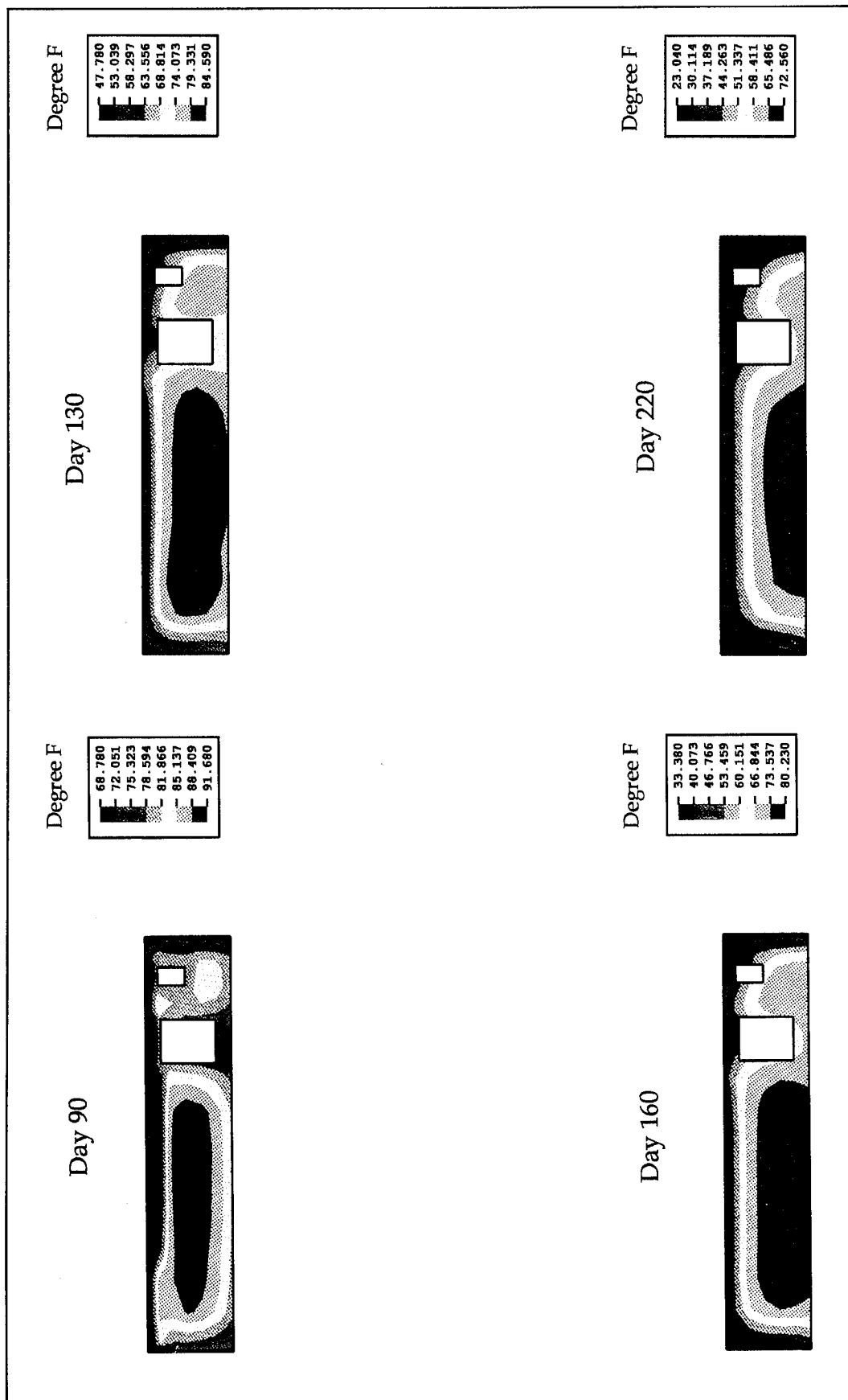


Figure 56. Three-dimensional contours on longitudinal slice L3

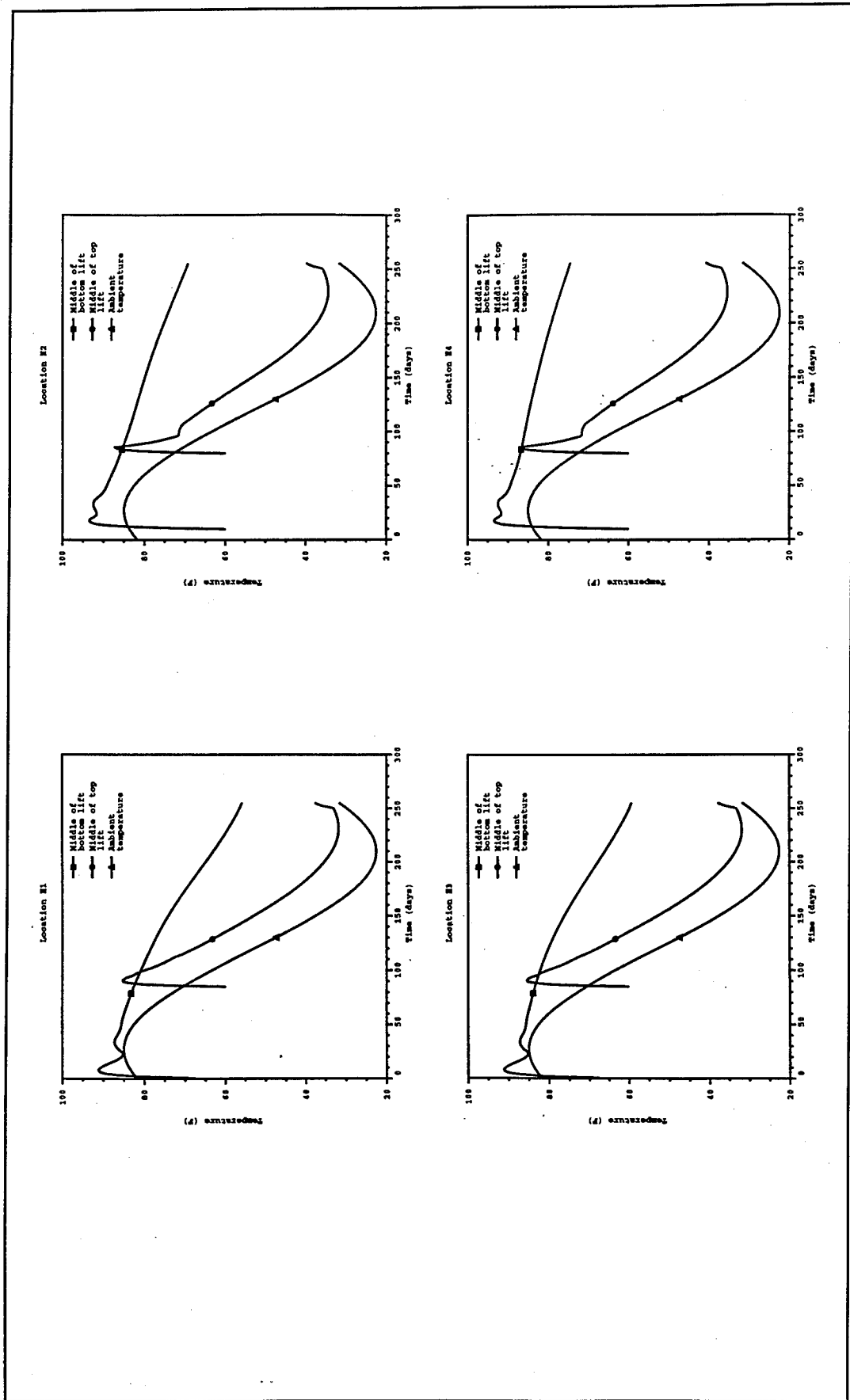


Figure 57. Temperature histories at selected points

Day 100

Percentage of  
Cracking Criteria

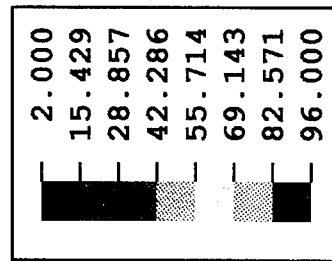


Figure 58. Three-dimensional crack potential contour on top of bottom lifts

analyses are present and identify the added mechanisms developed because of 3D effects. This discussion will also identify those 3D effects that are difficult to capture in 2D analyses and how these effects can influence the structural behavior after they occur.

The first cracks appear between day 100 and day 105 near the lower inside corner of the land wall culvert near the upstream edge of the monolith, as indicated by the crack potential plot, Figure 58. This cracking is consistent with that predicted in the 2D transverse slice analyses and appears earlier in time due to the thermal gradient that develops in 3D to the upstream free surface. Cracking continues to develop in the culvert corners near the upstream edge through day 135, as seen in Figure 59. This figure also shows new cracking not seen in 2D caused by transverse stress along the upstream free surface of the monolith. The colder free surface tries to shrink relative to the hotter material inside, while the piles and general thickness of the monolith constrain this deformation, creating tensile stress. Note that the piles occur on the first row of nodes away from the free surface and the first row of elements is unconstrained. From the thermal contour plot, Figure 49, the thermal gradient is seen to be fairly uniform along the upstream and downstream free edge. The temperature difference over approximately 6 ft of concrete on the upstream edge is about 30 °F on day 130 and about 36 °F on day 160. The cracking initiates at the location of the termination of the third #18 reinforcing bar extending into the slab area from under the walls. This stiffness discontinuity provides a stress concentration for crack initiation. By day 150 (Figure 60) these cracks have extended through the thickness of the monolith, and additional cracks are in evidence on this free surface. Additionally, cracks in the top of the slab near the middle wall have opened. These begin about day 140 near the free surface and progress along the slab and wall juncture. These cracks follow the constraint against thermal shrinkage mechanism established in the 2D analyses. Two cracks can also be seen on the land wall free surface midway along the length at the base of the monolith caused by the thermal gradient near this free surface which from Figure 49 is about 30 °F over 5 to 6 ft on day 160.

Cracks have also formed on the downstream surface of the monolith at the middle wall juncture and have spread up over the gallery and along the top of the slab along the slab and wall corner intersection. These cracks follow the mechanism just described for the upstream surface cracking. The cracks initiate later in time and higher up the face because this area has less thermal gradient than the upstream face due to the cooling effect of the culvert, which allows heat to flow in two directions in the lifts forming the downstream surface. The added transverse constraint of the monolith near the symmetry line and the stress riser at the corner of the floor and wall combine to cause this crack formation and subsequent growth along the top of the slab. There is also cracking on the downstream edge of the sill where it intersects the middle wall.

Figure 61 identifies crack patterns at day 170 and shows extensive crack growth from the upstream edge cracks discussed previously. These

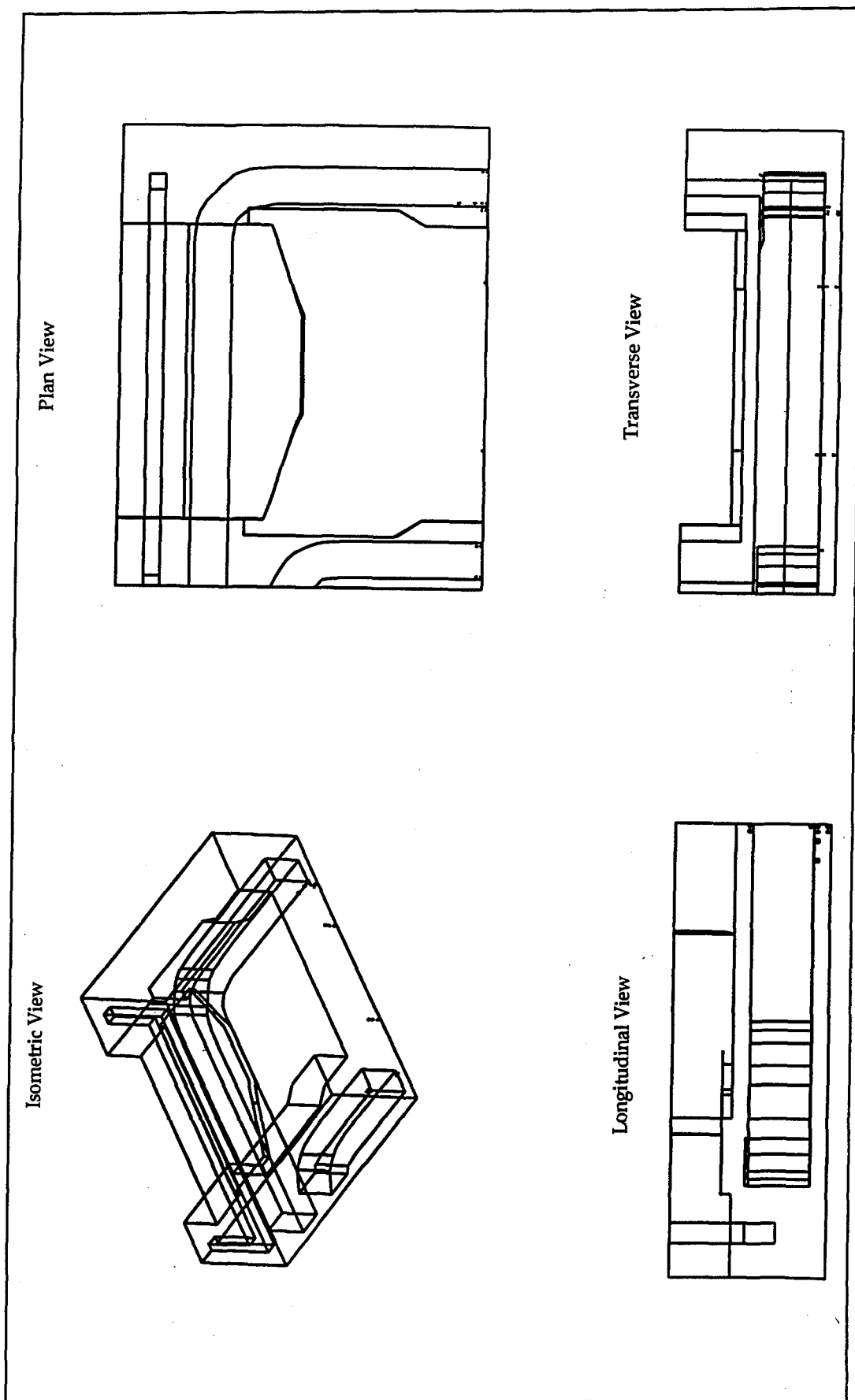


Figure 59. Three-dimensional cracking patterns on day 135

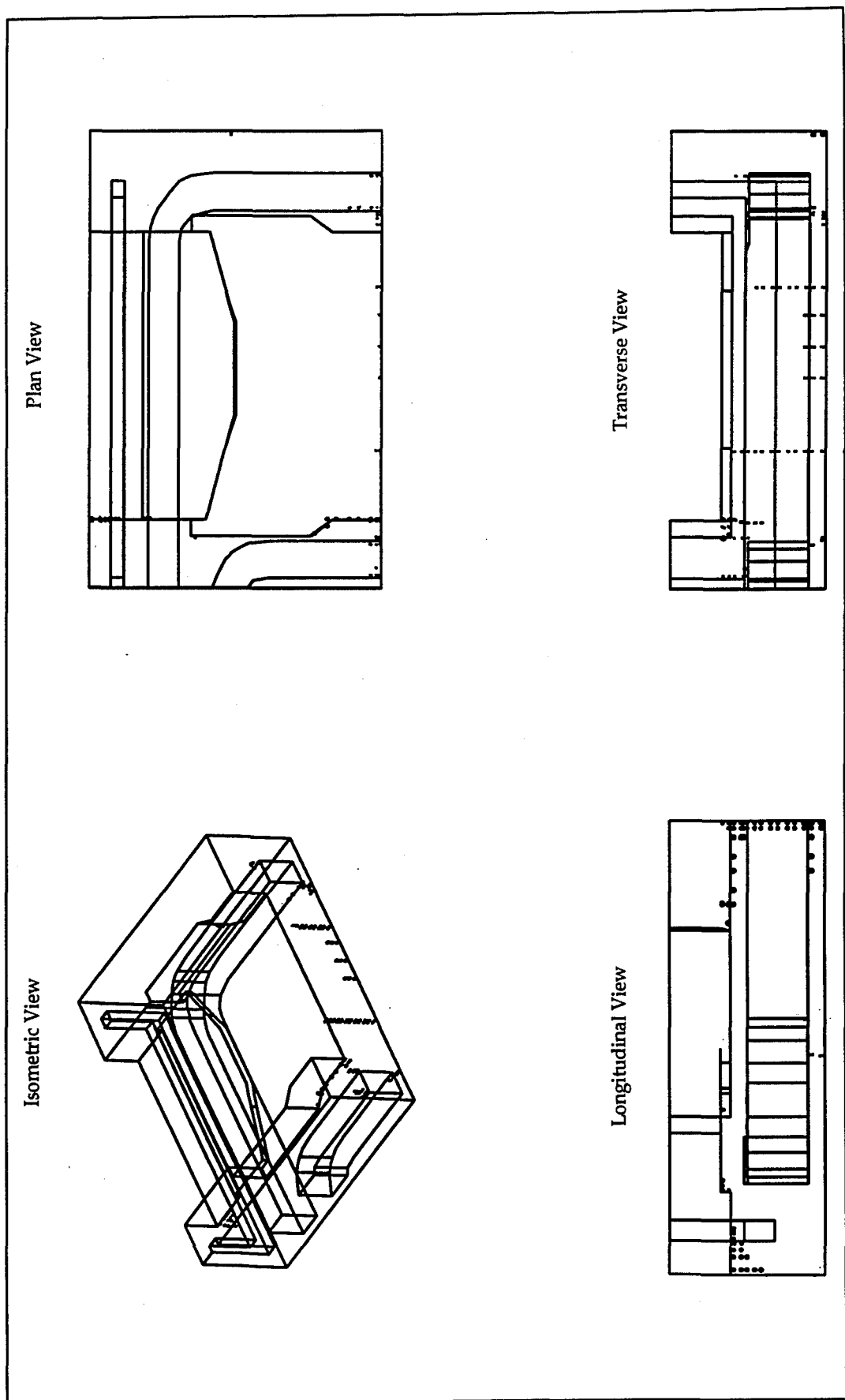


Figure 60. Three-dimensional cracking patterns on day 150

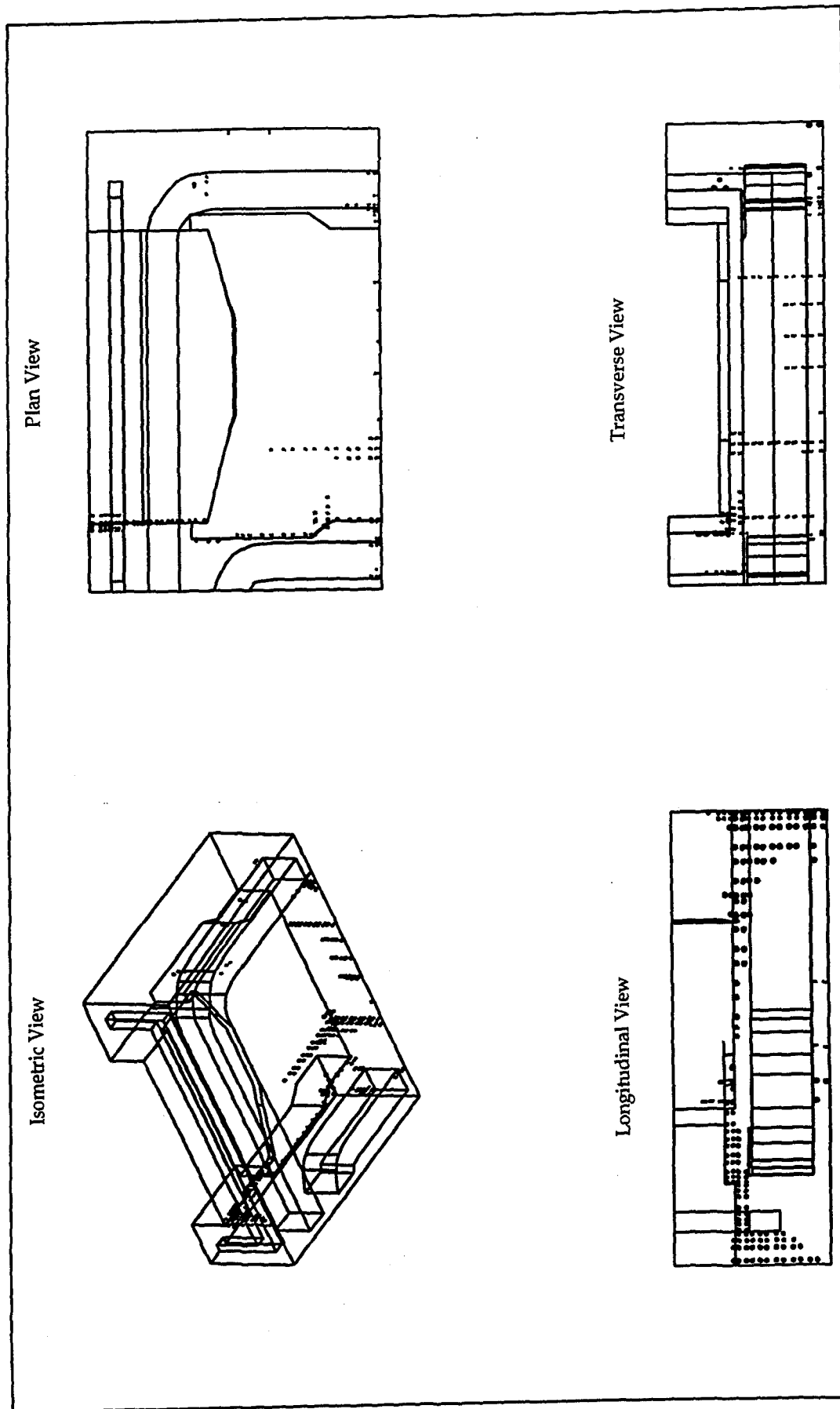


Figure 61. Three-dimensional cracking patterns on day 170

cracks now extend well down the monolith longitudinally and deep into the slab thickness in a pattern indicating that the driving force extends inward from the corner edge. The mechanism causing this cracking is from the 3D effect of the two free surfaces both wanting to curl outward from the temperature gradient at the free surface. This causes a bending moment about the corner of the top of the slab and the free edge of the monolith. Figure 62 is the transverse stress contour for the longitudinal plane of these cracks and illustrates this bending mechanism. The high tensile stresses can clearly be seen along the top of the slab and both free edges due to the induced bending about the two upper corners. The larger bending stresses occur on the upstream corner because of the higher thermal gradients. This drives the cracks that initiated along the upstream face on day 135 into the slab longitudinally and into the thickness. The plan view of these crack patterns in Figure 61 shows that the cracking at this location extends more than one element in width. This also indicates that the cracking is bending driven and is of structural concern. The crack extension from the downstream face well into the slab and through the sill thickness can also be seen on the longitudinal view of this figure. This figure also shows cracks caused by longitudinal stress occurring up the face of the middle wall near the miter gate seating block. This is another 3D surface effect. The cracking patterns for day 200 (Figure 63) show the continued cracking progression under these mechanisms as the structure is subjected to the coldest part of the year. The cracks extending from the upstream edge extend completely through the slab inward of the free surface and along the top of the slab to the upstream edge of the sill. Cracking in the top of the slab along the sill intersection is now evident. The crack directions shown in the plan view of this figure indicate these cracks are due to a combination of the longitudinal bending stress, identified in the 2D longitudinal slice analyses, and the transverse bending stress. Some additional spreading of these crack patterns is seen through day 225.

Figure 64 shows the final crack pattern plot at day 255 after service loads have been applied. No new cracks opened under service loads, and, in general, the stress causing existing cracks was relieved due to the mitigation of the winter-induced thermal gradients by flooding with water. However, no existing cracks closed under application of service loads. An estimate of crack size will be deduced from the reinforcing bar stress discussion in the next section.

### **Reinforcing bar stresses**

The extensive cracking seen in this 3D analysis necessitates an evaluation of reinforcing bar integrity. Examination of reinforcing bar stresses is also a useful tool in establishing the structural response mechanisms that are driving the cracking. As established in the 2D analyses, when cracks occur and the reinforcing bar picks up load, a bending mechanism is in effect whereby the induced stresses must be redistributed. If the reinforcing bar at the crack location does not pick up significant additional

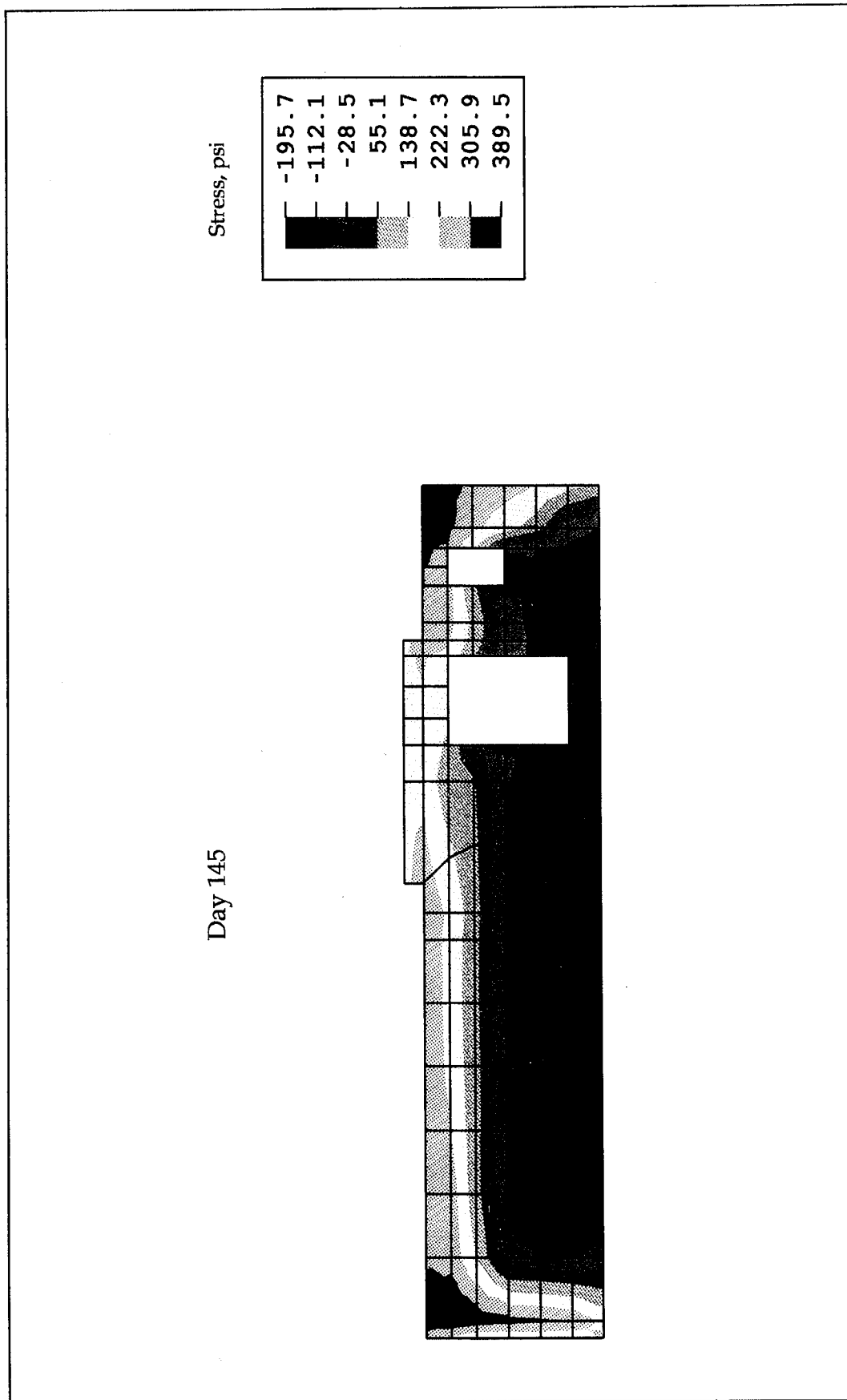


Figure 62. Transverse stress for longitudinal slice at crack location

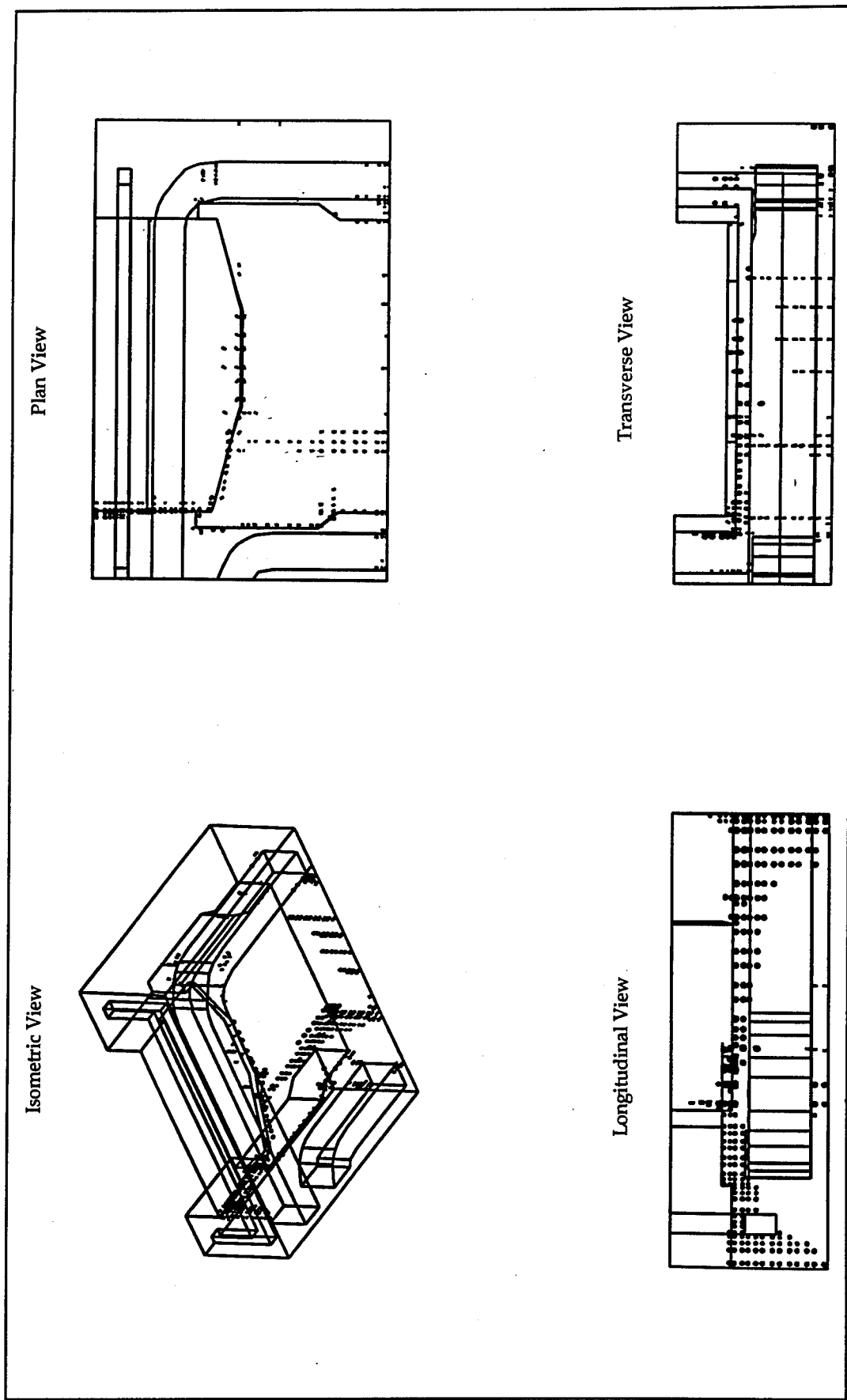


Figure 63. Three-dimensional cracking patterns on day 200

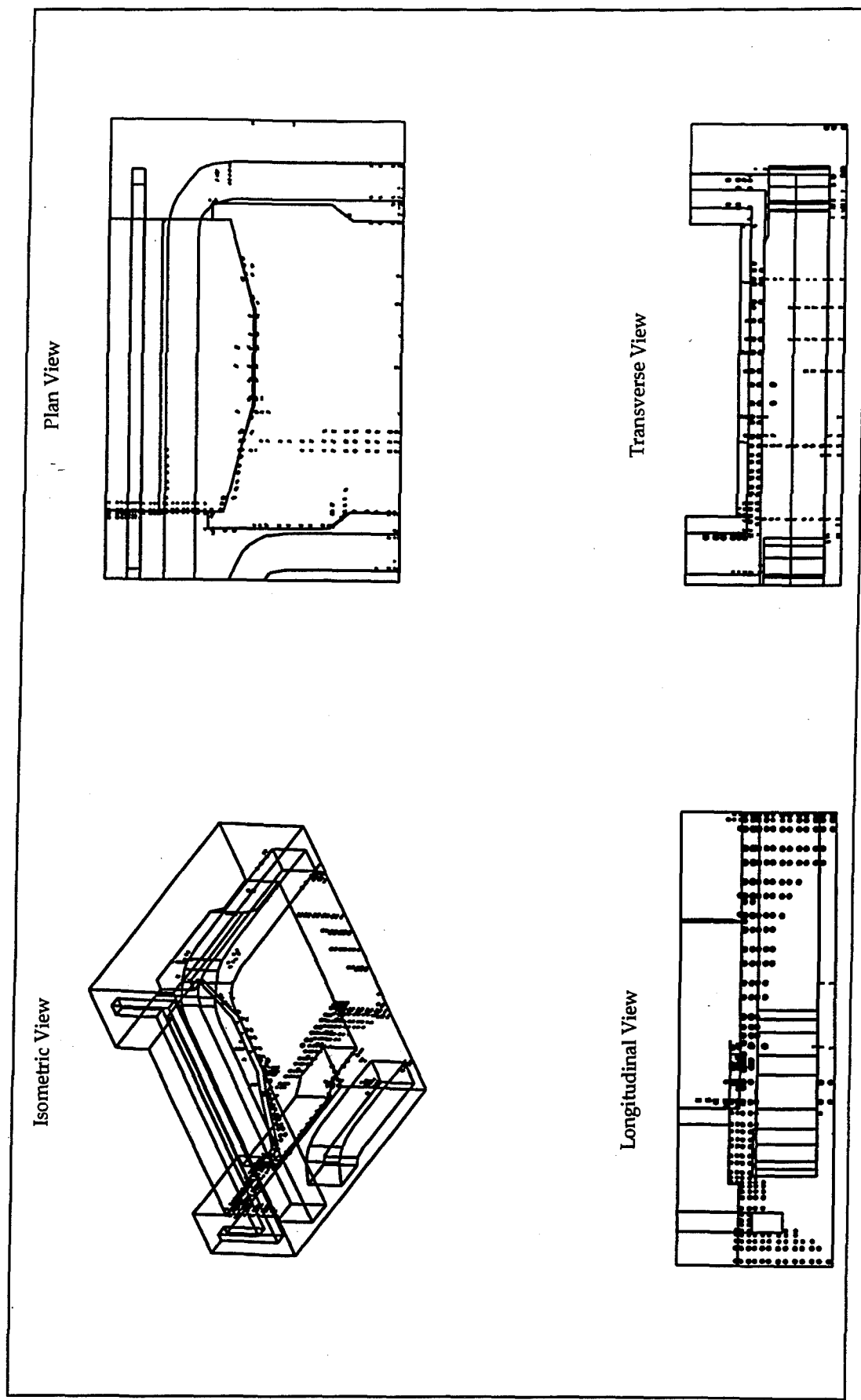


Figure 64. Three-dimensional cracking patterns on day 255

load, the cracking is due to constraint against thermal shrinkage and the stress is mitigated by the cracking. The two areas of most concern from this analysis are the large cracks opening in the upstream chamber from the free edge to the sill and the cracks starting at the downstream edge by the middle wall and spreading through the slab and inward through the sill.

Figure 65 shows the reinforcing bar stress history for the two #18 transverse bars in the top of the slab for two locations longitudinally from the free edge at the crack location. This plot gives a picture of the stress distribution. The stress is maximum at the free edge and decreasing as it moves longitudinally down the chamber. This confirms the bending mechanism acting about the upstream edge along the top of the slab. It is seen that these cracks begin spreading into the slab around day 160 and subside around day 225 when the peak reinforcing bar stress reaches 21 ksi. The tendency for crack closure as the weather warms and the unloading effect of the service loads is also in evidence. These plots also serve as a basis for estimating the crack opening size. Since the reinforcing bar is elastic, the strain can be obtained by dividing the stress by the bar modulus, and the crack opening at the reinforcing bar can be estimated by multiplying this strain by the effective length of the element. These cracks are thus estimated to be 0.05 in. wide, 6 in. into the slab.

Figure 66 shows the reinforcing bar stress in the #18 bars on the downstream portion of the slab at the cracked location. This plot shows the relief from constraint against thermal shrinkage after cracking. This cracking begins about day 145 and subsides around day 210, corresponding to the earlier placement sequence of the top of the slab which begins on the downstream edge and works toward the upstream edge. For a peak reinforcing bar stress of 17 ksi, a peak crack width of 0.02 in. is predicted (these cracks also occur in a smaller element).

The area underneath the culvert on the land wall side attracts a concentration of cracking through the base at the upstream free edge. The #18 bar stresses in this area are shown in Figure 67. These show bending mechanisms, including some loading and unloading and the effects of additional cracking around day 210, with peak stress at 18 ksi. For these element sizes, crack widths around 0.01 in. are predicted in the middle of the lift at the reinforcing bar location. Cracking above the culvert under the middle wall has extended well up into the wall region near the upstream free surface. Stresses for the #18 bar near this location also reach 18 ksi. These cracking areas are very localized and are strongly influenced by the 3D effects of heat flow at the upstream free surface.

## Conclusions

The 3D effects captured by this analysis proved to be very significant for this monolith. The cracking mechanisms identified in the 2D parameter studies are in evidence and consistent in the 3D analysis. In addition,

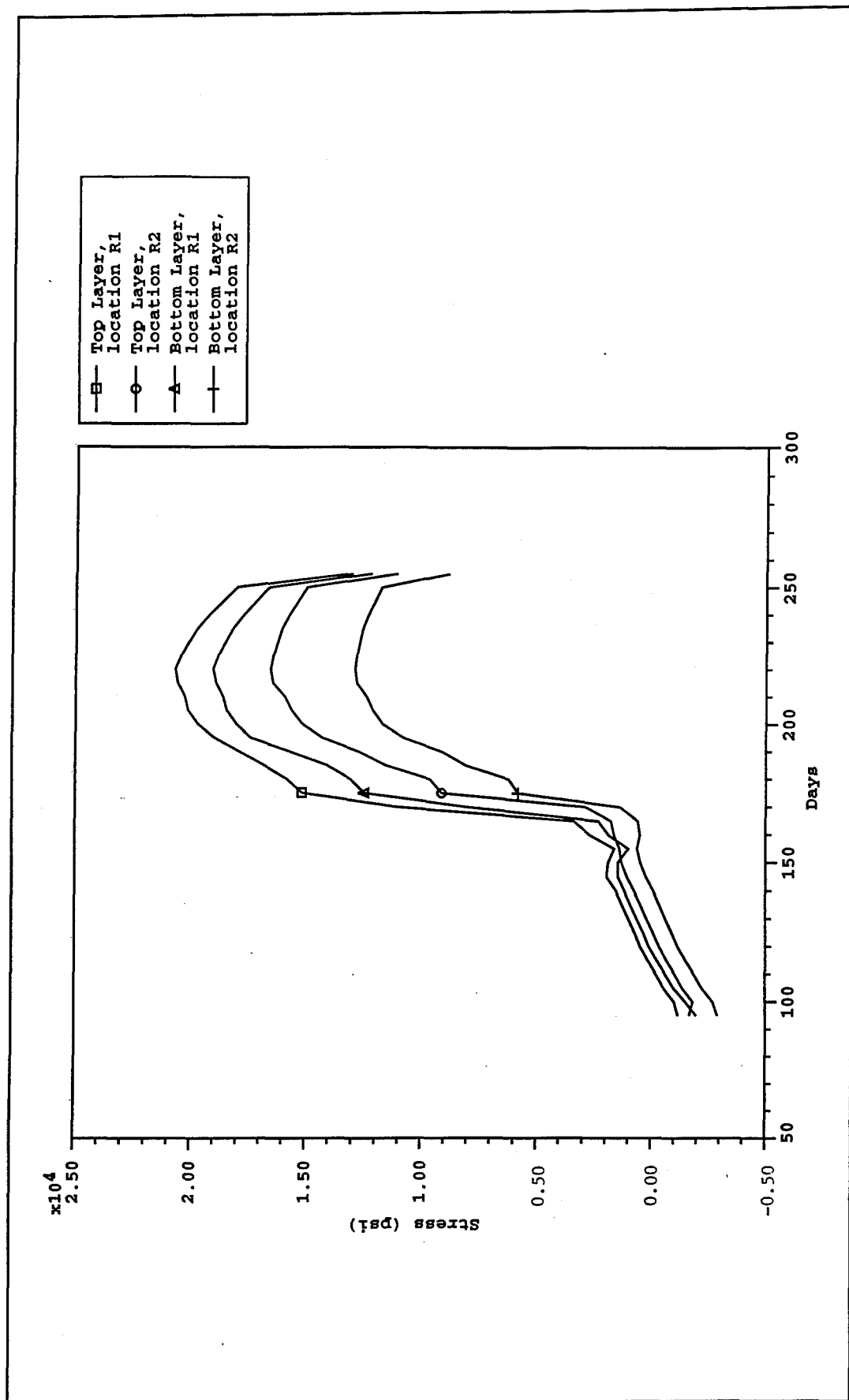


Figure 65. Steel stresses in #18 bars in top of slab on upstream edge

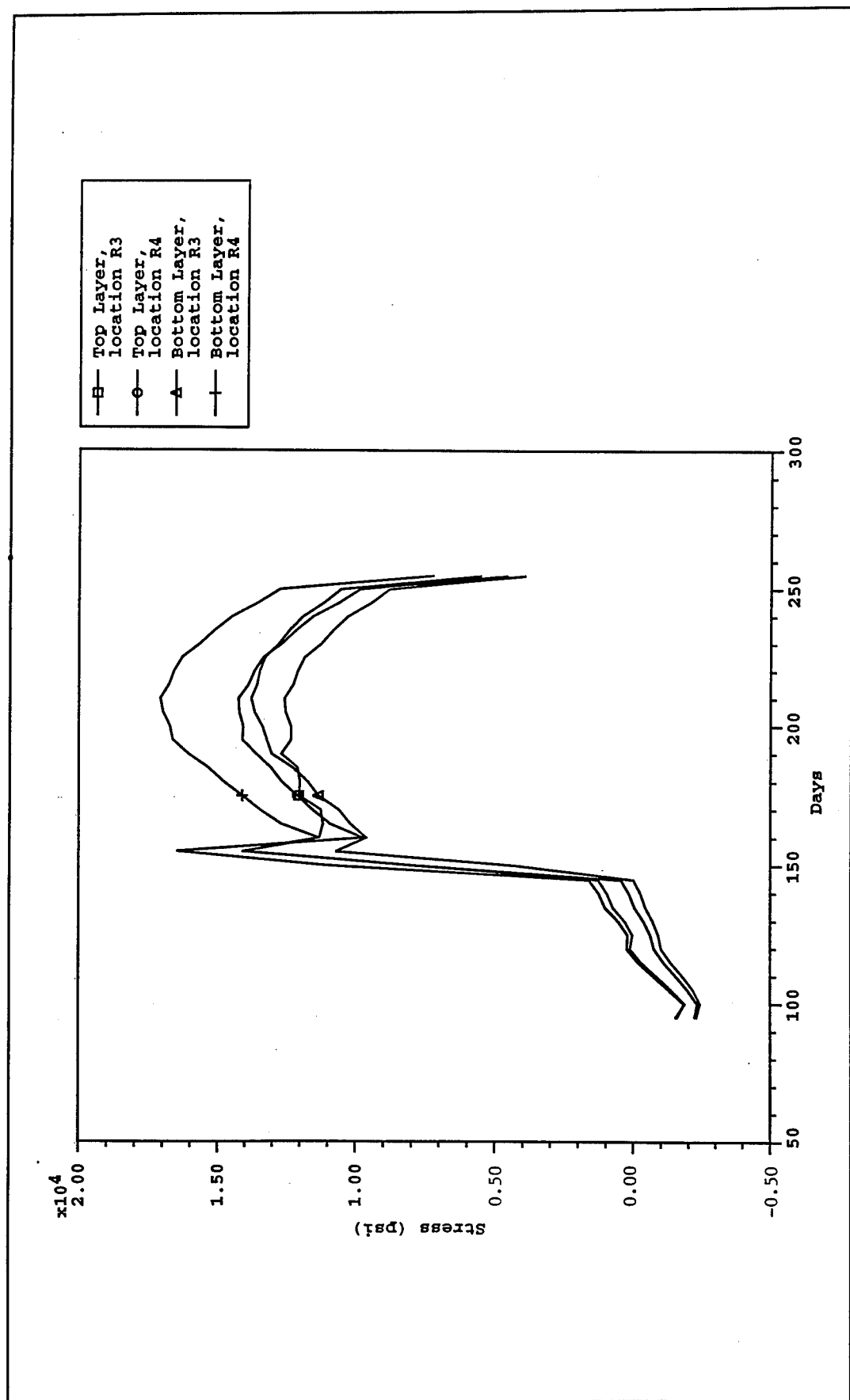


Figure 66. Steel stresses in #18 bars in top of slab on downstream edge

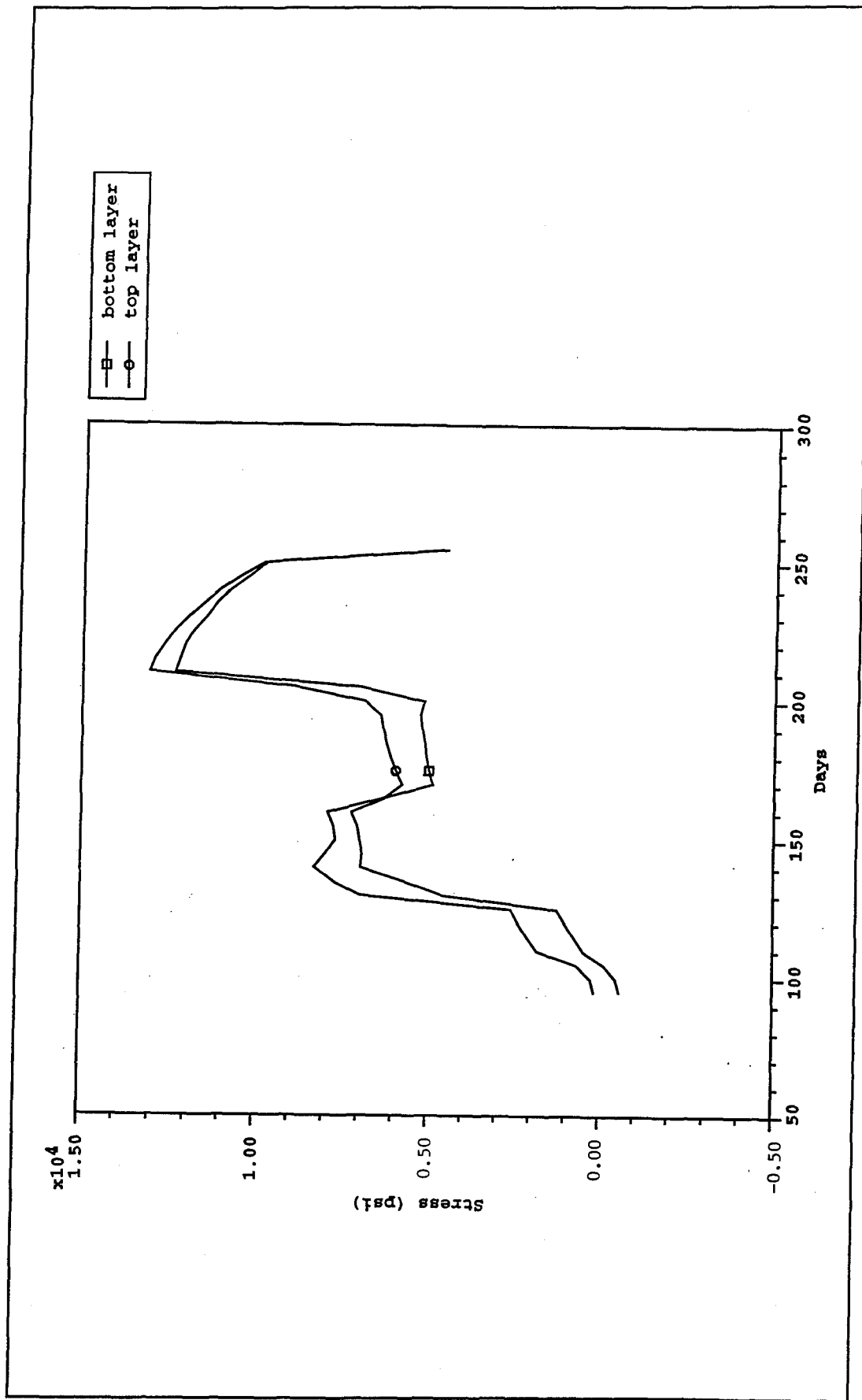


Figure 67. Steel stresses in #18 bars in bottom of slab under culvert

however, a 3D bending response occurs about the edges of the top of the slab along both the upstream and downstream faces. This bending mechanism, which acts to tear the monolith longitudinally from the edges, is driven by the thermal gradients acting on the free surface of the top of the slab and the vertical free surfaces. This 3D effect cannot be captured in either a 2D transverse or longitudinal slice analysis. A 2D transverse slice assumes the temperatures are constant out of plane, and the 2D longitudinal slice assumes the stress distribution is constant in the transverse direction. The cracks are extended into the slab from the top corners by the transverse stress developed as both the top of the slab and the free edge try to curl outward due to the thermal gradients at the two surfaces. The constraining effects of the piles and the general thickness and stiffness of the structure prevent this deformation pattern. The location along the slab for this longitudinal crack development appears to be initiated by the stiffness discontinuity set up by the termination of the third #18 bar. The mesh also changes to a larger element size at this location, and this could also have some slight influence on the initial crack location. This transverse stress acts over a large region of the slab and thus opens a fairly wide distribution of cracks in the transverse direction. The cracking on the downstream edge of the monolith is mitigated somewhat by the additional cooling effect on the lifts forming the downstream free surface due to the culvert and gallery. Mitigating measures for this 3D bending effect are to reduce substantially the heat flow in the longitudinal directions to the free edges of the monolith. This also applies to the vertical surfaces of the walls.

Based on these results, it is recommended that the design of the lower miter gate monolith be investigated further. Since it appears that near adiabatic conditions will be required on the free edges from an insulation standpoint, a design that reduces the concrete mass in the thick slab is recommended for investigation. One approach that has been discussed is to form large void regions between culverts using the thick slab design. Another approach may be to design the monolith cross section based on the shape of the chamber monoliths with a thinner slab section, and construct culvert crossovers and a chamber floor section on top of the reduced slab thickness. Any reduction in the slab thickness should mitigate cracking, and another look at moving culverts more underneath the walls and recovering the extra 2 ft of slab thickness may be in order. In addition, a passive post-tensioning system might be considered in the top slab by tying off the reinforcing bar and using an expansive cement. The #18 reinforcing bar should not be terminated within the slab region because this acts as a crack starter, and heavy duty insulation is needed on exposed surfaces. Additional analyses are recommended to evaluate the effectiveness of these modifications. Because of the extensive cracking that developed in this landside model, a model of the riverside half of the monolith might also be considered before the design is finalized to check for other 3D cracking potentials.

# 7 Slab Redesign Analysis

---

## Design and Model Description

Based on the cracking predicted in the 3D analysis, a redesign of the slab portion of the lower miter gate monolith was undertaken. Because this longitudinal cracking pattern is driven by the 3D thermal gradients developed in the large concrete mass regions of the slab, the objective of the redesign is to reduce the difference in temperature between the interior of the slab, driven by the heat of hydration, and the exterior surfaces of the slab which are driven by the ambient temperatures. After consideration of many options, including post-tensioning, placement intervals, placement temperatures, low strength concrete filler, active cooling pipes, and insulation, the Olmsted NISA review team decided on an approach to reduce the amount of concrete mass by introducing void regions within the slab. Considering constructability and cost, the design chosen by the team for investigation consisted of using 12-ft-diameter corrugated steel culvert pipes placed on end at 15-ft centers within the slab regions containing large concrete mass. These pipes are 18 ft long and rest on the 5-ft lifts that form the bottom of the slab. The primary function of these pipes is to provide a stay-in-place form to create a void region and remove concrete mass. In addition, however, by placing the pipe segments on end rather than as long sections lying horizontal (similar to a crossover culvert), the pipes also provide large surface areas for heat convection. The pipe voids are not closed until the lift forming the top of the slab is placed and thus can convect heat from the interior lifts as the whole slab is being constructed. Based on a 26-ft-thick slab section (discussed later), this void geometry reduces the concrete mass by approximately 50 percent. In addition to the 40 voids, consisting of 6 rows of 7 pipes minus 2 at the corners under the miter gate loads, 9 voids, each 3 ft high, were created underneath the gallery crossover along the downstream edge. The crossover galleries were also widened from 6 to 10 ft as a measure to reduce heat-generating concrete mass.

As a secondary action for crack mitigation and for reinforcing bar cage constructability, the culvert along the landside was moved outward to be centered under the landside wall. This creates additional concrete thickness between the culvert corner and the chamber floor and allows the slab

thickness to be reduced back to the original 26-ft thickness. A 4-ft by 45-deg chamfer between all vertical surfaces and the chamber floor was also included in the new geometry design.

A new finite element mesh was constructed for this new geometry using the same basic assumptions for element sizes and for the stub wall modeling. Additional nodal lines in the longitudinal and transverse directions are required to adequately model the holes created by the pipe voids. Because of the difficulties encountered with using prism elements in the previous mesh, a decision was made to avoid prism elements in the new model. Instead, the curved surfaces of the culvert bends and all angled surfaces are modeled approximately using brick elements in a stepped arrangement. Since these areas showed small cracking potentials in the previous analysis, this approximation to the geometry was preferred over dealing with potential numerical problems encountered with prism elements. For conservatism, no credit is taken for the structural capacity of the corrugated steel pipe in the model since it is primarily designed as a stay-in-place form. Figure 68 illustrates the finite element model in several stages of incremental construction for the new slab geometry design. Figure 69 identifies the IJK numbering system used for node identification. Additional reinforcement detailing for this design was provided by the Louisville District, and Figure 70 shows a schematic for the steel reinforcement bars included in this model. Service loads followed that described for the conventional slab 3D analysis.

## Unit Cell Evaluation

The composite slab configuration, using upright corrugated steel pipe to form void regions, was designed to reduce thermal gradients within the slab. The void regions eliminate heat-generating concrete mass, and the increased surface area provides a path for heat removal through convection as the slab is constructed. However, this design also reduces the structural capacity of the slab, and an evaluation of the effect on structural response was undertaken in a unit cell analysis. This evaluation considers a typical unit cell in the middle of the chamber and models both the conventional solid section design and the composite void design. By exposing both configurations to the same incremental loading, a relative comparison of the structural capacity can be obtained. Since the mechanical load applied to the surface of a single cell will be different than that seen by the cell in the complete monolith under thermal-induced loads, the magnitude of loads applied in the single cell evaluation has little meaning. However, because the transverse bending load is representative of that seen by the material under actual conditions, the relative response of the composite slab compared with the solid slab can be established.

The unit cell model is constructed by considering a section of the slab in the chamber region under uniform bending in the transverse direction. If the void is centered on this section, then through symmetry, a quarter of

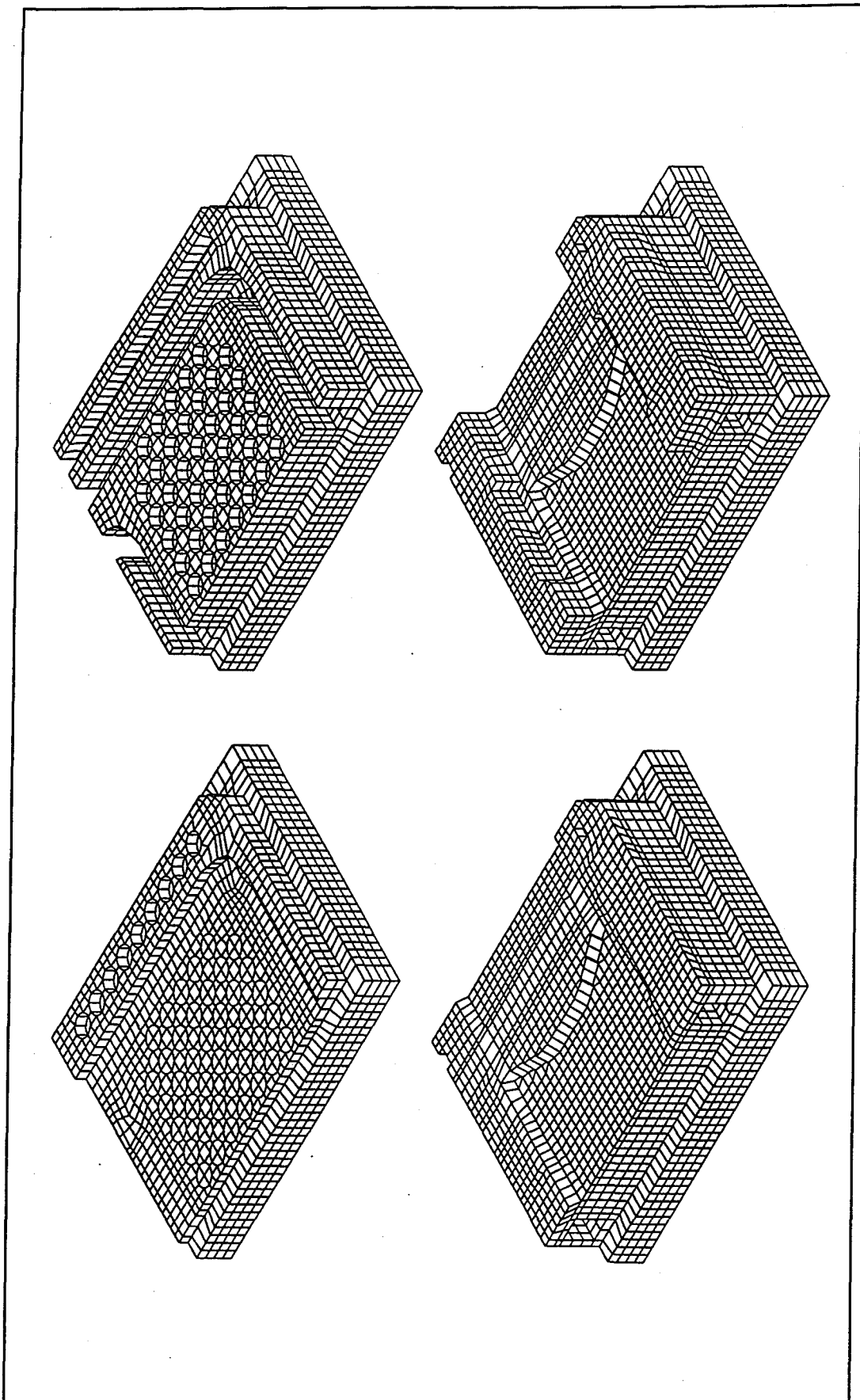


Figure 68. Three-dimensional finite element model for composite slab design

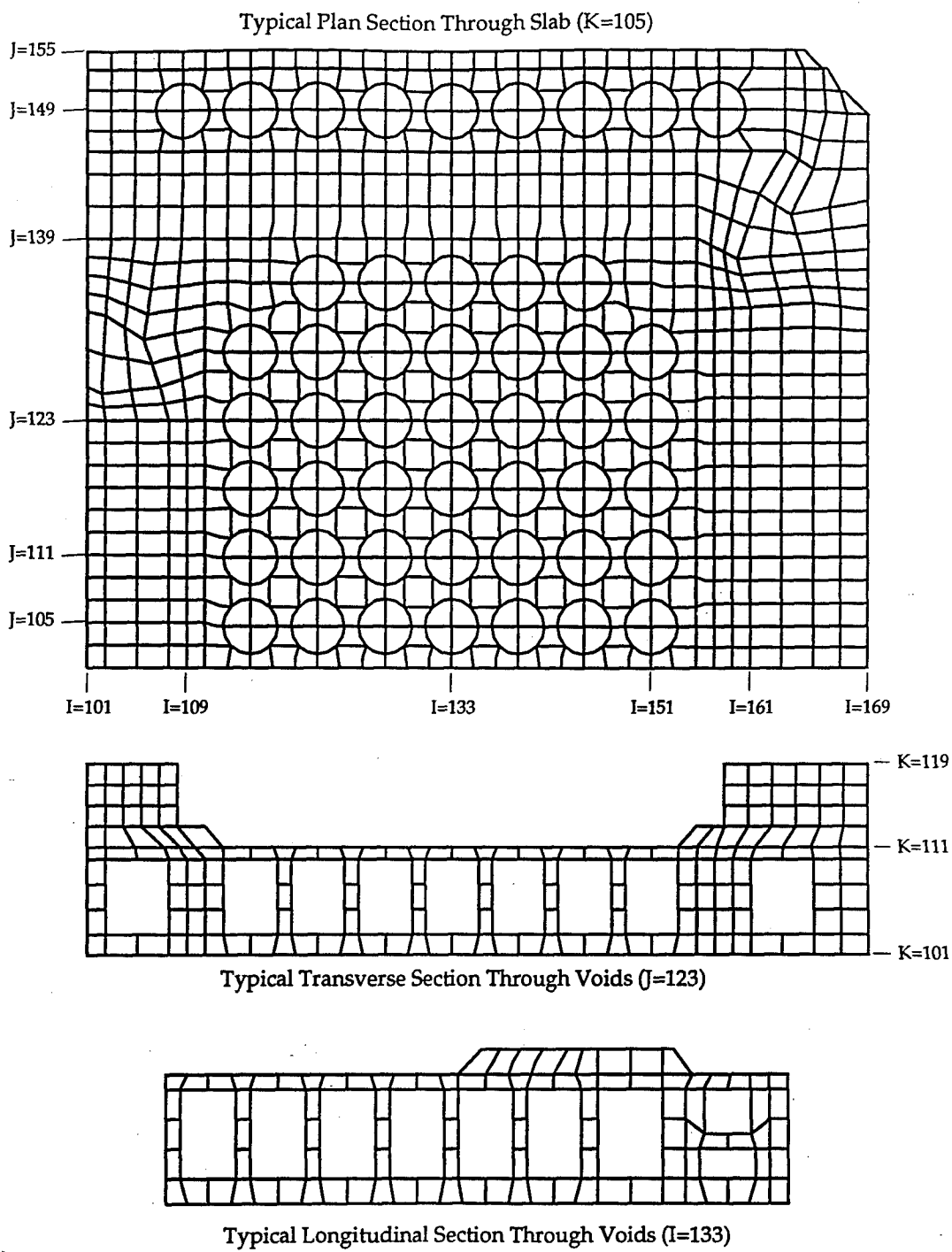


Figure 69. IJK numbering convention for composite slab model

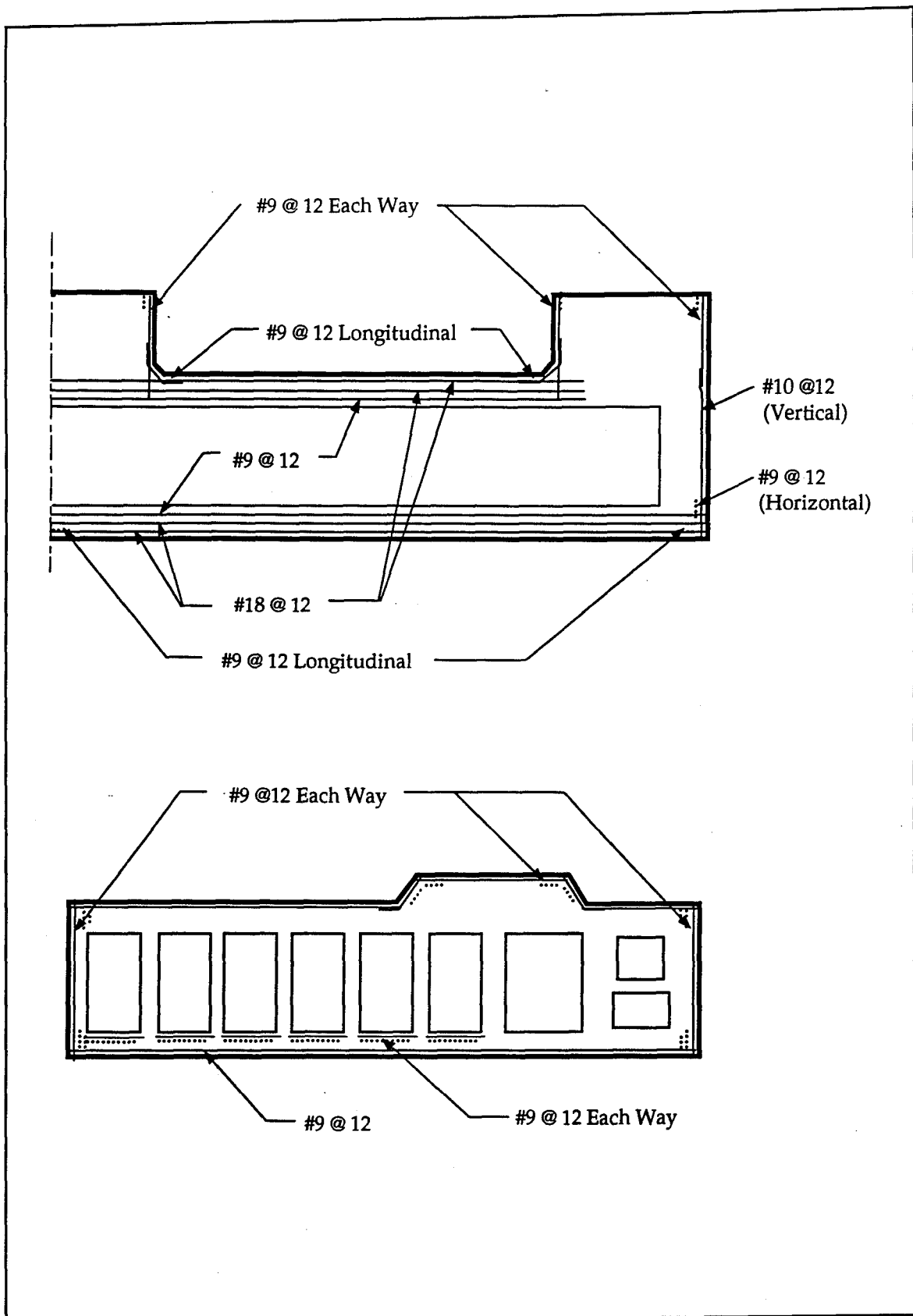


Figure 70. Schematic of reinforcement for composite slab design

the 15-ft by 15-ft volume containing the void can be modeled. Figure 71 illustrates this unit cell model and Figure 72 shows the mesh used for both the void model and the solid model. Note that the same mesh discretization was used in each with elements removed for the void model to avoid mesh sensitivity issues in the relative comparison. The new cell has 5 ft of solid concrete on the bottom containing the two layers of #18 reinforcing bar plus a row of #9 bars, then 18 ft of plain concrete either solid or containing a quarter of a 6-ft radius cylindrical hollow void, and finally a 3-ft section of solid concrete reinforced as in the bottom section. No modeling of the corrugated steel shell forming the void was included to be conservative and to be consistent with the model developed for the 3D analysis.

Three faces of the model contain symmetry displacement boundary conditions, and vertical rigid body motion is removed through one row of nodes with zero vertical displacement boundary conditions along the bottom of the model. The bending load is applied through a force couple, tension on the top and compression on the bottom. These faces act on the top and bottom row of nodes on the free face and impose a linear distribution of force along the face due to constraint conditions imposed on the nodes along the face. These loads are then incrementally applied, and the applied moment is plotted versus rotation of the face for both the solid and void models.

Since these loads are being evaluated in a nonthermal environment, no creep response was included and the concrete properties were taken for mature Mixture 11 Olmsted concrete at 120 days. Similarly, since the loads are evaluated in a post-cracking regime, the plastic strain hardening behavior of the reinforcing bars is included. Table 3 provides the concrete properties used, and Table 4 gives the properties used for the steel reinforcing bar.

The results are summarized in Figure 73 which shows the applied moment versus bending rotation of the solid and void models. This plot shows that the ultimate capacity of the two designs is very similar (within 5 percent), as expected, since the ultimate capacity is dependent on the yield in the top reinforcing bar and the concrete crushing in the compression block. However, since our application is concerned with cracking, it is seen that the void section begins cracking at a 30 percent lower load than the solid section. This is due to the reduced volume of concrete available to carry load in the void section on the tension side of the bending response. Because the overall stiffness of the composite design is also reduced, this cannot be extrapolated to indicate that the composite design will begin cracking at a 30 percent reduction in the thermal gradient, but it does indicate that the composite design is more susceptible to cracking under bending. The composite slab has a 30 percent reduction in tolerance to induced bending relative to the solid design.

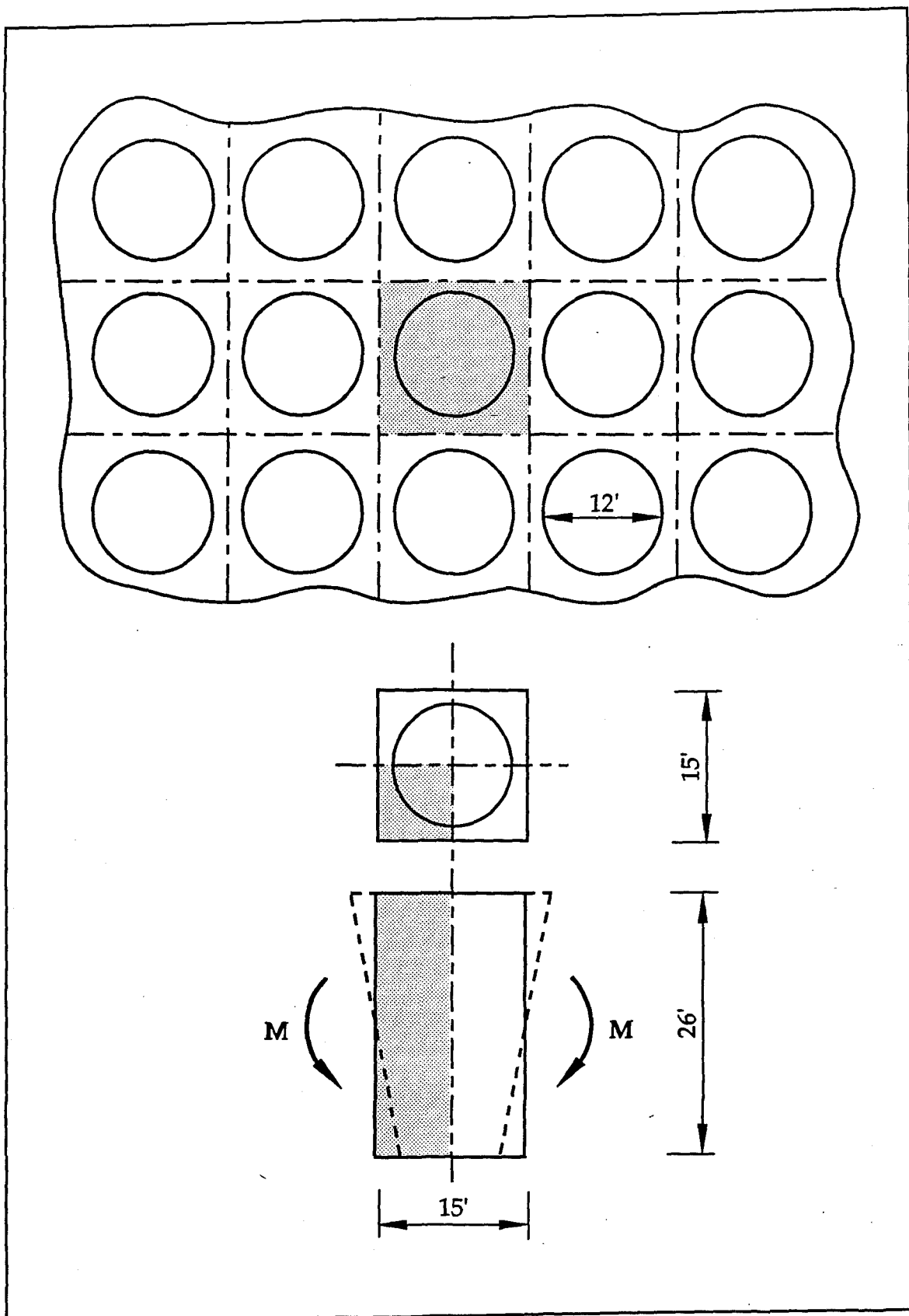


Figure 71. Model for unit cell evaluation (Continued)

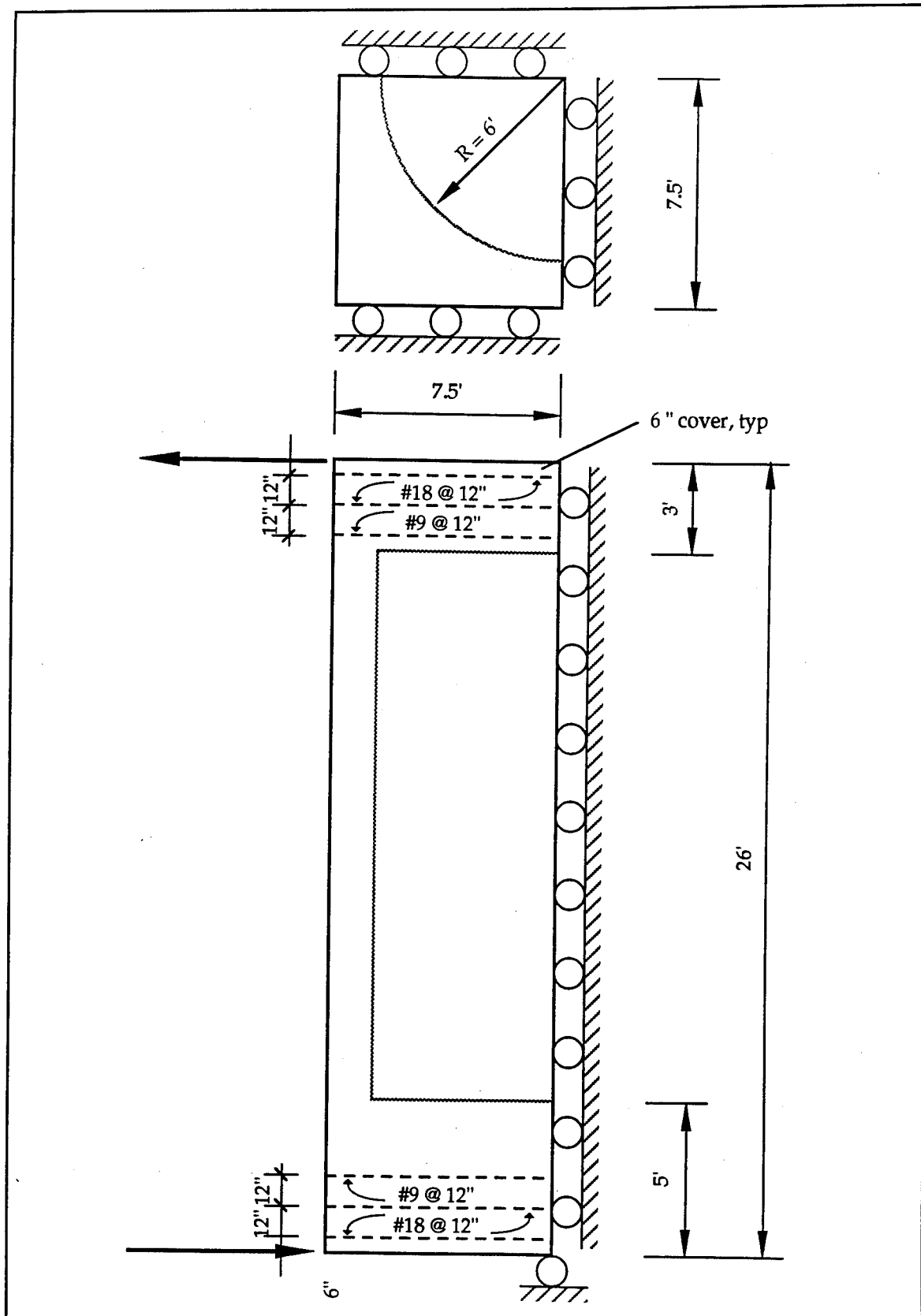


Figure 71. (Concluded)

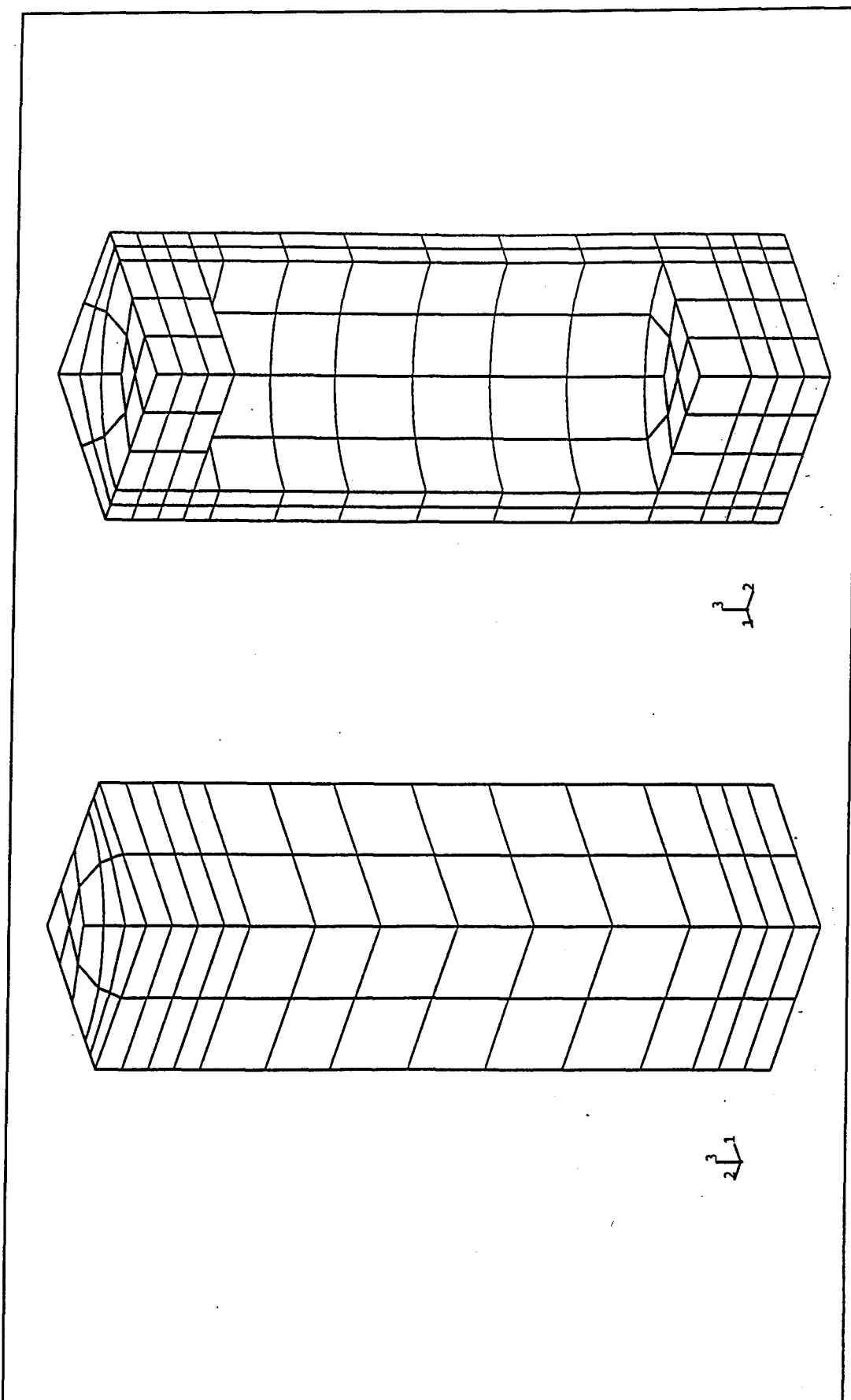


Figure 72. Finite element mesh for unit cell calculations

**Table 3**  
**Concrete Material Properties**

Fracture strain	$100 \times 10^{-6}$ in./in.
Compressive strength	4,720 psi
Poisson's ratio	0.15

**Table 4**  
**Reinforcing Bar Material Properties**

Modulus	$2.9 \times 10^7$ psi	
Poisson's ratio	0.30	
Plasticity	Strain (in./in.)	Stress (psi)
	0.0	66,000
	0.006	67,000
	0.01	70,000
	0.048	85,000
	0.066	90,000
	0.100	95,000
	0.150	98,000
	0.200	10,000

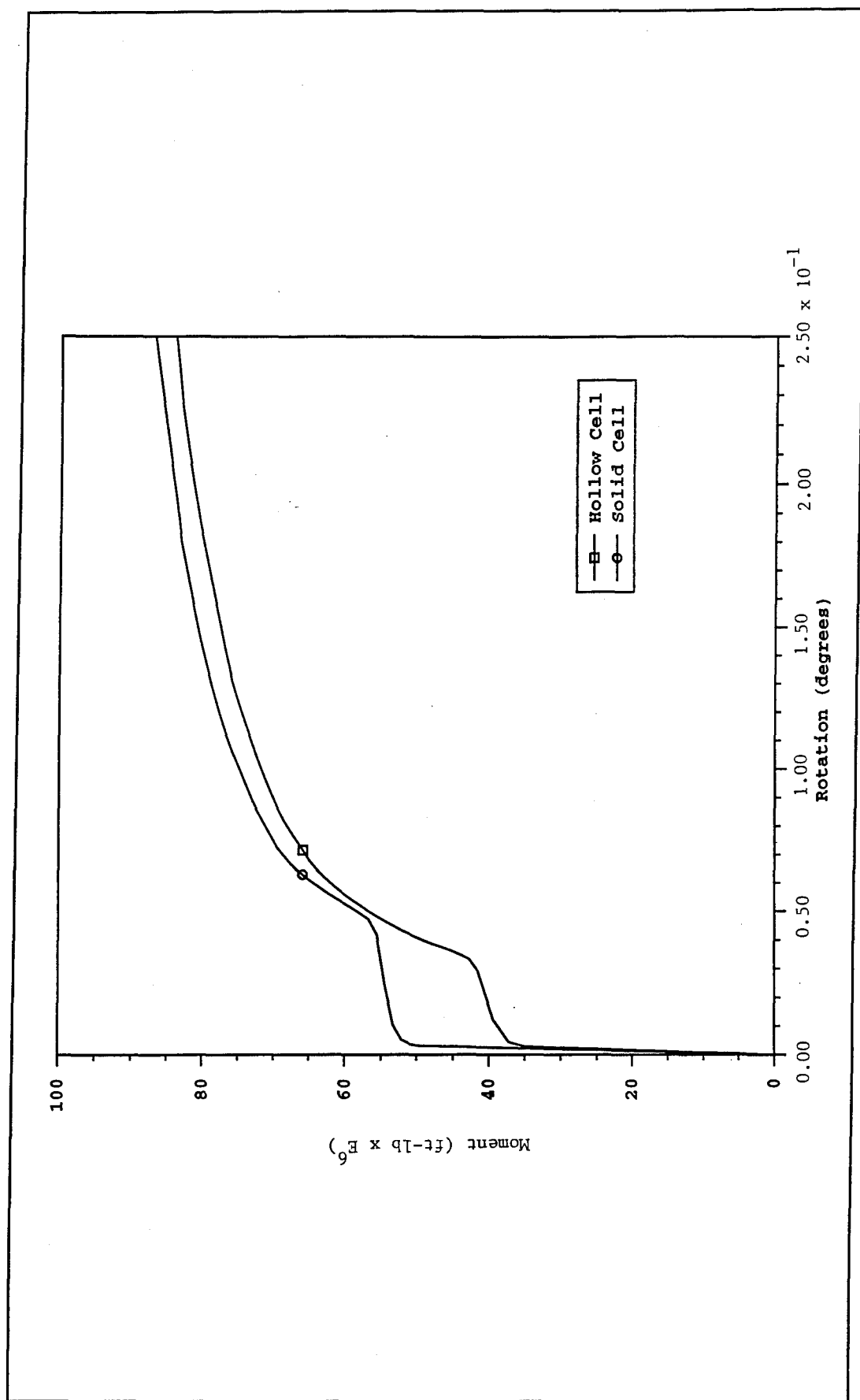


Figure 73. Relative strength of composite slab to conventional slab

## Analysis Results

Several modifications were included in the thermal analysis for the composite slab design. The introduction of the vertical corrugated pipes eliminated a substantial volume of concrete in the slab under the landside chamber. This allowed the lift placement heights to increase from 5 ft to 6 ft in these regions around the pipe voids, eliminating three lift placements from the construction process. Thus, the top of the slab is placed 15 days earlier than the previous 3D analysis for the conventional solid slab design. The film coefficients used on the surfaces of the cylindrical voids are computed from an assumed average wind circulation velocity of 1 mph and by treating the 3/8-in.-thick steel pipe, which was not modeled explicitly, as formwork. Thus, the film coefficient for concrete based on 1-mph wind velocity is

$$h_a = 1.086 + 0.225(1.466) = 1.416 \text{ Btu/ft}^2 \text{ - hr - } ^\circ\text{F}$$
$$= 0.236 \text{ Btu/in.}^2 \text{ - day - } ^\circ\text{F}$$

The insulation R value of the steel pipe is

$$R_s = \frac{t_s}{k_s} = \frac{0.375}{62} = 0.006 \text{ in.}^2 \text{ - day - } ^\circ\text{F/Btu}$$

and the effective film coefficient for the concrete surface is

$$h = \frac{1}{\frac{1}{h} + R_s} = 0.2356 \text{ Btu/in.}^2 \text{ - day - } ^\circ\text{F}$$

Also for this analysis, vertical insulation with an R value of 2.0 hr-ft<sup>2</sup>-°F/Btu was applied for 45 days on concrete placed after November 15. Concrete less than 30 days old on November 15 also received insulation for 45 days beginning on November 15. Because of the stub wall modeling, only the last two lifts of each wall had insulation applied.

### Cracking response

The results of the thermal-induced stress and cracking analysis are presented herein. Although some differences occur in the thermal loading conditions as discussed above, the composite slab design was subjected to conditions very similar to the conventional design analysis. The composite slab design experiences substantially more cracking than the conventional design. Figures 74 through 78 show the predicted cracking at days 120, 130, 140, 180, and 255, respectively. For the specified day, each of these figures shows a plan view, a transverse view looking from the upstream side, and a longitudinal view looking from the landside. Each view is an outline of the structure with cracking patterns, so that all

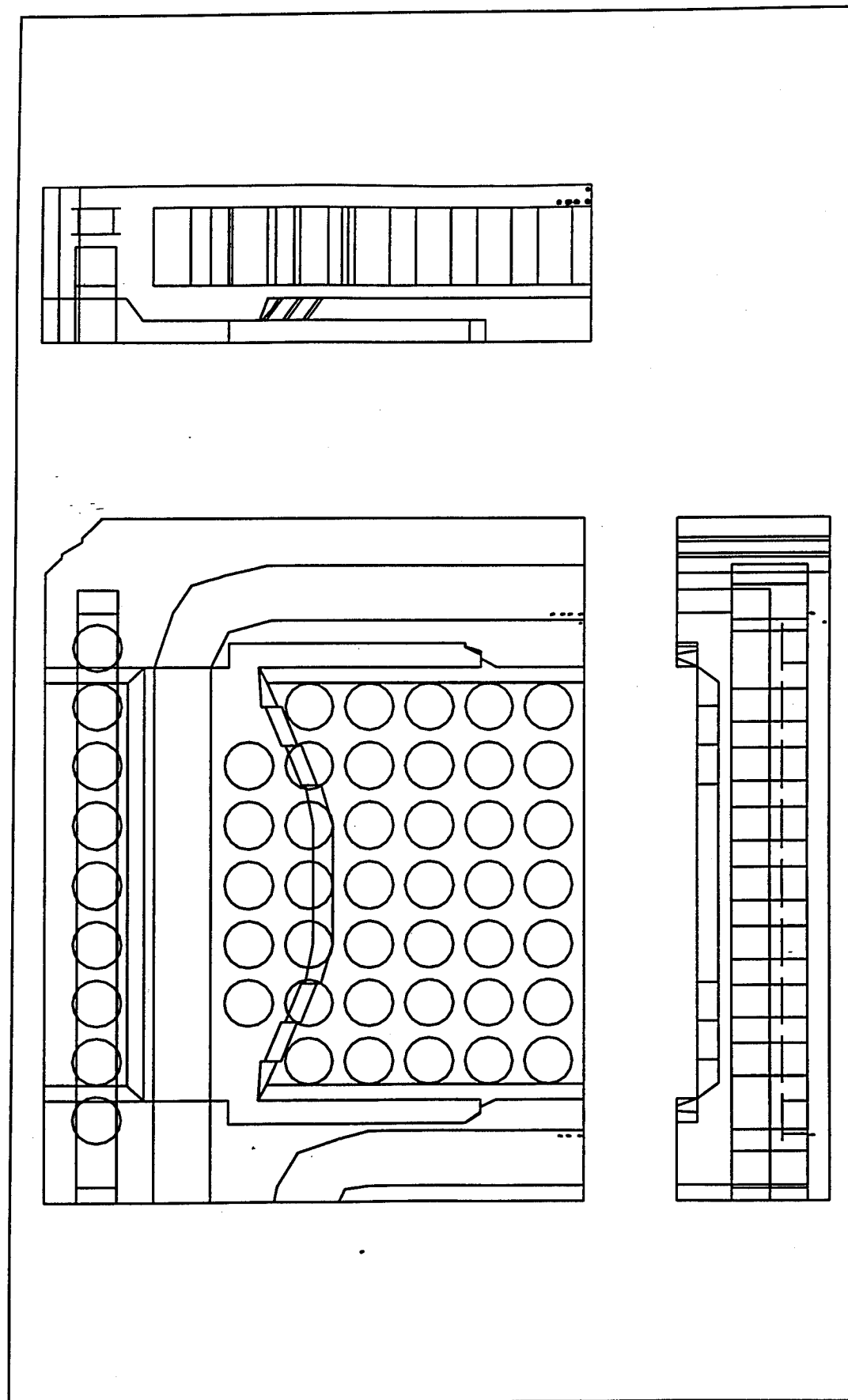


Figure 74. Composite slab analysis cracking pattern at day 120

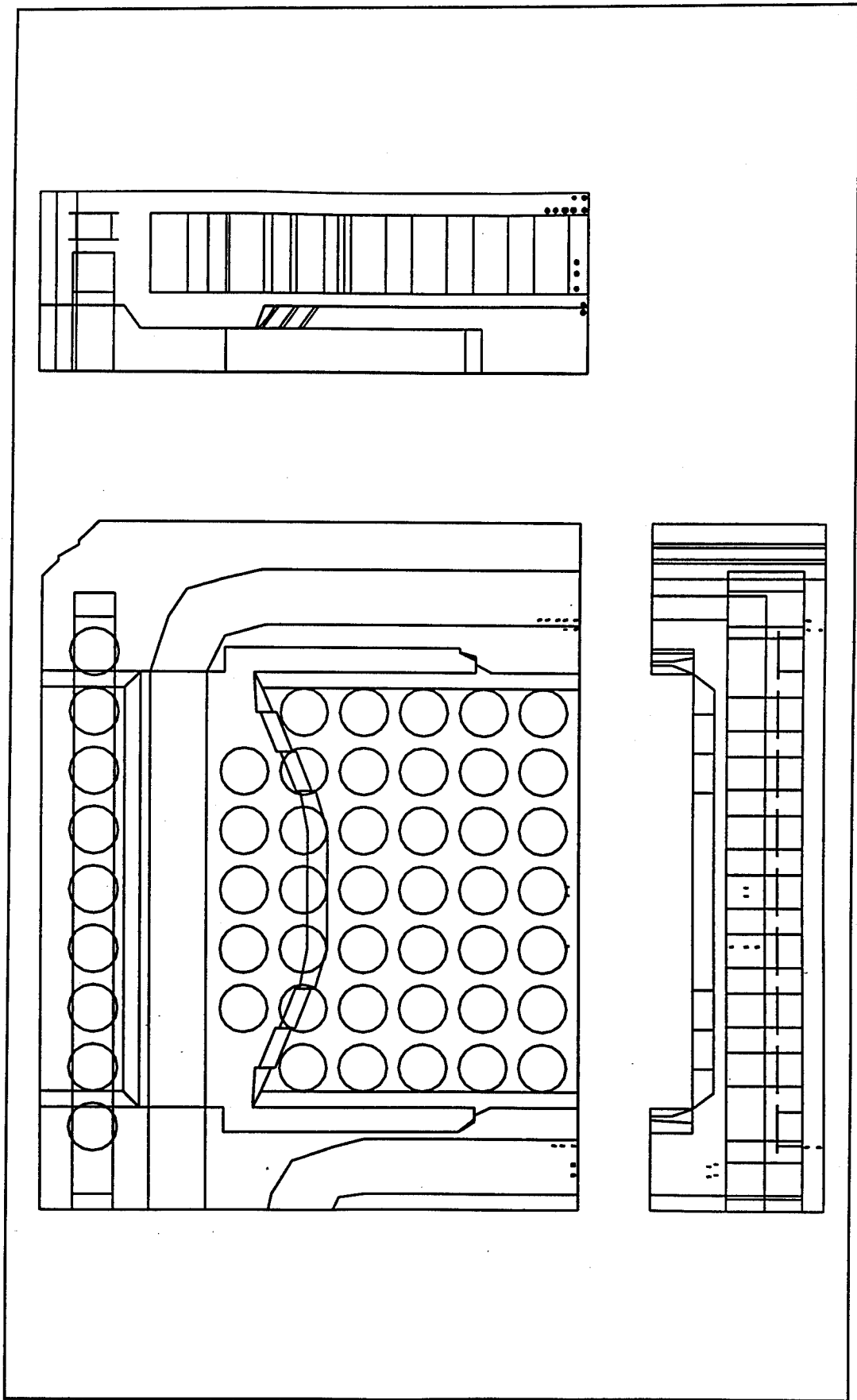


Figure 75. Composite slab analysis cracking pattern at day 130

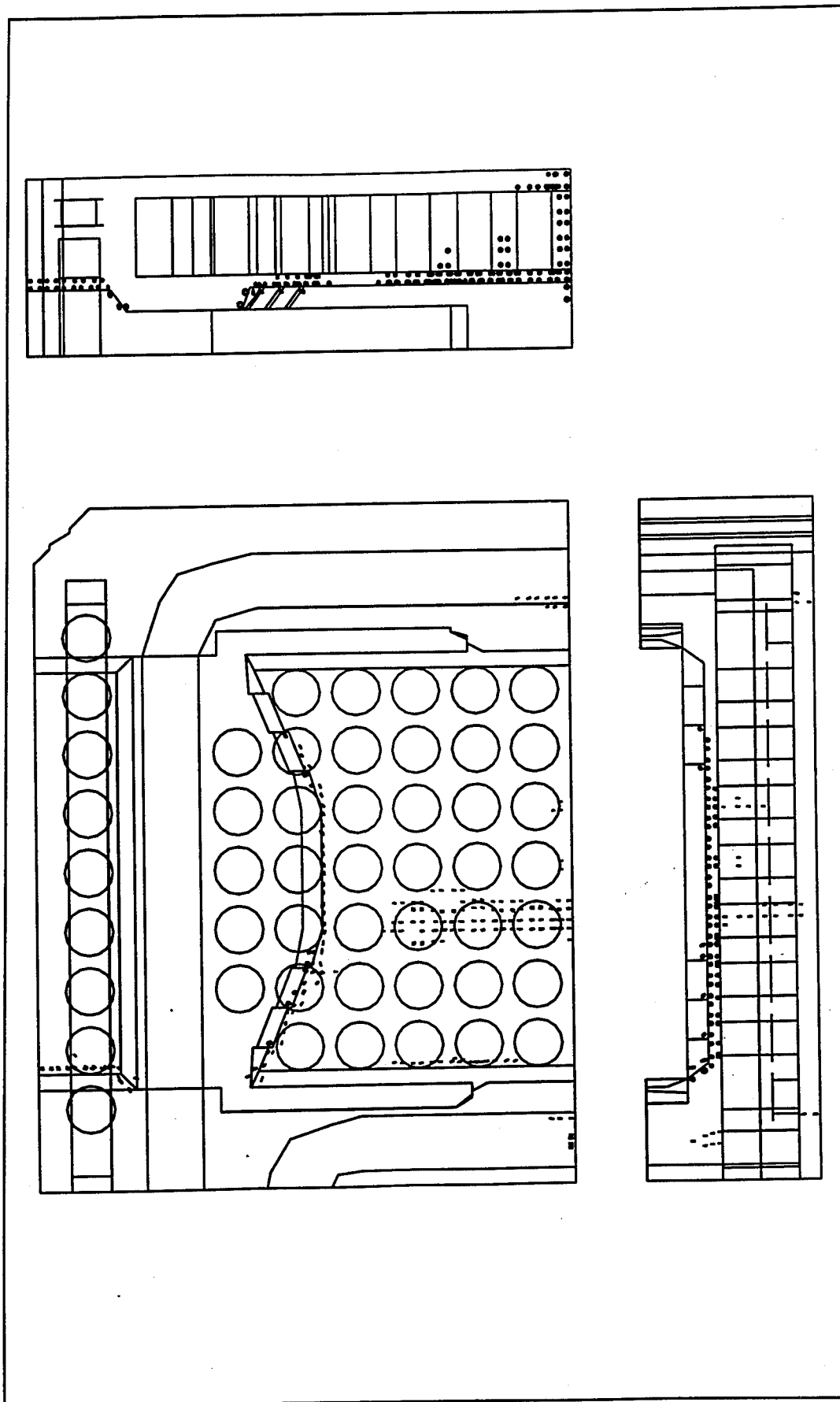


Figure 76. Composite slab analysis cracking at day 140

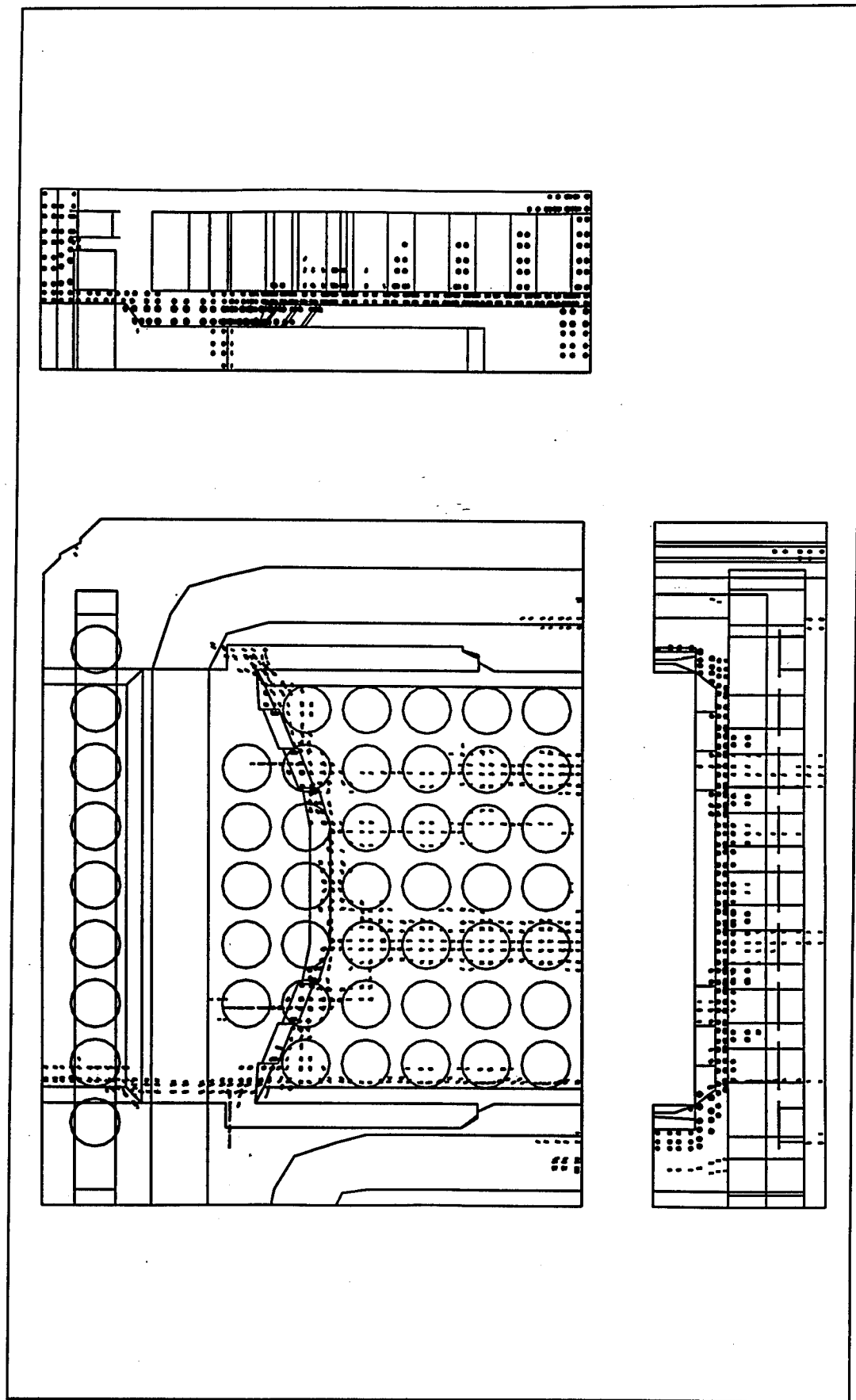


Figure 77. Composite slab analysis cracking pattern at day 180

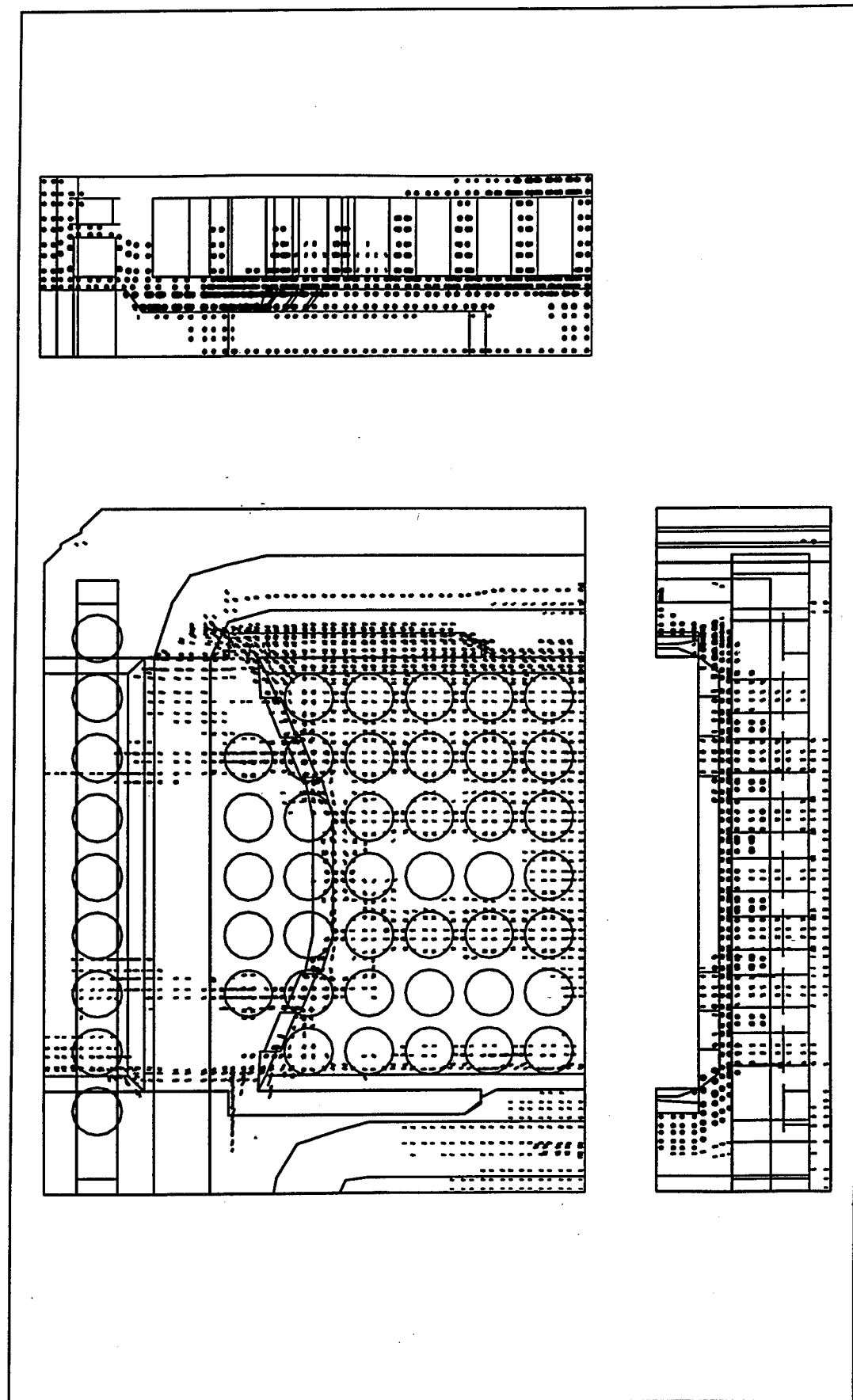


Figure 78. Composite slab analysis cracking pattern at day 255

cracking locations are seen in each view. For each cracked point, a circle is drawn to represent the plane of the crack which is perpendicular to the stress that causes the crack. Thus a crack due to transverse stress is shown as a line (a circle on edge) in the transverse view and by a circle in the longitudinal view.

Cracking first begins around day 110 near the upstream face under the culverts and progresses to that shown in Figure 74 by day 120. This cracking follows that seen in the previous 3D analysis. It is caused by the thermal gradients at the culvert face and at the free edge of the monolith and concentrated by the stress risers near the corners of the culverts. Figure 75 shows cracking developing along the face of the middle cylindrical voids at the upstream edge by day 130. Recall that in the previous analysis, cracking begins on the upstream face on the bottom lifts about day 135 and progresses upward to the top of the slab by day 150. Note that because three lift placements are eliminated in the composite slab design, the slab is completed 15 days earlier in its construction sequence. The cracks in this analysis are again caused by the thermal gradient at the upstream free edge which is moderated lower in the slab because of the reduced heat due to the void design. The stress risers at the surface of the cylinders cause the first cracks to appear there rather than on the free surface.

Figure 76 shows the extent of cracking on day 140 for the composite slab analysis, which is similar to that shown on day 170 for the conventional slab analysis. There are cracks caused by direct tensile stress due to constraint against thermal shrinkage in the top of the slab at the 45-deg chamfer intersection with the middle wall. There are cracks in the top of the slab along the sill intersection with the chamber floor due to longitudinal bending. There are cracks through the top 3 ft of the slab from the downstream face to the back of the sill at the middle wall due to transverse stress from the thermal gradients at the free surfaces. Most prominent is the wide cracking pattern driving longitudinally into the chamber from the corner of the upstream edge and chamber floor. These cracks are from transverse stress caused by the restraint of the structure against deformation due to the thermal gradients acting through the thickness of the slab and to the upstream free surface as discussed in the previous 3D analysis.

Figure 79 is a contour of the vertical displacement component along the bottom of the slab at day 130 and illustrates the thermal-induced deformation pattern. The negative values in the middle portion of the slab are downward deformation, and the gradients along the upstream and downstream edges show an upward curling along the edges. This figure also shows the bending pattern induced in the transverse direction along the edges. Along the upstream edge, the fairly sharp kinks occur at the in-board edges of the culverts and are the result of the cracking under the culverts. The bending pattern between the culverts shows the maximum to be biased from the center line of the chamber toward the center wall and is the mechanism that initiates cracking at this location.

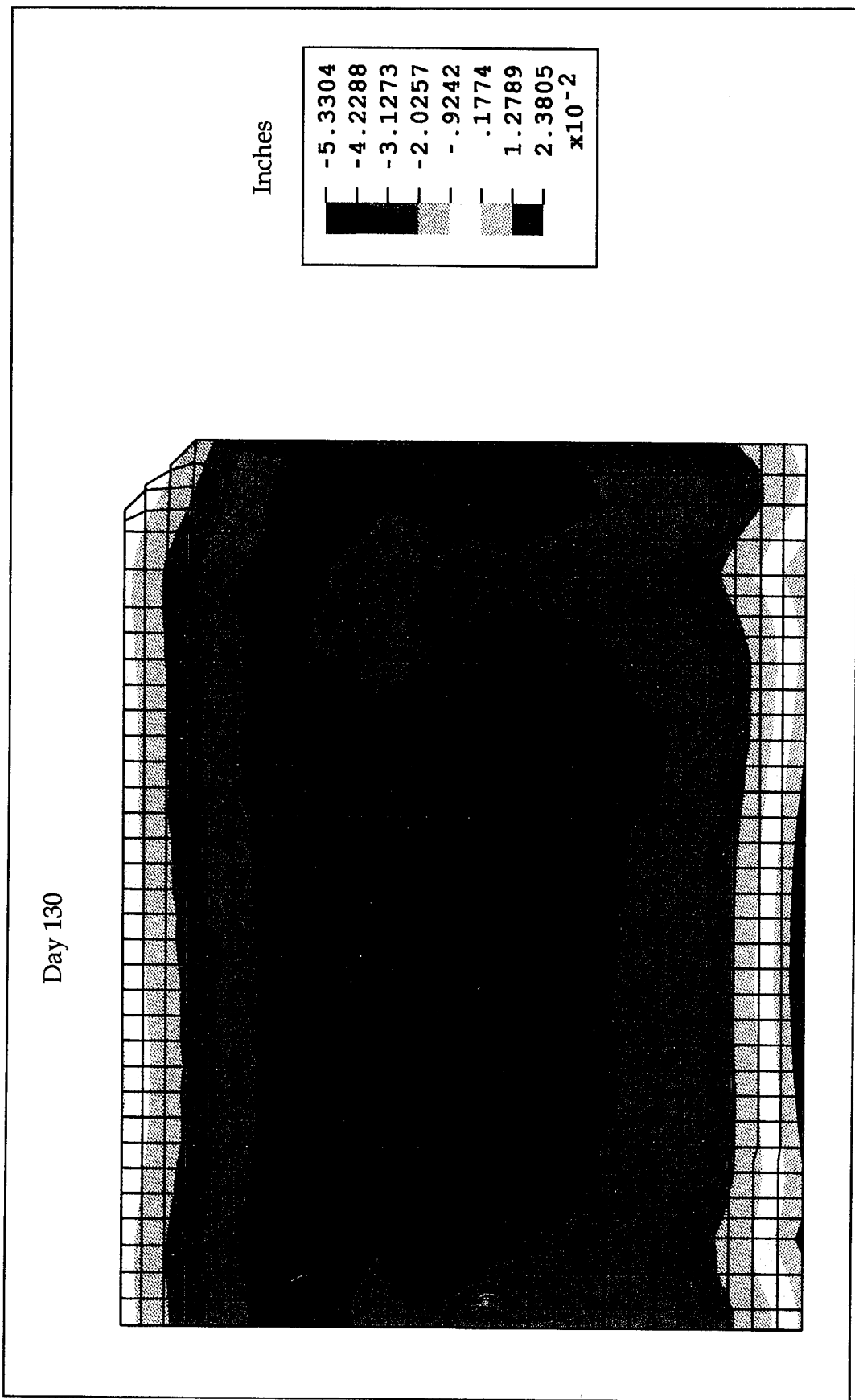


Figure 79. Vertical displacement contour on bottom of slab

Figure 77 shows the extensive cracking that has developed by day 180. An additional wide cracking pattern has driven longitudinally into the chamber near the landside wall. The cracking from the downstream edge at the center wall has extended longitudinally to the upstream edge of the sill throughout the depth of the sill and the top 3 ft of the slab. It has also traveled down through the crossover gallery and through the full thickness of the slab between the downstream edge and the gallery and pipe voids. The cracking under the sill upstream edge due to longitudinal bending has extended into and up the center and landside walls, especially severe in the center wall. The cracking on the upstream face above the center wall culvert that initiated by day 140 has also extended upward and inward into the center wall. Figure 78 is included at day 255 after service loads to indicate the very severe and unacceptable cracking that develops for this composite slab design under the assumed construction conditions.

### Thermal response

Figure 80 provides a map for locating sections and points where thermal results are presented. Thermal contours are provided for plane sections, both on the bottom and top surfaces of the slab, and for the longitudinal and transverse sections shown. The points labeled H1-H4 are the locations for time histories of temperatures. Each location has two points plotted, one in the middle of the bottom lift (2-1/2 ft from the bottom of the slab) and one in the middle of the top lift (1-1/2 ft from the top of the slab). The points labeled P1-P4 are locations where temperature profiles through the slab are taken. These show temperature distributions through the thickness of the slab at various days.

Figure 81 provides thermal contours for the distribution of temperature on the bottom of the slab for days 120, 140, 160, and 180. Although not taken at the same days as the contours for the previous analysis, shown in Figure 49, the thermal gradients to the free edges have been reduced slightly, mainly because the interior temperatures are reduced and the free surfaces are still driven by ambient temperatures. For example, at day 160 the temperature difference over about 6 ft is 36 °F in the conventional design and 30 °F in the composite design at the bottom of the slab. Heavy insulation on free surfaces in the slab is required to reduce these gradients significantly. Figure 82 shows the thermal gradients on the top surface of the slab at days 120, 140, 160, and 180. These plots are difficult to compare with those of the previous analysis in Figure 49 since the top slab is placed 15 days earlier and insulation on the vertical surfaces of the walls is used in this analysis. However, the expanse of area between the walls and upstream of the sill is seen to be very comparable in the two analyses as expected, since it is insulated the same and is driven by the same ambient temperature.

Figures 83 and 84 show thermal contours for longitudinal and transverse sections, respectively, for days 120, 140, 160, and 180. These plots show an error in processing the temperatures for this analysis. The

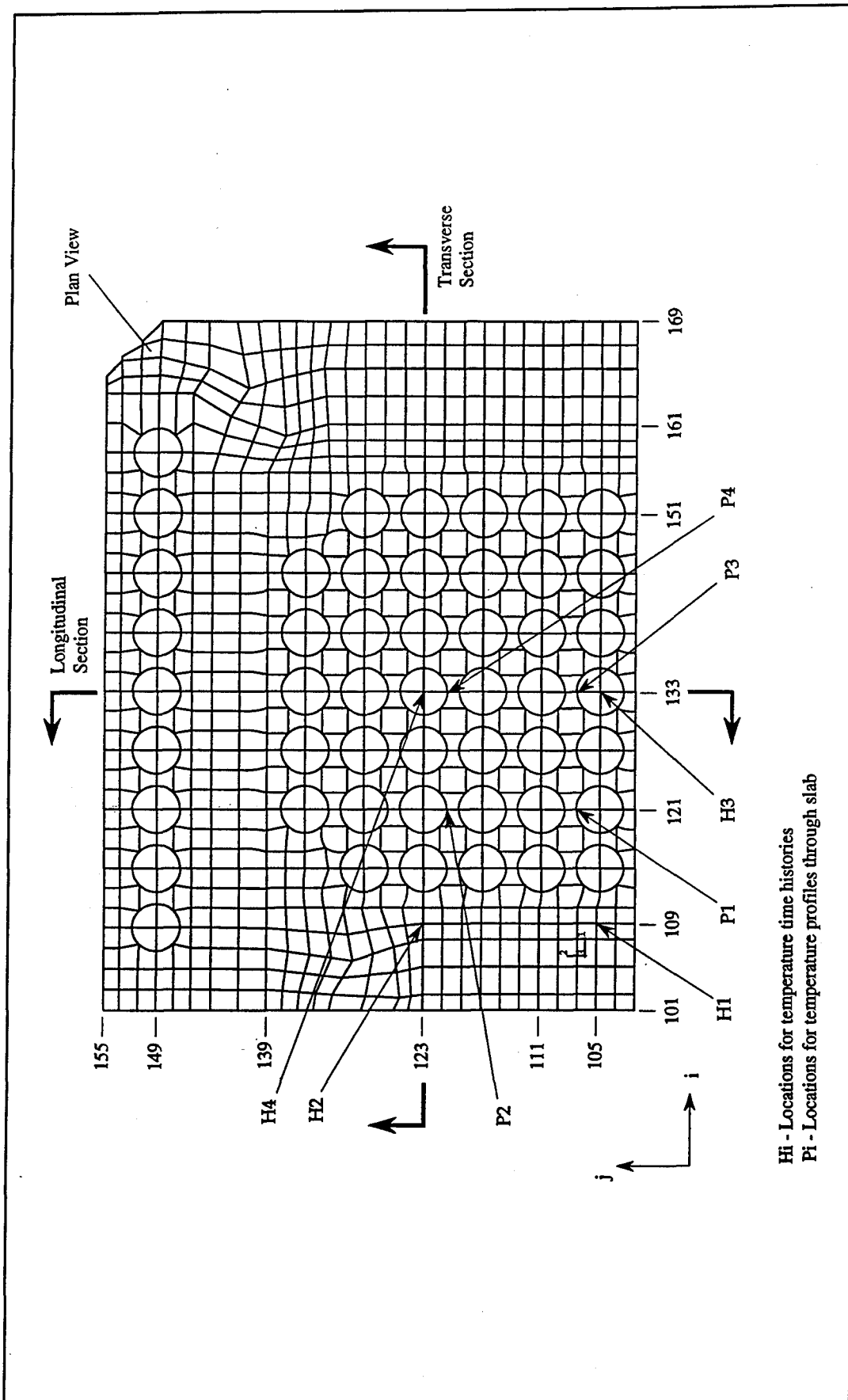


Figure 80. Composite slab thermal results location map

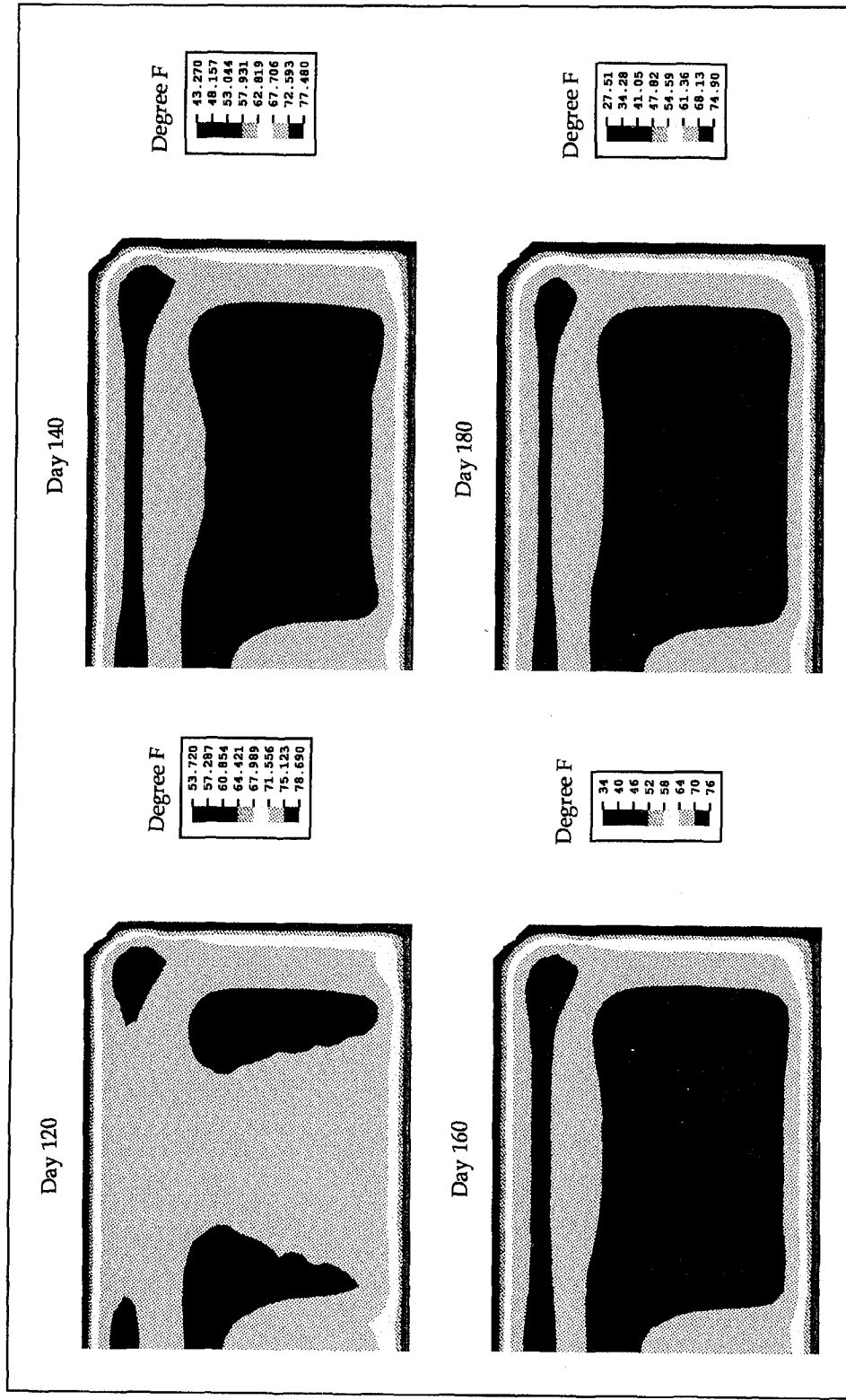


Figure 81. Composite slab thermal thermal contours on bottom of slab

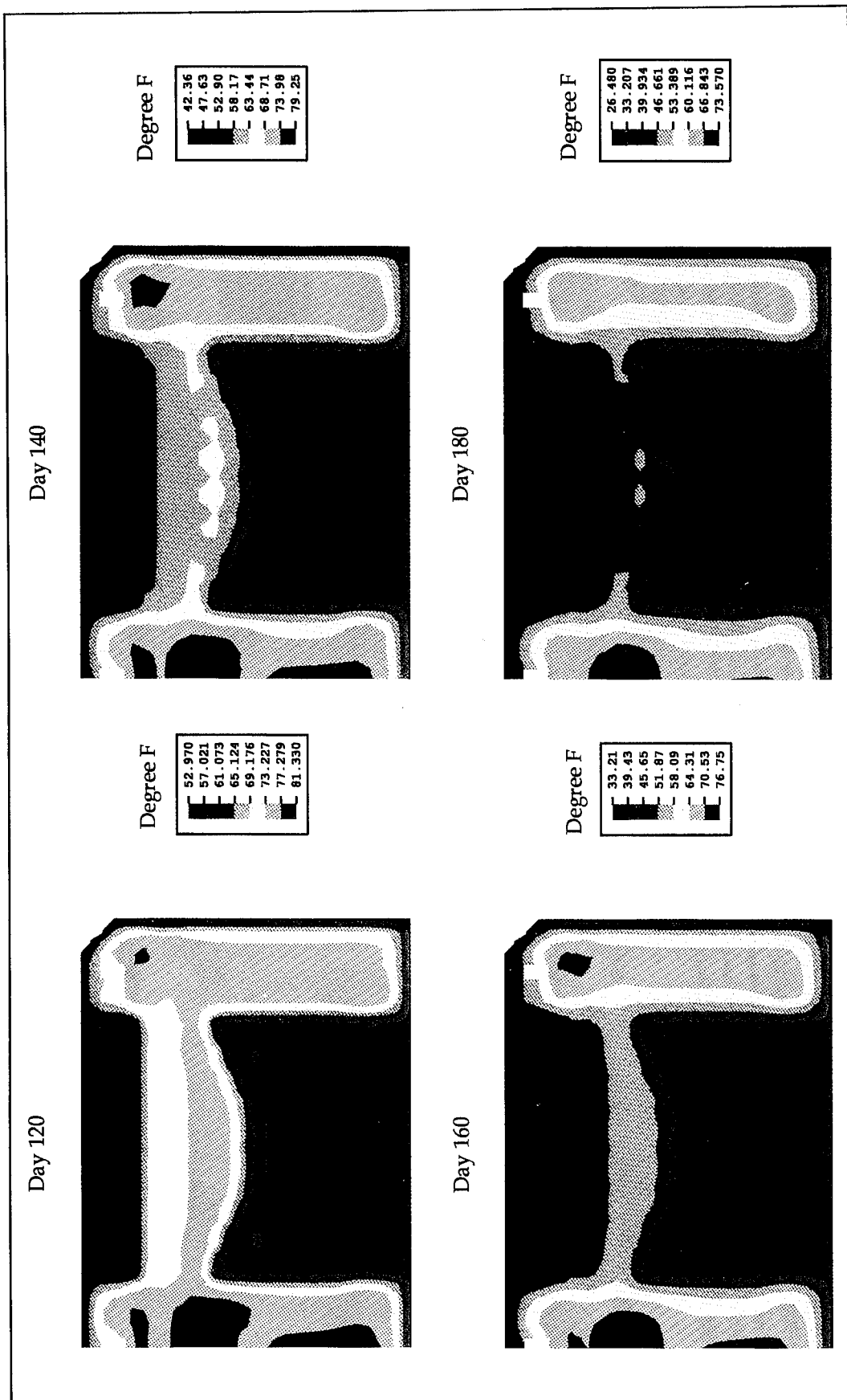


Figure 82. Composite slab thermal contours on top of slab

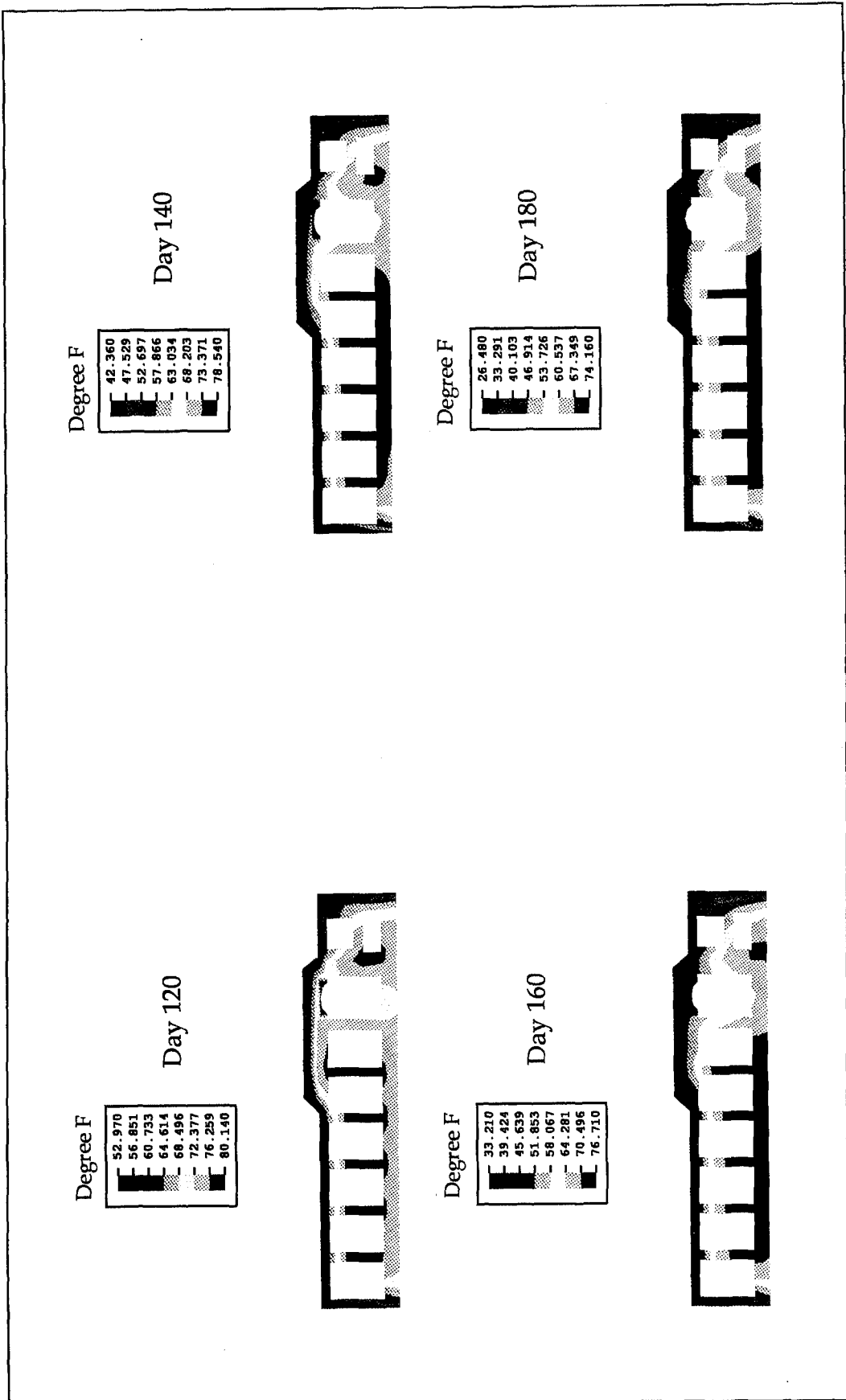


Figure 83. Composite slab thermal contours for longitudinal section

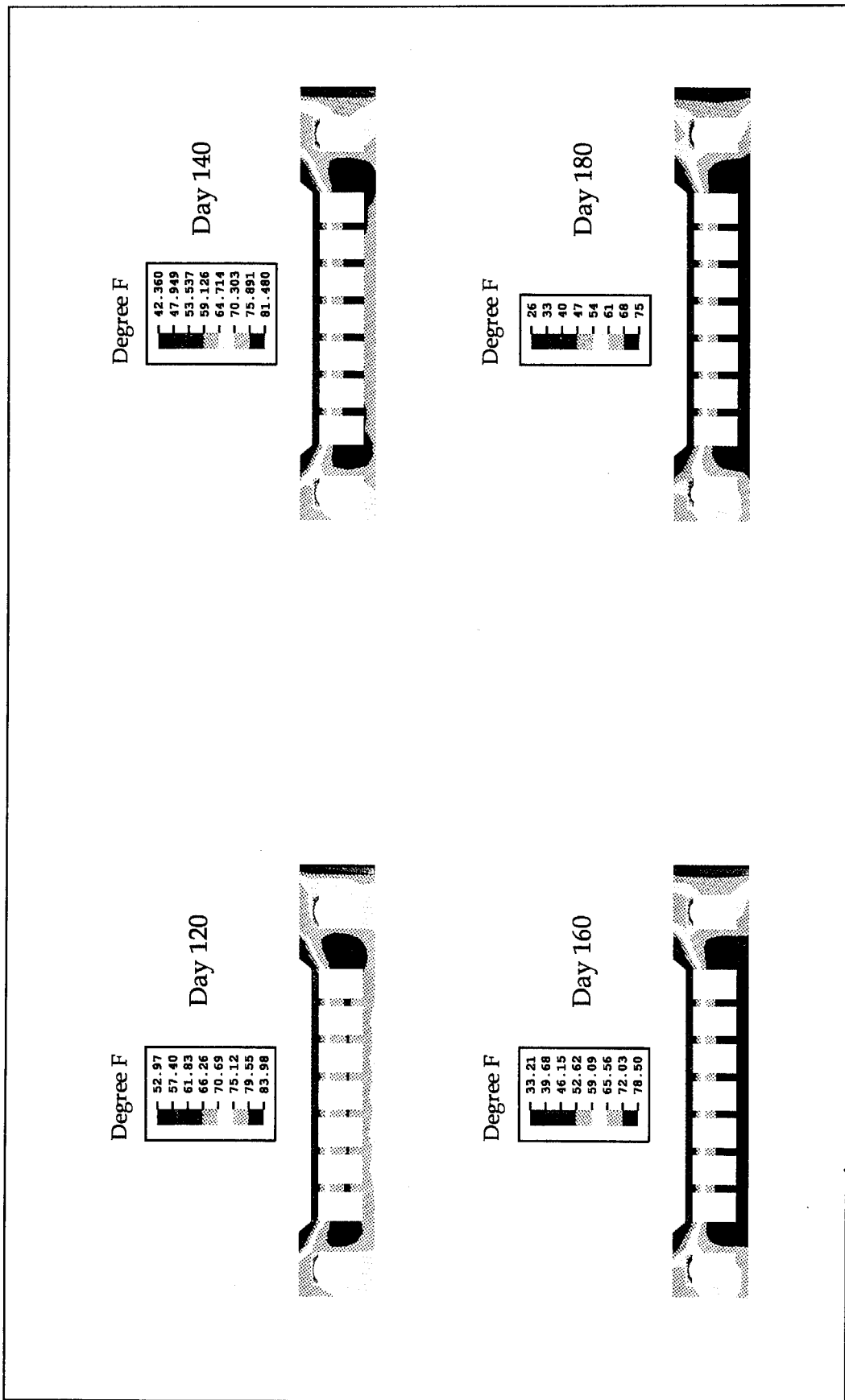


Figure 84. Composite slab thermal contours for transverse section

temperatures for the line of nodes along the center line of the top of the culverts were not saved in the post-processing file. These nodes were present in the thermal solution, and all temperatures are calculated correctly in the thermal solution. However, the temperatures for these nodes were not written to the post file and thus were set to zero when processed for plotting. These nodes are also given zero temperatures in the stress solution since the same file is used to transfer temperatures to the stress solution. However, by examining the stress solution, especially the cracking patterns, it is determined that this error does not influence or invalidate the extensive cracking seen in the analysis. This error was discovered after the stress analysis was underway, and it was decided to continue to meet the analysis deadline rather than rerun the analysis since bigger problems were in evidence. For Figures 83 and 84, the minimum temperatures are set to those shown in Figure 81 to illustrate the thermal gradients near the upstream edge and top of the slab. These figures show the effects of the pipe voids in cooling the interior region of the slab and pushing the thermal gradient more toward the top of the slab.

To better quantify the effect of the pipe voids, Figure 85 shows the distribution of temperature through the thickness of the slab for the four locations identified in Figure 80 for days 120, 140, 160, and 180. Figure 86 shows the corresponding temperature profiles at similar locations for the conventional slab design. Examining location P4 (in the middle of the chamber away from walls and free edges), the temperature on the bottom of the slab is reduced by approximately 7 °F and the peak temperatures are reduced by approximately 9 °F. The temperature is also about 2 °F colder on the top surface of the slab in the composite slab design, presumably because the top lift is only 3 ft thick compared with the 5-ft lift in the conventional design. In addition, the flattening of the gradient in the lower part of the slab can be seen in the composite design compared with the conventional design. Because of the void surfaces, the heat generated in the middle part of the slab is dissipated away from the bottom part of the slab. This causes the peak temperatures to occur higher up in the composite design which increases the gradient in the upper portion of the slab. For example, consider day 120 at location P4, the peak temperature occurs about 10.4 ft up into the slab (out of 28 ft) for the conventional design analysis and almost 13 ft up into the slab (out of 26 ft) for the composite slab design analysis.

Figure 87 shows temperature histories at selected points identified in Figure 79 for the composite slab design analysis. Each location shows the temperature history for a point in the middle of the bottom lift and for a point in the middle of the top lift compared with the ambient temperature. The double peaks at locations H1 and H2 are due to heat generated from the lifts forming the walls. The histories of the points in the top lift for locations H3 and H4 show a peak from internal heat of hydration after placement and then closely follow the ambient temperature with a slight lag time. Note that the effect of applying the sand insulation around day 80 is only just discernible at this depth in the top slab. The change in slope of the temperature history in the bottom lift when the top lift is placed is due

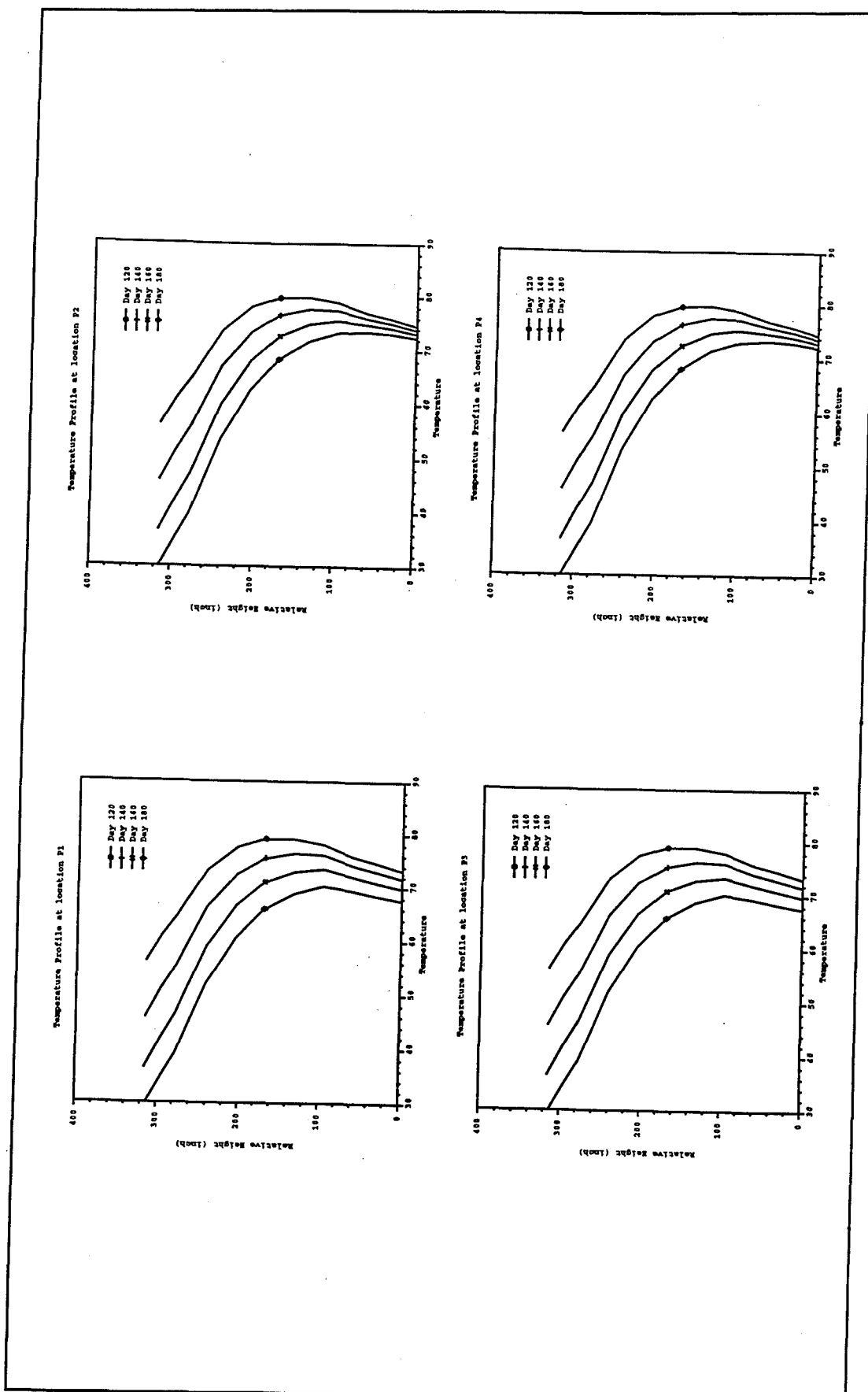


Figure 85. Composite slab temperature profiles

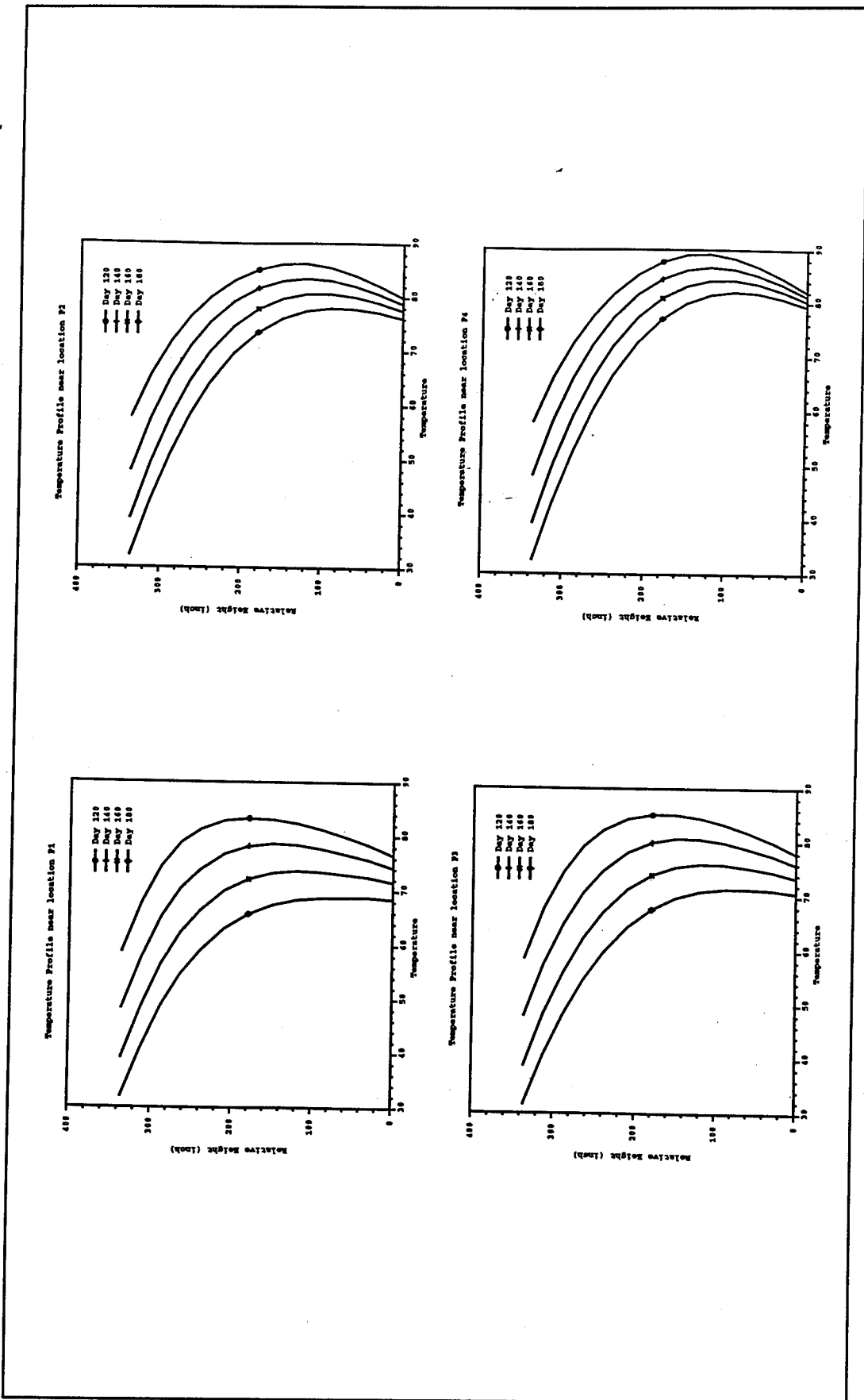


Figure 86. Conventional slab temperature profiles

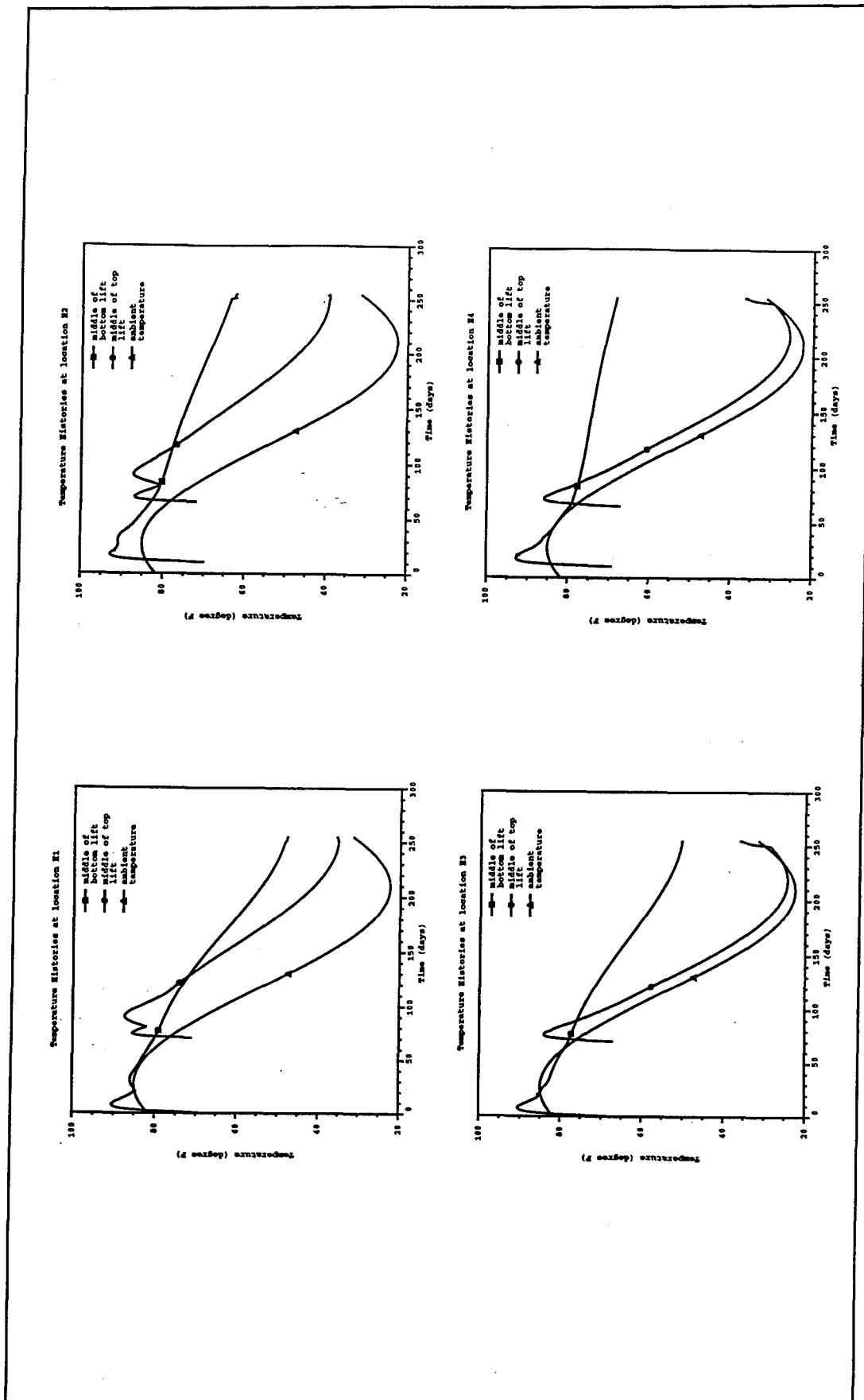


Figure 87. Composite slab temperature histories

to the closing of the pipe voids, which removes further heat loss through the void surface area.

## Conclusions

The intent of the composite slab design is to reduce the potential for thermal-induced cracking during construction by reducing the thermal gradients within the slab. The vertically oriented sections of corrugated steel pipe placed at intervals within the slab region reduce the volume of heat-generating concrete and provide surface area for transferring heat to the ambient temperature during construction of the slab. Under the assumed construction conditions, this composite slab design succeeded in reducing the peak temperatures by about 10 °F within the slab. Since the temperature of the top surface of the slab, lightly insulated with moist sand, is controlled by the ambient temperature, this should correspondingly reduce the overall gradient in the slab. However, the additional heat transfer through the pipe surface area, which continues until the top lift is placed, creates a more uniform temperature distribution in the base of the slab and pushes the peak temperature within the slab toward the top of the slab. This creates a relatively high thermal gradient in the top half of the composite slab and is similar to that found in the conventional design analysis. The composite design was also conservatively modeled in this analysis without any credit for the structural characteristics of the steel pipe. From the single cell analysis, the model of the composite design is approximately 30 percent more susceptible to cracking than the conventional design. Thus, the composite design is subjected to approximately the same thermal gradient in the top portion of the slab and is less tolerant to cracking. This combination is the main cause for the extensive cracking found in the analysis. Also contributing to the extensive cracking is the lift placement sequence for the composite design. Because the pipe voids reduced the volume of concrete, the number of lifts in the slab could be reduced, and the top lift for the slab was placed 15 days earlier in the composite design. For the assumed start date, this translates into an increase of approximately 8 °F in the reference temperature for the top lift. Thus, for a given colder ambient temperature, the top of the composite slab develops approximately 30 micro strains of additional thermal strain compared with the conventional design. This effect will be more significant for colder weather and is credited for the continued extensive cracking later in the analysis.

The composite slab design for massive concrete structures has a potential for reducing construction costs by eliminating substantial concrete volume without the need for extensive formwork. Thus, the following recommendations are provided for defining better construction parameters and modeling to further investigate the constructability of the monolith using a composite slab design.

- a. The peak temperatures within the slab are reduced by the pipe voids. The surface temperatures are still controlled by the ambient temperature. Insulation with the highest practical R rating, around  $R = 20$ , should be placed on all free surfaces of the slab after the top slab is placed. The surest way to reduce the thermal gradient within the slab is to keep the surface temperature as high as possible during the cold weather. For construction costs, high R-value insulation has been avoided in these analyses. However, it seems clear that, for this monolith and assumed start date, heavy insulation will be required.
- b. Venting of the voids with either an active or passive cooling system after the top of the slab is placed should be considered. This will continue to remove internal heat thereby reducing the thermal gradient.
- c. Requiring a placement temperature of  $50^{\circ}\text{F}$  instead of  $60^{\circ}\text{F}$  for the top lift of the slab will lower the reference temperature of the top of the slab and reduce thermal stress.
- d. The placements for the top of the slab should be delayed for 15 to 30 days. This also reduces the reference temperature in the top of the slab as mentioned above by placing it at a lower ambient temperature. Waiting 30 days will provide an ambient of about  $54^{\circ}\text{F}$  for the initial lift forming the top of the slab. In addition, this allows the interior of the slab to continue cooling through the surfaces of the pipe voids.
- e. The effects of the above recommendations can be investigated through a quarter-model study to determine the relative gain versus construction costs. Examination of the plan view thermal contours, Figures 81 and 82, shows that a transverse cut halfway before the sill ( $j = 123$  in Figure 80) intersects the contours at right angles. Thus using insulated conditions on this cut and modeling the upstream portion in a quarter-symmetric thermal study will provide a good simulation of the thermal response. The best combination for reducing thermal gradients can then be applied to the half-symmetric model to conduct the full thermal-cracking analysis.
- f. The unknown factor for recommendation *d.* above is the effect on global response of the structure for the partially completed slab that can only be determined by the stress solution. Recall that the 10-day placement increment study in the 2D analyses caused substantial cracking under the culverts due to the bending response of the “notched beam” cross section. Waiting 30 days for placement of the top of the slab may cause cracking under the culverts before the full slab cross section is available for resisting the thermal-induced bending deformation.

- g. Finally, for the composite slab design analysis, a recommendation is in order to further investigate the structural model used for the corrugated pipe construction. The initial effort used the conservative approach to ignore any structural credit for the corrugated steel pipe. This was done in the absence of detailing information for this new design to speed the modeling effort.
- h. As a fall-back position and to further the understanding of the constructability of these massive concrete structures, it is also recommended that the conventional slab design be modified and re-analyzed. The geometry changes in the culvert location and slab thickness should be incorporated into the conventional design model and analyzed using the R-20 insulation on free surfaces of the slab after the top of the slab is placed. This should reduce the thermal gradient enough in this construction scenario to prevent the cracking predicted for this design. If construction costs for using the corrugated steel pipe in the composite design escalate for some reason and exceed the savings for the reduced volume of concrete, a fall-back position will be available.

# 8 Three-Dimensional Parametric Heat Transfer Study

---

## General

As discussed in Chapter 7, the cracking which the analysis showed occurring in the base slab was attributed primarily to the thermal gradient occurring at the exposed faces of the base slab. Through discussions it was agreed that the best way to eliminate the problem was to provide insulation with a high insulating value to keep the surface temperatures from dropping too low or to vent the cells in the slab to reduce the temperature in the middle of the slab. Other items considered as mentioned in Chapter 7 were to use a placing temperature of 50 °F and to delay placement of the top lifts of the base slab for 15 to 30 days instead of 5 days. The final plan of action for performing the 3D parametric heat transfer study is discussed below.

## Parameters of the Study

In order to determine the best solution to the extensive cracking problem and to evaluate results in the quickest possible manner, five different plans with varying parameters were developed for the performance of heat transfer analyses only. In addition, to expedite the analyses even further it was agreed that a quarter-model of the monolith could be used in the evaluation as discussed in the conclusions of Chapter 7. Using the thermal gradients produced from these analyses on the quarter-model a decision could then be made as to which plan would be the most beneficial in reducing the gradient at the surface of the base slab and a full-scale NISA could be performed on the half-model used in the previous analysis (discussed in Chapter 7).

The five plans used the recommendations stated in Chapter 7 as well as combinations of those recommendations. The five plans selected were:

- Plan A Add insulation to exposed surfaces on both the top and sides of the base slab at a value of  $R = 20$ . Insulation will be applied at day 110 after the start of construction.
- Plan B Ventilate the cells in the base slab after the top lift is placed. A film coefficient of  $h = 0.2 \text{ Btu/day-in.}^2 \cdot {}^{\circ}\text{F}$  is to be applied to the walls of the cylinders.
- Plan C Concrete will be placed at  $50 \text{ }^{\circ}\text{F}$ .
- Plan D Use parameters from both Plans A and B; i.e. insulate base slab surfaces to  $R = 20$  and ventilate the cylinders in the slab.
- Plan E Use parameters from Plans A, B, and C; i.e. insulate base slab surfaces to  $R = 20$ , ventilate the cylinders in the slab, and place the concrete at  $50 \text{ }^{\circ}\text{F}$ .

In addition, a 30-day placing interval was imposed on the placing of the last three lifts of the base slab which forms the tops of the culverts and the cylinders. A 5-day interval was used for all other lift placements.

The quarter-model used in the analyses discussed in this chapter is shown in Figure 88. The finite element mesh was developed by simply eliminating the elements downstream of a line which bisects the fourth row of cylinders from the upstream edge of the monolith. As with the center-line boundary in the center wall, an adiabatic condition was placed on this new line of symmetry as well. Except for the changes noted in the discussion earlier, all other parameters of the analyses will remain the same as were used before.

## Results of Analyses

Results of the parametric heat transfer study are presented in Figures 89-91. The figures show temperature contours at days 120 (Figure 89), 140 (Figure 90) and 170 (Figure 91) for a longitudinal section down the center line of the chamber. The longitudinal sections provide sufficient information with respect to the thermal gradients which occur both at the top of the slab and at the upstream edge of the slab to determine which plan will provide the necessary benefits. Also, since the previous analyses showed that the cracking began around day 130 then results through day 170 should be sufficient for making a determination as to which of the proposed plans would provide the necessary benefits. It should be noted that the plots in Figures 89-91 also show the foundation elements of the finite element mesh, but since the temperatures were not saved for the foundation no contours are shown in this portion of the grid.

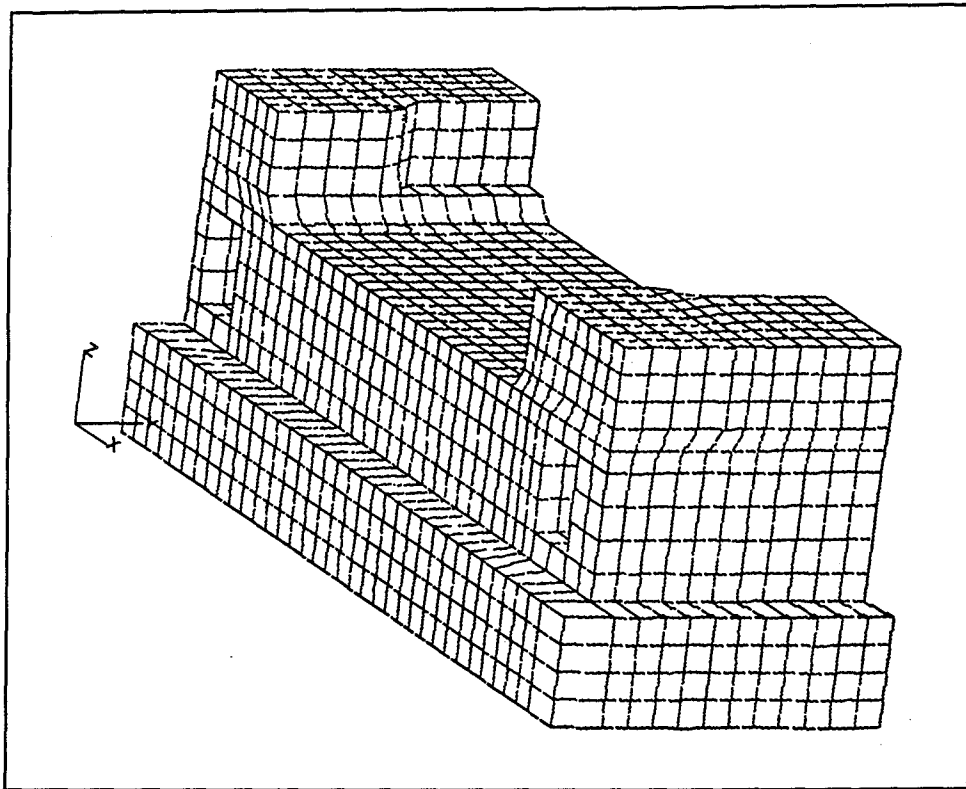


Figure 88. Finite element mesh for quarter-model

This is also the reason there appears to be a very steep gradient below the base of the structure.

The plots shown in Figure 89 are taken at day 120 of the analysis. Even though day 120 is only 10 days after insulation is added and ventilation started, differences in the five analyses are already evident. Plan A at day 120 (Figure 89(a)) shows that a fairly even gradient exists through the slab and at the upstream face and that the temperature differential from top to bottom of the slab is only about 12 °F. Plan B at day 120 (Figure 89(b)) shows that through most of the slab the temperatures are moderated significantly but a gradient of approximately 8 °F exists through the bottom 5 ft of the slab. Plan C at day 120 (Figure 89(c)) is very similar to Plan A at day 120 except a fairly steep gradient exists at the upstream face of the monolith. Plans D and E at day 120 (Figures 89(d) and 89(e), respectively) are nearly identical to each other and are both very similar to Plan B at day 120.

At day 120 the thermal gradients for all five plans are not very severe. This can be attributed primarily to the 30-day placement interval used for the top lift and because the ambient temperature is only about 58 °F at day 120. The one concern that does surface at day 120 is the gradient which occurs in the bottom lift for the plans which include ventilation.

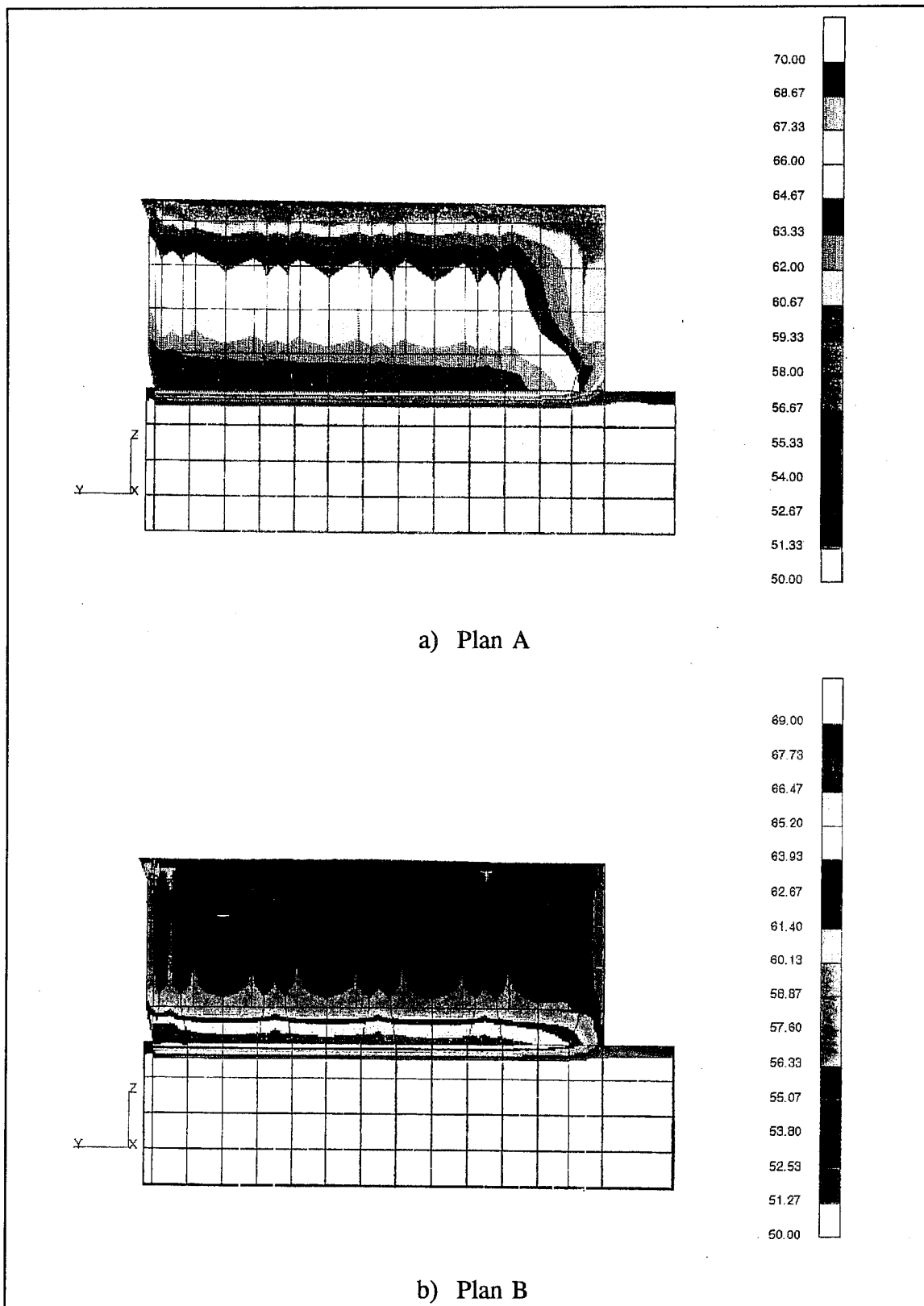


Figure 89. Temperature contours, day 120, at the center line of the lock chamber  
(Sheet 1 of 3)

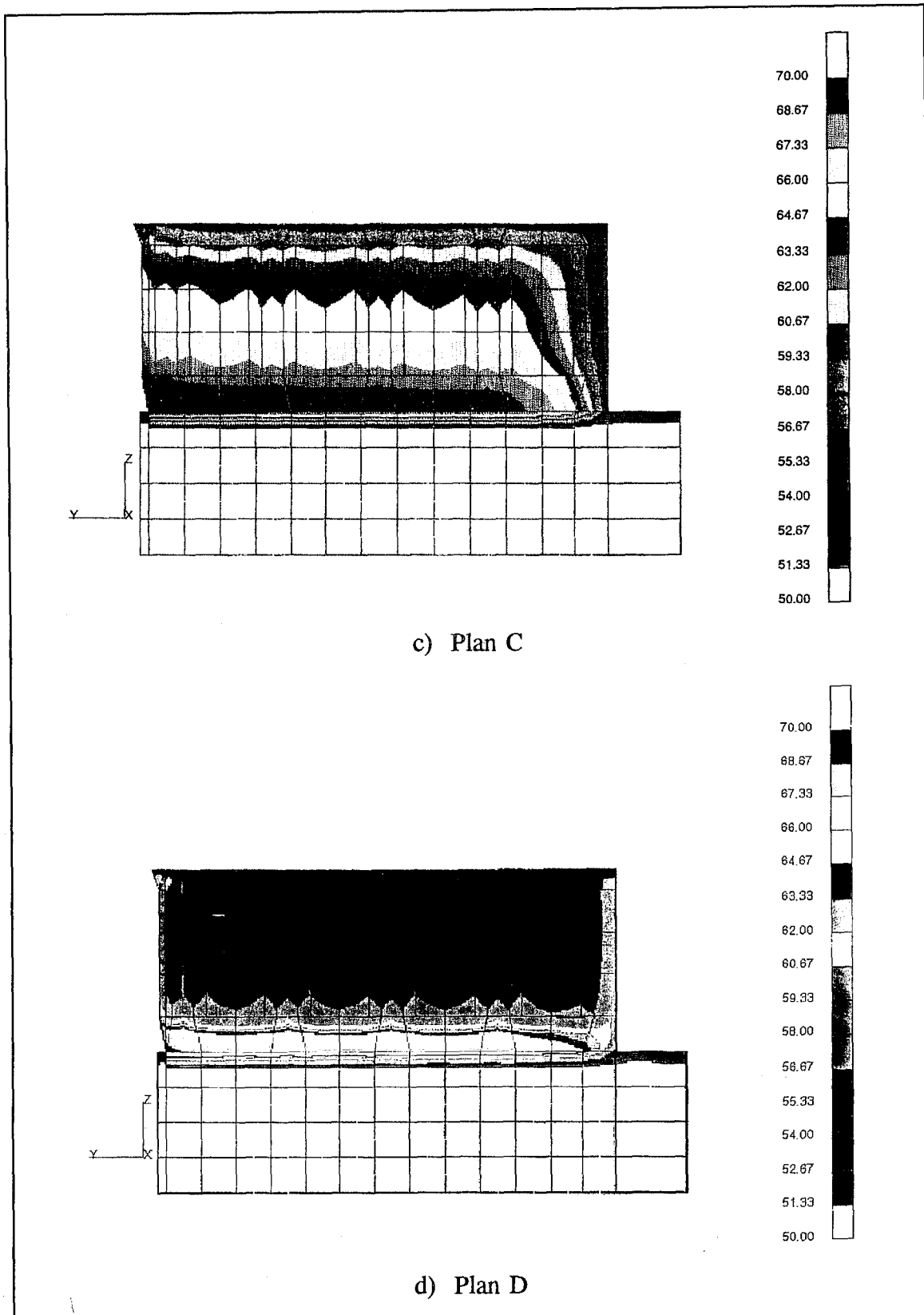


Figure 89. (Sheet 2 of 3)

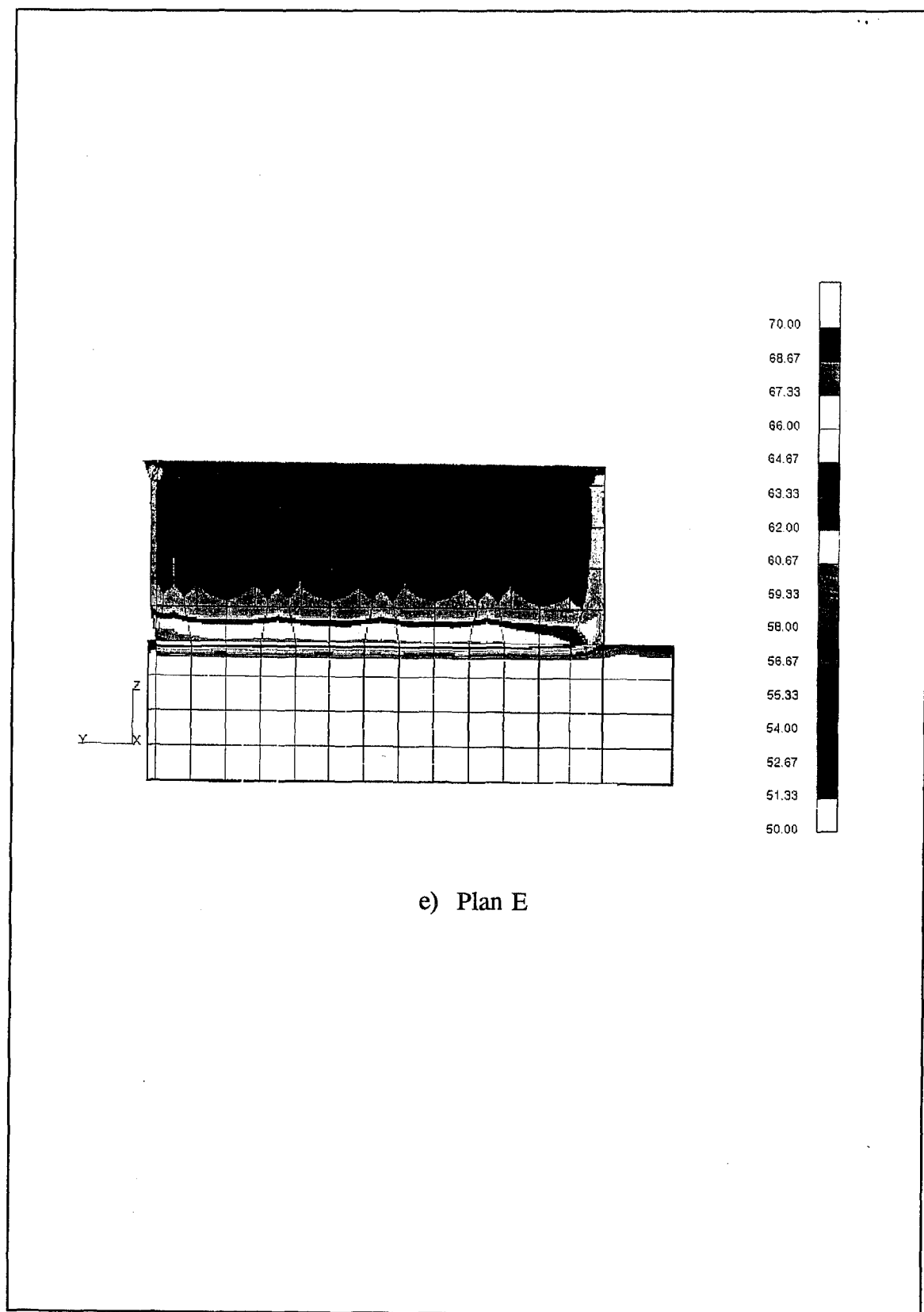


Figure 89. (Sheet 3 of 3)

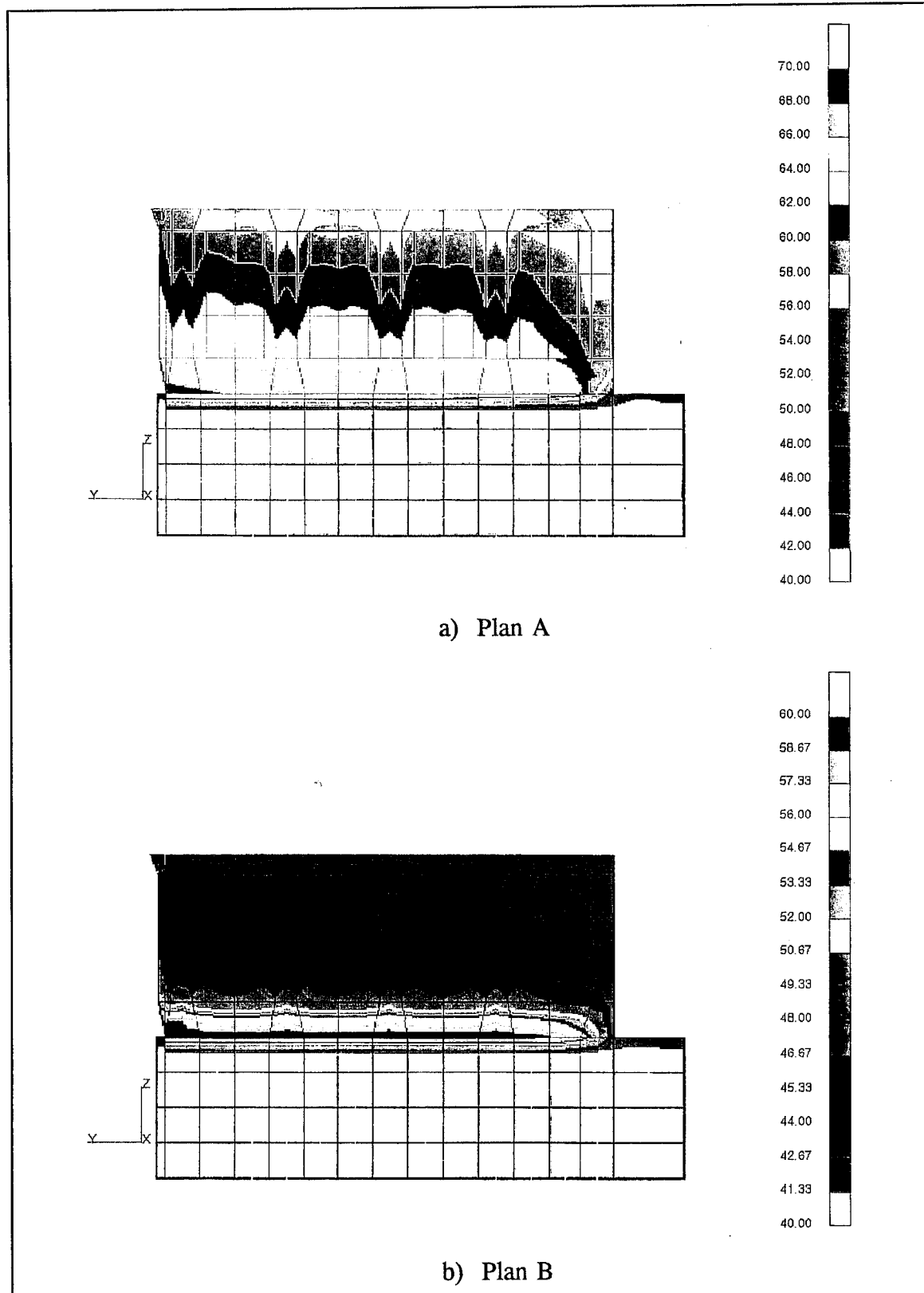


Figure 90. Temperature contours, day 140, at the center line of the lock chamber  
(Sheet 1 of 3)

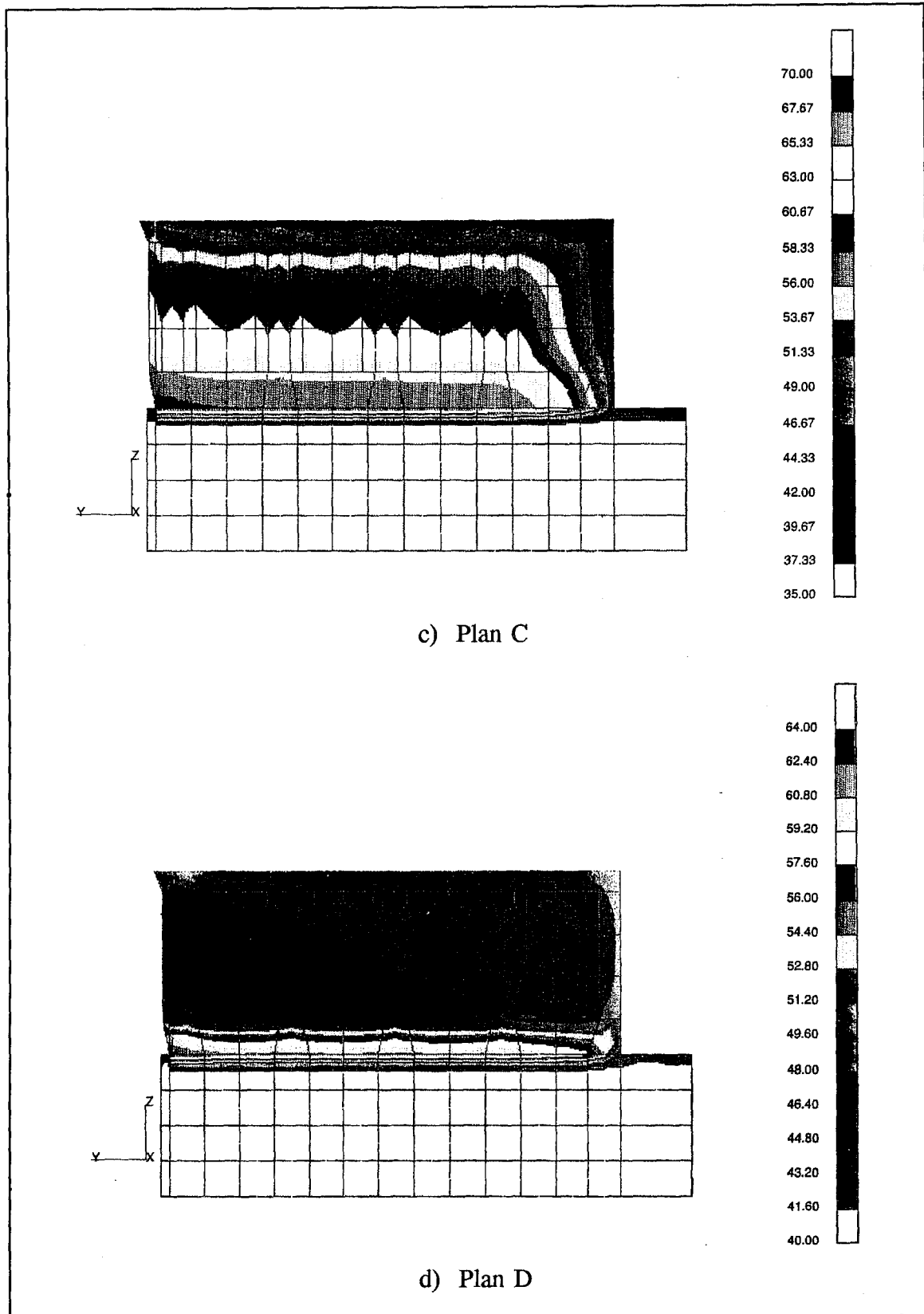


Figure 90. (Sheet 2 of 3)

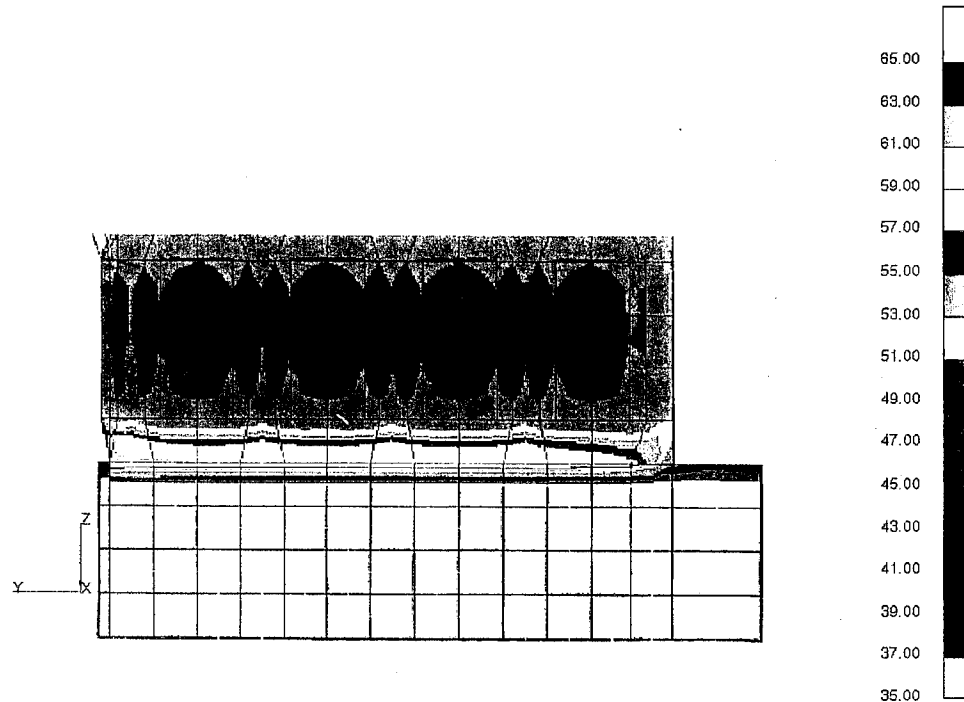


Figure 90. (Sheet 3 of 3)

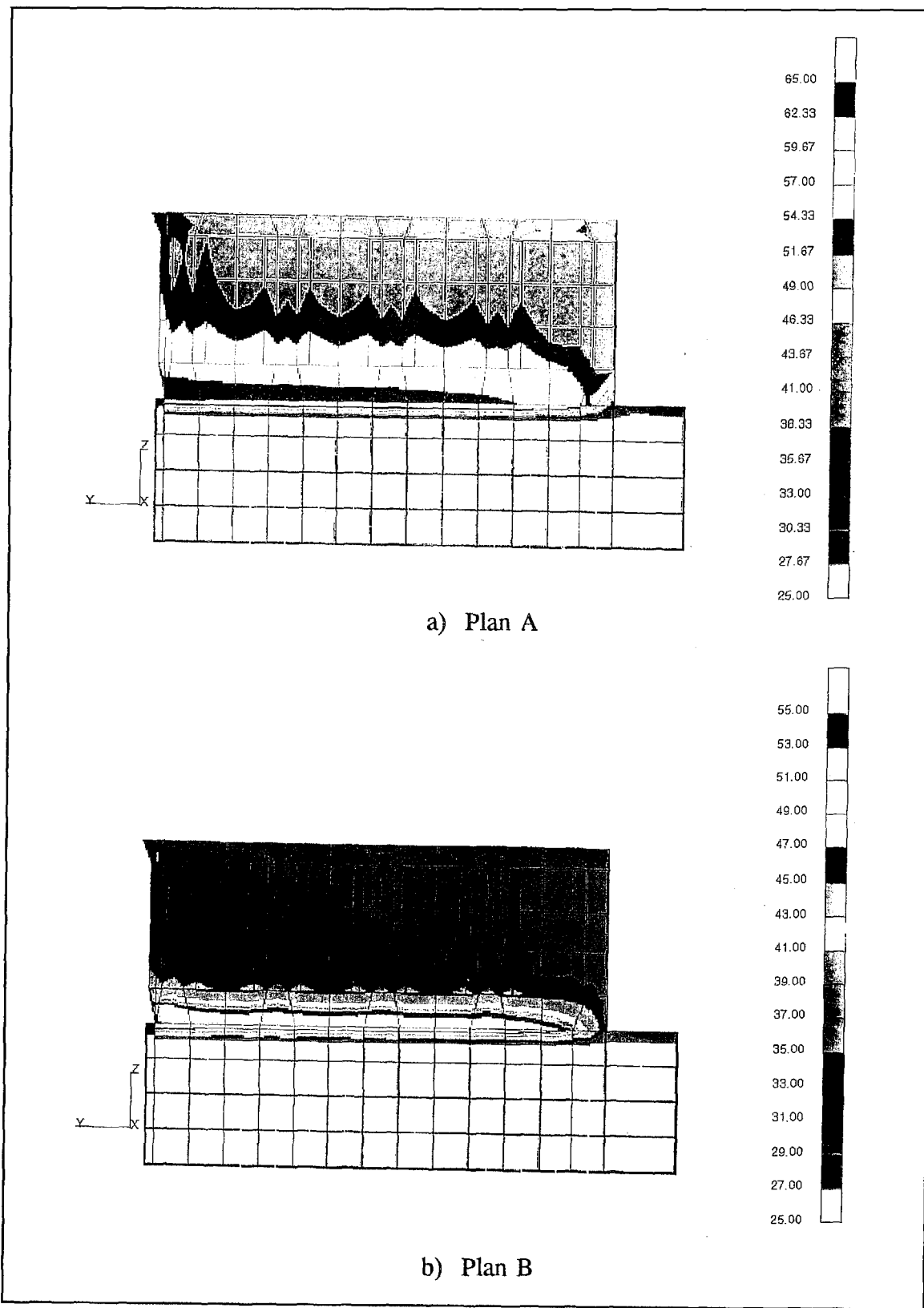


Figure 91. Temperature contours, day 170, at the center line of the lock chamber  
(Sheet 1 of 3)

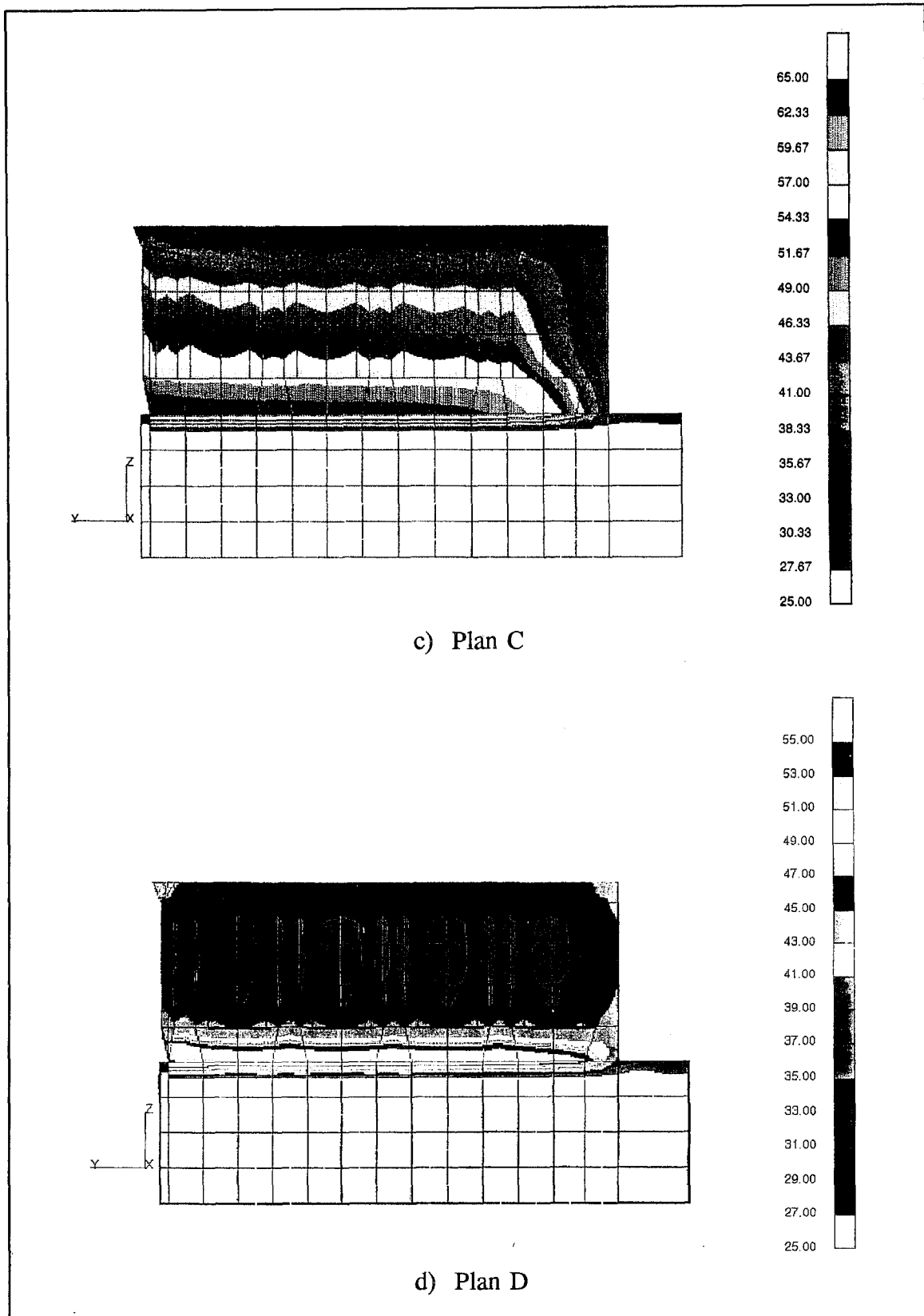


Figure 91. (Sheet 2 of 3)

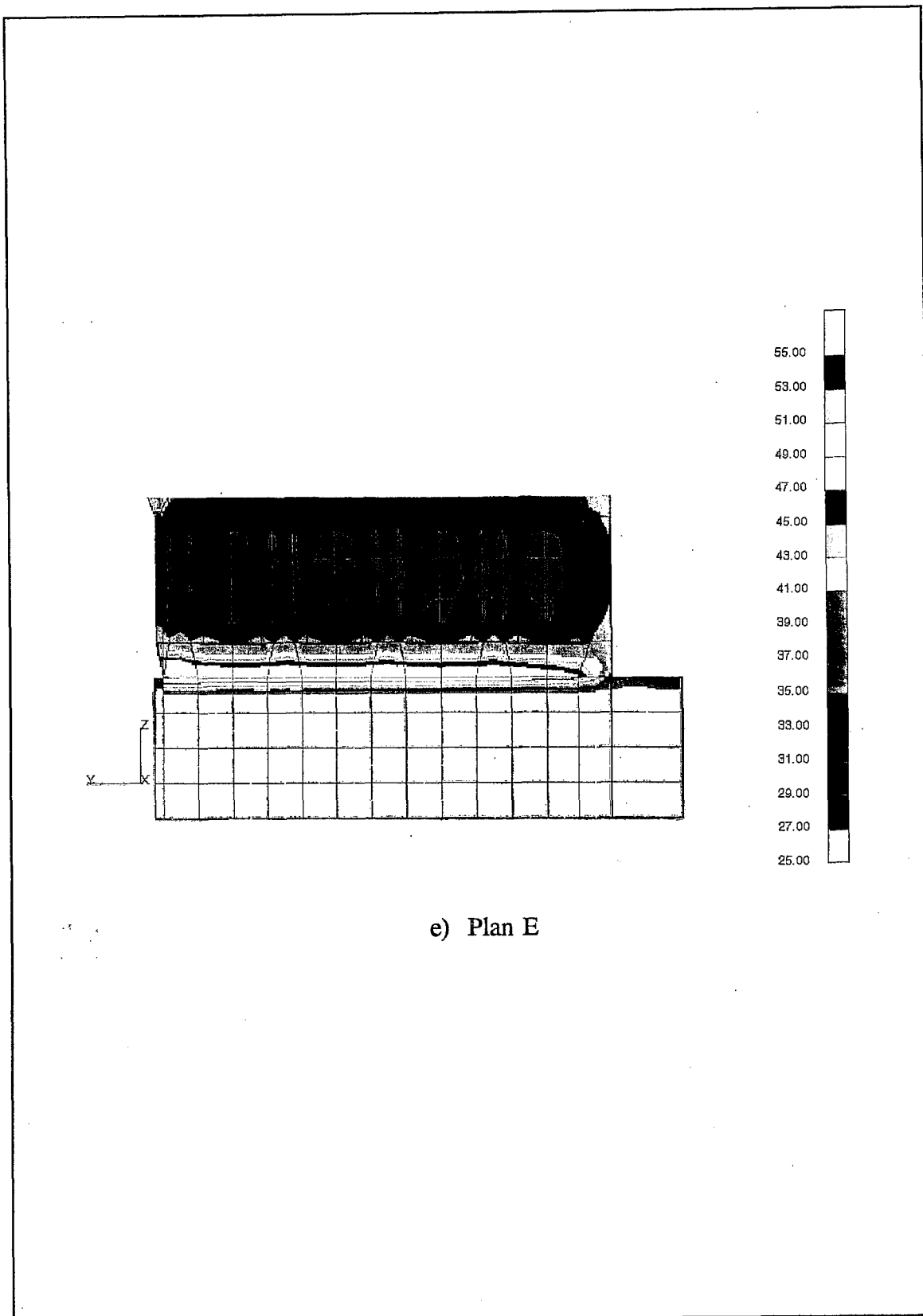


Figure 91. (Sheet 3 of 3)

Results at day 140 of the analyses are shown in Figure 90. Plan A at day 140 (Figure 90(a)) shows a very even gradient through the slab thickness and at the upstream face of the monolith. The overall temperature difference is 12 °F, which is the same difference observed at day 120. As at day 120, Plan B at day 140 (Figure 90(b)) shows very constant temperatures within the major portion of the slab but a gradient in the bottom lift. This gradient in the bottom lift has increased from 8 °F at day 120 to approximately 10 °F at day 140. Plan C at day 140 (Figure 90(c)) is beginning to exhibit large gradients vertically (20+ °F) and horizontally (15-20 °F). At 140 days, Plans D and E (Figures 90(d) and 90(e), respectively) are again nearly identical and approach the behavior seen in Plan B.

The only plan in which gradients are beginning to get high is in Plan C which was anticipated since the only differences from the previous analysis are the placing temperature and the delay in placement of the top lift. Overall gradients remain low for the other plans but the gradient in the bottom lift for the plans with ventilation is increasing.

Day 170 results are presented in Figure 91. As at days 120 and 140, day 170 of Plan A (Figure 91(a)) shows that the gradient through the slab remains low (14 °F) and fairly evenly distributed. As at the previous times shown, Plans B, D, and E at day 170 (Figures 91(b), 91(d) and 91(e), respectively) are all very similar. As before, a very constant temperature exists through a large portion of the base slab and the gradient in the bottom lift has increased to 16 °F at day 170. Finally, Plan C at 170 days (Figure 91(c)) exhibits large gradients in the vertical and horizontal directions.

The trends which occurred between day 120 and day 140 continue between day 140 and day 170. The items of note are that overall gradients for Plan C are becoming high and that the gradients in the bottom lift for the ventilated cases are also increasing to larger than desired values.

## Conclusions

Based on the results presented it became apparent that Plan A was the most desirable case for achieving the desired objective. The overall gradient through the slab remained low for Plan A and was uniform as well. In addition, the gradient at the front of the slab was also low.

Plans B, D, and E also achieved the objective of lowering the gradient at the top and upstream faces of the base slab. The problem with these three plans was that they also introduced an undesirable gradient through the bottom lift. While this gradient was not as severe as some of the gradients seen at the surface of the previous analysis (reference Chapter 7), there was concern that the gradient was high enough to create a problem at the bottom of the slab.

Plan C provided the least benefit of the five plans, although all of the effects of Plan C cannot be ascertained in a heat transfer analysis since the lower placing temperature modeled in Plan C will result in a lower stress-free reference temperature. The lower stress-free temperature should produce benefits in the stress analysis but it was felt that there would still be a cracking problem if Plan C were used.

Therefore, Plan A was the selected plan and will be the plan used for the full NISA of the half-model used in the previous analysis. Since the half-model will be used, the heat transfer analysis will need to be performed again to provide the necessary temperatures for the stress analysis. Some additional items will also change for the analysis of the half-model. A decision was made to increase the thickness of the top lift from 3 ft to 4 ft to provide a section with a higher structural load-carrying capacity. Also, the exposed foundation is to be insulated with the  $R = 20$  insulation. The effect of not having the foundation insulated can be seen by looking at the bottom, upstream corner of the plots of the insulated cases (Plans A, D, and E).

# 9 Analysis of Heavily Insulated Floor

---

## Analysis Parameters

Based on the quarter-grid heat transfer analyses, a new analysis was proposed for the half-grid model with voids used in Chapter 7. Modifications for this analysis are listed below.

- a. Placement of the top floor level (lifts 13, 14, and 15) was delayed until 30 days after the final placement of the preceding level. This allowed the floor lifts already in place to cool to near ambient temperature prior to placing the top level and sealing the cylindrical voids.
- b. Fifteen days after placement of lift 15 the entire floor with the exception of the area under the sill was insulated using an R value of 20 hr·ft<sup>2</sup>·°F/Btu. This insulation was also applied to the exposed sides of the floor. Five days after placement of the sill, the sill and surrounding walls to el 261 were insulated. The purpose of this insulation was to allow cooling to take place at a gradual and consistent rate throughout the floor, resulting in lower temperature gradients. The area of insulation is shown in Figure 92.
- c. In previous analyses, a film coefficient of 0.01 Btu/day·in.<sup>2</sup>·°F was used to model convection on the inside faces of closed openings. However, this was larger than the convection coefficient for the insulated floor surfaces. Therefore, the film coefficient for insulated floor surfaces was also used in all closed voids in the floor. The film coefficient for insulated floor surfaces was

$$h = \frac{1}{\frac{1}{h_a} + R_{insul}} = 0.008 \text{ Btu/in.}^2 \text{ - day - } ^\circ\text{F}$$

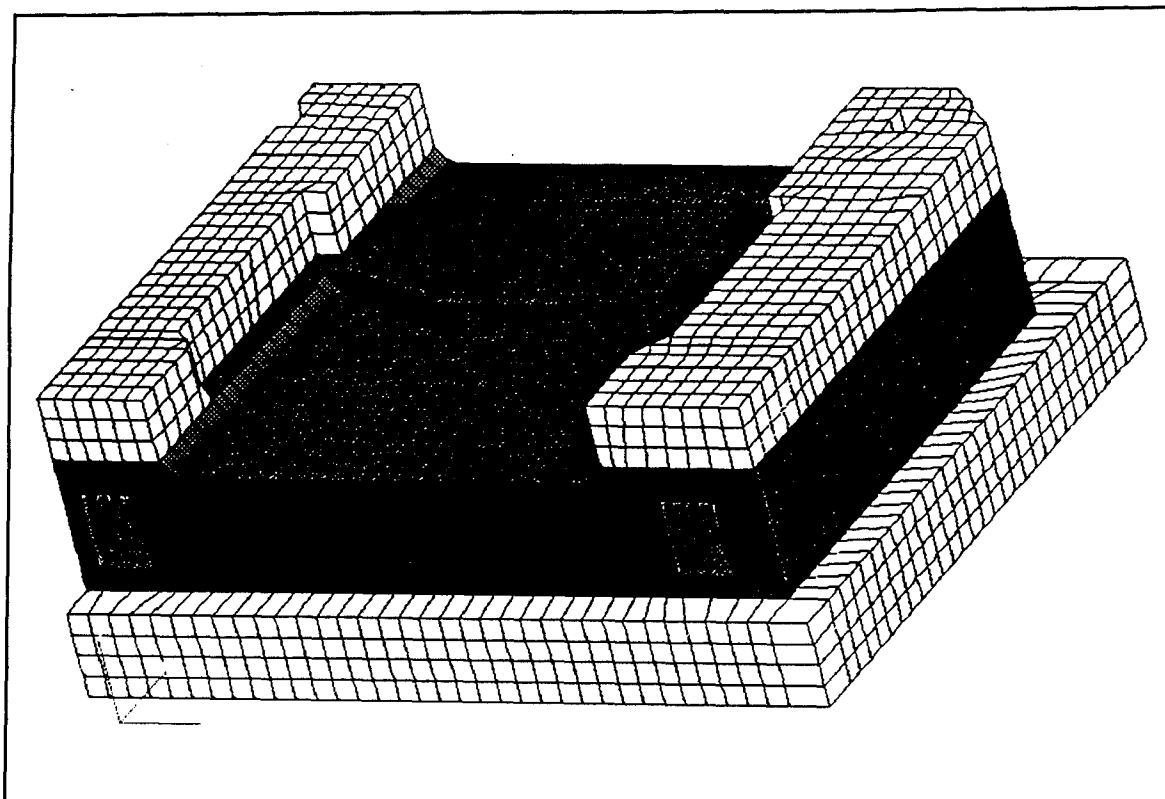


Figure 92. Area of floor insulation

Significant milestones in the heat transfer analysis are listed in Table 5 below. The complete lift placement sequence is shown in Appendix B.

**Table 5**  
**Heat Transfer Analysis Milestones**

Day	Event
55	Last floor lift placement prior to 30-day delay for top floor level
85	Lift 13 placed (downstream section of top lift)
90	Lift 14 placed (center section of top lift)
95	Lift 15 placed (upstream section of top lift)
110	Floor insulated with $R = 20$
120	Sill placed
125	Sill insulated with $R = 20$
145	Walls insulated with $R = 2$
175	First wall insulation removed
210	Last wall insulation removed
255	Insulation removed, flooded with water

## Analysis Results

The combination of early cooling due to cylindrical voids and culvert openings in the floor and delayed placement of the top floor lifts reduced temperatures throughout most of the floor to near ambient by day 85.

After placement of the top floor level, the insulation allowed only gradual heat loss, resulting in much smaller temperature gradients than those seen in previous analyses. The result of this reduction in thermal gradients was that only minor cracking occurred in the monolith floor.

### Thermal results

Temperature contours at the top of the bottom floor level (el 235), the top of the floor (el 257) and at the transverse and longitudinal sections shown in Figure 80 are presented in Figures 93 through 96. Temperature contours on day 90, immediately prior to the placement of lift 14, are shown in Figure 93. Ambient temperature at this time was approximately 68 °F. Temperatures in the floor, except at thick sections around culverts, varied from 68 °F at the top of the floor to 74 °F at the base. At the downstream side of the floor, where cylindrical voids were sealed by the cross-over gallery, the floor remained at a higher temperature. In this area, temperatures at the base ranged from 76 °F to 85 °F.

Temperature contours on day 120, just prior to the placement of the sill and 10 days after placement of the floor insulation, are shown in Figure 94. Temperatures throughout the floor were fairly uniform by this time except at the thick inside walls of the culverts and in the exposed section of floor where the sill would be placed. Temperatures throughout the area cooled by voids ranged from 71 °F at the base to about 67 °F at the top, with minimum temperatures approximately 14 °F above ambient. Temperatures in areas without floor voids were as high as 73 °F at the base and 66 °F at el 257. The cooler temperatures in the uninsulated area can be seen in the contours at el 257 and in the longitudinal section. The isolated warm spots that occur in areas without floor voids can be seen in the plan at el 235 and in the transverse section.

By 180 days, the minimum temperature in the floor was approximately 50 °F, 24 °F above the ambient temperature. Temperatures in the areas with floor voids can be seen in the longitudinal section of Figure 95, and were approximately 64 °F at the base and 50 °F at the top of the floor. Even in the areas without voids, temperature gradients were less than 25 °F as can be seen in the transverse section of Figure 95. In Figure 83 from the previous analysis, temperature gradients across the floor at 180 days are greater than 40 °F. The longitudinal section also shows that the downstream side of the monolith is several degrees warmer than the upstream side. This is due to the thicker section at the sill, the early closing of the voids at the downstream side, and the thick section of concrete between the culvert and the crossover gallery.

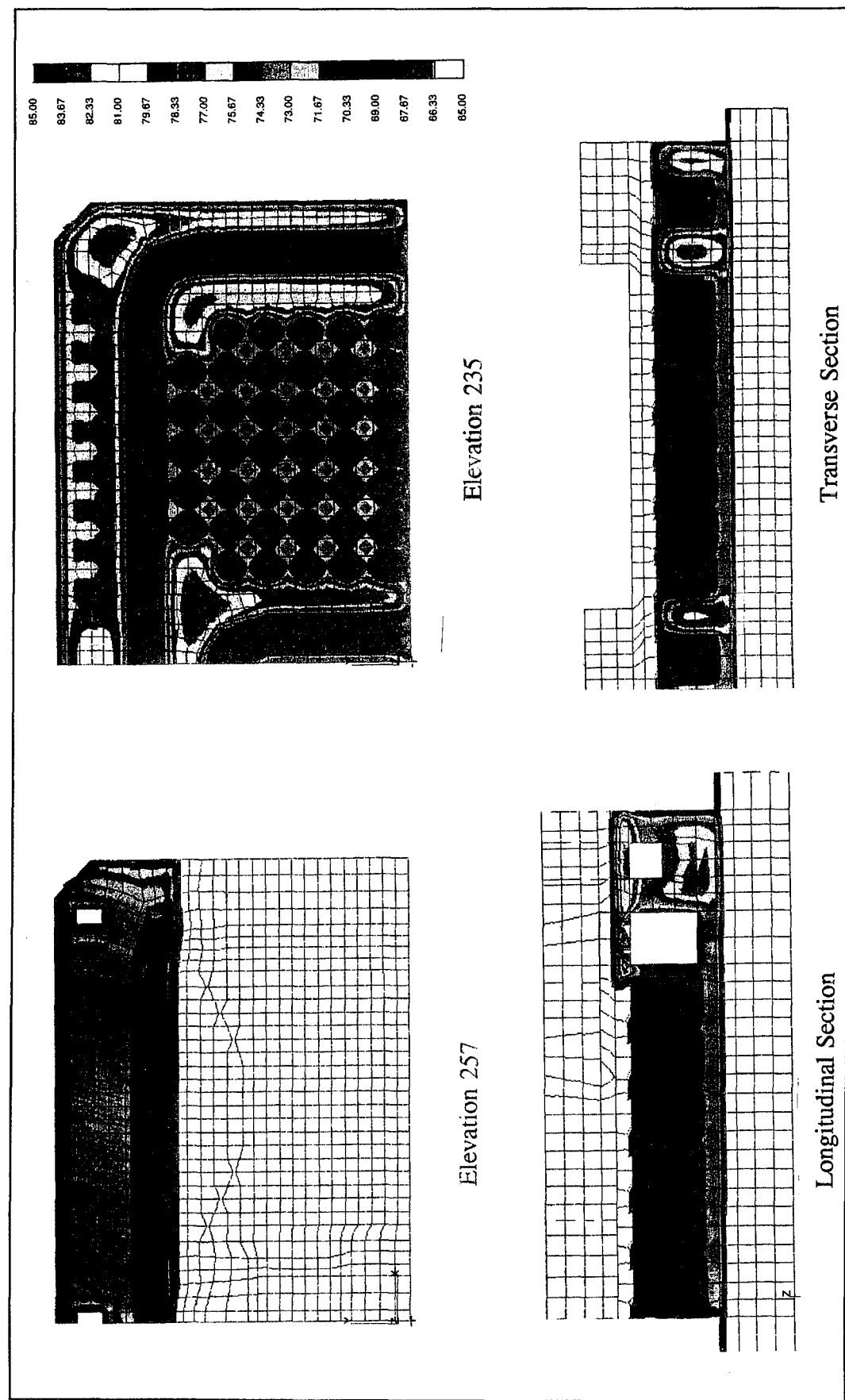


Figure 93. Temperature contours, day 90

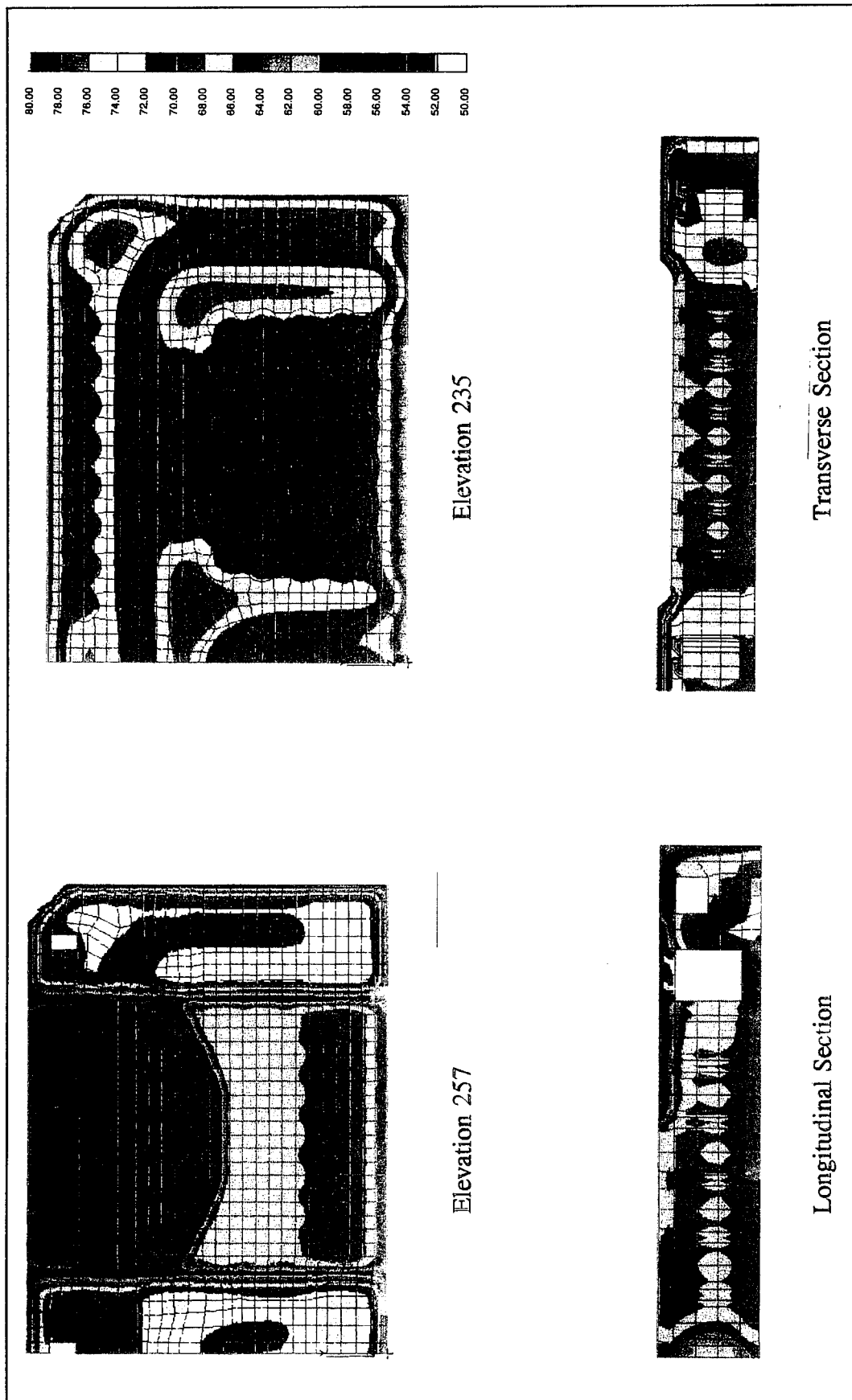


Figure 94. Temperature contours, day 120

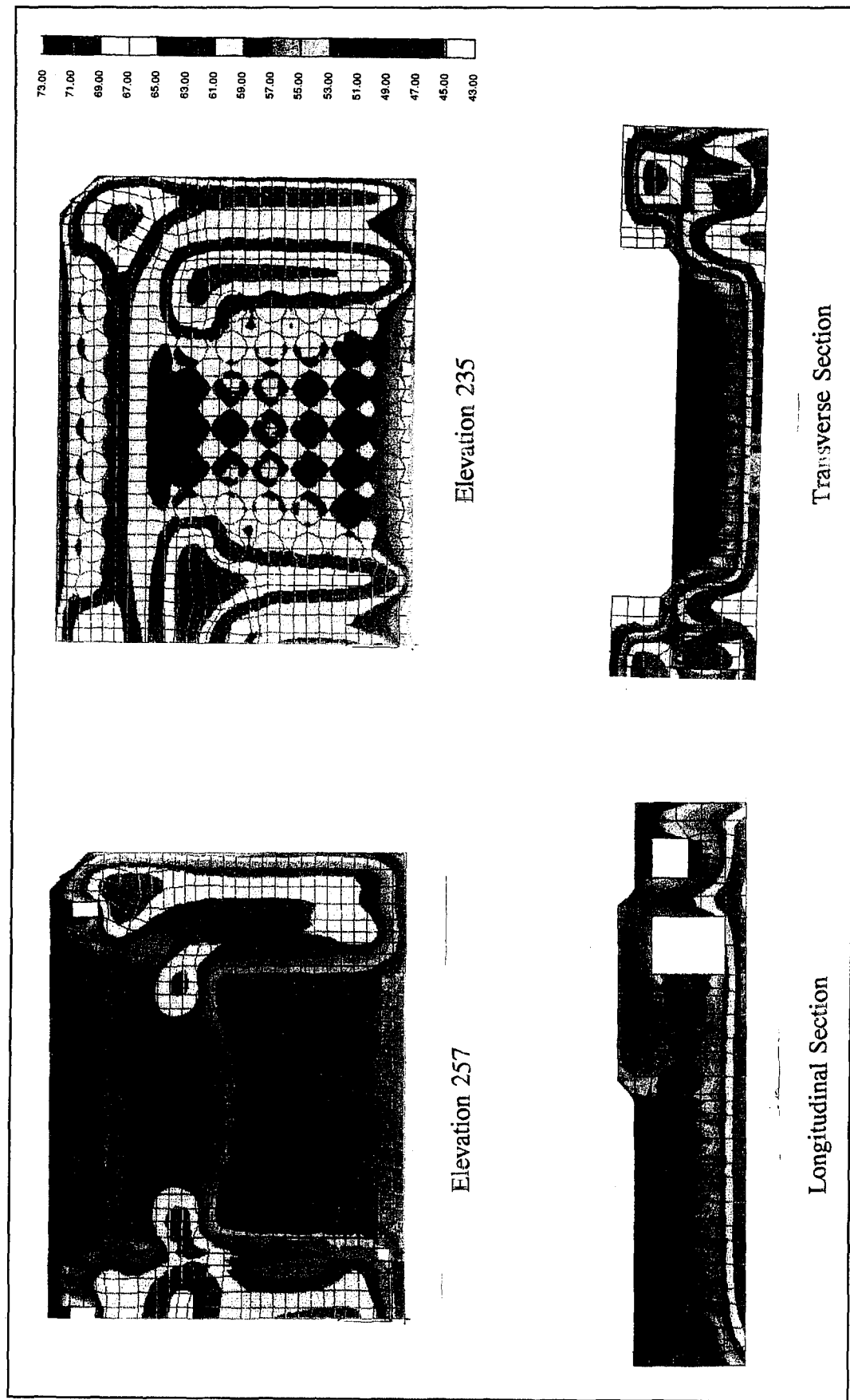


Figure 95. Temperature contours, day 180

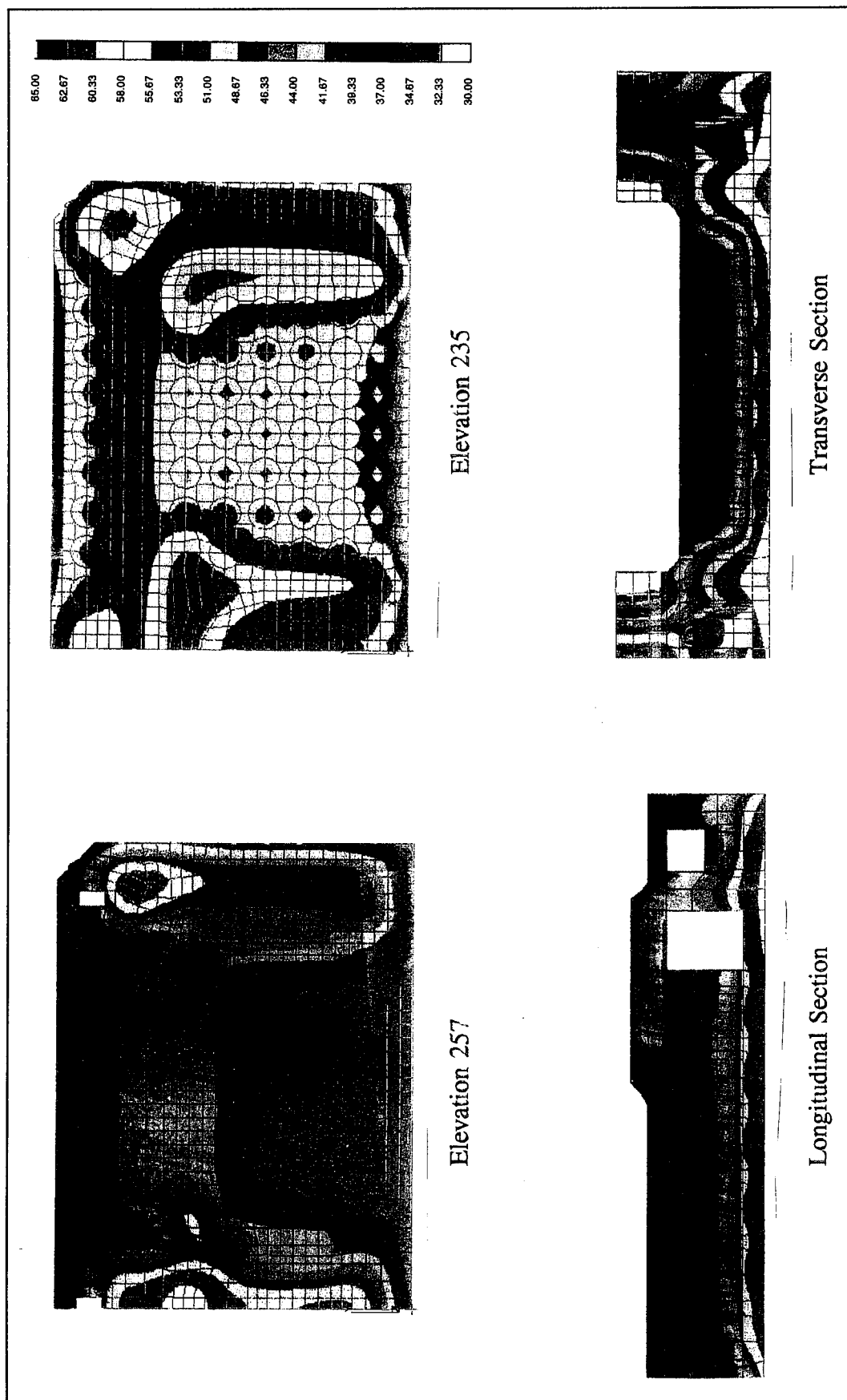


Figure 96. Temperature contours, day 255

By day 255, the minimum temperature at the top of the floor was approximately 35 °F, only slightly above the ambient temperature of 32 °F. However, because of the insulation, the cooling of the floor was accomplished gradually and maximum vertical floor gradients shown in the longitudinal section of Figure 96 were only about 20 °F to 25 °F. Vertical temperature gradients were distributed across the entire floor section, with a maximum vertical gradient in the bottom lift of only 5 °F.

Temperature gradients across the floor can be seen more clearly in Figures 97 through 100. Figures 97 and 98 consist of temperatures across the section at four locations in the floor at four times: 120, 140, 160, and 180 days. The four locations are shown in Figure 80. These points are all located at the inside face of cylindrical voids, and the temperature profiles for all were similar at a given time. In each, the maximum gradient at 180 days was approximately 15 °F and at day 255 was approximately 20 °F. Figures 99 and 100 show temperature histories at the center of the top and bottom floor lifts at four locations in the floor. Two of these locations (H1 and H2) are in a culvert wall and two (H3 and H4) are at the center of cylindrical voids. Locations are shown in Figure 80. While temperatures were higher at the culvert wall, vertical temperature gradients were smaller than in the cooler locations at the cylindrical voids. As can be observed in the plots at H3 and H4, temperatures throughout the floor decreased at a much slower rate than the ambient temperature. In the temperature history plots from the previous analysis, shown in Figure 87, temperatures at nodes in the top lift decreased at the same rate as the ambient temperature, and in locations H3 and H4 were only slightly above ambient after day 110, resulting in a maximum temperature gradient of 45 °F at day 215. In the current analysis, floor temperatures continued to decrease, although at a slower rate than before, even after the minimum ambient temperature was reached, since the ambient temperature was still well below the floor temperature. By day 255, the temperature curves at the top of the floor were close to intersecting the ambient curve. After day 255 the top of floor temperature was controlled by the water temperature, and gradients could be expected to decrease further.

### Stresses and cracking

Plots of crack potentials at el 257 and at the upstream monolith face at 120, 180, and 255 days are shown in Figures 101 through 103. Crack locations at 120, 180, and 255 days are shown in Figures 104 through 106. Vertical cracking was initiated at the bottom of the land wall culvert near the upstream face of the monolith between days 92 and 95. Plots of stresses in the x-direction in this area are shown in Figure 107. The plot at day 92 indicates high tension at the top of the floor under the culvert opening. A contour plot of vertical displacements at the bottom of the monolith in Figure 108 shows that the floor is "curling up" at the upstream edge, with the largest vertical displacements occurring under the culvert openings. This vertical displacement is resisted by the stiffness of the thick floor section, resulting in localized higher displacements and

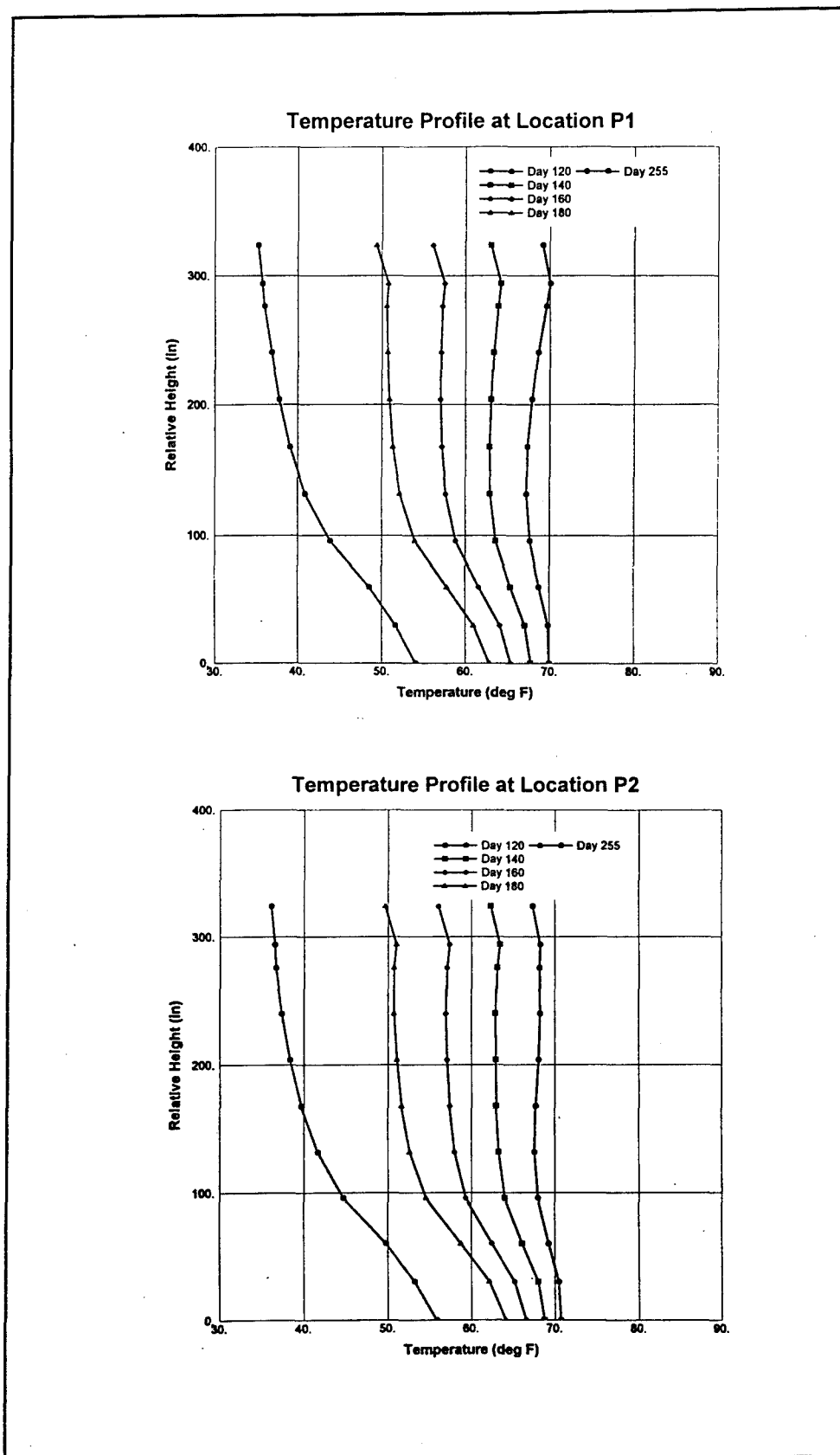
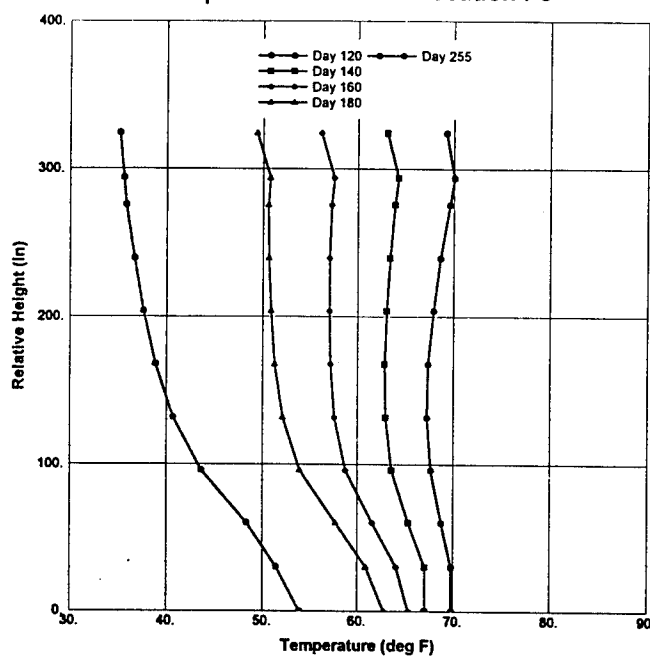


Figure 97. Temperature profiles at locations P1 and P2

Temperature Profile at Location P3



Temperature Profile at Location P4

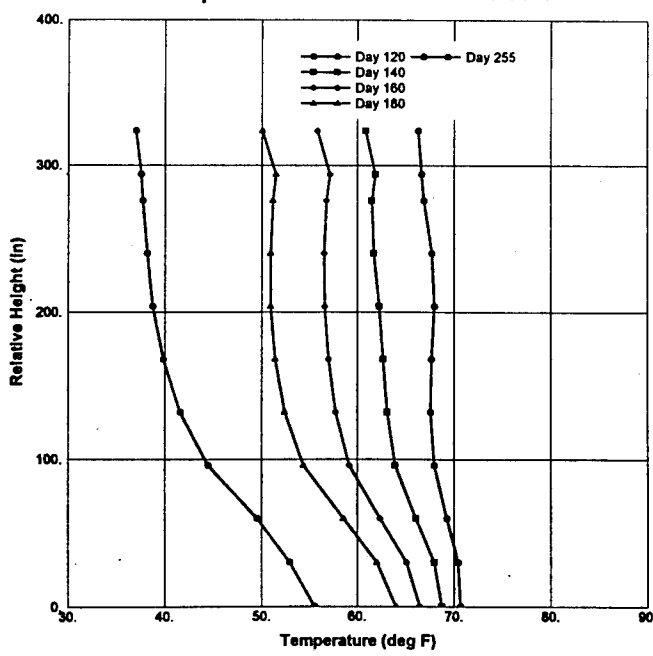


Figure 98. Temperature profiles at locations P3 and P4

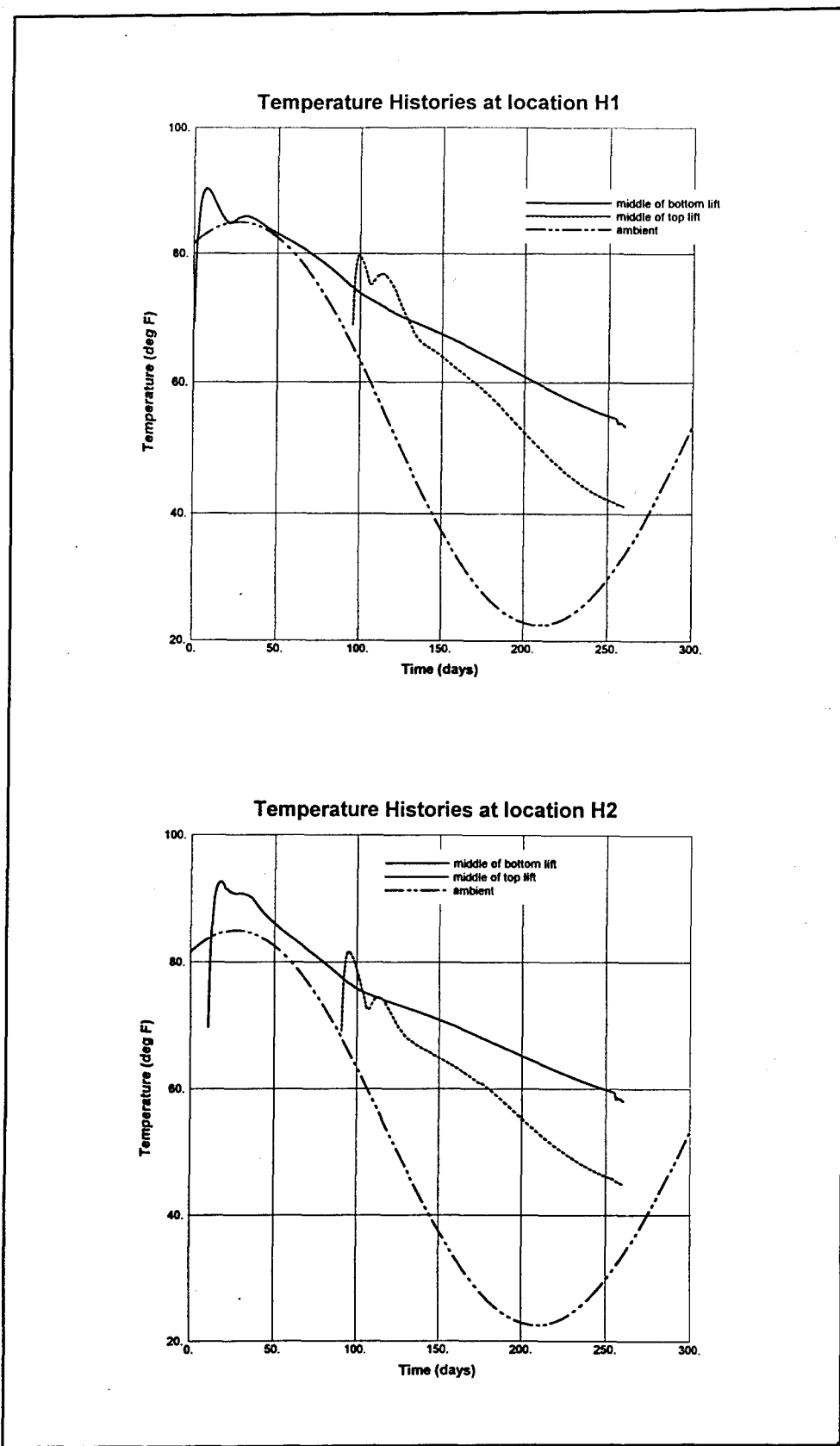
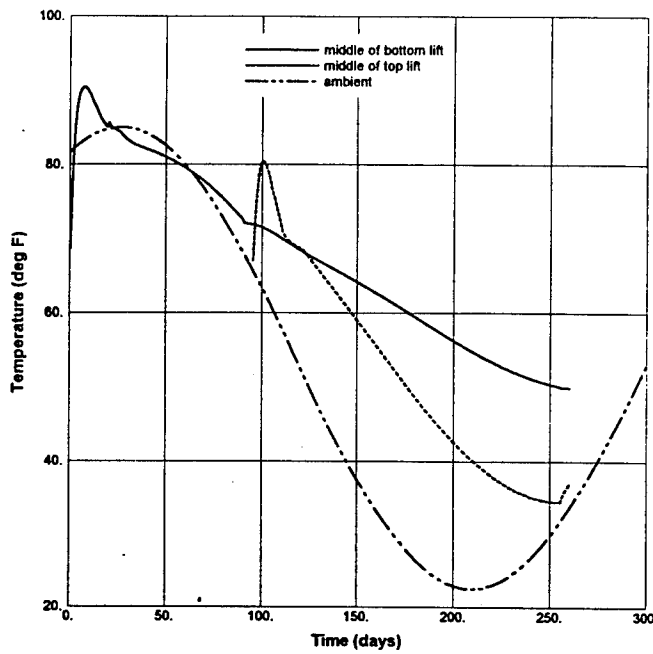


Figure 99. Nodal temperature histories at H1 and H2

Temperature Histories at location H3



Temperature Histories at location H4

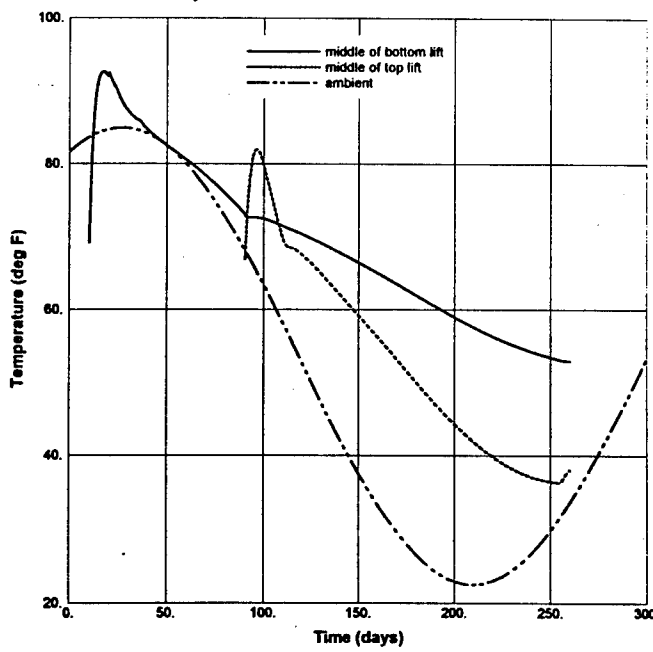


Figure 100. Nodal temperature histories at H3 and H4

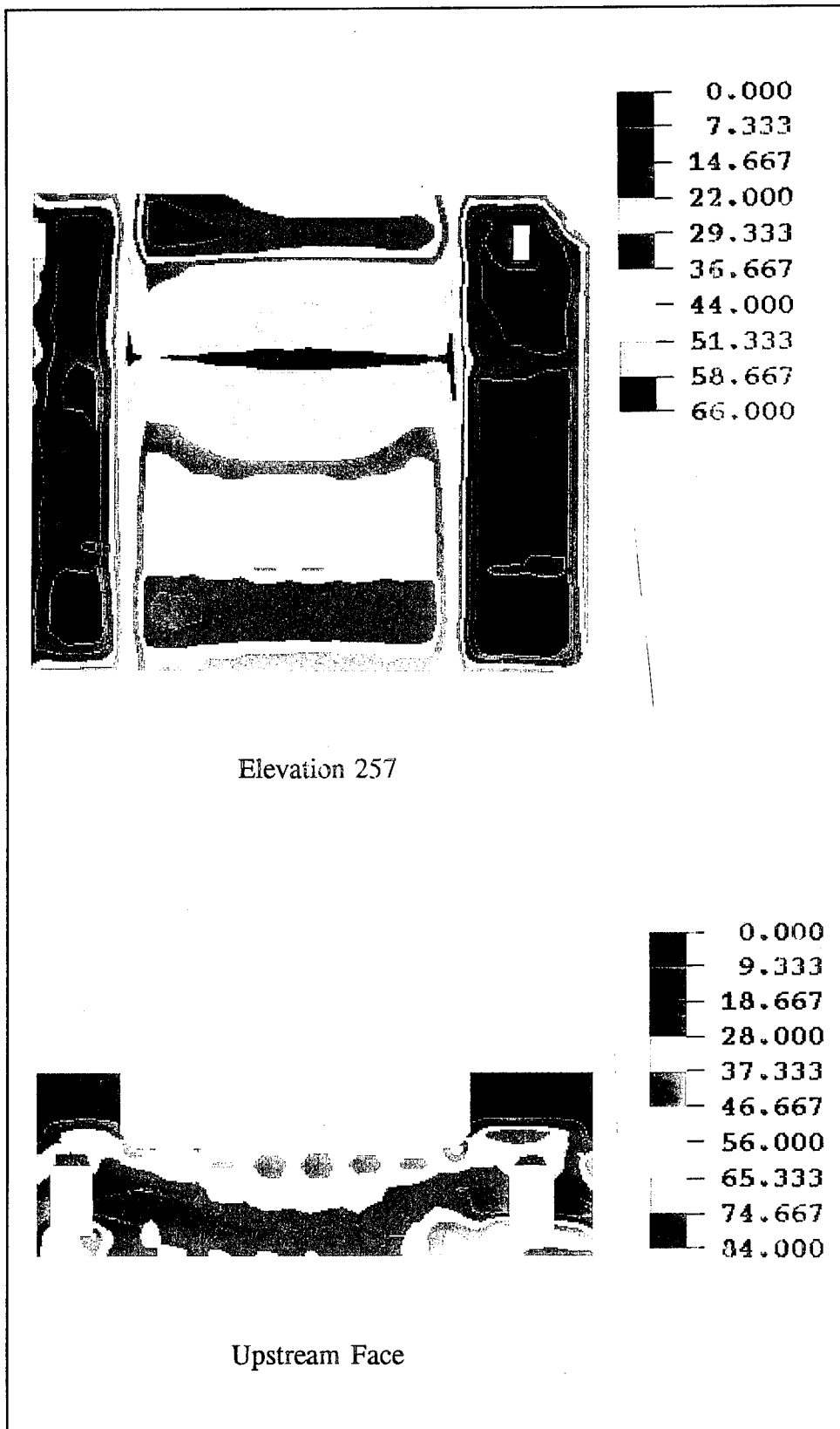
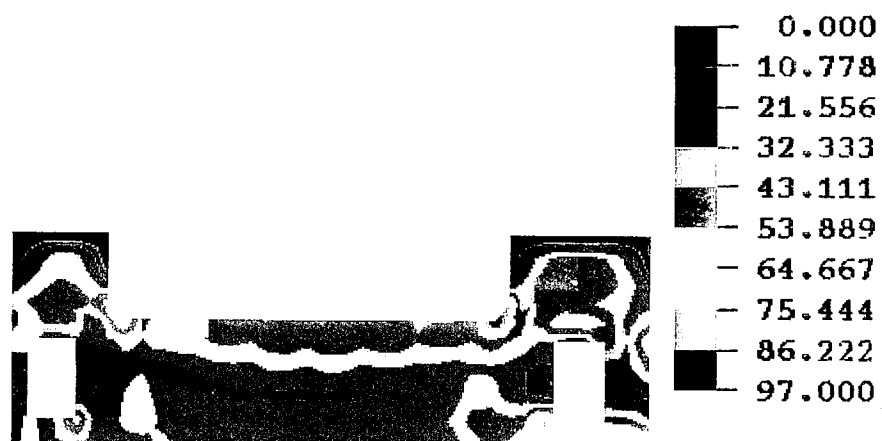


Figure 101. Crack potential contours, day 120



Elevation 257



Upstream Face

Figure 102. Crack potential contours, day 180

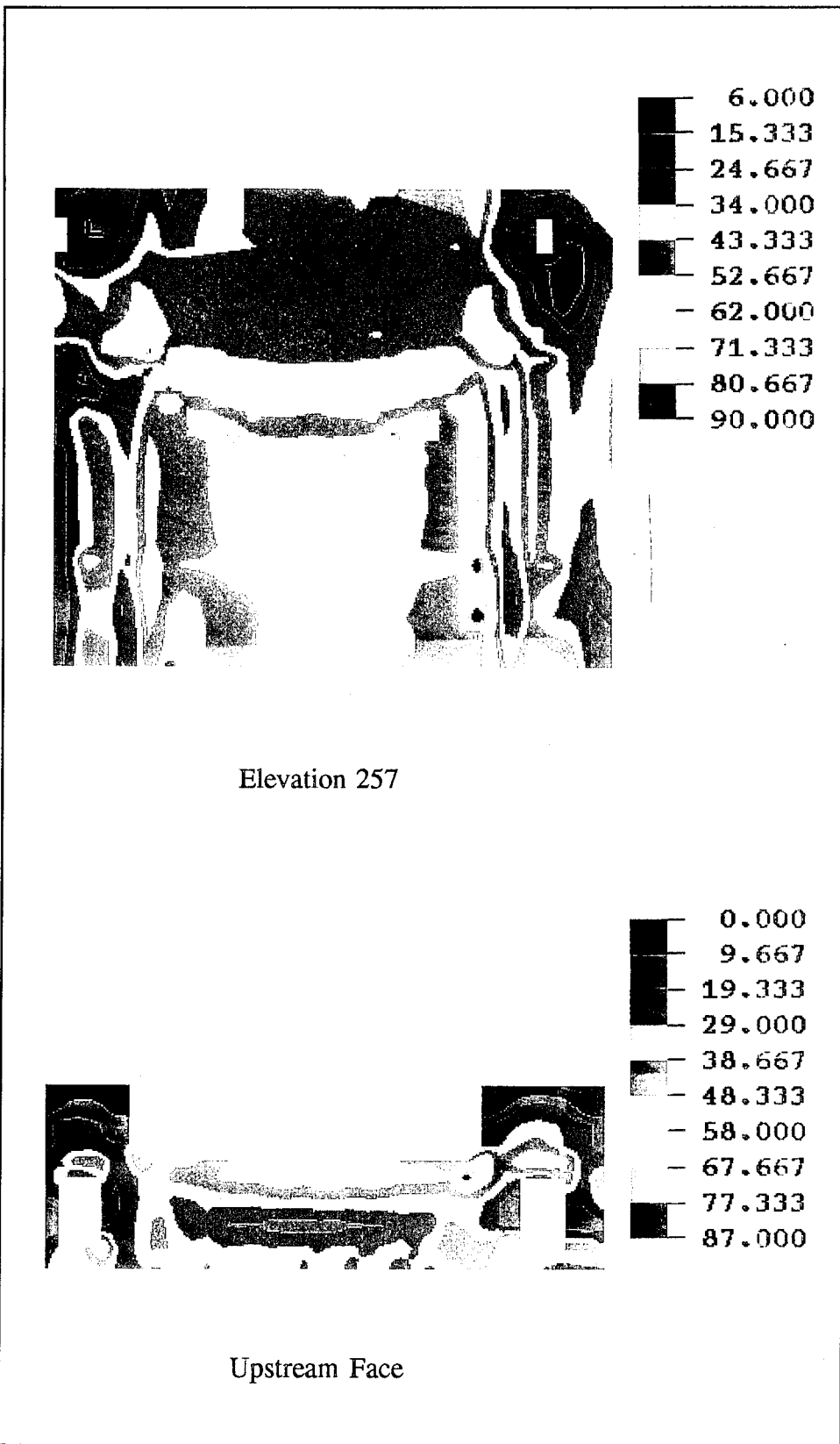


Figure 103. Crack potential contours, day 255

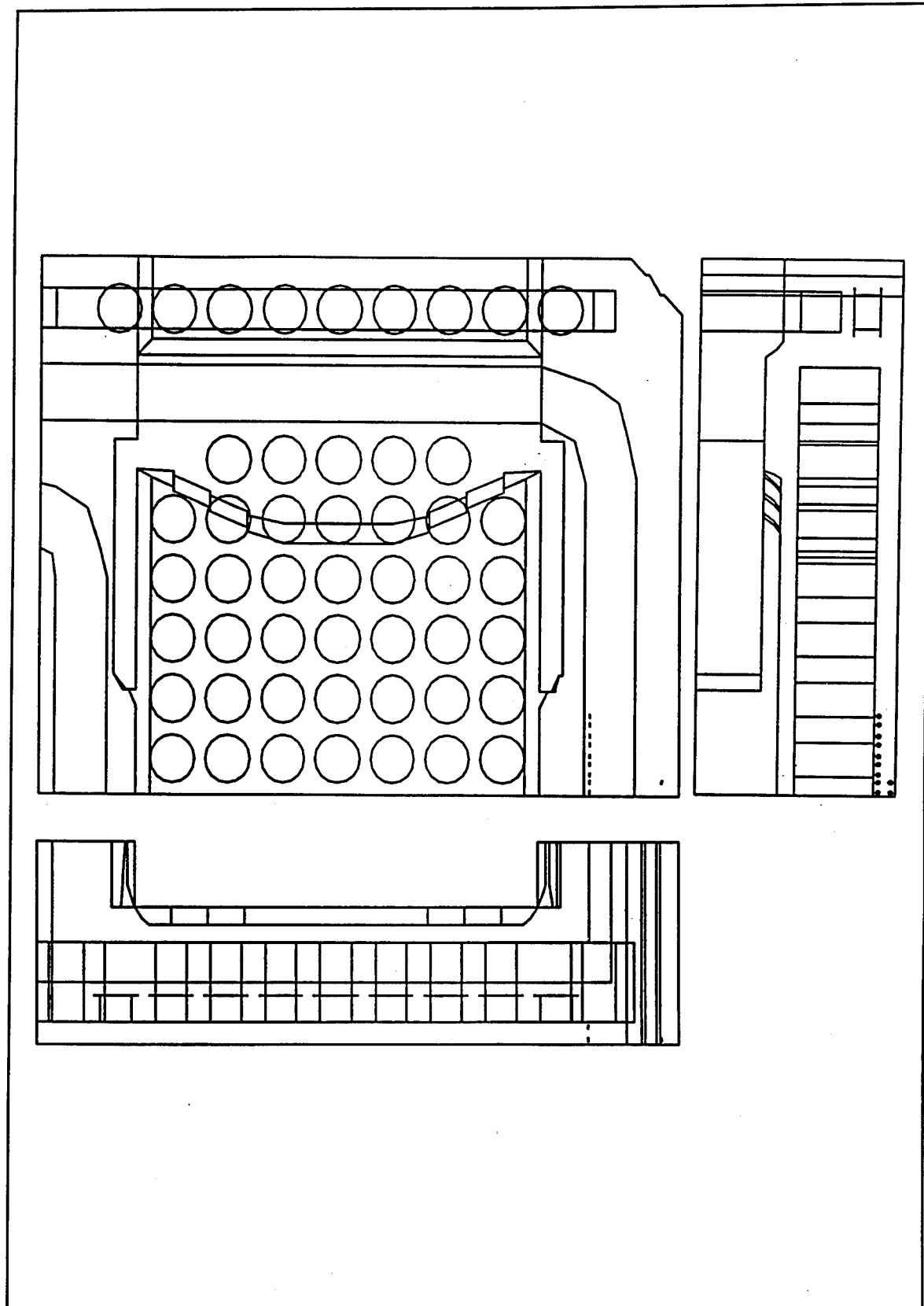


Figure 104. Crack locations, day 120

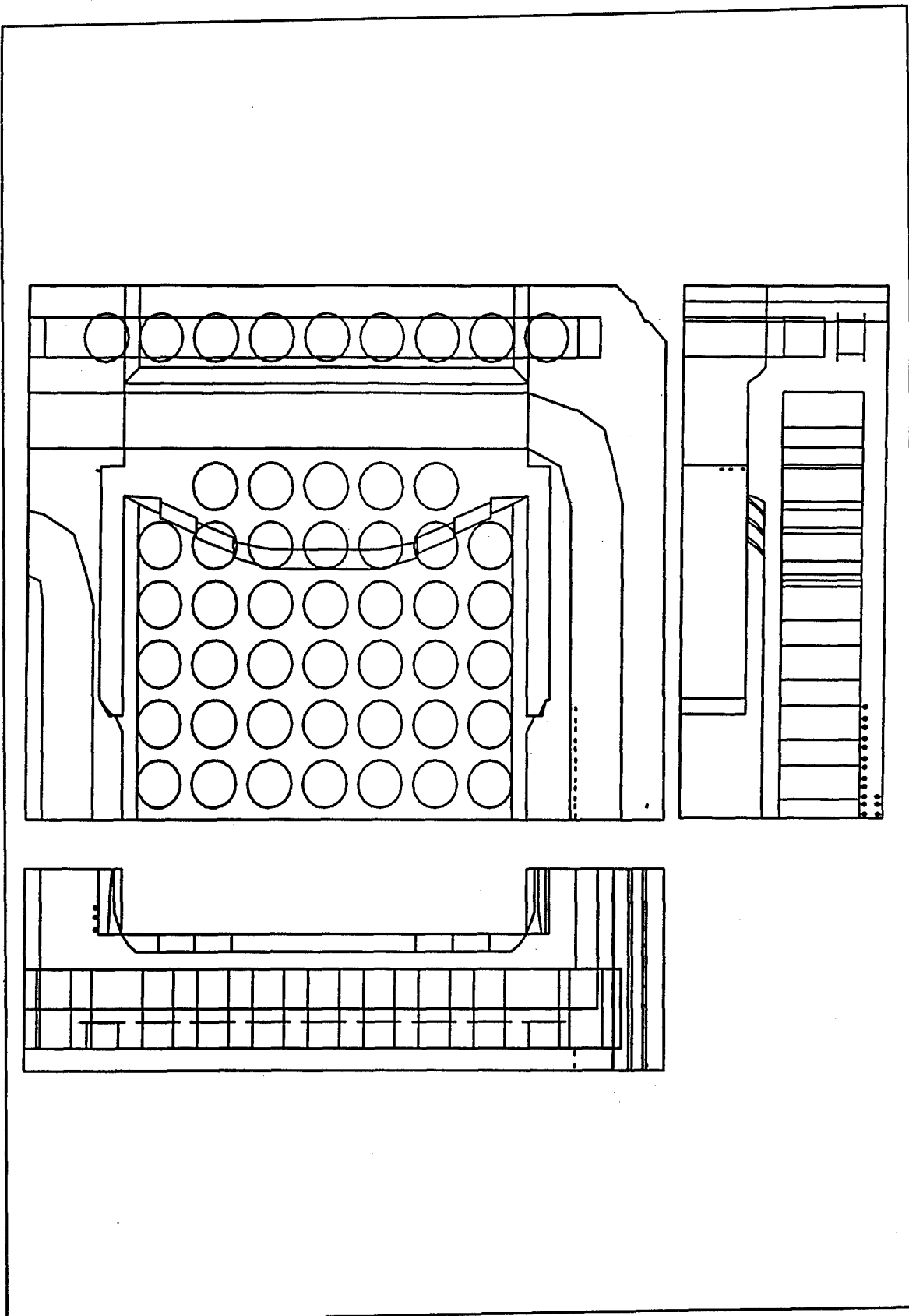


Figure 105. Crack locations, day 180

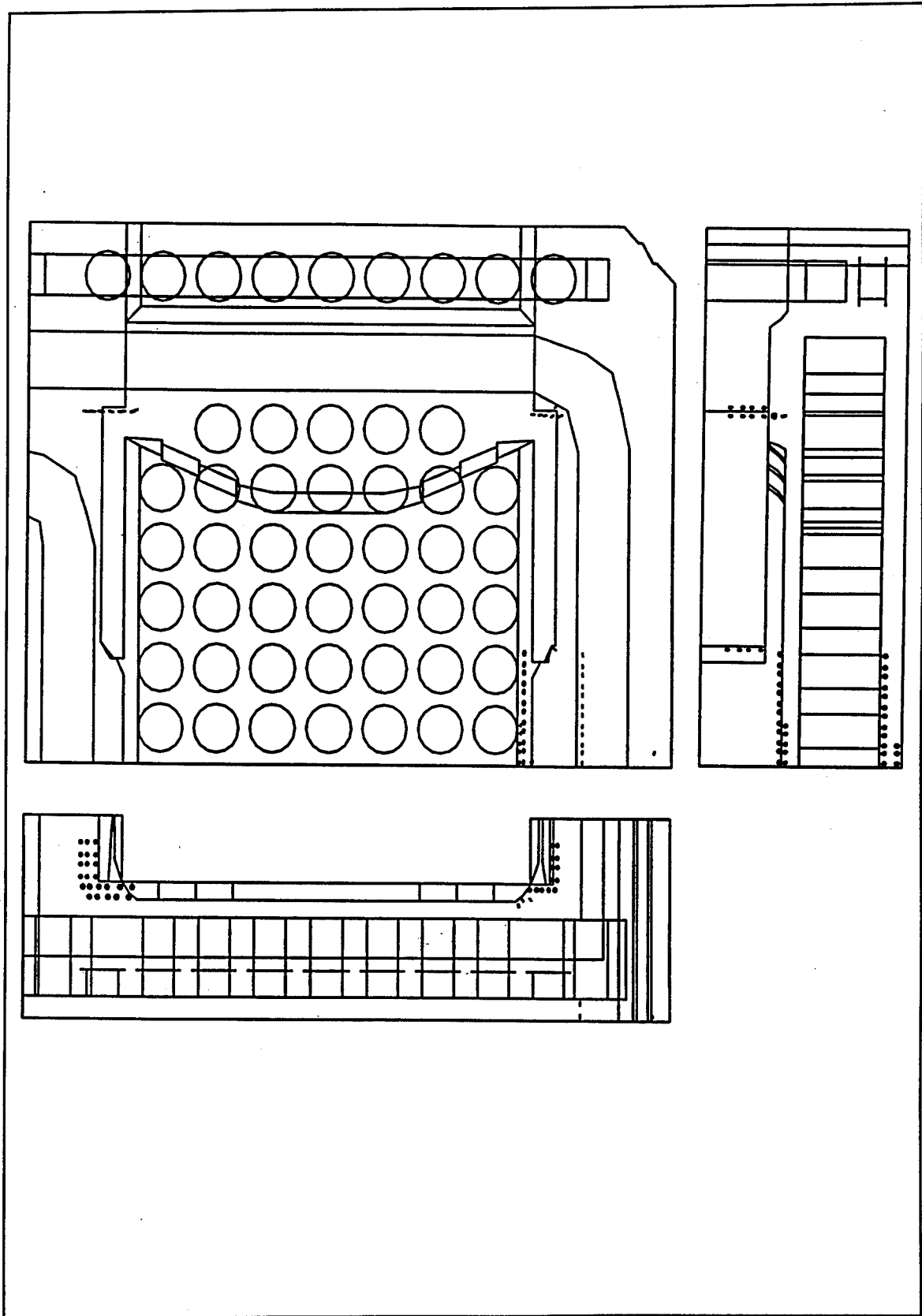


Figure 106. Crack locations, day 255

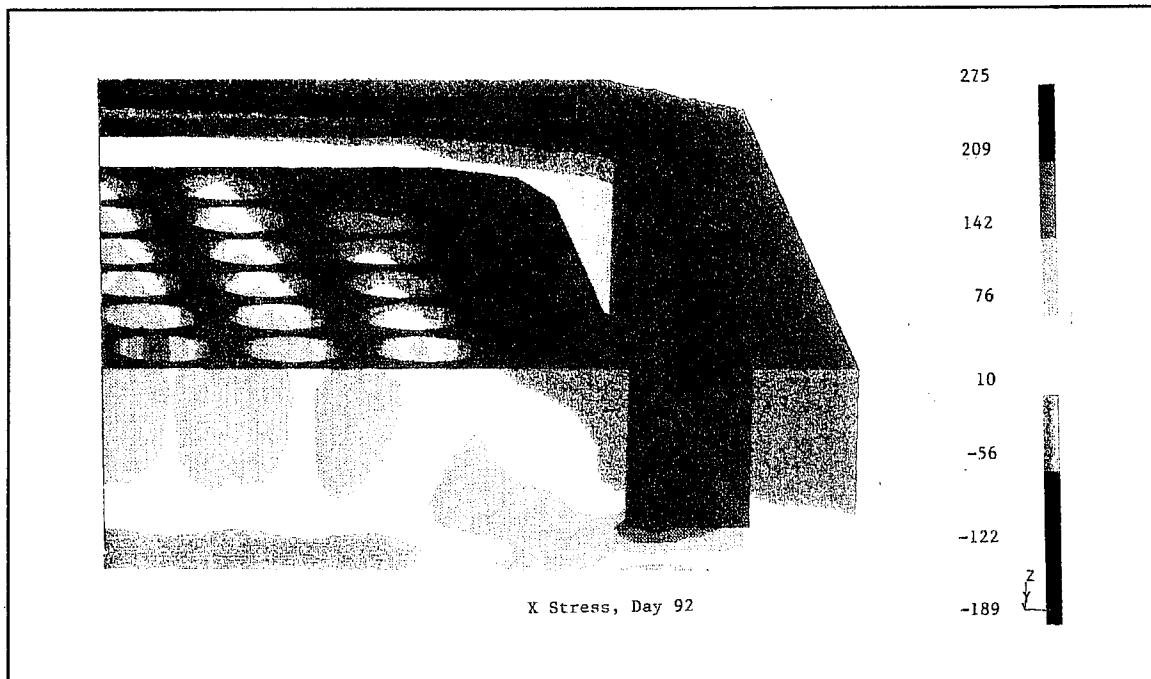


Figure 107. X stresses at upstream face of landwall culvert

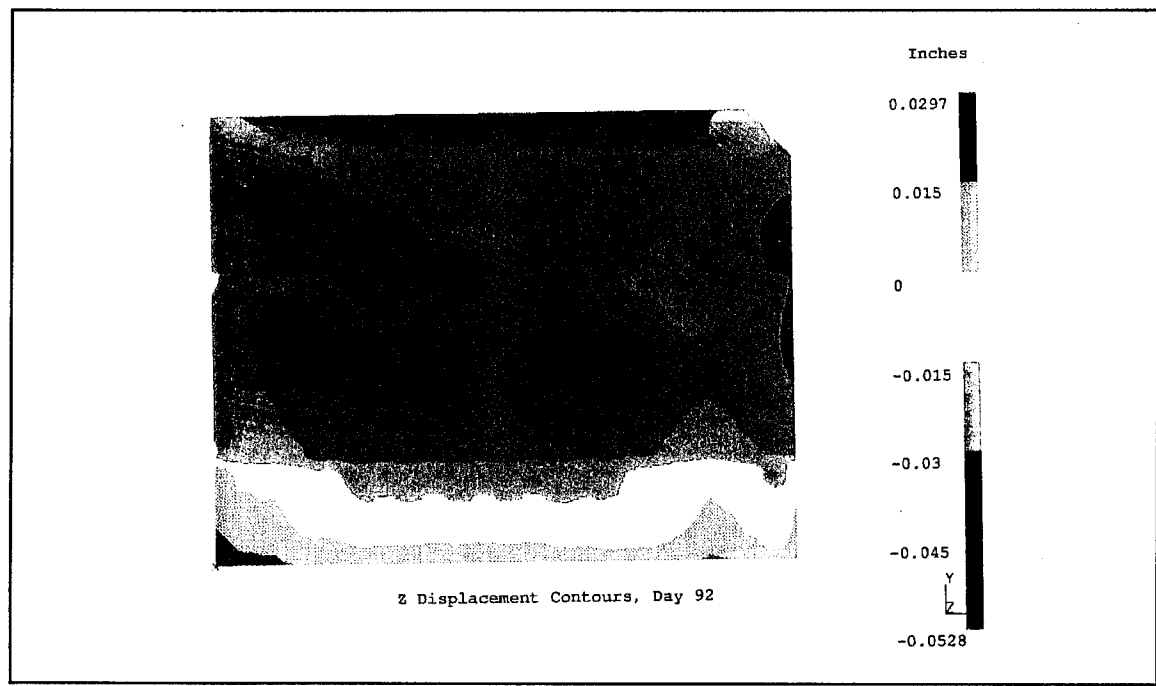


Figure 108. Vertical displacement contours at base of monolith

stresses at culvert openings. A thick floor should be expected to curl as it cooled, since the top surface would be cooler and would contract more than the bottom surface. However, throughout the analysis, the downstream side of the monolith was much warmer than the upstream side, and this could have resulted in curling at the upstream face only. Although this crack extended through the floor at one point and never closed, cracking in this area did not increase after day 120. The first cracking occurred in element 4091. Stresses in the reinforcing steel located at the base of this element never exceeded 5 ksi and are shown in Figure 109. Stresses in reinforcing steel normal to the crack at the top of the element were calculated for the period from 90 to 130 days based on nodal displacements on either side of the crack. The maximum crack opening calculated from nodal displacements was less than 0.04 in., with a maximum reinforcing stress of less than 33 ksi, and crack width began to decrease after day 115. Nodal displacements and calculated reinforcing stresses are shown in Figure 110.

Little cracking occurred between days 105 and 180, and cracking potentials were low at el 257 and at the upstream face on day 120, shown in Figure 101. In contrast, cracking at the top floor surface began at day 130 in

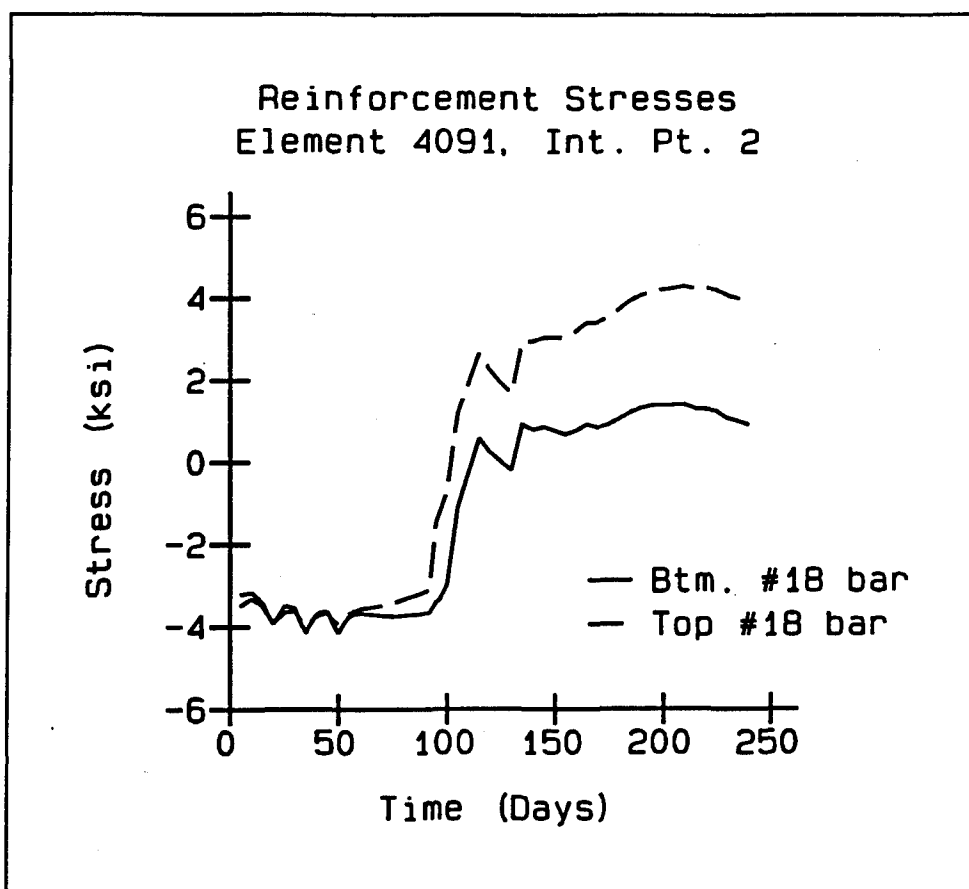
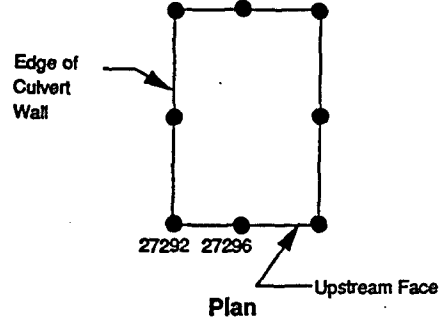
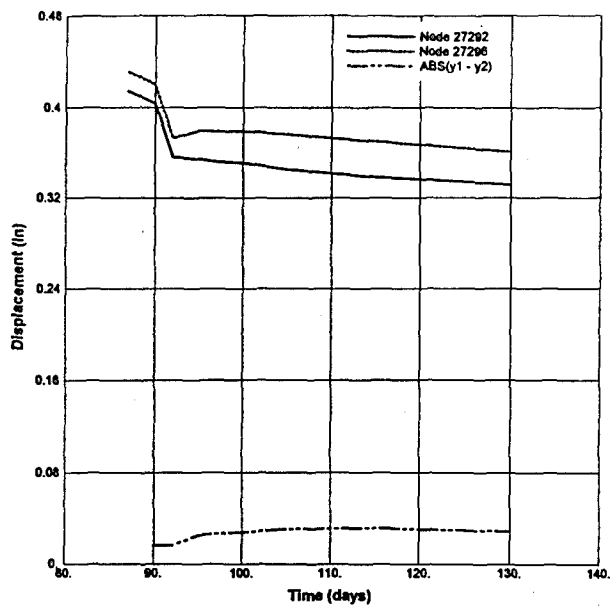
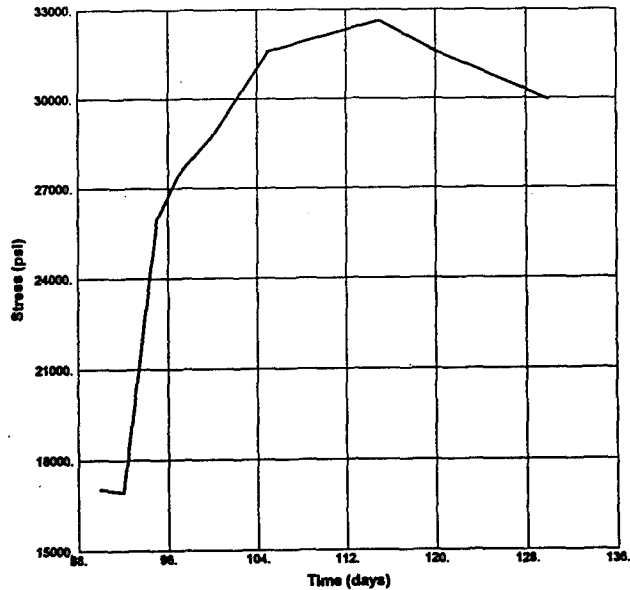


Figure 109. Stresses in reinforcing steel, element 4091



Nodal Displacements and Location



Reinforcing Stress

Figure 110. Nodal displacements and reinforcing stresses at top of crack

the previous analysis. The maximum crack potential of 65 percent occurred in the area left uninsulated for placement of the sill. Maximum principal stresses at these two faces, shown in Figure 111, were low except in the uninsulated area of the floor at the sill.

The next significant cracking occurred after the lift 22 insulation was removed on day 175. In Figure 105, crack plots at day 180 show vertical cracks in lift 22 at the corner of the miter gate recess. Cracking in the stub walls at the miter gate recesses continued until shortly after all wall insulation was removed. This cracking extended into the sill at the base of the wall but did not extend through the top element of the stub wall. Stresses in horizontal reinforcement near the wall face were not saved, since cracking in the floor was the primary concern. However, approximate reinforcing stresses were calculated based on nodal displacements on either side of the crack. Nodal displacements and calculated reinforcing stresses are shown in Figures 112 and 113. Maximum crack openings were less than 0.02 in. and cracks began to close after day 220. Maximum calculated reinforcing stresses were less than 12 ksi.

Crack potentials in Figures 102 and 103 are less than 60 percent except in floor areas directly under the chamfers between the floor and the walls or under the sill chamfers. Plots of third principal stress at el 257 and at the transverse and longitudinal sections from Figure 80 are shown in Figures 114 and 115. Maximum values at the top of the floor on day 180 were less than 240 psi, and only rose to about 280 psi by day 255. Tensile principal stresses at the monolith surface for days 180 and 255 are plotted in Figure 116. At day 180, principal stresses along the entire exposed wall face at the miter gate recess were near 400 psi. By day 255, stresses along this face had dropped to less than 240 psi. This drop in tensile principal stress at the face of uninsulated walls was due to the increase in ambient temperature after day 220 and to the relief to tensile stresses provided by cracking. However, sudden decreases in temperature from cold fronts could still leave walls vulnerable to further cracking.

## Conclusions

The application of insulation with an R value of 20 hr-ft<sup>2</sup>·°F/Btu accomplished the objective of reducing thermal gradients across the floor during winter months. The combination of the cooling efficiency of the cylindrical voids, the prolonged cooling period due to the delay in placing the top floor layer, and the heavy insulation applied to the floor reduced thermal gradients sufficiently to prevent cracking in the top of the floor. Maximum cracking potentials throughout the analysis were less than 70 percent at el 257 and in the upstream face except at localized areas in the chamfers and wall faces.

High stresses and cracking in the walls directly above the floor occurred when insulation was removed as the concrete reached an age of

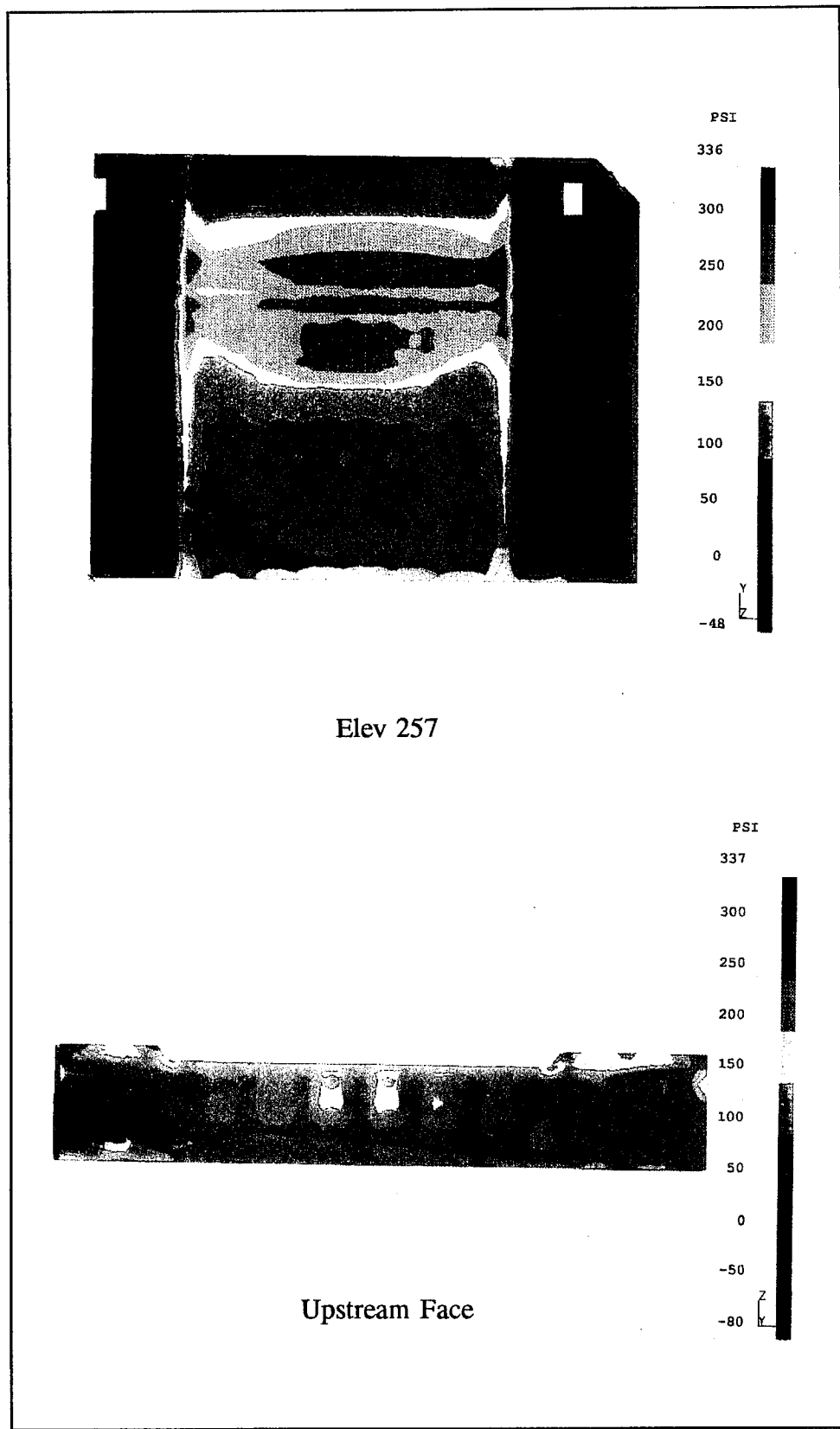
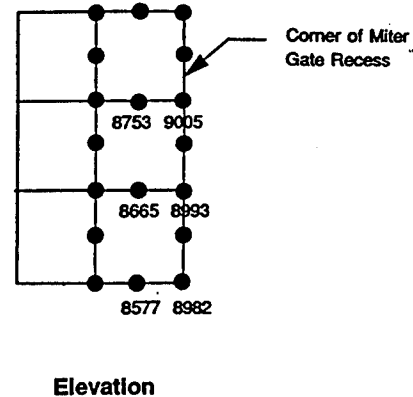
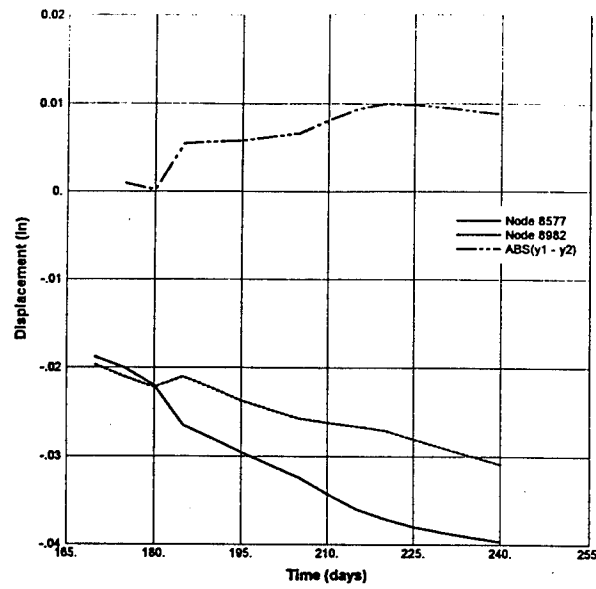
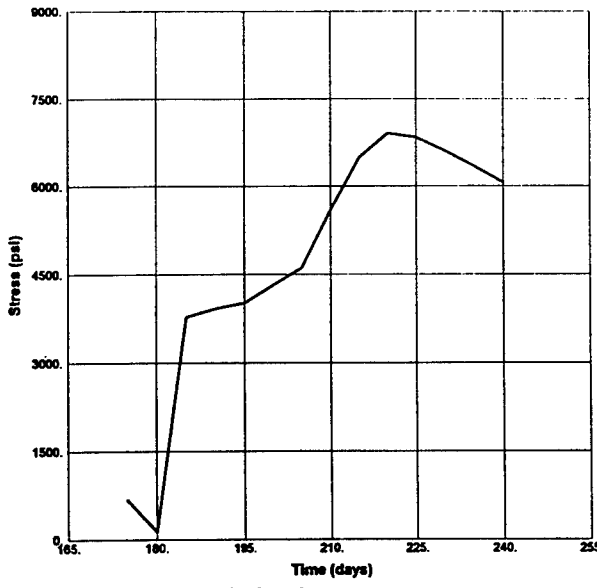


Figure 111. Maximum principal stresses, day 120



**Nodal Displacements and Location**



**Figure 112. Nodal displacements and reinforcing stresses at base of wall crack**

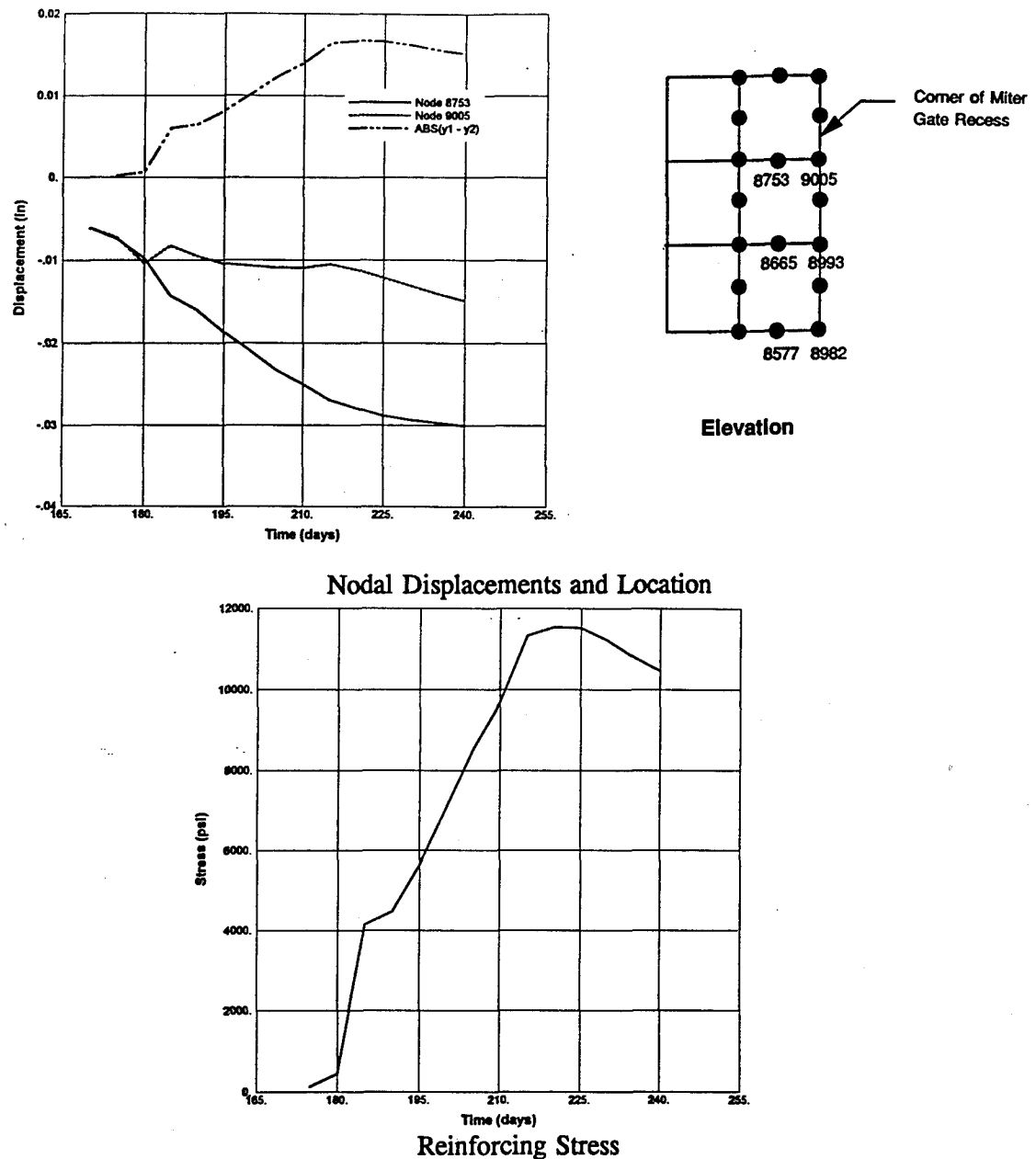


Figure 113. Nodal displacements and reinforcing stresses at wall crack

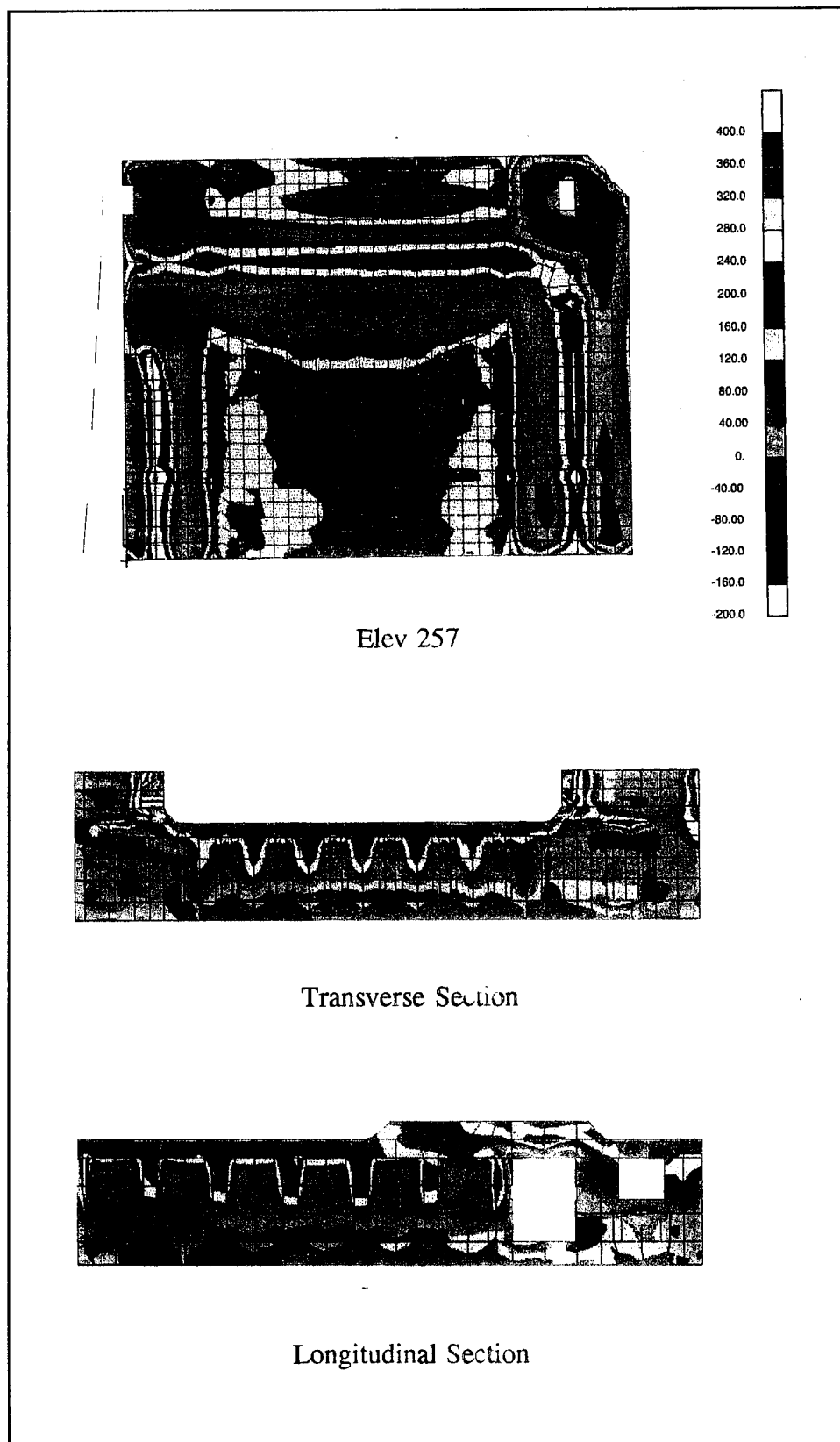


Figure 114. Third principal stress, day 180

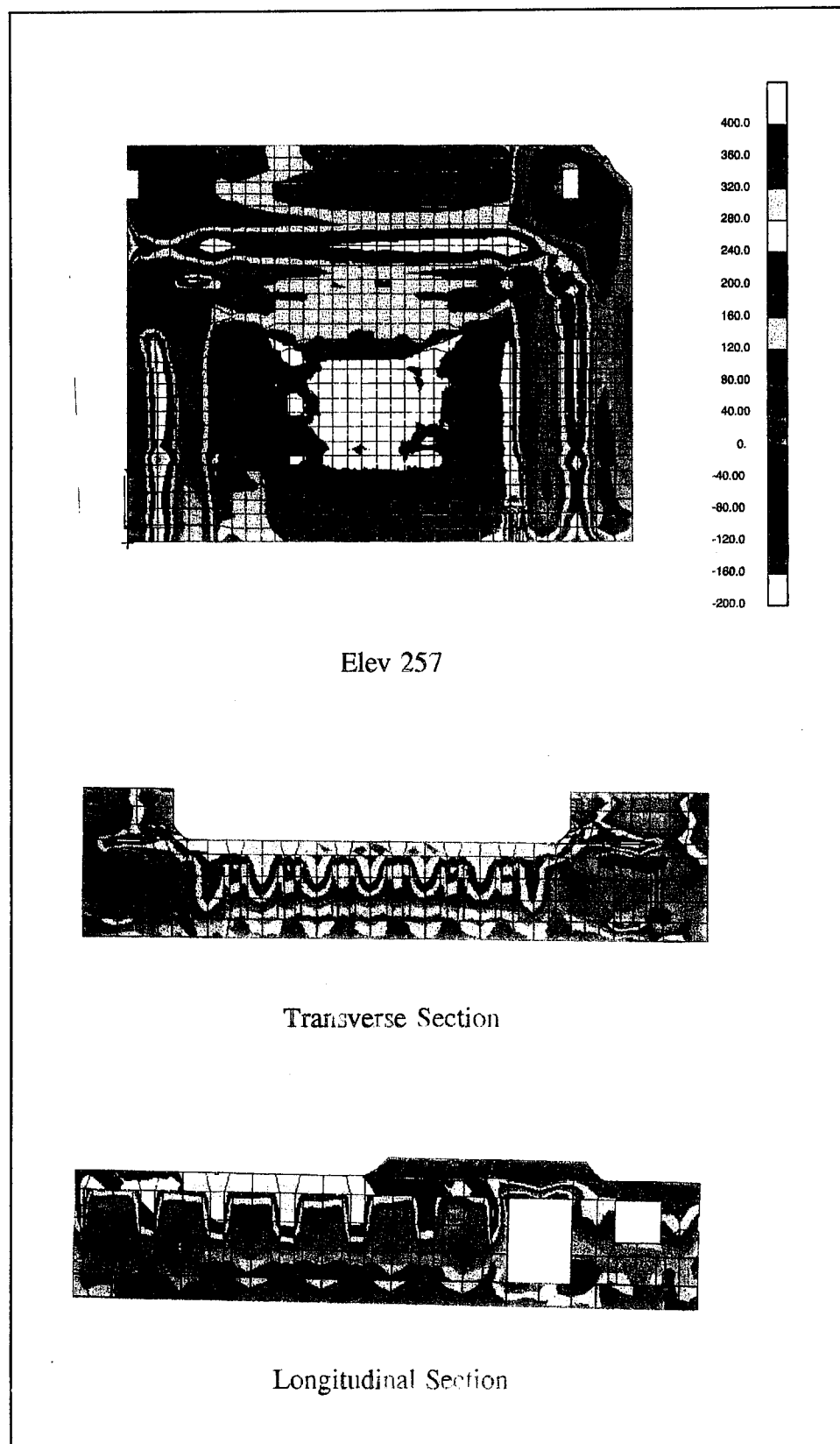


Figure 115. Third principal stress, day 255

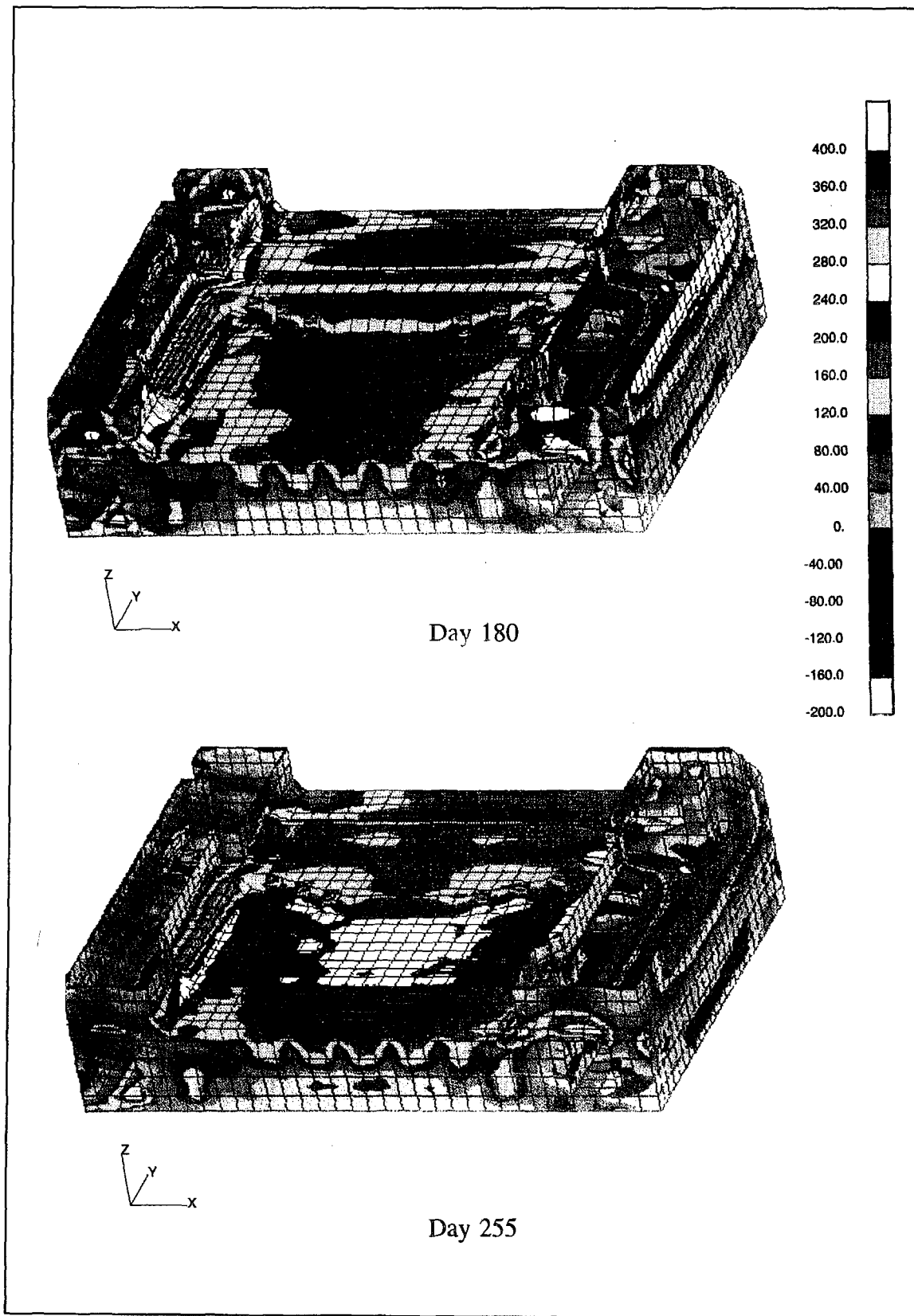


Figure 116. Third principal stress, monolith outer surface

45 days. The section change at the miter gate recess was particularly vulnerable to cracking, and this area directly above the floor should be protected for a longer period of time.

However, all of the cracking that occurred was limited in nature. Although cracks did not close, cracking stopped after a short period of time, crack widths were small, and reinforcing stresses were low. None of these cracks will compromise the structural integrity of the monolith, and the wall cracking can be reduced or eliminated by increasing the insulation time.

## Heat Transfer Analysis with $R = 10$

Since the results of the analysis described earlier in this chapter with an insulation value of  $R = 20 \text{ hr-ft}^2 \cdot ^\circ\text{F/Btu}$  indicate that this high insulation value was more than sufficient for mitigating the cracking problem observed in the previous analysis, a heat transfer analysis using an insulation value of  $R = 10 \text{ hr-ft}^2 \cdot ^\circ\text{F/Btu}$  was performed. The additional heat transfer analysis was performed in an attempt to demonstrate that thermal gradients could be sufficiently reduced using a lower value and still achieve an acceptable situation with respect to cracking in the slab. The analysis was identical to the heat transfer analysis described earlier in the chapter except that  $R = 10 \text{ hr-ft}^2 \cdot ^\circ\text{F/Btu}$  was used for insulation on the top and sides of the slab. Another difference is because of some file manipulation errors when performing the analysis, only the last several days of heat generation are modeled for the lifts above el 252 (top lift of base slab and above). As will be seen in the results, this error is conservative since if the heat generation had been modeled properly, the temperatures in the top of the base slab would have been higher which would reduce the thermal gradients actually observed in the analysis.

The results of this analysis are best observed through the use of temperature profiles as were shown in Figures 85, 97, and 98 of the previous analyses. Figure 117 shows the temperature profiles at locations P1, P2, P3, and P4 (reference Figure 80). When comparing the profiles in Figure 117 for the analysis with  $R = 10$  to Figures 97 and 98 for the analysis with  $R = 20$ , it can be seen that the shapes of the profiles at days 120, 140, 160, and 180 are all very similar. Closer observation will show that the temperatures at the base are nearly identical for the two analyses while the temperatures at the top are different by approximately  $8 \text{ }^\circ\text{F}$ . It can be seen in these plots how the lack of proper modeling of the heat generation in the  $R = 10$  analysis results in a higher gradient than would have occurred had it been modeled properly.

Even as the results currently are presented, it appears that  $R = 10$  would be sufficient for providing the needed insulation. In addition to the temperature profiles, contours of temperatures at days 120, 180, and 255 in Figure 118 show that the temperature gradient through the thickness of

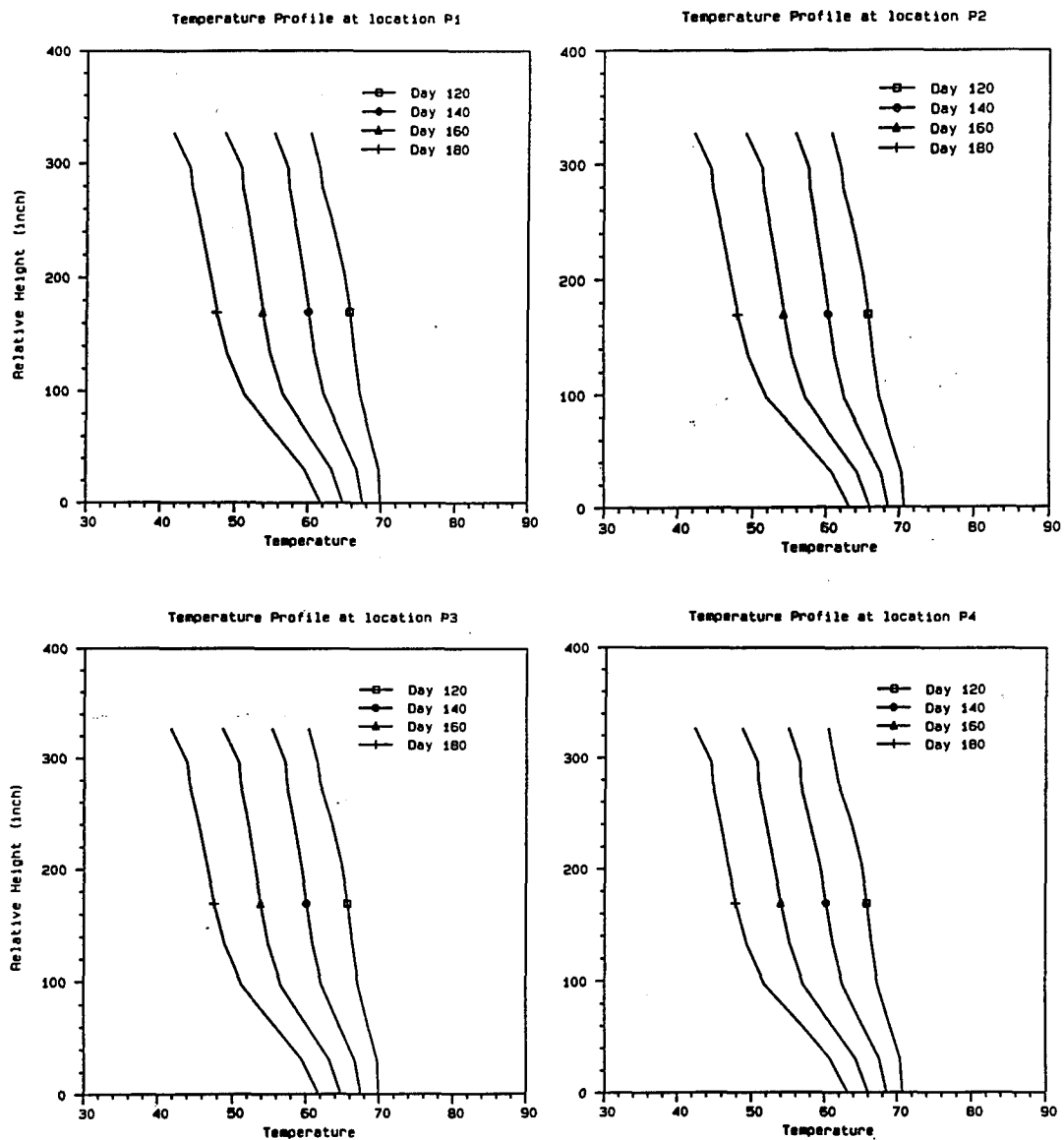


Figure 117. Temperature profiles for  $R = 10$

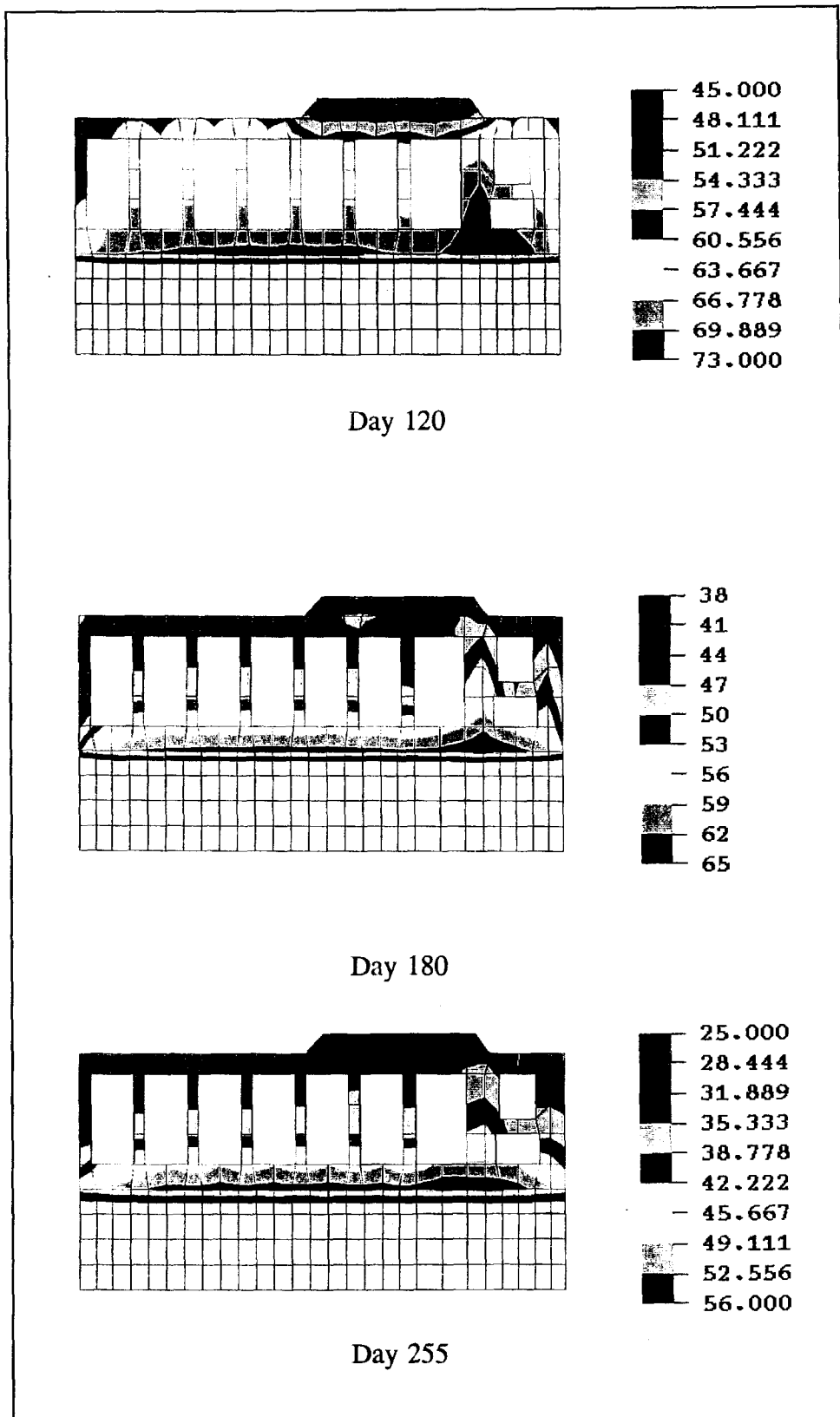


Figure 118. Thermal contours of longitudinal section

the slab is very gradual. As with the temperature profiles, the temperature contours are very similar to the contours seen for the  $R = 20$  analysis.

Based on the fact that the gradient does not increase significantly between the  $R = 10$  analysis and the  $R = 20$  analysis and that the percent of the cracking criteria which occurs in the base slab remains at or below 70 percent, it can be concluded that using an insulation value of  $R = 10$  hr- $ft^2\text{-}^{\circ}\text{F/Btu}$  would provide adequate protection to the base slab. Being able to insulate to a value of  $R = 10$  is a significant benefit since it would, of course, be much less costly than insulation with a value of  $R = 20$  and would be much easier to achieve.

# 10 Summary, Conclusions and Recommendations

---

## Summary and Conclusions

A systematic investigation for the constructability of the lower miter gate monolith for the Olmsted locks has been conducted using nonlinear, incremental structural analysis (NISA) methods to evaluate thermal-induced cracking. To evaluate cracking potential, the complete construction sequence is simulated including placement of each lift, form removal, heat of hydration, heat conduction and convection from free or insulated surfaces, gravity loads, reinforcement, foundation interaction, and service loads. These analyses required advanced concrete constitutive relations that can model the response of concrete from a few hours of age and include the interaction of time- and temperature-dependent creep, aging, shrinkage, and cracking. Two-dimensional studies were used for initial scoping calculations and to examine combinations of several construction parameters in both longitudinal and transverse slice models. The conclusions and lessons learned from these studies are described in detail in the respective chapters. The intent was to define a construction scenario based on 2D assumptions that appear to strike a good balance between mitigation of cracking potential and cost by placing as few restrictions on construction as possible. Extreme conditions, such as severe high and low average daily temperatures occurring in the same year and worst-case start dates and material properties were used for conservatism. The proposed construction parameters were then used in a 3D evaluation to assess the final impact on the potential for cracking during construction of the structure.

In addition to providing specific data for design considerations for this monolith, information for advancing the maturing methodology used for this NISA of massive concrete structures was obtained. In particular, the issue of the appropriateness of 2D analyses in lieu of 3D analyses for these types of evaluations was notable. The conclusion from this study is clear: not all potential cracking mechanisms from 3D thermal and structural response can be captured from 2D models for massive concrete structures. The major concern requiring 3D analysis is the presence of large concrete mass regions in which substantial thermal gradients can exist in

two directions. The more critical area identified by 3D analysis in this monolith was not at geometric changes, such as culvert bends or wall junctions, but near the middle of the chamber involving thick regions of concrete with two free surfaces exposed to cold ambient temperatures.

A significant advancement in the understanding of the thermal-induced cracking behavior of this specific monolith, and of massive concrete structures in general, has been compiled in this effort. A significant outcome of this analysis effort that bears repeating is the development of the composite slab design concept for massive concrete structures. This concept evolved from discussions and brainstorming in meetings with the Olmsted NISA review team fueled by the cracking predictions from the 3D analysis presented in Chapter 6. The specific configuration modeled in Chapter 7 was first proposed by Mr. Tom Hugenber of CEORD-PE-G. Although the initial evaluation presented in Chapter 7 produced unacceptable cracking for the assumed construction conditions, the use of the cylinders in combination with delaying the placement of the top lift by 30 days and insulating the surfaces of the base slab with a high insulation value produced results which proved to create an acceptable solution. Since the reduction in mass appears to exceed the reduction in stiffness, this composite slab concept has potential advantages in dynamic integrity as well as in crack mitigation during construction.

## Recommendations

Based on the results presented in this report, the following recommendations are made:

- a. Use the composite slab design as presented in Chapter 7 except the placement of the top lift of the base slab should be delayed for 30 days instead of the typical 5-day interval and all exposed surfaces of the base slab and sill should be insulated to a value of at least  $R = 10 \text{ hr-ft}^2 \text{-}^{\circ}\text{F/Btu}$ .
- b. The construction sequence of the lift placements specified in the contract documents should follow the sequence used in the analysis as shown in Appendix B.
- c. The insulation applied to the exposed surfaces of the base slab (as stated in the first recommendation) should be left in place for a minimum of two winter seasons or until the cofferdam is rewatered.
- d. Insulation on the walls for a distance of 15 ft above the sill elevation should be left in place for a period of 90 days after the concrete is placed and should have an insulation value of  $R = 4 \text{ hr-ft}^2 \text{-}^{\circ}\text{F/Btu}$ . An insulation value of  $R = 2 \text{ hr-ft}^2 \text{-}^{\circ}\text{F/Btu}$  for a period of 45 days (same as insulation provisions for the walls of the chamber monolith) may be specified for portions of the wall above this elevation.

- e. Since the 3D analysis for this monolith clearly identified a critical cracking potential that could not be captured in 2D models, it is recommended that 3D evaluations be conducted for these types of structures if they include design features for which there is no previous experience. In all cases, the time and cost associated with performing a 3D analysis should be carefully weighed against the benefits which will be received from such an analysis. Because of the size of these structures, the incremental construction process, and the need to closely follow the time-dependent material response, the effort involved in these 3D NISA calculations and in evaluating the voluminous data generated is substantial. An observation is therefore made for the need to conduct research into developing a simplified methodology for 3D design analysis for constructability evaluation of massive concrete structures. It appears feasible that a technique can be established whereby full 3D thermal calculations are performed, and then 3D cracking analysis snapshots conducted at selected critical times to determine bounding cracking potentials for design evaluations.
- f. Since the composite slab design has potential for improving the dynamic integrity of the monolith due reduced mass, an effort in the area of continuum modeling for evaluating these potential dynamic response advantages is also recommended.

## References

---

ANATECH. (1992). "ANACAP-U, ANATECH Concrete Analysis Package, Version 92-2.2, User's Manual," La Jolla, CA.

\_\_\_\_\_. (1992). ANA-92-0130, Theory Manual, La Jolla, CA.

Garner, S., and Hammons, M. (1991). "The development and use of a time-dependent cracking model for concrete," Technical Report SL-91-7, U.S. Army Engineer Waterways Experiment Station, Vicksburg, MS.

Garner, S., Bombich, A. A., Norman, C. C., Merrill, C., Fehl, B., and Jones, H. W. (1992). "Nonlinear, incremental structural analysis of Olmsted Locks and Dams," Technical Report SL-92-28, U.S. Army Engineer Waterways Experiment Station, Vicksburg, MS.

Hammons, M., Neeley, B., Alexander, M., Bombich, A., and Garner, S. (1991). "Concrete mixture selection and characterization study, Olmsted Locks and Dam, Ohio River," Technical Report SL-91-9, U.S. Army Engineer Waterways Experiment Station, Vicksburg, MS.

Headquarters, U.S. Army Corps of Engineers. (1990). "Special design provisions for massive concrete structures," ETL 1110-2-324, Washington, DC.

Norman, C. D., Campbell, R. L., Sr., and Garner, S. (1988). "Analysis of concrete cracking in lock wall resurfacing," REMR-GS-15, U.S. Army Engineer Waterways Experiment Station, Vicksburg, MS.

Rashid, Y. R., and Dunham, R. S. (1985). "Concrete model considering aging, creep and cracking," Report No. ANA-85-0027, ANATECH International Corp., La Jolla, CA.

U.S. Army Engineer Waterways Experiment Station. (1949). Handbook for Concrete and Cement, Designation CRD C 44-63, "Method of Calculation of Thermal Conductivity of Concrete," Vicksburg, MS.

# **Appendix A**

## **Subroutine HETVAL**

---

```

SUBROUTINE HETVAL (CMNAME, TEMP, TIME, DTIME, SVAR, FLUX, PREDEF)
IMPLICIT DOUBLE PRECISION (A-H,O-Z)
DIMENSION SVAR(1), PREDEF(1)
CHARACTER*8 CMNAME
C*****
C
C   Calculate and return Volumetric Heating Rate at each integration
C   point for each concrete element by material name  R James 10/27/92
C   This method is independent of element numbers - Each lift is
C   given a material name using *HEAT GENERATION material option
C
C   NQ1  is no. of points in T1 & Q1 arrays
C   Start time for each lift based on 5 day placement increments
C   NOTE - FLUXES IN Q1 ARRAY OBTAINED FROM WES
C         - ASSUMED UNITS ARE BTU/(hr-in**3)
C         - BASED ON SPEC. WT = 0.08449,  SPEC.HEAT = .22 & HOURS
C
C*****
C
PARAMETER (NQ1=21)
DIMENSION Q1(NQ1), T1(NQ1)
SAVE Q1, T1
C
C          OLMSTEAD MIXTURE 11
DATA T1 /      6.00,    12.00,    18.00,    24.00,    30.00,
$          36.00,    48.00,    60.00,    84.00,   108.00,
$          120.00,   144.00,   168.00,   192.00,   216.00,
$          240.00,   264.00,   288.00,   336.00,   360.00,
$          648.00 /
DATA Q1 /0.00846090,0.01001042,0.01284686,0.00521171,0.00539755,
$          0.00567338,0.00520116,0.00414147,0.00338928,0.00279045,
$          0.00224723,0.00194696,0.00160559,0.00138042,0.00117012,
$          0.00091299,0.00071519,0.00058468,0.00037927,0.00030453,
$          0.00015165 /
C
FLUX = 0.0
C
C   Find lift number of current material
C   Assume name is of form xxLIFTii where ii is lift number
C
L = INDEX(CMNAME,'LIFT')
IF (L .EQ. 0) RETURN
READ (CMNAME(L+4:L+5),100) LIFT

```

```

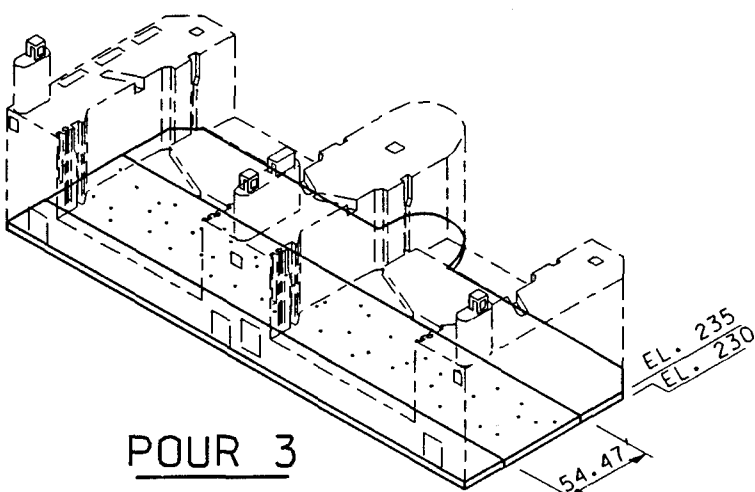
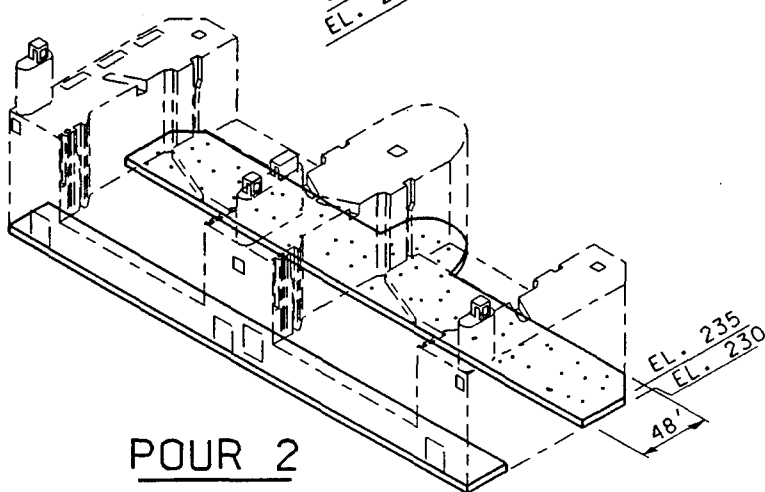
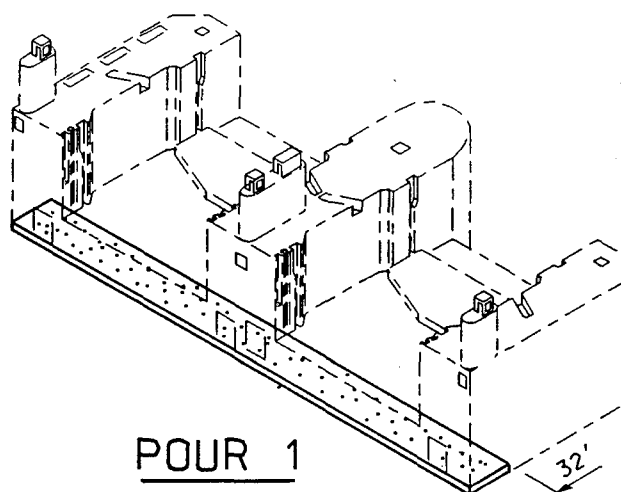
100 FORMAT (I2)
    IF (LIFT .EQ. 0) RETURN
C
C   Compute start time of lift based on 5 day placement intervals
C
    START = FLOAT(LIFT-1) * 5.0
    TREL = (TIME - START) * 24.
    IF (TREL .LT. 0.0) RETURN
C
C   Find discrete flux value - no interpolation
C
    DO 20 I=1,NQ1
        IF (TREL .LE. T1(I)) THEN
            FLUX = Q1(I) * 24.
            GOTO 40
        ENDIF
20 CONTINUE
C
C   Heat generation is zero if relative time is past T1(NQ1)
C
40 CONTINUE
CC      PRINT 9000, CMNAME,LIFT,TIME,TREL,FLUX
CC 9000 FORMAT (' MATERIAL,LIFT,TIME,TREL,FLUX = ',A8,I4,3(1X,1PG12.4))
    RETURN
    END

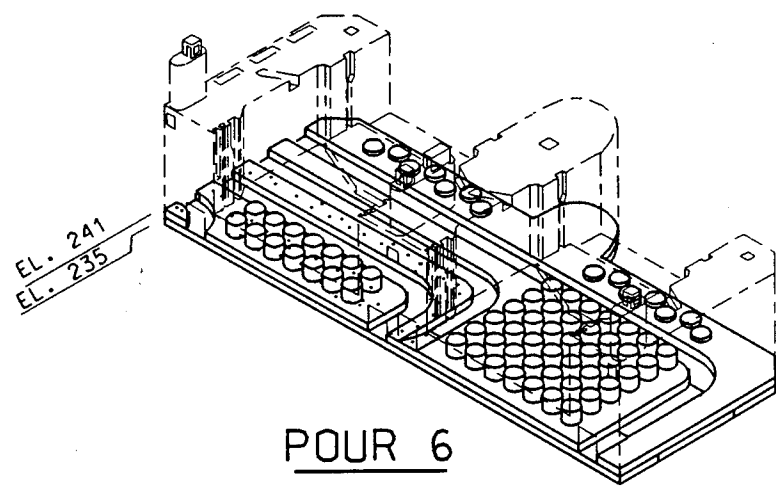
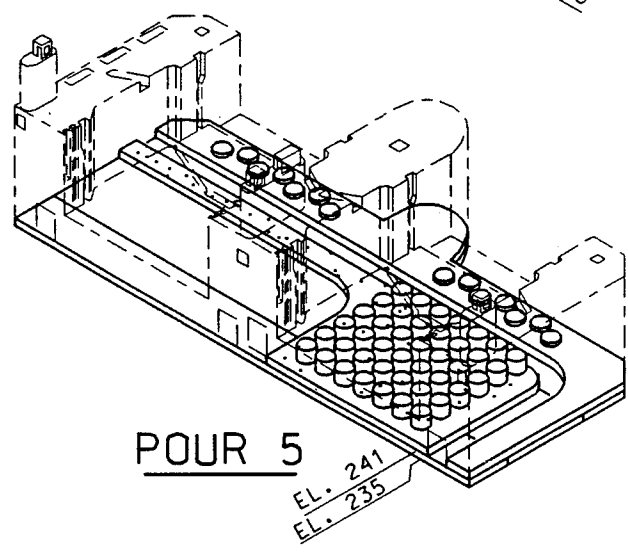
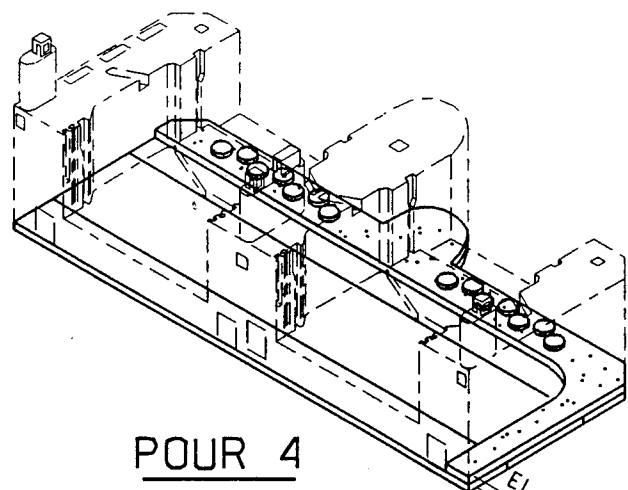
```

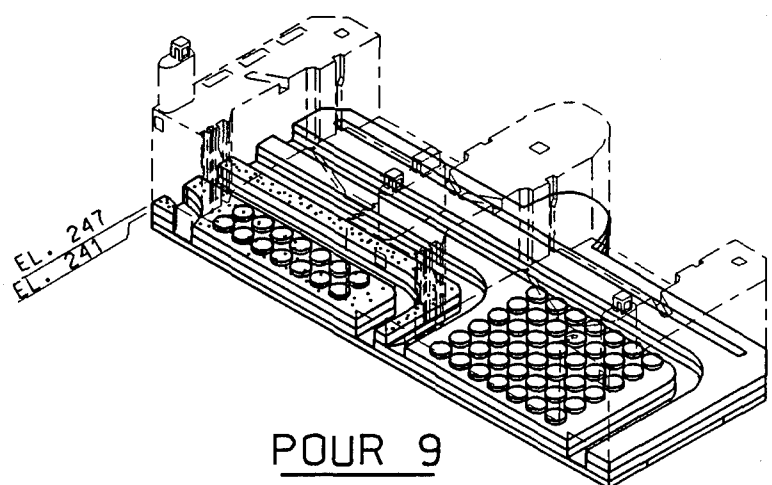
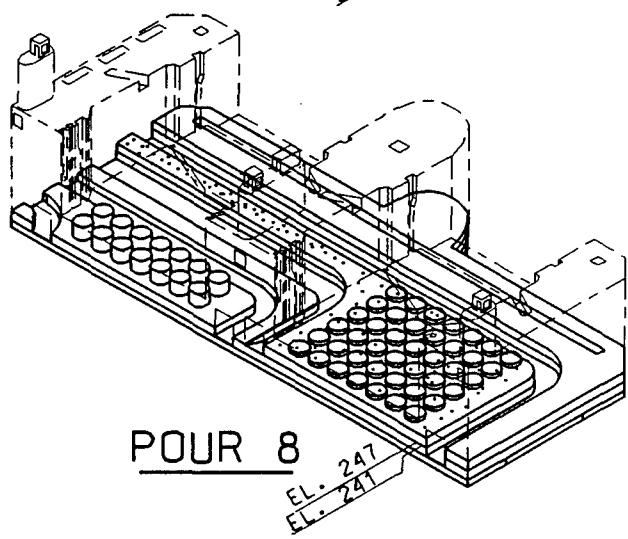
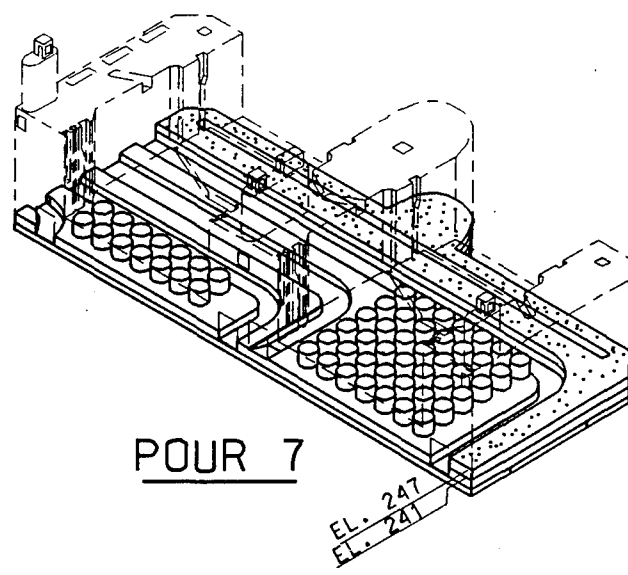
## **Appendix B**

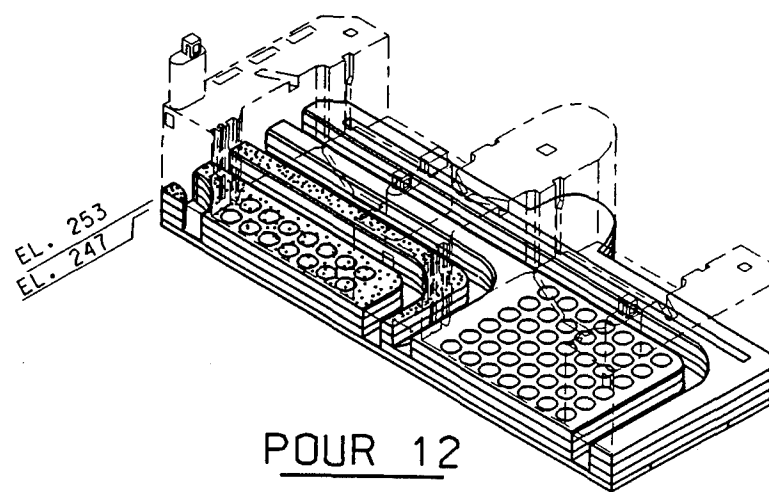
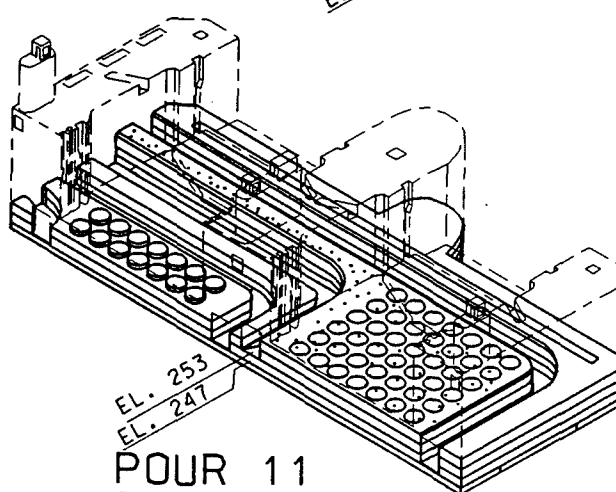
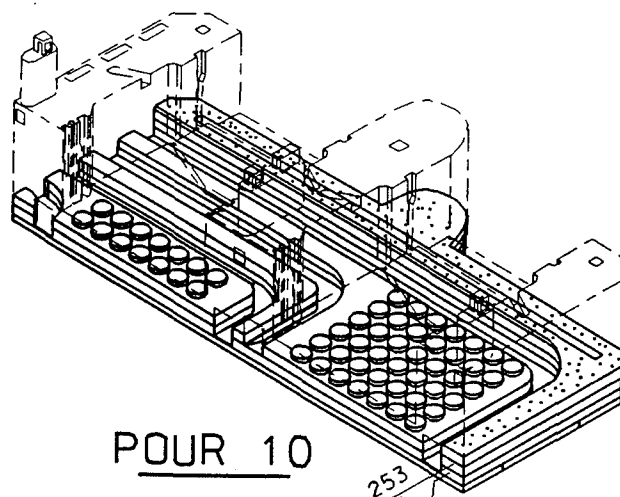
## **Lift Placement Sequence**

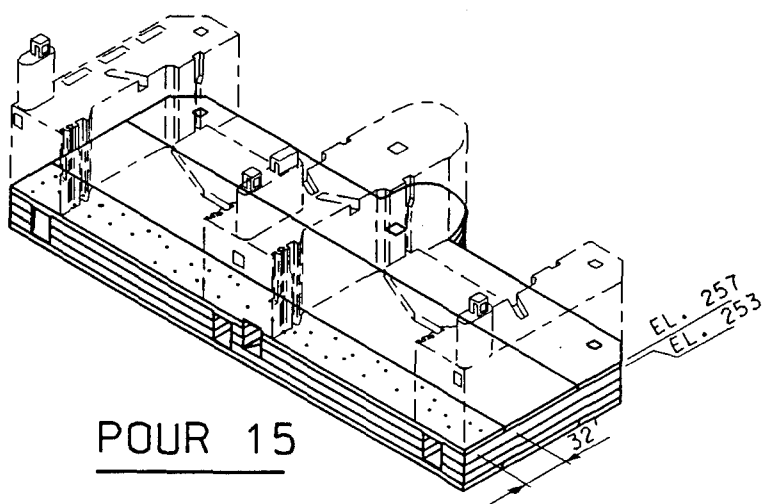
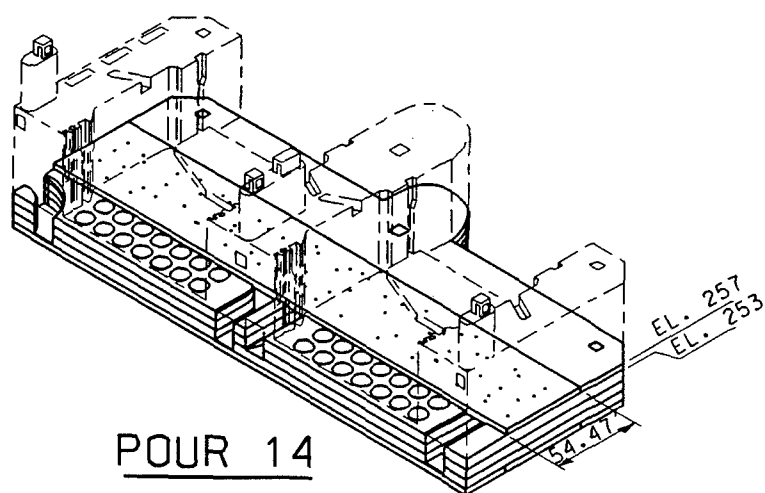
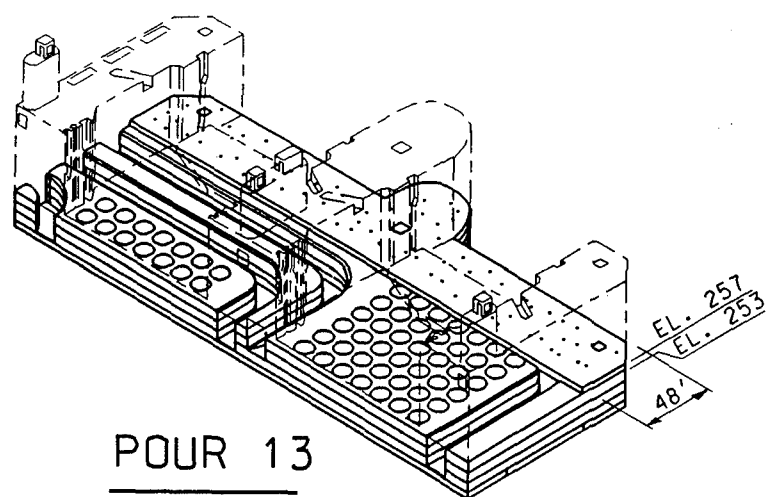
---

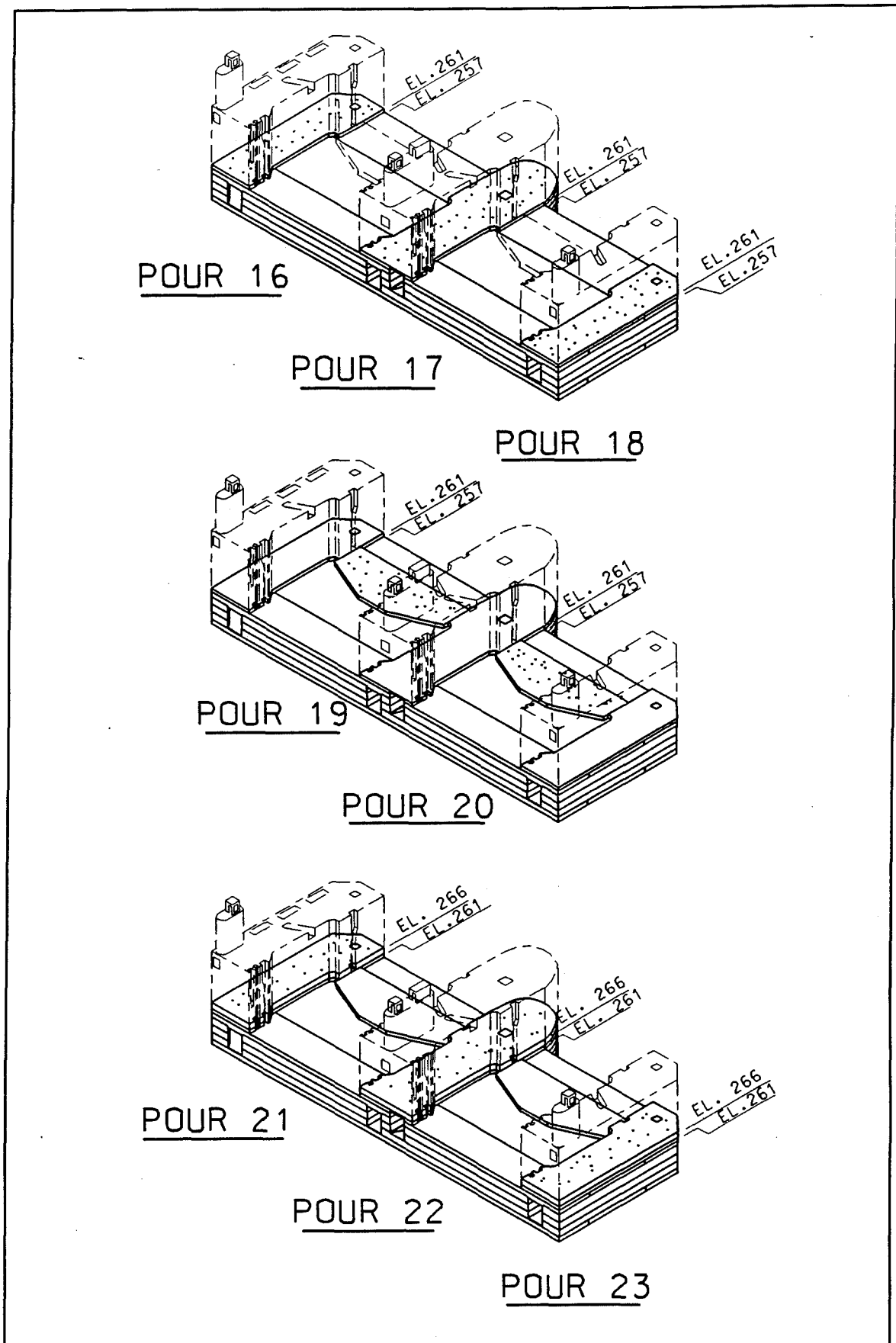


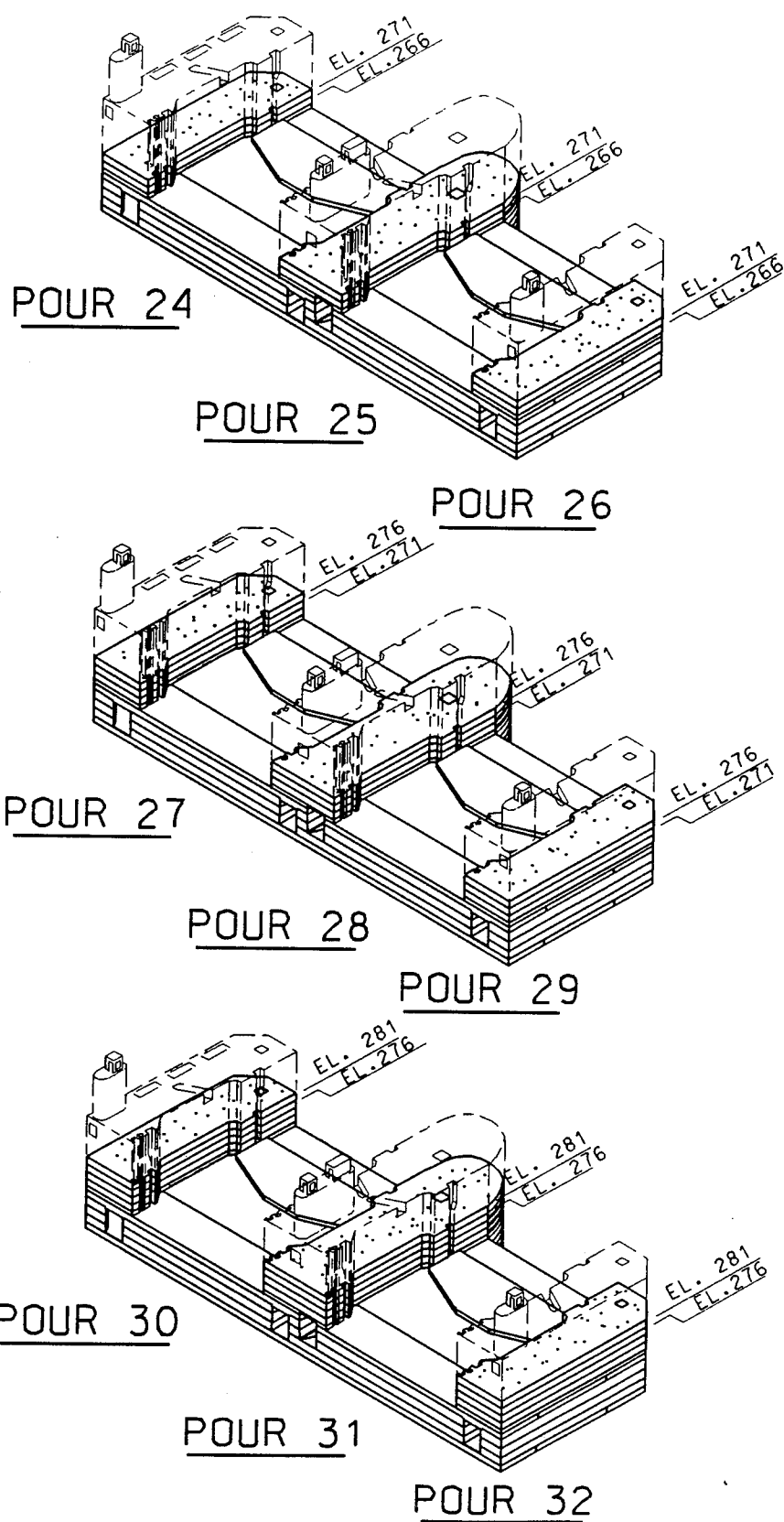


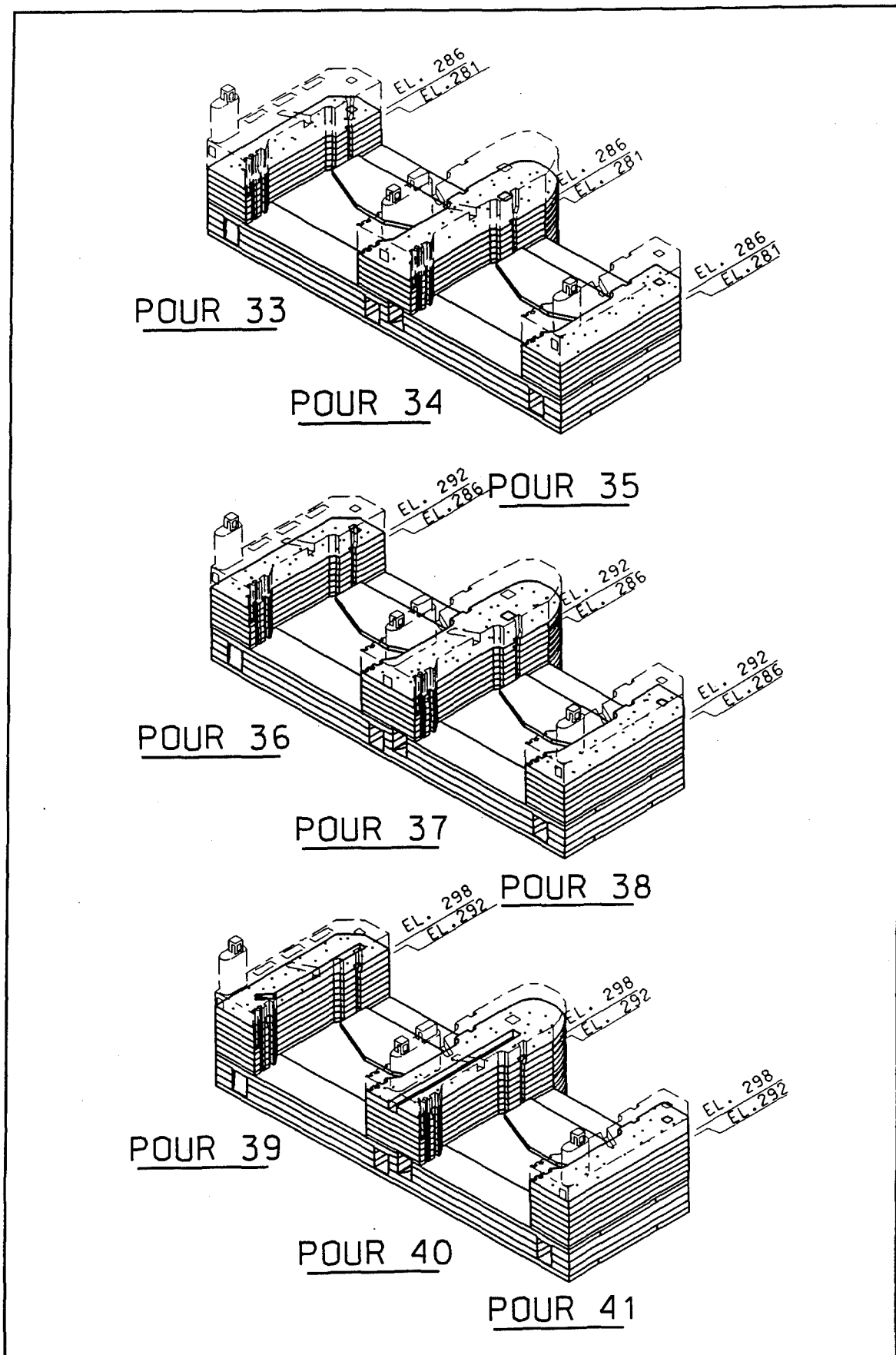


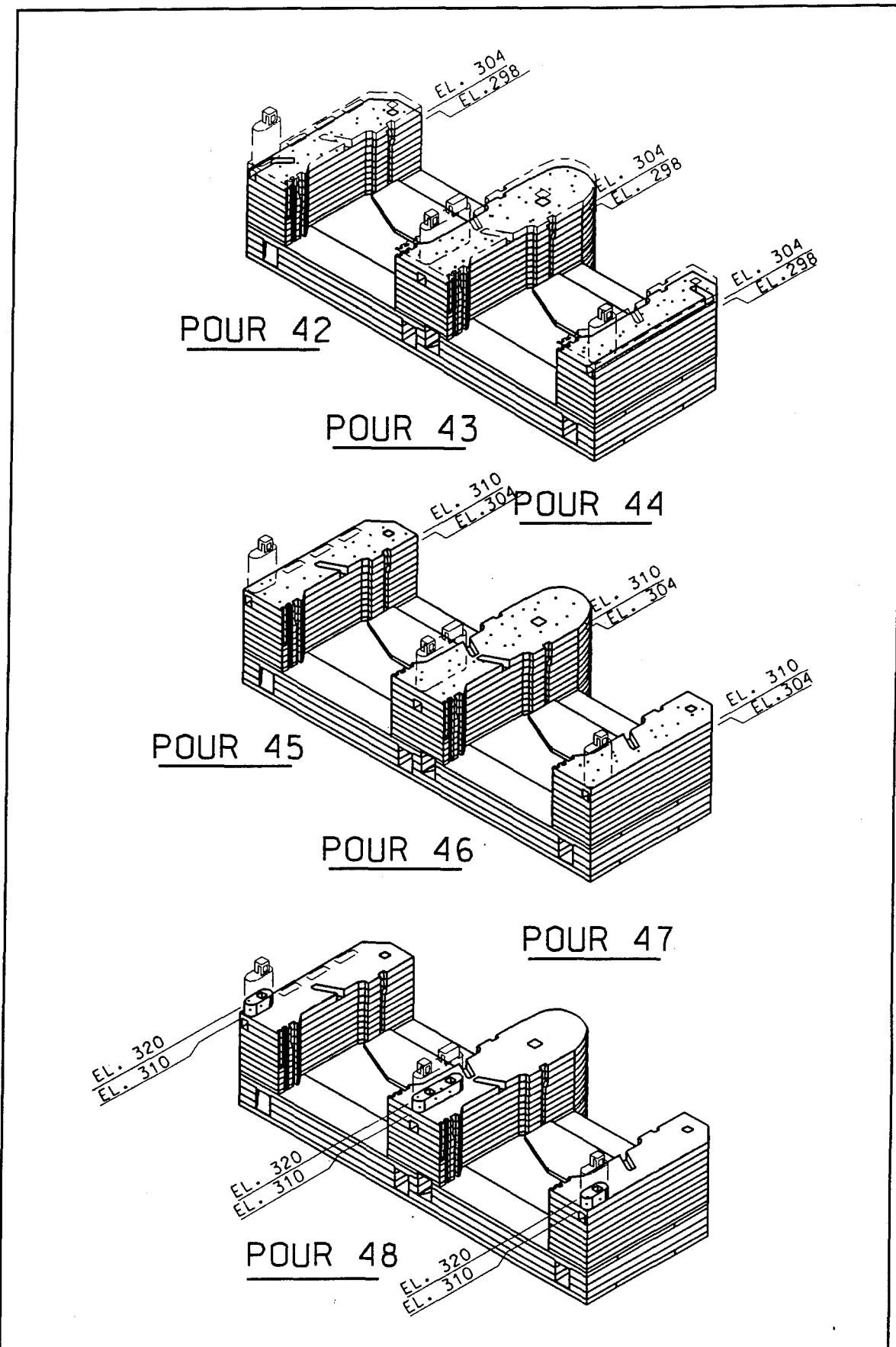


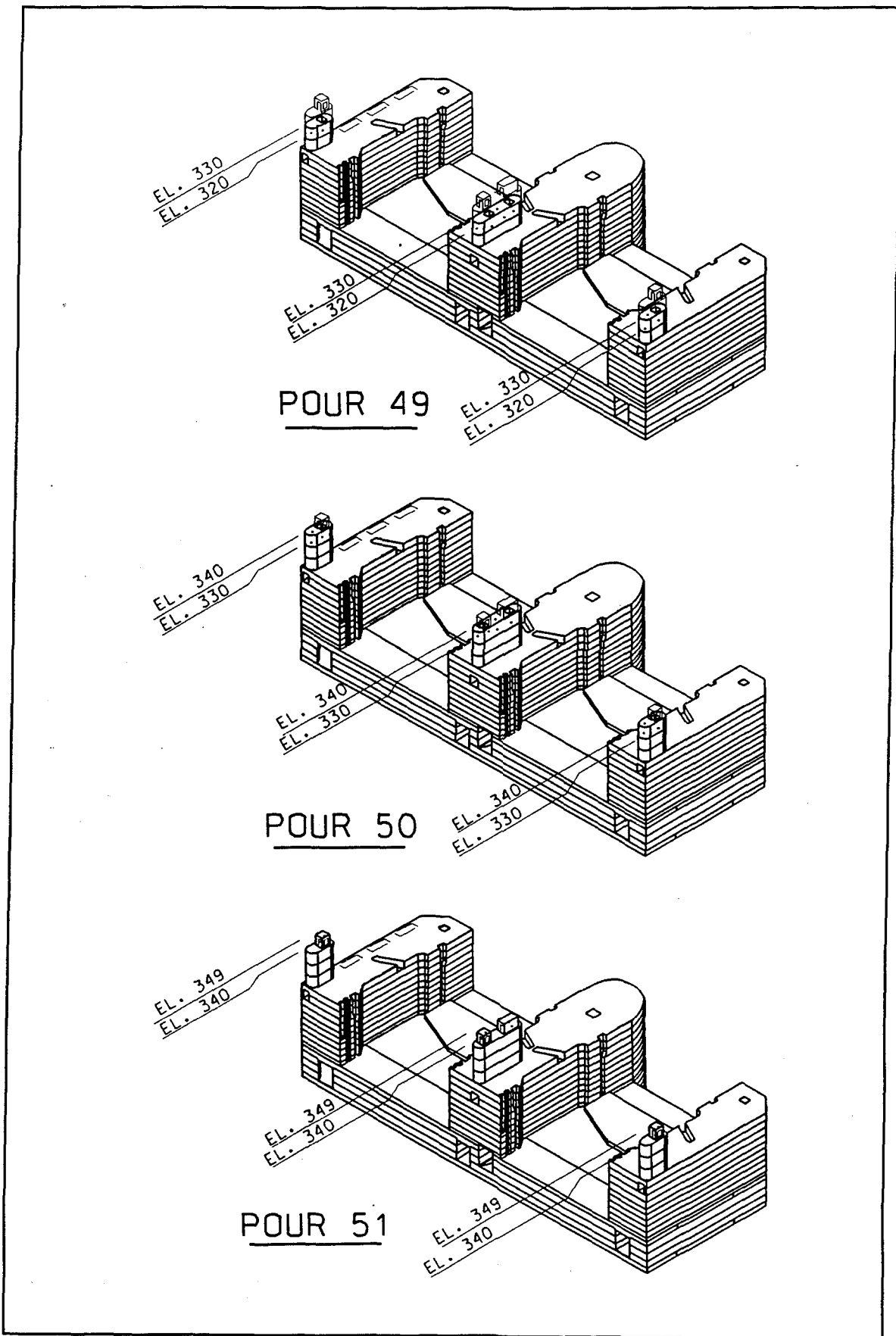












# REPORT DOCUMENTATION PAGE

Form Approved  
OMB No. 0704-0188

Public reporting burden for this collection of information is estimated to average 1 hour per response, including the time for reviewing instructions, searching existing data sources, gathering and maintaining the data needed, and completing and reviewing the collection of information. Send comments regarding this burden estimate or any other aspect of this collection of information, including suggestions for reducing this burden, to Washington Headquarters Services, Directorate for Information Operations and Reports, 1215 Jefferson Davis Highway, Suite 1204, Arlington, VA 22202-4302, and to the Office of Management and Budget, Paperwork Reduction Project (0704-0188), Washington, DC 20503.

<b>1. AGENCY USE ONLY (Leave blank)</b>			<b>2. REPORT DATE</b> August 1995	<b>3. REPORT TYPE AND DATES COVERED</b> Final report
<b>4. TITLE AND SUBTITLE</b> Nonlinear, Incremental Structural Analysis for the Lower Miter Gate Monolith at Olmsted Locks and Dam			<b>5. FUNDING NUMBERS</b>	
<b>6. AUTHOR(S)</b> Barry D. Fehl, Sharon Garner, Randy J. James, Robert S. Dunham, L. Zhang			<b>8. PERFORMING ORGANIZATION REPORT NUMBER</b> Technical Report ITL-95-6	
<b>7. PERFORMING ORGANIZATION NAME(S) AND ADDRESS(ES)</b> See reverse.				
<b>9. SPONSORING/MONITORING AGENCY NAME(S) AND ADDRESS(ES)</b> U.S. Army Engineer District, Louisville P.O. Box 59 Louisville, KY 40201-0059			<b>10. SPONSORING/MONITORING AGENCY REPORT NUMBER</b>	
<b>11. SUPPLEMENTARY NOTES</b> Available from National Technical Information Service, 5285 Port Royal Road, Springfield, VA 22161.				
<b>12a. DISTRIBUTION/AVAILABILITY STATEMENT</b> Approved for public release; distribution is unlimited.			<b>12b. DISTRIBUTION CODE</b>	
<b>13. ABSTRACT (Maximum 200 words)</b> <p>The Olmsted Locks and Dam will be constructed on the Ohio River at mile 964.4 and will replace two existing locks. Extensive investigations have been undertaken to determine the constructability of the lock using nonlinear, incremental structural analysis (NISA) methods as outlined in ETL 1110-2-324, "Special Design Provisions for Massive Concrete Structures." The need for the comprehensive studies was a result of the fact that the Olmsted Locks will be constructed using the unprecedented W-frame type construction.</p> <p>This report is a part of the third phase of the study for evaluation of the constructability of the Olmsted Locks. The first two phases evaluated parameters such as creep, shrinkage, plane stress, plane strain, placing schemes, and concrete mixtures and results are reported in a WES report "Nonlinear, Incremental Structural Analysis of Olmsted Locks and Dam."</p> <p>Results of both two- and three-dimensional (2D and 3D) analyses performed on the lower miter gate monolith are presented herein. Preliminary analyses were performed using 2D models to assess effects of construction parameters prior to performing the 3D analyses. Results of 3D analyses showed that 2D analyses may not provide sufficient information when considering the effects of temperature.</p>				
<b>14. SUBJECT TERMS</b> Aging modulus Cracking Creep			<b>15. NUMBER OF PAGES</b> Heat of hydration Incremental construction Nonlinear Shrinkage Temperature Thermal stress 272	
<b>16. PRICE CODE</b>				
<b>17. SECURITY CLASSIFICATION OF REPORT</b> UNCLASSIFIED	<b>18. SECURITY CLASSIFICATION OF THIS PAGE</b> UNCLASSIFIED	<b>19. SECURITY CLASSIFICATION OF ABSTRACT</b>	<b>20. LIMITATION OF ABSTRACT</b>	

7. (Concluded).

U.S. Army Engineer Waterways Experiment Station  
3909 Halls Ferry Road, Vicksburg, MS 39180-6199;  
ANATECH Research Corporation  
5435 Oberlin Drive, San Diego, CA 92121